**The Dissertation Committee for Sean Patrick Berglund Certifies that this is the approved version of the following dissertation:**

# Mixed Metal Oxide Semiconductors and Electrocatalyst Materials for Solar Energy Conversion

**Committee:**

C. Buddie Mullins, Supervisor

Allen J. Bard

Brian A. Korgel

Gyeong S. Hwang

Keith J. Stevenson

# Mixed Metal Oxide Semiconductors and Electrocatalyst Materials for Solar Energy Conversion

**by**

**Sean Patrick Berglund, B.S.**

**Dissertation**

Presented to the Faculty of the Graduate School of

The University of Texas at Austin

in Partial Fulfillment

of the Requirements

for the Degree of

**Doctor of Philosophy**

**The University of Texas at Austin**

**December 2013**

## Acknowledgements

First I would like to acknowledge my advisor, Prof. C. Buddie Mullins, who has done a tremendous job of expanding the research areas and productivity of the group since I joined five years ago. I truly appreciate his advice, encouragement, sincerity, and willingness to make time for each of his graduate students. I would also like acknowledge Prof. Allen J. Bard for all of the wisdom and guidance he provided to those of us working in electrochemistry and photo-electrochemistry.

I feel fortunate to have joined Prof. Mullins' research group when I did because I had the opportunity to work with many intelligent, hard-working, and likeable people. I thank Dr. David Flaherty for mentoring me during my first year and teaching me about surface science and high vacuum apparatus. Collectively, I would like to thank Dr. Nathan Hahn, Dr. Son Hoang, Dr.Yong-Mao Lin, and Paul Abel for assistance with materials research and setting up equipment in multiple labs that I was able to use. I thank Dr. Nathan Hahn for sharing his strong understanding of photo-electrochemistry. Over the years I observed Dr. Son Hoang grow as researcher and an individual. I greatly appreciate his help and companionship in the lab. I thank the rest of Prof. Mullins' group as well, especially Dr. Ming Pan, Alex Rettie, and Will Chemelewski, and two visiting researchers, Huichao He and Yiqing Sun.

During my time at the University of Texas at Austin I have been able to collaborate with many outstanding researchers. In particular, I acknowledge Stephen Fosdick and Prof. Dick Crooks for collaboration on bi-polar electrodes projects. I recognize Dr. Hyun Park, Dr. Heechang Ye, and Dr. Heung Chan Lee in Prof. Bard's research group for assistance with projects involving $BiVO_4$ and the array dispenser/scanner. Dr. Kyoung E. Kweon and Prof. Gyeong Hwang also provided

theoretical insights for $BiVO_4$. I thank Dr. Vincent Holmberg and Prof. Brian Korgel for expertise in UV-Vis measurements, and Joe McCrate, Tyler Elko-Hansen, and Prof. Ekerdt for facilitating silicon cleaning/etching.

I owe thanks to Mark Ramsdale for teaching me about LabVIEW and for helping me set up the deposition chamber and array scanner. Several undergraduate students worked with me on research projects including Sybil Wong, Paul Núñez, Raymond Fullon, and Ryan Minter. I wish them well in future endeavors. Many staff members at the University of Texas at Austin assisted me with equipment fabrication and materials analysis, especially Mike Ronalter, Butch Cunningham, Jim Smitherman, Eddie Ibarra, Dr. Hugo Celio, Dr. Andrei Dolocan, Dr. Joy (Xiaole) Chen.

For financial support I acknowledge the National Science Foundation Graduate Research Fellowship program and the University of Texas at Austin Cockrell School of Engineering for the Thrust 2000 Graduate Fellowship in Engineering (Harry P. Whitworth endowed and Wayne Nance Family endowed).

I returned to academia after five years of working in industry and I was immediately impressed by the maturity, intelligence, and work ethic of my incoming class in the chemical engineering Ph.D. program. I thank them for accepting me and for helping me make it through my first year classes and qualifying exams including Dr. Josh Katzenstein, Zach Smith, Will Kelton, Paul Abel, Dr. Thomas Lewis, Dr. Amanda Lanza, Dr. Bill Liechty, Dr. Eric Young, and Richelle Thomas. I am especially grateful to Will Kelton, Zach Smith, and Regina Smith for their long-lasting friendship.

Last but not least, I would like to thank my parents John and Judy Berglund, who have continuously supported me even at a time when I should have been further along in my career and other aspects of life. They were there for me during the best and worst moments and I will always be in debt to them for their love and support.

# Mixed Metal Oxide Semiconductors and Electrocatalyst Materials for Solar Energy Conversion

Sean Patrick Berglund, Ph.D.

The University of Texas at Austin, 2013

Supervisor: Charles Buddie Mullins

The sun is a vast source of renewable energy, which can potentially be used to satisfy the world's increasing energy demand. Yet many material challenges need to be overcome before solar energy conversion can be implemented on a larger scale. This dissertation focuses on materials used for solar energy conversion through photo-electrochemical (PEC) processes. It discusses methods for improving PEC materials, namely mixed metal oxide semiconductors, by nanostructuring, incorporation of additional elements, and application surface electrocatalysts.

In this dissertation several material synthesis techniques are detailed. A high vacuum synthesis process known as reactive ballistic deposition (RBD) is used to synthesize nanostructured bismuth vanadate ($BiVO_4$), which is studied for PEC water oxidation. Additionally, ballistic deposition (BD) is used to incorporate Mo and W into nanostructured $BiVO_4$ to improve the PEC activity. An array dispenser and scanner system is used to incorporate metals into copper oxide (CuO) and copper bismuth oxide ($CuBi_2O_4$) and over 3,000 unique material compositions are tested for cathodic photoactivity. The system is also used to test 35 elements as single component metal oxides, mixed metal oxides, and dopants for titanium dioxide ($TiO_2$) for use in dye-

sensitized solar cells (DSCs). Lastly, RBD is used to deposit tungsten semicarbide ($W_2C$) onto p-type silicon (p-type) substrates as an electrocatalyst for PEC proton reduction.

In many cases, the synthesis techniques and new material combinations presented in this dissertation result in improved PEC performance. The materials are thoroughly assessed and characterized to gain insights into their nanostructure, chemical composition, light absorption, charge transport properties, catalytic activity, and stability.

# Table of Contents

## List of Tables

# List of Figures

# Chapter 1: Introduction

## SUSTAINABLE ENERGY CHALLENGE

One of the greatest challenges facing mankind in the 21st century is the development of sustainable energy production to satisfy the world's increasing energy demand. Industrialized nations need energy to maintain a high standard of living and developing nations need energy to modernize. World power consumption is currently around 15 TW and is expected to increase to nearly 25 TW by the year 2035.[1,2]

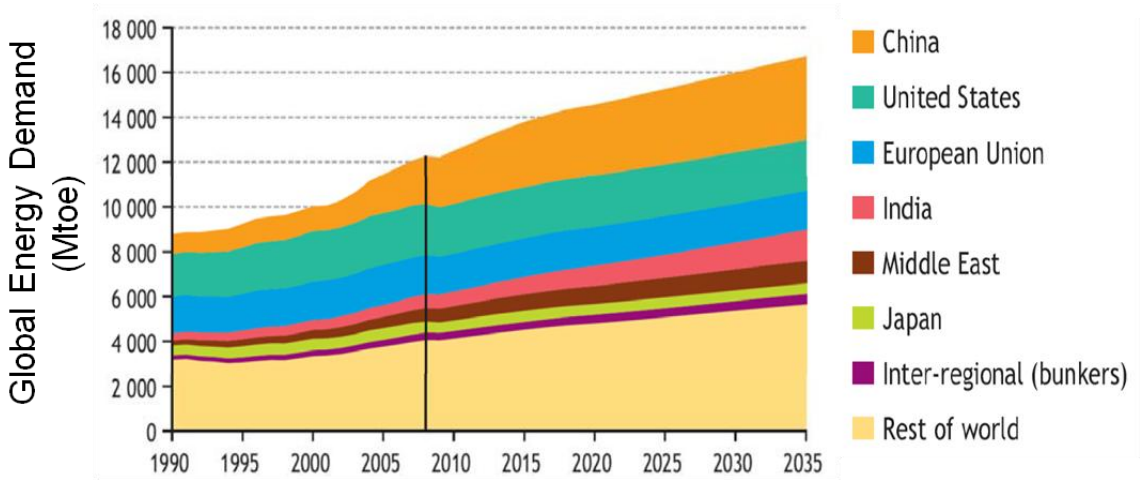


Figure 1.1 Global energy demand in million tonnes of oil equivalent (Mtoe).[1]

Fossil fuels, which currently account for 85% of the world's energy supply, will not be able to satisfy the continued increase in demand because reserves are in finite supply. Based on current world energy consumption rates the estimated reserves are 53 years for oil, 109 years for coal, and 56 years for natural gas.[3] Another concern with the use of fossil fuels is the emission of greenhouse gases such as $CO_2$, which contribute to global warming. Energy-related $CO_2$ emissions through 2035 are anticipated to result in a long-term average temperature increase of at least 3 $^{o}$C.[4] To reduce our dependence on fossil

fuels and decrease $CO_2$ emissions we must explore alternative sources of energy that are sustainable. Perhaps the largest source of renewable energy available to us is the sun, which irradiates the earth's surface with approximately 120,000 TW of power.[5] If we can harness 0.01% of this irradiation then we can meet the current world energy demand. This may be possible using solar energy conversion technologies.

## SOLAR ENERGY CONVERSION

Photovoltaic (PV) devices or solar cells convert solar energy into electricity and are the most common type of solar energy technology in use.[6] The electricity produced by a PV device can be used to drive a load or stored in the energy grid for later use. Unfortunately PV devices can be prohibitively expensive compared to existing fossil fuel technologies. The levelized cost of energy is at least 5 times higher for PV technology than for electricity generation from coal.[2] Another challenge with PV technology is issue of inconsistent electricity production due to variability in the solar flux (day/night, seasons, weather, etc.) combined with variability in demand. Expansion of energy production by PV will require the development of less expensive PV materials and a flexible electricity storage grid.

Photo-electrochemical (PEC) devices offer another means of solar energy conversion.[5,7] Such devices can be used for PEC water splitting (photoelectrolysis of water) in which hydrogen and oxygen are evolved from water according the overall water splitting reaction:

$$H_2O_{(l)} \xrightarrow{h\nu} O_{2(g)} + H_{2(g)} \qquad (\Delta G^0 = 237.2\ \text{kJ/mol})$$

The hydrogen that is produced can be collected and utilized a clean burning fuel, which does not emit greenhouse gases. An advantage of PEC water splitting is that hydrogen has high energy density by weight and can be stored or transported indefinitely until it is

needed. Hydrogen is also an important feedstock for the petroleum and chemical industries. Unfortunately, the production of hydrogen by PEC water splitting is even more cost prohibitive than electricity generation by PV so PEC devices are not currently in use on a practical level. It has been proposed that a cost effective PEC device should have a solar-to-hydrogen (STH) efficiency of at least 10%.[8] At the same time the PEC device should be composed of earth-abundant and long-lasting materials.

**PHOTO-ELECTROCHEMICAL MATERIALS**

Two main types of materials are utilized as photo-electrodes in PEC devices for the water splitting half-reactions. n-type semiconductors are typically used as photoanodes for the water oxidation reaction while p-type semiconductors are usually used as photocathodes for the proton reduction reaction. The half reactions are shown below along with their standard electrochemical potentials:

$$2\,H_2O_{(l)} \rightarrow O_{2(g)} + 4\,H^+_{(aq)} + 4\,e^- \qquad (E^0 = +1.23\ \text{V}\ \textit{vs.}\ \text{NHE})$$

$$4\,H^+_{(aq)} + 4\,e^- \rightarrow 2\,H_{2(g)} \qquad (E^0 = 0.00\ \text{V}\ \textit{vs.}\ \text{NHE})$$

In order for a semiconductor material to drive one of the water splitting half reactions, the band edges (conduction band and valence band) must straddle the corresponding electrochemical potential. In addition, the band gap energy ($E_g$) should be small enough that the material can absorb a large portion of the solar spectrum often denoted by Air Mass 1.5 (AM 1.5).[9] Figure 1.2 shows the band edge positions of several PEC materials used for water oxidation and proton reduction along with their maximum theoretical photocurrent density (based on $E_g$). Under AM 1.5 illumination, 10% STH efficiency corresponds to a photocurrent density of approximately 8 mA/cm$^2$

p-type and n-type semiconductors can also be joined together in multi-junction device to improve the overall efficiency.[10] In fact the goal of 10% STH efficiency has

already been achieve with multi-junction photocathodes composed of high quality, single-crystal semiconductor materials such as Si, GaAs, GaP, and InP.[11-13] However such devices are extremely expensive to make and unstable for long periods under illumination in aqueous electrolytes.

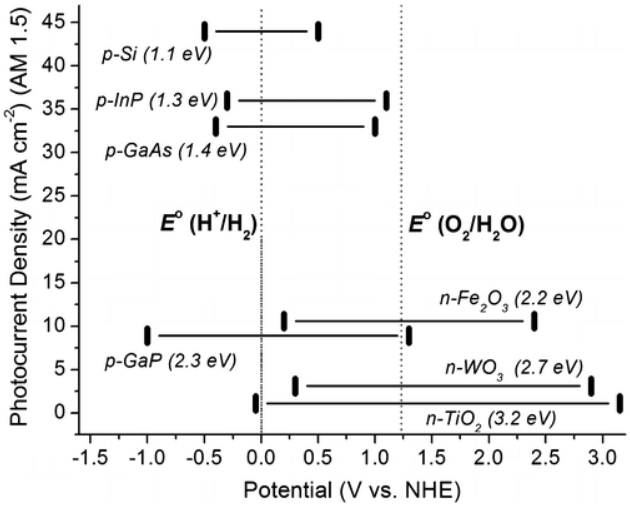


Figure 1.2. Plot of the band edges for select semiconductor materials used for PEC water splitting.[7] The optical band gap ($E_g$) of each material is in parenthesis while the conduction and valence bands are represented by the left and right hashes, respectively. The ordinate indicates the maximum theoretical photocurrent density under AM 1.5 illumination.

Poly-crystalline metal oxide semiconductors such as $TiO_2$, $Fe_2O_3$, $WO_3$, and $BiVO_4$ are an attractive alternative to single-crystal semiconductors, especially as photoanode materials for the water oxidation reaction.[5,7,14] Metal oxides are less expensive to process and are inherently more stable to oxidation as they are already oxidized. However, metal oxides suffer from the problem of low carrier mobility and generally produce low photo-conversion efficiencies. Therefore metal oxides must be developed further for PEC water splitting.

To obtain high efficiency, metal oxide photo-electrodes should be thick enough to absorb a large fraction of incident light but not too thick or they will suffer from excessive electron-hole recombination.[15] For most metal oxides, the required thickness for adequate light absorption is significantly longer than the electron and hole diffusion lengths. This makes optimization of both charge transport and light absorption a challenge. Nanostructuring can be used to help overcome this challenge. The nanorod morphology shown in Figure 1.3 allows for light absorption along the length of the nanorods while shortening the distance that photo-generated holes must travel in the radial direction. Other types of nanostructure morphologies such as dendritic, fractal, and packed nanoparticles offer similar advantages. Nanostructure also increases the specific surface area available for the water oxidation or proton reduction reactions.

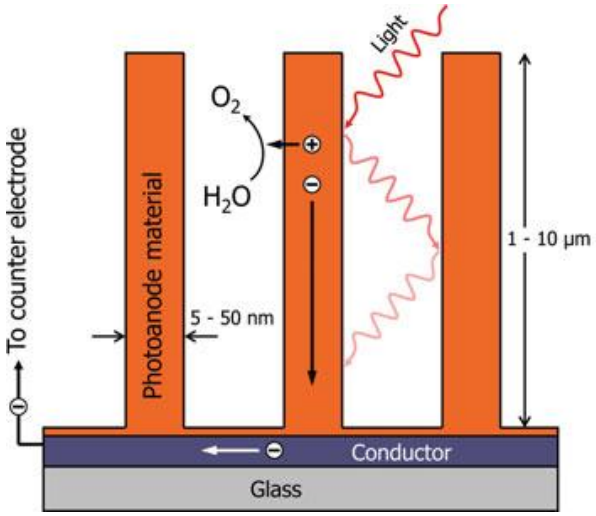


Figure 1.3 Schematic of a nanostructured photoanode consisting of high aspect ratio nanorods (5-50 nm diameter, 1-10 µm length).[5] The nanorods shorten the travel distance of photo-generated holes (+) in the radial direction while still allowing for adequate light absorption in the co-axial direction.

Another method for improving the efficiency of metal oxides for PEC water splitting is through incorporation of additional elements or doping with impurities.[16-18]

Incorporation of certain elements has been shown to improve charge transport by increasing the conductivity of some metal oxides. For example the photoactivity of $BiVO_4$ can be increased by incorporation of Mo and W as shown in Figure 1.4.[19-21] Incorporation of elements can also alter the band structure, which has been demonstrated for doped $TiO_2$ experimentally and through density functional theory calculations.[22,23]

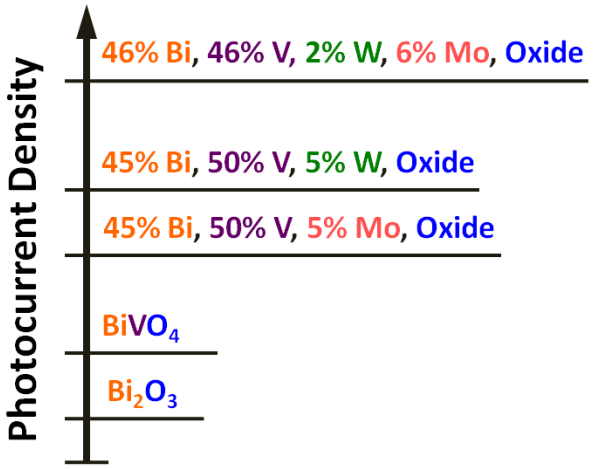


Figure 1.4 Diagram of the relative photocurrent density for incorporation of Mo and W into $BiVO_4$ at potentials between 0.4 and 0.8 V vs. RHE.[20,21]

Finally, an electrocatalyst can be applied to the surface of PEC materials to increase efficiency by improving the reaction kinetics for the water oxidation or proton reduction reactions. The most recent benchmark photocurrent density for metal oxides (~3 $mA/cm^2$ under AM 1.5 illumination) was achieved using nanostructured $\alpha$-$Fe_2O_3$ with a fractal morphology and $IrO_2$ nanoparticles as an electrocatalyst.[24] The record efficiency PEC devices composed of Si, GaAs, GaP, and InP utilized metals such as Rh and Pt as electrocatalysts. Ir, Rh, and Pt are extremely rare elements, which makes them expensive to use for solar energy conversion technologies. Alternative electrocatalyst materials must be developed to make PEC water splitting more cost effective.

## DYE-SENSITIZED SOLAR CELLS

The last type device that will be mentioned is the dye-sensitized solar cell (DSC), which is a PEC device that is used to convert solar energy into electrical energy. DSCs use a reversible redox couple (e.g. iodide/triiodide) contained between a counter electrode and a thin layer of dye molecules that are anchored to a wide bandgap metal oxide semiconductor such as nanoporous $TiO_2$.[25] During light absorption, the dye molecules rapidly inject photo-excited electrons into the conduction band of the semiconductor while the redox species continuously regenerate the oxidized dye molecules to the ground state and transport charge to the counter electrode. Large scale DSC modules with efficiencies of over 8% have been fabricated.[6] New metal oxide materials may offer further improvements in efficiency.

## DISSERTATION OVERVIEW

This dissertation consists of 7 chapters. Chapter 1 provided background information on sustainable energy challenges and solar energy conversion. It introduced the subject of photo-electrochemical (PEC) water splitting and summarized methods for improving the efficiency of PEC materials. The next 5 chapters (chapter 2, 3, 4, 5, and 6) describe scientific studies which aimed at improving metal oxide and electrocatalyst materials for PEC water splitting and DSCs. Each study has been published or submitted for publication in peer-reviewed journals. Chapter 7 contains concluding remarks and recommendations for future studies.

Chapter 2 describes nanostructured $BiVO_4$ films that are synthesized by co-evaporation of bismuth and vanadium in an oxygen ambient, a process referred to as reactive ballistic deposition (RBD). The films are tested in various electrolyte solutions to assess their activity for photoelectrochemical water oxidation. Deposition parameters, including the V/Bi atomic flux ratio and the incident angle of deposition, are adjusted.

Films deposited with excess vanadium (V/Bi=2) and incident angles of deposition at 65° show the highest initial photocurrents with IPCE values above 21% for light wavelengths of 340-460 nm (in 0.5 M $Na_2SO_4$ at 1.0 V vs. Ag/AgCl). With continued illumination the excess vanadium in these films dissolves into the electrolyte and the photocurrents drop by 60-75% before reaching steady-state. The steady-state photocurrent and IPCE values (above 14% for 340-460 nm light) are higher than the initial values for films synthesized with stoichiometric amounts of vanadium and bismuth (V/Bi=1) and incident angles of deposition at 65°. Stoichiometric $BiVO_4$ films remain stable under illumination but their photocurrents are limited by surface reaction kinetics. The addition of cobalt as an electrocatalyst to the surface of these films increases their photocurrent by a factor of three.

Chapter 3 describes a follow-up study on porous, nanostructured $BiVO_4$ films that are incorporated with Mo and W by simultaneous evaporation of Bi, V, Mo, and W in vacuum followed by oxidation in air. Synthesis parameters such as the Bi:V:Mo:W atomic ratio and deposition angle are adjusted to optimize the films for photoelectrochemical water oxidation. Films synthesized with a Bi:V:Mo:W atomic ratio of 46:46:6:2 (6% Mo, 2% W) demonstrate the best PEC performance with photocurrent densities 10 times higher than for pure $BiVO_4$ and greater than previously reported for Mo and W containing $BiVO_4$. The films consist of a directional, nanocolumnar layer beneath an irregular surface structure. Backside illumination utilizes light scattering off the irregular surface structure resulting in 30-45% higher photocurrent densities than for frontside illumination. To improve the kinetics for water oxidation Pt is photo-deposited onto the surface of the 6% Mo, 2% W $BiVO_4$ films as an electrocatalyst. These films achieve quantum efficiencies of 37% at 1.1 V vs. RHE and 50% at 1.6 V vs. RHE for 450 nm light

Chapter 4 changes the focus to metal oxides for the proton reduction reaction. It involves a combinatorial chemistry study in which a dispenser and scanner system is used to create and screen Bi-M-Cu oxide arrays for cathodic photoactivity, where M represents 1 of 22 different transition and post-transition metals. Over 3,000 unique Bi:M:Cu atomic ratios are screened. Of the 22 metals tested, 10 show a M-Cu oxide with higher photoactivity than CuO and 10 show a Bi-M-Cu oxide with higher photoactivity than $CuBi_2O_4$. Cd, Zn, Sn, and Co produce the most photoactive M-Cu oxides, all showing a 200% - 300% improvement in photocurrent over CuO. Ag, Cd, and Zn produce the highest photoactivity Bi-M-Cu oxides with a 200% - 400% improvement over $CuBi_2O_4$. Most notable is a Bi-Ag-Cu oxide (Bi:Ag:Cu atomic ratio of 22:3:11) which shows 4 times higher photocurrent than $CuBi_2O_4$. This material is capable of evolving hydrogen under illumination in neutral electrolyte solutions at 0.6 V vs. RHE when Pt is added to the surface as an electrocatalyst.

Chapter 5 details an electrocatalyst study for the proton reduction reaction with single crystalline silicon as the photocathode material. p-Si/$W_2C$ photocathodes are synthesized by evaporating tungsten metal in an ambient of ethylene gas to form tungsten semicarbide ($W_2C$) thin films on top of p-type silicon (p-Si) substrates. As deposited the thin films contain crystalline $W_2C$ with a bulk W:C atomic ratio of approximately 2:1. The $W_2C$ films demonstrate catalytic activity for the hydrogen evolution reaction (HER) and p-Si/$W_2C$ photocathodes produce cathodic photocurrent at potentials more positive than 0.0 V vs. RHE while bare p-Si photocathodes do not. The $W_2C$ films are an effective support for Pt nanoparticles allowing for a considerable reduction in Pt loading. p-Si/$W_2C$/Pt photocathodes with Pt nanoparticles achieve photocurrent onset potentials and limiting photocurrent densities that are comparable to p-Si/Pt photocathodes with 9 as

much Pt. This makes $W_2C$ an earth abundant alternative to pure Pt for use as an electrocatalyst on photocathodes for the HER.

Chapter 6 explains how the combinatorial chemistry approach is used to screen dye-sensitized solar cell (DSC) materials. 35 elements are investigated as single component metal oxides and as dopants for $TiO_2$ for use in DSCs. An array dispenser and scanner system is utilized for high throughput testing of the single component metal oxides and hundreds of doped $TiO_2$ compositions. The optimal dopant concentrations are identified and summarized according to their effect on short circuit current ($I_{SC}$) and open circuit voltage ($V_{OC}$). New dopant candidates are discovered including several post-transition metals, which show improvements in DSC performance when incorporated at compositions of 6% In $TiO_2$, 6% Sn $TiO_2$, and 6% Sb $TiO_2$ (metals basis). These compositions are used to synthesize scaled-up DSC devices for detailed characterization. Incorporation of 6% In into $TiO_2$ enhances $V_{OC}$ substantially and increased $I_{SC}$ slightly, 6% Sn improves $I_{SC}$ while preserving $V_{OC}$, and 6% Sb increases $I_{SC}$ significantly but decreases $V_{OC}$. When co-incorporated, Cr and Sb show a complimentary interaction, which reduces the resistance to charge transport in the DSC device. 2% Cr, 6% Sb $TiO_2$ show higher $I_{SC}$ and $V_{OC}$ values than 6% Sb $TiO_2$ and considerably higher $I_{SC}$ than 2% Cr $TiO_2$. The fill-factor for 2% Cr, 6% Sb $TiO_2$ is relatively low, but the maximum power is higher than the other compositions due to the higher currents. The $V_{OC}$ values for DSC devices with different compositions correlates linearly with the measured flat-band potentials ($E_{FB}$).

**REFERENCES**

(1) Global Energy Perspectives, 2011.

(2) Annual Energy Outlook 2013, 2013.

(3) BP Statistical Review of World Energy June 2013, 2013.

(4) World Energy Outlook 2012, 2012.

(5) van de Krol, R.; Grätzel, M. Photoelectrochemical Hydrogen Production; Springer: New York Dordrecht Heidelberg London, 2012.

(6) Peter, L. M. Philosophical Transactions of the Royal Society a-Mathematical Physical and Engineering Sciences 2012, 369, 1840-1856.

(7) Walter, M. G.; Warren, E. L.; McKone, J. R.; Boettcher, S. W.; Mi, Q.; Santori, E. A.; Lewis, N. S. Chemical Reviews 2010, 110, 6446-6473.

(8) Bard, A. J.; Fox, M. A. Accounts of Chemical Research 1995, 28, 141-145.

(9) Chandra, S. Photoelectrochemical Solar Cells; Gordon and Breach Science Publishers: New York, 1985.

(10) Nozik, A. J.; Memming, R. d. The Journal of Physical Chemistry 1996, 100, 13061-13078.

(11) Aharon-Shalom, E.; Heller, A. Journal of The Electrochemical Society 1982, 129, 2865-2866.

(12) Ueda, K.; Nakato, Y.; Sakai, Y.; Matsumura, M.; Tsubomura, H. Journal of Applied Physics 1988, 64, 1513-1518.

(13) Khaselev, O.; Turner, J. A. Science 1998, 280, 425-427.

(14) Kudo, A.; Miseki, Y. Chemical Society Reviews 2009, 38, 253-278.

(15) Osterloh, F. E. Chemical Society Reviews 2013, 42, 2294-2320.

(16) Asahi, R.; Morikawa, T.; Ohwaki, T.; Aoki, K.; Taga, Y. Science 2001, 293, 269-271.

(17) Zou, Z.; Ye, J.; Sayama, K.; Arakawa, H. Nature 2001, 414, 625-627.

(18) Woodhouse, M.; Parkinson, B. A. Chemistry of Materials 2008, 20, 2495-2502.

(19) Rettie, A. J. E.; Lee, H. C.; Marshall, L. G.; Lin, J.-F.; Capan, C.; Lindemuth, J.; McCloy, J. S.; Zhou, J.; Bard, A. J.; Mullins, C. B. Journal of the American Chemical Society 2013, 135, 11389-11396.

(20) Berglund, S. P.; Rettie, A. J. E.; Hoang, S.; Mullins, C. B. Physical Chemistry Chemical Physics 2012, 14, 7065-7075.

(21) Park, H. S.; Kweon, K. E.; Ye, H.; Paek, E.; Hwang, G. S.; Bard, A. J. The Journal of Physical Chemistry C 2011, 115, 17870-17879.

(22) Yin, W.-J.; Tang, H.; Wei, S.-H.; Al-Jassim, M. M.; Turner, J.; Yan, Y. Physical Review B 2010, 82, 045106.

(23) Hoang, S.; Berglund, S. P.; Hahn, N. T.; Bard, A. J.; Mullins, C. B. Journal of the American Chemical Society 2012, 134, 3659-3662.

(24) Tilley, S. D.; Cornuz, M.; Sivula, K.; Grätzel, M. Angewandte Chemie International Edition 2010, 49, 6405-6408.

(25) Grätzel, M. Journal of Photochemistry and Photobiology C: Photochemistry Reviews 2003, 4, 145-153.

# Chapter 2: Photoelectrochemical Oxidation of Water Using Nanostructured $BiVO_4$ Films

## INTRODUCTION

Photoelectrochemical splitting of water into hydrogen and oxygen has great potential for solar energy conversion and storage. Since the first experimental demonstration of photoelectrochemical water splitting using $TiO_2$ in the 1970's[1] many different semiconductor materials have been tested.[2-5] However, none of these have been put into practical use in a large scale system. In order to efficiently split water, a photoelectrochemical system must meet many requirements. The system must be composed of materials with band gaps small enough (<3.0 eV) to absorb a large portion of the solar spectrum including visible light. Concurrently, the conduction and valence bands of the materials must straddle the proton reduction and water oxidation redox potentials. The materials should promote facile charge transfer and have high surface area with active sites for both proton reduction and water oxidation. Lastly, the system should be composed of materials that are inexpensive and long lasting otherwise it will not be practical for large scale energy conversion.[6] To date, no known materials satisfy all the above requirements for efficient and cost-effective water splitting.

Recently, $BiVO_4$ has attracted attention due to its high photocatalytic activity for oxygen evolution in aqueous solutions under visible light irradiation relative to other known materials tested under similar conditions.[2] $BiVO_4$ exists in three main polymorphs: the zircon structure with tetragonal crystal system and the scheelite structure with monoclinic and tetragonal crystal systems. The monoclinic crystal system has been reported as the most photoactive form of $BiVO_4$.[7,8] The bandgap of monoclinic $BiVO_4$ has been shown to be 2.3-2.4 eV by experiment[7,9-11] and 2.16 eV (direct band gap) from density functional theory (DFT) calculations.[12] Based on the stoichiometry of $BiVO_4$, the

oxidation states and atomic orbitals are given by: $Bi^{3+}$ ($5d^{10}6s^2$), $V^{5+}$ ($3d^0$), and $O^{2-}$ ($2p^6$). The valence band is formed by coupling of Bi 6s and O 2p orbitals while the conduction band is primarily controlled by V 3d orbitals, with contributions from the O 2p and Bi 6p orbitals.[12,13] The conduction band edge of $BiVO_4$ has been estimated to be at 0 V vs. NHE at pH 0,[14] which corresponds to a valence band edge of 2.4 V vs. NHE at pH 0 (using 2.4 eV as the band gap). Since the conduction band is not more negative than the $H^+$ reduction potential (0.0 V vs. NHE at pH 0), pure $BiVO_4$ cannot evolve substantial amounts of $H_2$ from $H_2O$ without an applied bias on an inert metal counter-electrode. Even with the addition of Pt as an electrocatalyst $BiVO_4$ did not show activity for $H^+$ reduction when illuminated in an aqueous methanol (hole-scavenging) solution.[15] On the other hand, the valence band of $BiVO_4$ is below the water oxidation potential (1.23 V vs. NHE at pH 0) indicating that $BiVO_4$ is thermodynamically capable of evolving $O_2$ from $H_2O$. Several researchers have confirmed that $BiVO_4$ can oxidize water by measuring $O_2$ evolution from aqueous solutions containing $Ag^+$ as a sacrificial reagent ($Ag^+/Ag$ redox potential at 0.7991 V vs. NHE[16]).[7,8,15,17,18] Although $BiVO_4$ is not able to reduce $H^+$, it is still a promising material for water splitting as the photoanode in a multi-photon photoelectrochemical cell (PEC).

A variety of synthesis techniques have been used to produce $BiVO_4$ for photocatalytic testing. $BiVO_4$ was first synthesized for photocatalytic testing by solid-state reaction of $Bi_2O_3$ and $NH_4VO_3$ at high temperatures (970-1170 K)[15] and later by an aqueous process at room temperature using layered compounds of $KV_3O_8$ and $K_3V_5O_{14}$ with $Bi(NO_3)_3$, which showed improved photocatalytic activity.[7] Since then $BiVO_4$ has been prepared by room temperature hydrolysis,[8] metal-organic decomposition[19,20], chemical bath deposition,[21] various hydrothermal routes,[17,22,23] the sol-gel method,[10] solution combustion,[24] flame and ultrasonic spray pyrolysis,[25,26] co-precipitation,[27,28]

electrosynthesis,[29] and flame assisted synthesis.[30] Numerous researchers have modified the aqueous and hydrothermal routes with additional precursors,[31] morphology directing reagents,[32-34] sonication,[35] reflux,[36,37] and microwave irradiation.[38] With the exception of solid-state synthesis, the above methods involve some form of wet chemical processing. The present paper discusses the photocatalytic activity of $BiVO_4$ prepared by a vacuum deposition process in which pure bismuth and vanadium were co-evaporated in the presence of oxygen as a reactant gas. This deposition process is often referred to as reactive ballistic deposition (RBD) and is described in more detail later.[39-45] RBD can have advantages over wet chemistry methods including simultaneous control of the chemical composition and morphology during synthesis, and the elimination of additional reagents that may be required for wet chemical processing that are not desired in the final material.

In order to accurately assess the activity of a material for photoelectrochemical water splitting it is important to check several key metrics including solar to hydrogen (STH) efficiency, incident photon-to-current efficiency (IPCE), and absorbed photon-to-current efficiency (APCE).[46] Experimentally $BiVO_4$ has not been proven to evolve $H_2$ so the STH efficiency cannot be determined without applying a bias between the working and counter electrode. Efficiencies for $O_2$ evolution can be calculated but only a fraction of the recent studies on $BiVO_4$ report such information. A variety of solution species have been used in the study of the photocatalytic properties of $BiVO_4$ including $AgNO_3$, $Fe(NO_3)_3$, $Na_2SO_4$, NaOH, rhodamine B, methylene blue, and methyl orange. Of these solutions $Na_2SO_4$ is the most relevant to direct water splitting since the ionic species ($Na^+$ and $SO_4^{2-}$) will not react electrochemically at potentials between -0.414 V and 0.816 V vs. NHE (thermodynamic redox potentials for water splitting at pH 7). Some researchers have reported IPCE values for $BiVO_4$ using 3-electrode photoelectrochemical cells

containing $Na_2SO_4$ as the electrolyte. Particulate films of $BiVO_4$ synthesized by the sol-gel method showed IPCE values at ca. 0.01% (at 1.0 V vs. Ag/AgCl) for 380-460 nm light[10] and $BiVO_4$ synthesized by ultrasonic spray-pyrolysis showed IPCE values up to ca. 2% (at 0.7 V vs. SCE) for 450 nm light[47] in 0.1 M $Na_2SO_4$. In 0.5 M $Na_2SO_4$ with an applied bias of 1.0 V vs. Ag/AgCl under 380-460 nm light, particulate $BiVO_4$ prepared by laser ablation had IPCE values of ca. 0.5-2.5%[48], whereas $BiVO_4$ synthesized by room temperature hydrolysis had IPCE values of 1-2%[49], and $BiVO_4$ films prepared by modified metal-organic decomposition were on the order of 1-5%[50]. Modified metal-organic decomposition was also used to produce $BiVO_4$ with the highest IPCE values reported to date in 0.5 M $Na_2SO_4$ at 1.0 V vs. Ag/AgCl , which was ca. 20% for 380-440 nm light.[9] We have used RBD to alter the chemical composition and morphology of $BiVO_4$ films and enhance activity for photoelectrochemical water oxidation. Films synthesized with excess vanadium had initial IPCE values above 21% and steady-state values above 14% in 0.5 M $Na_2SO_4$ at 1.0 V vs. Ag/AgCl for light wavelengths of 340-460 nm, and films synthesized with stoichiometric $BiVO_4$ had IPCE values up to 1.2%.

## EXPERIMENTAL

Photoelectrochemical tests were conducted using a custom 3-electrode photoelectrochemical cell. The working electrode was a $BiVO_4$ film with an illumination area of 0.212 $cm^2$, the counter electrode was a platinum wire, and the reference electrode was a Ag/AgCl reference electrode (CH Instruments, CH111). The cell was controlled using CH Instruments potentiostats (CHI 832 and CH 660D). LSV scans were run from negative to positive potentials with a scan rate of 0.25 V/s. The illumination source was a filtered 100-W xenon lamp (Newport) positioned to provide light intensity close to AM1.5. Visible light was achieved using a colored glass filter (Newport, cut-on 420 nm).

IPCE measurements were performed using a mini monochrometer (Newport) and the power of each wavelength was measured using a handheld optical power meter with a UV enhanced Silicon photo-detector (Newport). IPCE values were calculated using the following equation:

$$IPCE\ (\lambda) = \frac{1240\ j_p\ (\lambda)}{\lambda\ E_\lambda\ (\lambda)}$$

where $j_P(\lambda)$ is the measured photocurrent density (mA/cm$^2$) and $E_\lambda(\lambda)$ is the incident light power density (mW/cm$^2$) for each wavelength, $\lambda$ (nm). The electrolyte solutions were made using de-mineralized water, $Na_2SO_4$ anhydrous, $Na_2SO_3$ anhydrous, sodium phosphate monobasic monohydrate, and sodium phosphate dibasic anhydrous (Fisher). Equal parts 1 M phosphate monobasic and 1 M phosphate dibasic were used to make the phosphate buffer solution. The pH of each solution was checked using a benchtop pH meter (OAKTON).

UV-Vis transmission spectroscopy measurements were performed using a Cary 5000 spectrophotometer. For Tauc plots the absorption coefficient ($\alpha$) was determined by:

$$\alpha = \frac{-\ln\left(10^{-Absorbance}\right)}{z}$$

where z is the film thickness. X-ray diffraction (XRD) measurements were taken on a Bruker-Nonius D8 diffractometer. The Cu Kα radiation source was operated at 40 kV and 40 mA and measurements were carried out in the θ/2θ mode with an incident angle of 5$^o$. Scanning electron microscope (SEM) images were acquired using a LEO 1530 SEM with 10 KV focus voltage and 30 μm aperture. $BiVO_4$ films deposited on substrates were broken in half and viewed on the SEM to obtain film thickness measurements. Film thickness was also verified using a Veeco NT9100 Optical Profiler scanning from bare FTO to the center of the $BiVO_4$ film. X-ray photoelectron spectroscopy (XPS)

measurements were performed on a Kratos AXIS Ultra DLD spectrometer with Mg Kα radiation. The concentration of Bi, V, O, and C were calculated from the integrated peak areas obtained after subtracting the background from each peak using the Shirley method.[51] Electrochemical impedance spectroscopy (EIS) measurements were conducted using the CH Instruments CH660D potentiostat and the built in software was used to create Mott-Schottky plots based on ideal semiconductor behavior.[16] Samples for inductively coupled plasma mass spectrometry (ICP-MS) were diluted 100x and 1000x and measured using an Agilent 7500ce Quadrupole ICP-MS with He as the collision gas to exclude any Cl:O overlap with mass 51 (vanadium).

**Description of Synthesis Parameters.**

The $BiVO_4$ films were synthesized using a high vacuum chamber equipped with two electron beam evaporators (Omicron, EFM 3s), an x-y-z sample manipulator mounted upon a rotary seal, and a quartz crystal microbalance (QCM) and controller (Maxtek Inc.), which has been described previously.[42] For a typical film synthesis, 1.5 cm x 1.5 cm fluorine-doped tin oxide (FTO) coated glass substrates (Pilkington, TEC15) were cleaned and sonicated in ethanol and rinsed with de-mineralized water before loading into the vacuum chamber. Bismuth granules (Alfa Aesar, 99,997% purity) in a molybdenum crucible were loaded into one evaporator and a 0.25" diameter vanadium rod (ESPI, 3N purity) was loaded into the other evaporator. The two evaporators were held in the same vertical plane and aimed at the center of the FTO substrate. This resulted in a 26° difference in direction of the flux from each evaporator. The sample manipulator was positioned approximately 10 cm away from each evaporating component and the deposition angle (γ) was adjusted to a fixed angle (0-90°) between the direction normal to the surface of the FTO and the evaporator plane as shown in Figure 2.1 (note that when

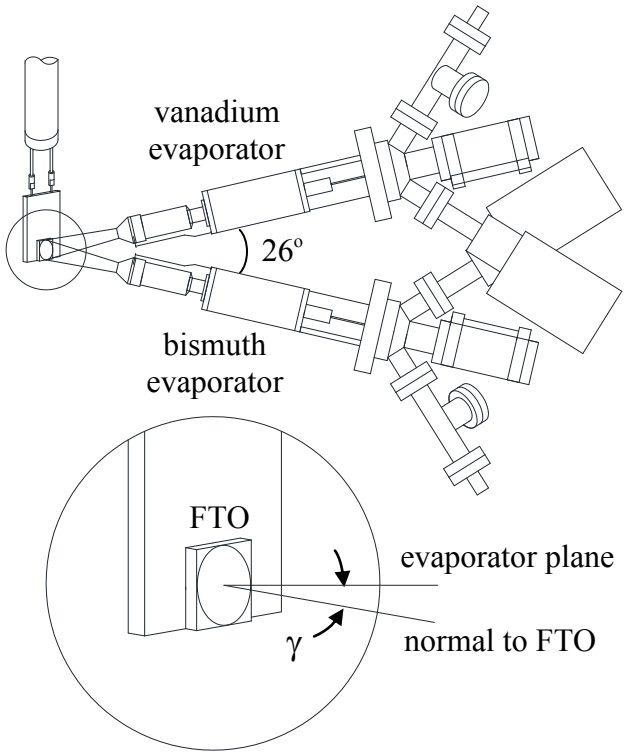


Figure 2.1. Schematic of sample and evaporator positioning inside the vacuum chamber. The deposition angle (γ) is the angle between the evaporator plane and the normal vector of the FTO substrate surface.

γ=0° there is actually an angle of 13° between each evaporator and the direction normal to the FTO surface). After loading the FTO substrates the vacuum chamber was pumped down to a base pressure below 5 x $10^{-8}$ Torr. A QCM was used to measure the deposition rate of each component (bismuth and vanadium) separately before starting film growth. The QCM measured deposition rate and the deposition angle were used to determine the atomic flux of each component and the deposition time required for the target film thickness. After checking the deposition rate the chamber was backfilled with oxygen (Matheson, UHP grade) to approximately 6 x $10^{-6}$ Torr and films were deposited on the FTO substrates at the ambient temperature of the chamber. The films were removed from

the vacuum chamber and annealed to 500°C in air for 2 hours using a muffle furnace (Neytech) with a temperature ramp rate of 10°C/min. Lastly, some of the films were submerged in 0.1 M $AgNO_3$ (Acros, 99.85% purity) or 0.1 M $Co(NO_3)_2$ (Alfa Aesar, 99.999% purity) for about 1 hour and then rinsed with de-mineralized water. This was done to add an electrocatalyst to the surface of the films, but we did not measure the oxidation states or relative amounts of Ag or Co that remained on the surface. Other researchers have reported similar surface treatments using $AgNO_3$ and $Co(NO_3)_2$.[9,52]

## RESULTS AND DISCUSSION

### Photoelectrochemical and Optical Measurements.

We attempted to optimize the photocatalytic activity of the $BiVO_4$ films synthesized by varying several important deposition parameters. Films were deposited using a V/Bi atomic flux ratio ranging from 1.0 to 2.9 and a deposition angle ($\gamma$) between 0° and 75°. Deposition time was varied to create films with total thicknesses between approximately 0.2 and 1 μm. The annealing temperature was kept constant at 500°C because there did not appear to be a significant difference in photocatalytic activity for films annealed in the range of 450 - 550°C. Films were tested with and without $AgNO_3$ or $Co(NO_3)_2$ surface treatment. Out of all the films synthesized, those deposited with a V/Bi atomic ratio of approximately two, an angle of incidence between 45° and 75°, and a final film thickness of approximately 0.5 μm consistently showed the highest initial photocurrents under white light illumination in 0.5 M $Na_2SO_4$ at an applied potential of 1.0 V vs. Ag/AgCl. Figure 2.2 shows a typical linear sweep voltammogram (LSV) for a film synthesized using the above synthesis parameters. The film had an onset potential of about 0.45 V vs. Ag/AgCl and visible light (wavelengths greater than 420 nm) accounted for more than

50% of the total photocurrent when compared to white light (visible light + wavelengths less than 420 nm).

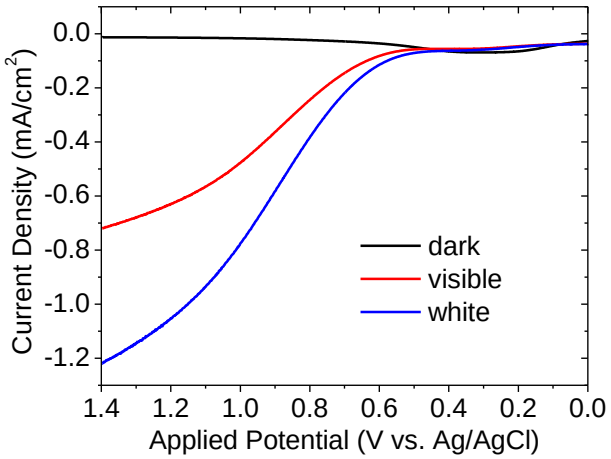


Figure 2.2. Linear sweep voltammogram of $BiVO_4$ film synthesized by RBD (V/Bi=2, $\gamma$=65°, thickness=0.5 μm) in 0.5 M $Na_2SO_4$ without irradiation (dark) and under illumination with visible light (visible) and white light (white) from a xenon lamp. The scan rate was 0.025 V/s.

V/Bi atomic ratio and deposition angle ($\gamma$) had a significant impact on the photocatalytic activity of the films synthesized by RBD. Figure 2.3 shows the initial IPCE values obtained for films deposited with different V/Bi atomic ratios, deposition angles, and surface treatments. The two films deposited with V/Bi=2, $\gamma$=65° and V/Bi=2, $\gamma$=0° (both shown in Figure 2.3a) contained the same total mass of material. The film deposited with V/Bi=2 and $\gamma$=65° (Figure 2.3a) and the film deposited with V/Bi=1 and $\gamma$=65° (Figure 2.3b) were each approximately 0.5 μm thick while the thickness of the film deposited at $\gamma$=0° (Figure 2.3a) could not be determined because it was composed of nanowires (SEM images shown later). As shown in Figure 2.3a, the film synthesized using the optimal deposition parameters (V/Bi=2, $\gamma$=65°) had the highest initial IPCE values. After illuminating this film for 3 hours at a constant potential of 1.0 V vs.

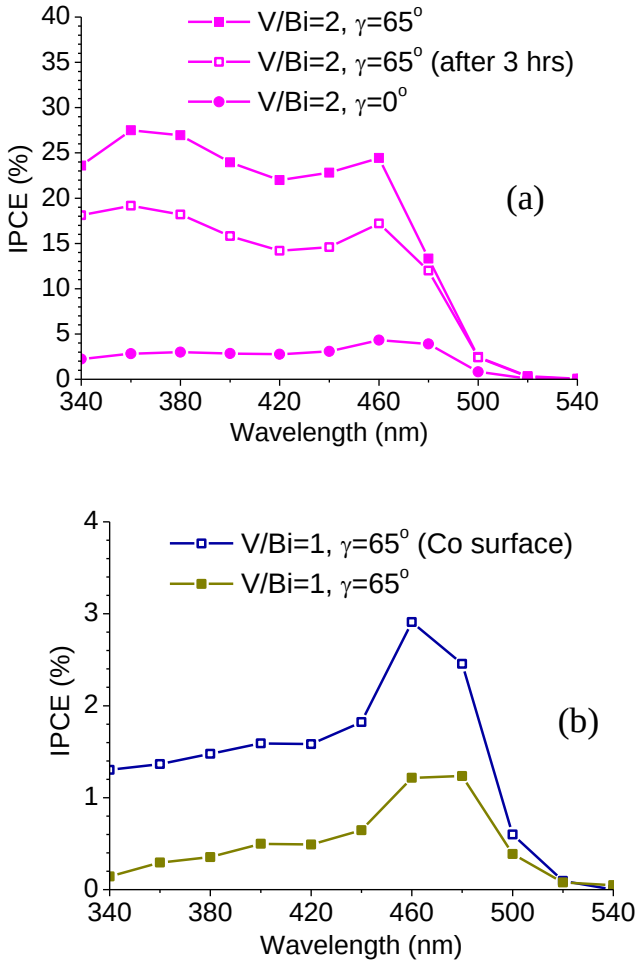


Figure 2.3. IPCE spectra for films synthesized with different V/Bi atomic ratios, deposition angles (γ), and surface treatments in 0.5 M $Na_2SO_4$ at an applied potential of 1.0 V vs. Ag/AgCl. Both films deposited at V/Bi=2 (a) had the same initial mass of material and both films deposited at γ=65° (a,b) were approximately 0.5 μm thick.

Ag/AgCl the IPCE values dropped but remained well above the IPCE values for all other films. For wavelengths less than 460 nm, the IPCE values remained at least 4 times higher than films deposited with the same V/Bi ratio at γ=0° and 14 times higher than films deposited with stoichiometric $BiVO_4$ (V/Bi=1) at γ=65°. Films deposited with V/Bi=1 and γ=0° had negligible photocurrents and efficiencies so the data is not included.

Co was added to the surface of the film with V/Bi=1 and γ=65° and improved the photoelectrochemical water oxidation efficiency as shown in Figure 2.3b. The addition of Co to the surface of the films synthesized with V/Bi=2 did not improve the efficiency. For all of the films, IPCE values dropped off rapidly for wavelengths higher than 460 nm and approached 0% at 520 nm as expected for a material with a band gap around 2.4 eV (517 nm light).

UV-Vis measurements were performed to determine differences in optical properties for the films synthesized with different deposition parameters. Figure 2.4 shows the UV-Vis absorbance spectrum for the three films synthesized with different V/Bi ratios and deposition angles. The spectrum for the film deposited at γ=0° showed a relatively high and flat UV-Vis absorbance for light with wavelengths above 500 nm. The flat section of absorbance was likely caused by diffuse reflection and scattering from the 100-300 nm diameter nanowires observed in these films. For the films deposited with

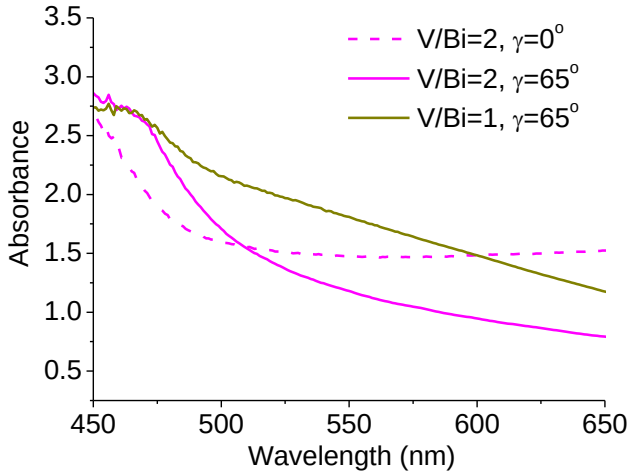


Figure 2.4. UV-Vis absorbance spectrum for films deposited with different V/Bi atomic ratios and deposition angles (γ). Films deposited at V/Bi=2 had the same mass of material and both films deposited at γ=65° were approximately 0.5 μm thick.

a higher angle of incidence ($\gamma$=65°) only the film deposited with higher flux of vanadium than bismuth (V/Bi=2) showed a sharp absorption onset. The Tauc plot for this film is shown in Figure 2.5 and points to a direct band gap of 2.45 eV, which is close to the experimentally determined band gap of 2.4 eV for monoclinic $BiVO_4$ synthesized by other methods.[7,9,10]

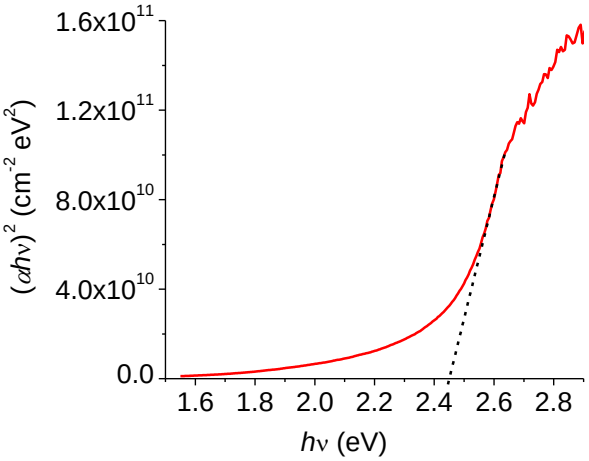


Figure 2.5. Tauc plot of film synthesized with deposition parameters resulting in highest photoactivity (V/Bi=2, $\gamma$=65°, thickness=0.5 μm) pointing to a band gap of approximately 2.45 eV.

XRD measurements were performed on the $BiVO_4$ films as deposited (Figure 2.6a) and after annealing to 500°C for 2 hours (Figure 2.6b). As deposited all films showed XRD peaks for $SnO_2$ from the FTO substrate along with crystalline bismuth, JCDPS 00-046-1088 and 00-044-1246, respectively. Films deposited with lower V/Bi ratios (a larger relative mass of bismuth) showed higher intensity peaks for crystalline bismuth relative to the $SnO_2$ peaks. As deposited there were no vanadium, bismuth oxide, vanadium oxide, or bismuth vanadate peaks. After annealing all films showed strong peaks for $SnO_2$ and monoclinic $BiVO_4$ (JCDPS 01-075-2480). The two tiny peaks at 2θ values of 20.1° and 21.5° match up with two of the highest intensity peaks in the XRD

pattern for $V_2O_5$ (JCPDS 01-089-0611) so there is some segregation of Bi and V even when the two components are deposited in equal amounts. However, the XRD patterns for V/Bi=1 and V/Bi=2 after annealing were almost identical and the highest $BiVO_4$ peak was 26 times more intense than the highest $V_2O_5$ peak. This suggests that excess vanadium is incorporated into the interstitial sites of films deposited with V/Bi=2.

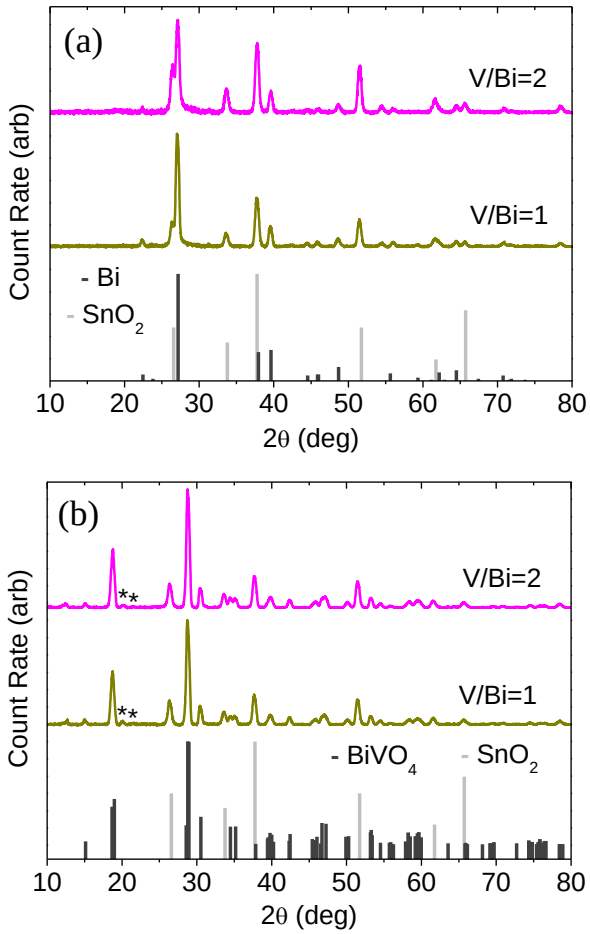


Figure 2.6. XRD spectrum for $BiVO_4$ films ($\gamma$=65°, thickness=0.5 μm) with V/Bi=2 and V/Bi=1. As deposited (a) and after annealing at 500°C for 2 hours (b). JCPDS peak intensities and locations are plotted below the data for $SnO_2$ (00-046-1088), crystalline Bi (00-044-1246), and monoclinic $BiVO_4$ (01-075-2480). The * symbol indicates the highest intensity JDCPS peaks for $V_2O_5$ (01-089-0611).

The nanostructure and morphology of the films was observed using a SEM. Figures 2.7 and 2.8 show SEM images for three different films before and after annealing at 500°C for 2 hours. Films that were deposited at $\gamma=0^{o}$ consisted of randomly oriented nanowires with diameters on the order of 100-300 nm as shown in Figure 2.7a. This was seen for all V/Bi atomic ratios that were tested. More glancing angles of incidence ($\gamma=65^{o}$) produced films with jagged, finely-structured surfaces as shown in Figure 2.7c

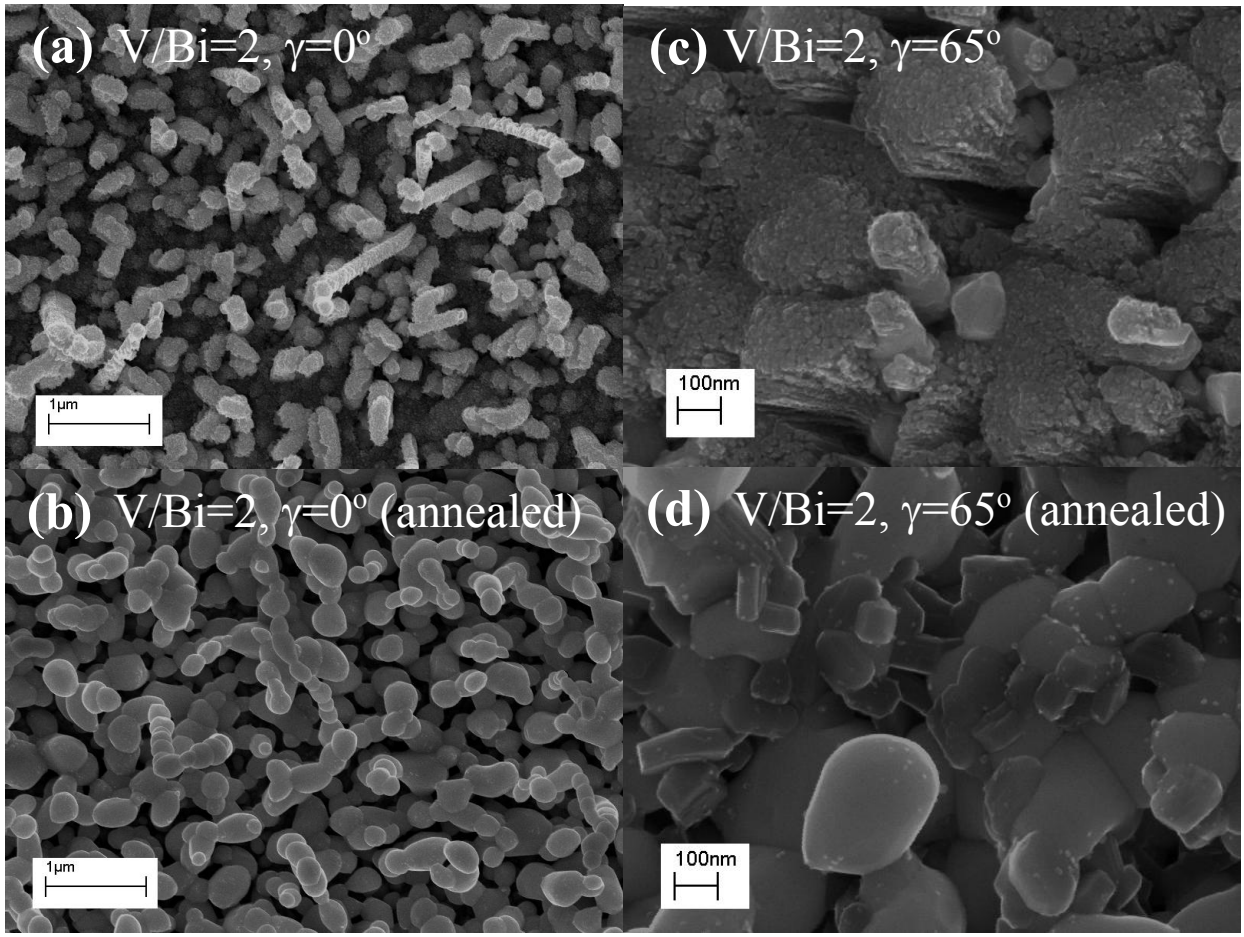


2. 7. SEM images of films deposited with the same total amount of material and a V/Bi atomic ratio of 2, but different deposition angles of $\gamma=0^{o}$ (a,b) and $\gamma=65^{o}$ (c,d) . Images (a,c) are as deposited and (b,d) are after annealing at 500°C for 2 hrs.

and Figure 2.8a. Before annealing, the films deposited at $\gamma=65^{o}$ show many fine features on the order of 10 nm or smaller. These features appear to sinter and smooth out after annealing to 500$^{o}$C resulting in irregular-shaped features 50 - 400 nm in size (Figures 2.7d and 2.8b). Based on these SEM images, annealing appears to reduce the surface area of the films.

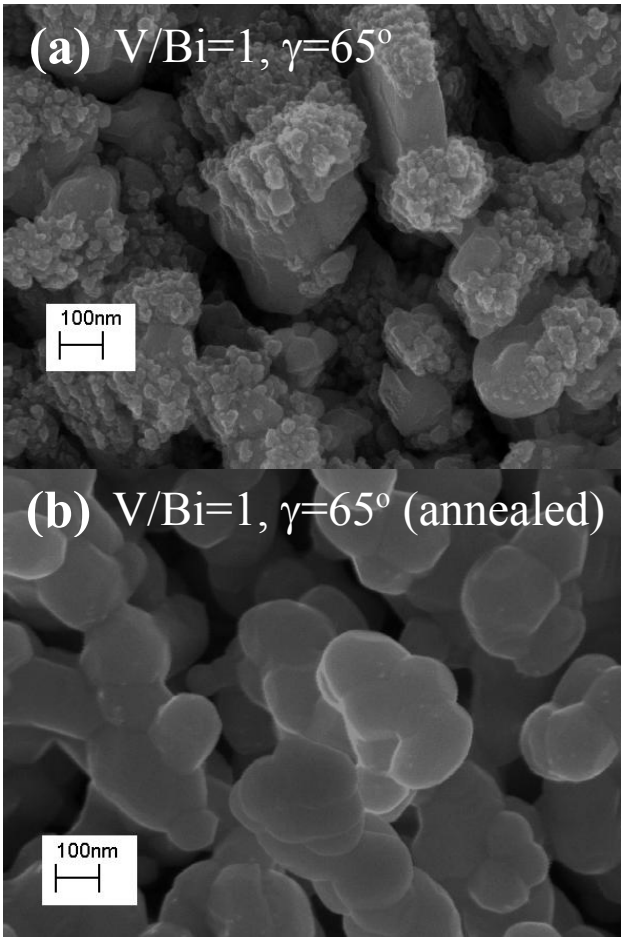


Figure 2.8. SEM image of a film synthesized by RBD (V/Bi=1, $\gamma=65^{o}$, thickness=0.5 μm). Image (a) is as deposited and (b) is after annealing at 500$^{o}$C for 2 hrs.

The dramatic differences in morphology and surface structure between films deposited at $\gamma=0^{o}$ and $\gamma=65^{o}$ can partially be explained by the mechanism of RBD at

glancing angles. Several researchers have studied the mechanism for film growth by ballistic deposition (BD) from a single evaporating component at oblique angles of incidence.[53,54] During the initial stages of BD at oblique angles of incidence, incoming atoms randomly land on the substrate surface creating topographically elevated clusters of atoms. With continued film growth the elevated clusters promote "self-shadowing", which often causes the film to grow porous, angled columns. The exact morphology and nanostructure of the resulting film is controlled by the self-shadowing effect and surface diffusion of the incoming atoms. Reactive ballistic deposition (RBD) involves the addition of a non-directional background gas which reacts with the incoming atoms on the surface of the film during deposition.[39] For co-evaporation of bismuth and vanadium at $\gamma=0^{o}$ ($13^{o}$ angle between each evaporator and the direction normal to the substrate) there was essentially no self-shadowing but there was surface diffusion. According to the Movchan and Demchishin structure zone model (SZM)[54-56] surface diffusion during film growth can be related to the ratio of the melting point of the depositing metal ($T_m$) and the temperature of the substrate ($T_s$). The melting point of bismuth (271.4 $^{o}$C) is much lower than that of vanadium (1,890 $^{o}$C). With the FTO left at ambient (near 25 $^{o}$C) during deposition, bismuth was near the bulk diffusion region ($T_s/T_m>0.5$) of the Movchan and Demchishin SZM, while vanadium was in the region without significant diffusion ($T_s/T_m<0.3$). Under these conditions it is expected that the rate of bismuth adatom diffusion is much greater than that of vanadium. In addition, bismuth adatoms did not appear to react with the background oxygen in the vacuum chamber during deposition. This was determined by measuring the deposition rate of bismuth while gradually leaking in oxygen (the measured deposition rate did not change in the presence of oxygen) and by analyzing the XRD data of films as deposited (peaks are observed for crystalline bismuth metal but not for bismuth oxide). On the other hand vanadium readily reacts with oxygen

during deposition. When vanadium was evaporated while gradually increasing the partial pressure of oxygen the measured deposition rate increased until it reached a maximum as the material forming on the QCM changed from vanadium metal to vanadium oxide. At low incident angles of deposition ($\gamma \approx 0^{o}$) the observation of nanowires is likely the result of a growth mechanism dominated by surface diffusion and segregation of bismuth atoms. It is also possible that bismuth or vanadium acts as a catalyst for vapor-liquid-solid (VLS) nanowire growth, which involves dissolution and subsequent precipitation of one of the components when a two component system is held above the eutectic point.[57] There is limited experimental phase-equilibria data available for the bismuth-vanadium system, especially for the pressures that were used during deposition ($6 \times 10^{-6}$ Torr), but it is plausible that the deposition conditions result in a eutectic point. Available phase diagrams show very low solubility of condensed phase bismuth (~20 ppm) in vanadium near the melting point of bismuth.[58] At higher deposition angles ($\gamma = 45^{o}$-$75^{o}$) the self-shadowing effect becomes more important than surface diffusion resulting in greater dispersion of bismuth and vanadium atoms so that nanowire growth by dissolution and subsequent precipitation cannot occur. For this reason films deposited at $\gamma = 65^{o}$ showed a more porous, finely-structured surface.

**Sacrificial Reagent Photoelectrochemical Measurements.**

It would not be practical to run a large-scale energy conversion system at an applied potential of 1.0 V vs. Ag/AgCl because the energy input required to sustain the bias would negate the energy output.[46] Furthermore, the thermodynamic water oxidation potential in $Na_2SO_4$ is less than 1.0 V vs. Ag/AgCl. The main reason for conducting PEC tests in $Na_2SO_4$ at 1.0 V vs. Ag/AgCl was to compare the activity of $BiVO_4$ films synthesized by RBD with that of $BiVO_4$ synthesized by other techniques.[9,48-50] At such a

positive bias, films deposited with excess vanadium (V/Bi=2) showed higher photocatalytic activity than films deposited with equal amounts of bismuth and vanadium (V/Bi=1), but this is not always the case for different electrolytes and lower applied biases. For example, particulate $BiVO_4$ prepared using layered compounds of $KV_3O_8$ and $K_3V_5O_{14}$ with $Bi(NO_3)_3$ showed the highest $O_2$ evolution rate from 0.05 mol/L $AgNO_3$ when the starting materials had a V:Bi ratio of 1:1.[7] Since testing was performed in a particulate PEC system there was no way to apply a bias. Likewise a recent scanning electrochemical microscopy (SECM) study found that a V:Bi ratio of 1:1 resulted in the highest photocurrent when using an applied potential of 0.2 V vs. Ag/AgCl in 0.1 M $Na_2SO_4$ along with 10 mM $Na_2SO_3$ as a sacrificial electron donor.[59]

We conducted PEC measurements in a variety of electrolyte solutions to further characterize the $BiVO_4$ films synthesized by RBD. Figure 2.9a shows the initial LSV scans for three films with different V/Bi ratios and surface treatments in 0.5 M $Na_2SO_4$. The film synthesized with V/Bi=1 showed lower cathodic current (light and dark) at the start of the scan and a shift to purely anodic photocurrent at potentials more positive than -0.55 V vs. Ag/AgCl. The film synthesized with V/Bi=2 had a higher cathodic current (light and dark) with large transient spikes (cathodic and anodic) at the start of the sweep. A small amount of dark current, but essentially no photocurrent was observed between -0.40 and 0.45 V vs. Ag/AgCl at which point anodic onset was observed (similar to the LSV in Figure 2.1). Therefore films synthesized with a V:Bi ratio of 1:1 do show higher photocatalytic activity as long as the applied potential is less positive than 0.45 V vs. Ag/AgCl, but they fail to achieve a high maximum photocurrent at more positive potentials. Figure 2.9a shows that the addition of Co to the surface of the V/Bi=1 film improved the maximum photocurrent by more than a factor of three. Cobalt complexes are known to be electrocatalysts for water oxidation.[52,60-62] Another chopped LSV is

shown in Appendix A (Figure A.1) for the film synthesized with V/Bi=2 after illuminating the film for 3 hours at a constant potential of 1.0 V vs. Ag/AgCl. It shows a more negative anodic onset potential, no dark current between -0.40 and 0.45 V vs. Ag/Ag/Cl, and a lower maximum photocurrent at higher potentials. The small amount of dark current and lack of photocurrent initially observed for the V/Bi=2 film was likely caused by excess vanadium (vanadium oxide) on the surface. Vanadium oxide dissolves readily in $Na_2SO_4$ and $V_2O_5$ electrodes have shown dark current for current vs. potential scans in the range of -0.2 and 0.405 V vs. SCE.[9,63]

Figure 2.9b shows LSV scans for two films in 0.5 M $Na_2SO_4$ and 0.5 M $Na_2SO_3$. The $Na_2SO_3$ was added to improve the surface kinetics of the oxidation reaction by providing a species ($SO_3^{2-}$) more easily oxidizable than water. In the combined electrolyte solution the V/Bi=1 film had a maximum photocurrent that was much closer to that of the V/Bi=2 film. This result provides evidence that pure $BiVO_4$ films were limited by the surface kinetics of the water oxidation reaction. Employing $Na_2SO_3$ also shifted the onset potentials to more negative values by increasing the pH of the solution and it nearly eliminated the transient spikes for both films. Several researchers have characterized the anodic and cathodic transient spikes for $Fe_2O_3$ films attributing the behavior to recombination or back reaction of photo-generated species (oxy- or hydroxyl) on the surface.[63-65] For the $BiVO_4$ films synthesized by RBD the transient spikes were primarily anodic, but may still be caused by surface recombination or a back reaction at the surface as they were nearly eliminated with the use of a redox species ($SO_3^{2-}$) which undergoes a facile, irreversible oxidation.

The chopped LSV scans in Figure 2.9a can be used to estimate the location of the flat band potential of the $BiVO_4$ films. For the V/Bi=1 film there was a clear transition from cathodic to anodic photocurrent around -0.55 V vs. Ag/AgCl. The photocurrent

transition was more difficult to distinguish for the V/Bi=2 film due to the dark current. EIS measurements were performed on this film and the resulting Mott-Schottky plot shown in Figure 2.10 indicates a flat band potential of approximately -0.7 V vs. Ag/AgCl. After 3 hours of PEC testing the chopped LSV for the V/Bi=2 film shows a transition from cathodic to anodic current near -0.5 V vs. Ag/AgCl (see Figure A.1).

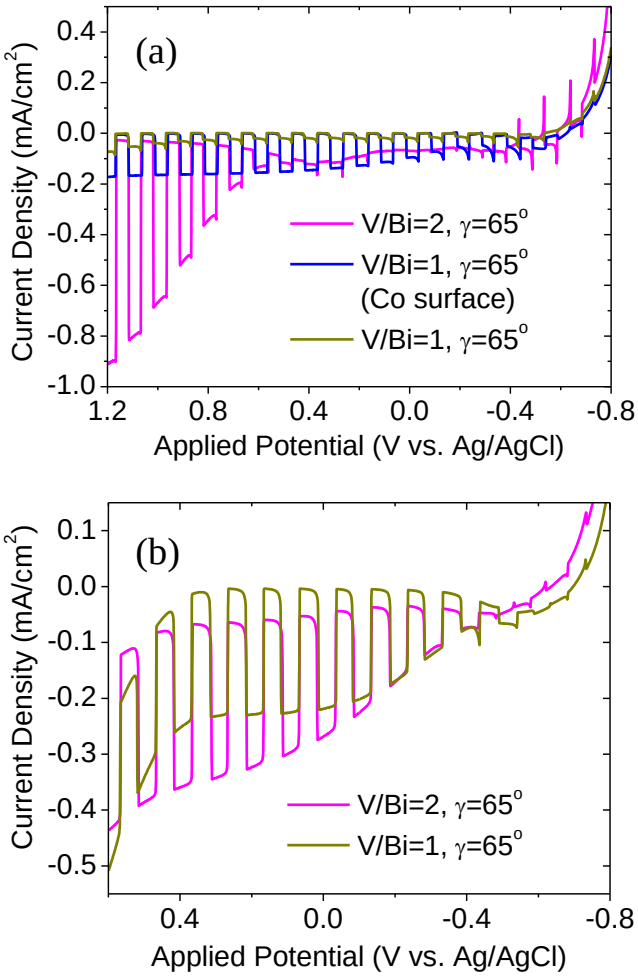


Figure 2.9. Chopped (dark and white light) LSV scans for films synthesized by RBD ($\gamma$=65°, thickness=0.5 μm) with different V/Bi ratios and surface treatments measured in (a) 0.5 M $Na_2SO_4$ and (b) 0.5 M $Na_2SO_4$ and 0.5 M $Na_2SO_3$. The scan rate was 0.025 V/s.

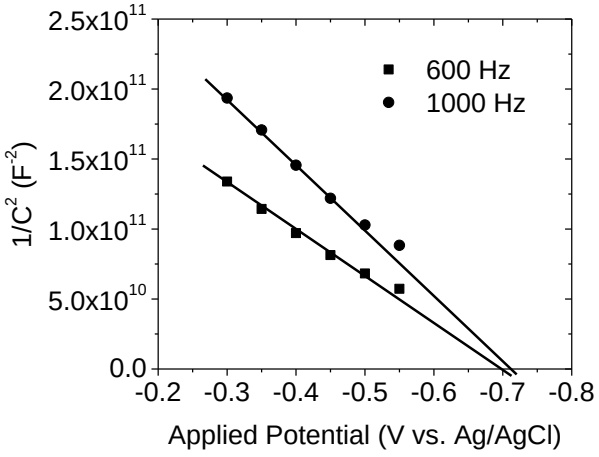


Figure 2.10. Mott-Schottky plot for $BiVO_4$ film synthesized by RBD (V/Bi=2, $\gamma$=65°, thickness=0.5 μm). The measurement was conducted in 0.5 M $Na_2SO_4$.

**Film Stability and Surface Characterization.**

For any material to be practical in a large-scale energy conversion system it must remain stable under illumination for long periods of time. There are limited reports in the literature on the long-term stability of $BiVO_4$. One group tested the stability of $BiVO_4$ synthesized by modified metal-organic decomposition and found that with a bias of 1.2 V applied to a Pt counter electrode the photocurrent dropped from 2 mA/cm$^2$ to a steady-state value of 0.5 mA/cm$^2$ (~75% drop) in less than 1 hour.[9] We conducted long-term PEC tests of $BiVO_4$ films in $Na_2SO_4$ solutions with a constant applied potential of 1.0 V vs. Ag/AgCl as shown in Figure 2.11. The discontinuities in photocurrent were caused by blocking the white light source to confirm the photoactivity and stopping/restarting the potentiostat near 5000 seconds. The photocurrent of the film deposited with V/Bi=2 dropped by more than 70% before it reached a relatively steady-state value while the V/Bi=1 film with Co on the surface reached a lower steady-state photocurrent almost immediately. Films deposited with V/Bi=1 but without Co were also stable but had lower photoactivity as shown in Figure 2.9a.

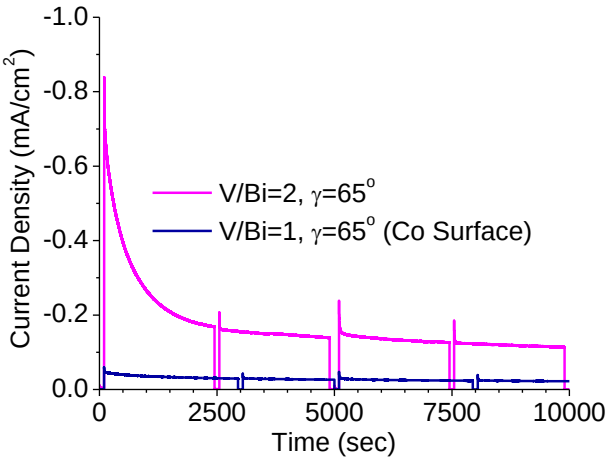


Figure 2.11. Amperometric i-t curve for $BiVO_4$ films synthesized by RBD ($\gamma$=65°, thickness=0.5 μm) with different V/Bi ratios and surface treatments in 0.1 M $Na_2SO_4$ at a constant applied potential of 1.0 V vs. Ag/AgCl.

A fraction of the photocurrent decay is caused by the build-up of oxygen bubbles on the film and local changes in pH. During PEC testing oxygen bubbles formed and became trapped between the film surface and the o-ring on the glass electrochemical cell reducing the geometric film surface area available for the reaction. In addition, the continuous oxidation of water produced $H^+$ ions, which decreased the pH of the electrolyte near the film shifting the redox potentials and slowing down the reaction. This was verified by comparing the photocurrent in pure 0.5 M $Na_2SO_4$ and a mixture of 0.5 M $Na_2SO_4$ and 0.5 M phosphate buffer solution (pH 6.8). The steady-state photocurrent was about 20% higher in the buffer solution as compared to $Na_2O_4$ (see Figure A.2 in Appendix A).

Most of the photocurrent decay was caused by changes in the chemical composition of the film. We used XPS to measure the film surface before and after PEC testing. Initially the film deposited with an atomic flux ratio of V/Bi=2 had a XPS

measured V/Bi ratio of 1.54. The binding energies of the elements were found to be 159.0 eV for Bi 4f 7/2, 516.8 eV for V 2p 3/2, and 529.8 eV for O 1s suggesting oxidation states of $Bi^{3+}$, $V^{5+}$, and $O^{2-}$.[66] After long-term PEC testing the locations of these peaks remained the same but the intensities had changed and the XPS measured V/Bi ratio dropped to 0.51 indicating a loss of vanadium at the surface. Table 2.1 summarizes photocurrent and XPS results for PEC testing and the XPS spectra are included in Appendix A (Figure A.3). We could not use XPS to measure the concentration and oxidation states of elements below the surface. The argon sputter etch gun on the Kratos AXIS Ultra DLD spectrometer was mounted with an incident angle of 45° and the $BiVO_4$ films had a porous structure so much of the film surface was shadowed during sputter etching. It is possible that the concentration of vanadium was higher in the bulk material than on the film surface.

| Film Condition | LSV Photocurrent +1 V vs. Ag/AgCl | Atomic % (neglecting C) O 1s | V 2p | Bi 4f | V/Bi Ratio |
|---|---|---|---|---|---|
| Initial | 0.91 mA/cm$^2$ | 66% | 21% | 14% | 1.54 |
| After 3 hrs | 0.36 mA/cm$^2$ | 71% | 10% | 20% | 0.51 |

Table 2.1. Photocurrent and XPS data for film synthesized by RBD (V/Bi=2, $\gamma$=65°, thickness=0.5 μm) taken before and after 3 hours of illumination in 0.5 M $Na_2SO_4$ at a constant applied potential of 1.0 V vs. Ag/AgCl. The concentration of Bi, V, O, and C were calculated from the integrated peak areas obtained after subtracting the background from each peak using the Shirley method.[51]

To further characterize the decay in photocurrent we used ICP-MS to measure Bi and V ion concentrations in the electrolyte before and after PEC testing. For the film

deposited with V/Bi=2, the V concentration in the electrolyte went from below the detection limits to 247 ppb after long-term PEC testing while the Bi concentration remained below detection. It is apparent that much of the initial photocurrent was due to photo-corrosion of excess vanadium into the electrolyte. For the film with V/Bi=1 and Co on the surface, the Bi and V concentrations in the electrolyte remained below the detection limits after long-term PEC testing. The ICP-MS results are tabulated in Appendix A (Table A.1.). Even though films synthesized with V/Bi=2 show a loss of vanadium so that the atomic ratio is reduced, the steady-state photocurrent of these films is higher than the photocurrent of films that are initially synthesized with V/Bi=1.

The film deposited with V/Bi=1 may be limited by other factors in addition to slow surface kinetics. As shown in Figure 2.4 the film with V/Bi=1 had a more gradual absorption line that became saturated near 460 nm possibly due to scattering or reflection. This makes it difficult to accurately calculate the APCE and distinguish whether poor charge transport or slow surface kinetics is the greater limiting factor.

We attempted to stabilize the photocurrent of the films deposited with V/Bi=2 by adding Ag or Co to the surface. Others have reported that pure $BiVO_4$ synthesized by metal-organic decomposition showed a decrease in photocurrent accompanied by a reduction of the V/Bi ratio at the surface when using a bias of 1.2 V applied to a Pt counter electrode. When the surface was treated with $AgNO_3$ the initial photocurrent was higher and both the photocurrent and surface concentration remained fairly stable.[9] We treated films synthesized by RBD with $AgNO_3$ but did not see an increase in photocurrent or stability during 3-electrode PEC measurements. Moreover films treated with $AgNO_3$ showed a significant dark current during LSV scans moving more positive of 0.25 V vs. Ag/AgCl. This was likely due to the oxidation of Ag. The addition of Co to the surface of films deposited with V/Bi=2 reduced the initial photocurrent by slowing down the photo-

corrosion of excess vanadium, but the final steady-state photocurrent was similar to that of films without Co on the surface. As shown in Figures 2.3b and 2.9a, Co treatment significantly enhanced the photocurrent and IPCE of films deposited with V/Bi=1.

## CONCLUSIONS

We have synthesized $BiVO_4$ films by reactive ballistic deposition (RBD) and reported on the photocatalytic activity for water oxidation. The photoactivity was higher for films deposited at more glancing angles of incidence ($\gamma=45^o$-$75^o$) than for films deposited at normal incidence ($\gamma=0^o$) primarily due to differences in surface structure and morphology. RBD was used to incorporate excess vanadium into $BiVO_4$ films, which increased the initial photocurrent at high applied potentials (1.0 V vs. Ag/AgCl); however, the excess vanadium dissolved into the solution with time under illumination and a large portion of the initial photoactivity can be attributed to photo-corrosion. The photocurrent dropped to a steady-state value that is still an order of magnitude greater than that for films synthesized with equal amounts of bismuth and vanadium, which were stable but limited by slow surface kinetics for the water oxidation reaction. The addition of Co to the surface of $BiVO_4$ films with equal bismuth and vanadium increases the photocurrent, but more work is needed to improve the light absorption and charge transport of these films so that they are closer to the maximum theoretical efficiency of a 2.3-2.4 eV bandgap material under AM1.5 illumination.

## REFERENCES


(1) Fujishima, A.; Honda, K. *Nature* **1972**, *238*, 37.

(2) Kudo, A.; Miseki, Y. *Chemical Society Reviews* **2009**, *38*, 253.

(3) Osterloh, F. E. *Chemistry of Materials* **2007**, *20*, 35.

(4) Bak, T.; Nowotny, J.; Rekas, M.; Sorrell, C. C. *International Journal of Hydrogen Energy* **2002**, *27*, 991.

(5) Maeda, K.; Domen, K. *The Journal of Physical Chemistry C* **2007**, *111*, 7851.

(6) Bard, A. J.; Fox, M. A. *Accounts of Chemical Research* **1995**, *28*, 141.

(7) Kudo, A.; Omori, K.; Kato, H. *Journal of the American Chemical Society* **1999**, *121*, 11459.

(8) Tokunaga, S.; Kato, H.; Kudo, A. *Chemistry of Materials* **2001**, *13*, 4624.

(9) Sayama, K.; Nomura, A.; Arai, T.; Sugita, T.; Abe, R.; Yanagida, M.; Oi, T.; Iwasaki, Y.; Abe, Y.; Sugihara, H. *The Journal of Physical Chemistry B* **2006**, *110*, 11352.

(10) Liu, H.; Nakamura, R.; Nakato, Y. *Journal of The Electrochemical Society* **2005**, *152*, G856.

(11) Long, M.; Cai, W.; Cai, J.; Zhou, B.; Chai, X.; Wu, Y. *The Journal of Physical Chemistry B* **2006**, *110*, 20211.

(12) Walsh, A.; Yan, Y.; Huda, M. N.; Al-Jassim, M. M.; Wei, S.-H. *Chemistry of Materials* **2009**, *21*, 547.

(13) Oshikiri, M.; Boero, M.; Ye, J. H.; Zou, Z. G.; Kido, G. *Journal of Chemical Physics* **2002**, *117*, 7313.

(14) Kohtani, S.; Yoshida, K.; Maekawa, T.; Iwase, A.; Kudo, A.; Miyabe, H.; Nakagaki, R. *Physical Chemistry Chemical Physics* **2008**, *10*, 2986.

(15) Kudo, A.; Ueda, K.; Kato, H.; Mikami, I. *Catalysis Letters* **1998**, *53*, 229.

(16) Bard, A. J.; Faulkner, L. R. *Electrochemical Methods: Fundamentals and Applications*, Second ed.; John Wiley & Sons, Inc.: New Jersey, 2001.

(17) Yu, J.; Kudo, A. *Chemistry Letters* **2005**, *34*, 850.

(18) Xi, G. C.; Ye, J. H. *Chemical Communications* **2010**, *46*, 1893.

(19) Galembeck, A.; Alves, O. L. *Thin Solid Films* **2000**, *365*, 90.

(20) Sayama, K.; Nomura, A.; Zou, Z.; Abe, R.; Abe, Y.; Arakawa, H. *Chemical Communications* **2003**, 2908.

(21) Neves, M. C.; Trindade, T. *Thin Solid Films* **2002**, *406*, 93.

(22) Liu, J.; Wang, H.; Wang, S.; Yan, H. *Materials Science and Engineering B* **2003**, *104*, 36.

(23) Gotic, M.; Music, S.; Ivanda, M.; Soufek, M.; Popovic, S. *Journal of Molecular Structure* **2005**, *744-747*, 535.

(24) Jiang, H.-q.; Endo, H.; Natori, H.; Nagai, M.; Kobayashi, K. *Journal of the European Ceramic Society* **2008**, *28*, 2955.

(25) Strobel, R.; Metz, H. J.; Pratsinis, S. E. *Chemistry of Materials* **2008**, *20*, 6346.

(26) Dunkle, S. S.; Helmich, R. J.; Suslick, K. S. *The Journal of Physical Chemistry C* **2009**, *113*, 11980.

(27) Ke, D.; Peng, T.; Ma, L.; Cai, P.; Jiang, P. *Applied Catalysis A: General* **2008**, *350*, 111.

(28) Yu, J.; Zhang, Y.; Kudo, A. *Journal of Solid State Chemistry* **2009**, *182*, 223.

(29) Dall'Antonia, L. H.; de Tacconi, N. R.; Chanmanee, W.; Timmaji, H.; Myung, N.; Rajeshwar, K. *Electrochemical and Solid-State Letters* **2010**, *13*, D29.

(30) Castillo, N. C.; Heel, A.; Graule, T.; Pulgarin, C. *Applied Catalysis B: Environmental* **2010**, *95*, 335.

(31) Rullens, F. o.; Laschewsky, A.; Devillers, M. *Chemistry of Materials* **2006**, *18*, 771.

(32) Zhang, L.; Chen, D.; Jiao, X. *The Journal of Physical Chemistry B* **2006**, *110*, 2668.

(33) Zheng, Y.; Wu, J.; Duan, F.; Xie, Y. *Chemistry Letters* **2007**, *36*, 520.

(34) Li, G.; Zhang, D.; Yu, J. C. *Chemistry of Materials* **2008**, *20*, 3983.

(35) Zhou, L.; Wang, W.; Liu, S.; Zhang, L.; Xu, H.; Zhu, W. *Journal of Molecular Catalysis A: Chemical* **2006**, *252*, 120.

(36) Zhou, L.; Wang, W.; Zhang, L.; Xu, H.; Zhu, W. *The Journal of Physical Chemistry C* **2007**, *111*, 13659.

(37) Su, J.; Guo, L.; Yoriya, S.; Grimes, C. A. *Crystal Growth & Design* **2009**, *10*, 856.

(38) Zhang, H.; Liu, J.; Wang, H.; Zhang, W.; Yan, H. *Journal of Nanoparticle Research* **2008**, *10*, 767.

(39) Dohnálek, Z.; Kimmel, G. A.; McCready, D. E.; Young, J. S.; Dohnálková, A.; Smith, R. S.; Kay, B. D. *The Journal of Physical Chemistry B* **2002**, *106*, 3526.

(40) Flaherty, D. W.; Dohnálek, Z.; Dohnálková, A.; Arey, B. W.; McCready, D. E.; Ponnusamy, N.; Mullins, C. B.; Kay, B. D. *The Journal of Physical Chemistry C* **2007**, *111*, 4765.

(41) Flaherty, D. W.; Hahn, N. T.; Ferrer, D.; Engstrom, T. R.; Tanaka, P. L.; Mullins, C. B. *The Journal of Physical Chemistry C* **2009**, *113*, 12742.

(42) Flaherty, D. W.; May, R. A.; Berglund, S. P.; Stevenson, K. J.; Mullins, C. B. *Chemistry of Materials* **2009**, *22*, 319.

(43) Hahn, N. T.; Ye, H.; Flaherty, D. W.; Bard, A. J.; Mullins, C. B. *ACS Nano* **2010**, *4*, 1977.

(44) Hahn, N. T.; Mullins, C. B. *Chemistry of Materials* **2010**, *accepted*.

(45) May, R. A.; Flaherty, D. W.; Mullins, C. B.; Stevenson, K. J. *The Journal of Physical Chemistry Letters*, **2010**, *1*, 1264.

(46) Chen, Z. B.; Jaramillo, T. F.; Deutsch, T. G.; Kleiman-Shwarsctein, A.; Forman, A. J.; Gaillard, N.; Garland, R.; Takanabe, K.; Heske, C.; Sunkara, M.; McFarland, E. W.; Domen, K.; Miller, E. L.; Turner, J. A.; Dinh, H. N. *Journal of Materials Research* **2010**, *25*, 3.

(47) Li, M.; Zhao, L.; Guo, L. *International Journal of Hydrogen Energy* **2010**, *35*, 7127.

(48) Murakami, Y.; Ikarashi, M.; Hashizume, M.; Nosaka, A. Y.; Nosaka, Y. *Electrochemical and Solid-State Letters* **2008**, *11*, H42.

(49) Long, M.; Cai, W.; Kisch, H. *The Journal of Physical Chemistry C* **2007**, *112*, 548.

(50) Chatchai, P.; Murakami, Y.; Kishioka, S.-y.; Nosaka, A. Y.; Nosaka, Y. *Electrochimica Acta* **2009**, *54*, 1147.

(51) Shirley, D. A. *Physical Review B* **1972**, *5*, 4709.

(52) Kay, A.; Cesar, I.; Gratzel, M. *Journal of the American Chemical Society* **2006**, *128*, 15714.

(53) Abelmann, L.; Lodder, C. *Thin Solid Films* **1997**, *305*, 1.

(54) Hawkeye, M. M.; Brett, M. J. *Journal of Vacuum Science & Technology A* **2007**, *25*, 1317.

(55) Movchan, B. A.; Demchish, A. V. *Physics of Metals and Metallography-USSR* **1969**, *28*, 83.

(56) Higo, M.; Fujita, K.; Tanaka, Y.; Mitsushio, M.; Yoshidome, T. *Applied Surface Science* **2006**, *252*, 5083.

(57) Wagner, R. S.; Ellis, W. C. *Applied Physics Letters* **1964**, *4*, 89.

(58) Smith, J. F. *Journal of Alloy Phase Diagrams* **1990**, *6*, 19.

(59) Ye, H.; Lee, J.; Jang, J. S.; Bard, A. J. *The Journal of Physical Chemistry C* **2010**, *114*, 13322.

(60) Brunschwig, B. S.; Chou, M. H.; Creutz, C.; Ghosh, P.; Sutin, N. *Journal of the American Chemical Society* **1983**, *105*, 4832.

(61) Svegl, F.; Orel, B.; Grabec-Svegl, I.; Kaucic, V. *Electrochimica Acta* **2000**, *45*, 4359.

(62) Kanan, M. W.; Nocera, D. G. *Science* **2008**, *321*, 1072.

(63) Hardee, K. L.; Bard, A. J. *Journal of The Electrochemical Society* **1977**, *124*, 215.

(64) Iwanski, P.; Curran, J. S.; Gissler, W.; Memming, R. *Journal of The Electrochemical Society* **1981**, *128*, 2128.

(65) Anderman, M.; Kennedy, J. H. *Journal of The Electrochemical Society* **1984**, *131*, 21.

(66) Wagner, C. D.; Naumkin, A. V.; Kraut-Vass, A.; Allison, J. W.; Powell, C. J.; John R. Rumble, J. NIST X-ray Photoelectron Spectroscopy Database

# Chapter 3: Incorporation of Mo and W into Nanostructured $BiVO_4$ Films for Efficient Photoelectrochemical Water Oxidation

## INTRODUCTION

Photoelectrochemical (PEC) water splitting to produce hydrogen and oxygen has great potential for solar energy conversion and storage; however, there are many material challenges that must be overcome to make it practical on a large scale. The materials used in a practical water splitting system should efficiently absorb a large portion of the solar spectrum, be catalytic for both water oxidation and proton reduction, promote facile charge transfer, be composed of abundant elements, and remain stable in electrolyte under illumination. For economic viability the system should have a solar-to-hydrogen (STH) efficiency of at least 10%.[1] Many different semiconductor materials have been tested for water splitting;[2-6] however, none of these materials meet all of the above requirements.

Progress has been made in the synthesis of multi-component semiconductor materials and the addition of dopants as a means of improving water splitting performance.[2,5,7-9] Studies have suggested that incorporating impurities into a semiconductor can improve photocatalytic performance by assisting with crystal growth during synthesis, creating catalytic sites, or altering the band structure and electronic properties. Significant improvements in photoelectrochemical performance and light absorption have been observed for incorporation of C, N, and S into $TiO_2$, and for incorporation of Si, Ti, Sn/Be, and Ti/Al into $\alpha$-$Fe_2O_3$.[10-17] Another semiconductor material that can be enhanced by the addition of various elements is monoclinic $BiVO_4$, an n-type material with a bandgap of 2.3-2.5 eV that is active for PEC water oxidation.[18-22] Compared to pure $BiVO_4$, several mixed metal oxides containing Bi and V such as $BiCu_2VO_6$, $BiZn_2VO_6$, and $Ca_{1-x}Bi_xV_xMo_{1-x}O_4$, have shown higher $O_2$ evolution rates

from aqueous solutions.[23-25] $BiV_{0.98}Mo_{0.02}O_4$ prepared by solid state reaction had an $O_2$ evolution rate from aqueous $AgNO_3$ that was nearly three times higher than $BiVO_4$.[26] Films formed by drop-casting and annealing a precursor solution containing Bi, V, and W (atomic ratio of 4.5:5:0.5) had 4.6 times higher photocurrent than stoichiometric $BiVO_4$ in 0.1 M $Na_2SO_4$ with 10 mM $Na_2SO_3$ as a sacrificial electron donor.[27] Using the same technique, Park et al. demonstrated that W/Mo doped $BiVO_4$ (Bi:V:W:Mo atomic ratio of 4.6:4.6:0.2:0.6) had 10 times higher photocurrent than $BiVO_4$ in a solution of 0.1 M $Na_2SO_4$ and 0.1 M $Na_2SO_3$.[28] Another study has shown improvement in incident photon-to-current efficiency (IPCE) with the addition of 1% W to $BiVO_4$ films deposited by spray pyrolysis on top of a thin interfacial layer of $SnO_2$.[29] Gas chromatography and oxygen reduction measurements have confirmed that photocurrent from pure and W doped $BiVO_4$ in $Na_2SO_4$ solutions is due to water oxidation.[27,30]

Herein we report the photoelectrochemical performance of Mo and W containing $BiVO_4$ films synthesized by simultaneous evaporation of elemental Bi, V, Mo, and W in vacuum followed by annealing in air. This synthesis technique allows for control of both the chemical composition and nanostructure to improve the photoactivity of the $BiVO_4$ films. Incorporation of 6% Mo and 2% W by this method resulted in a 10 fold increase in photocurrent over $BiVO_4$. The 6% Mo, 2% W $BiVO_4$ films had IPCE values above 24% for wavelengths of light between 360 and 450 nm at an applied potential of 1.6 V vs. RHE in a mixture of 0.1 $Na_2SO_4$ and 0.1 M phosphate buffer (pH 6.8), which is significantly higher than reported for this material using other synthesis techniques. The photo-deposition of Pt onto the surface of these films as an electrocatalyst improved the photocurrent onset potential drastically, resulting in IPCE values above 37% at 1.1 V vs. RHE and above 50% at 1.6 V vs. RHE.

## EXPERIMENTAL

### Description of Synthesis Parameters

The films were deposited in a high vacuum system consisting of a main chamber and load-lock chamber for sample exchange. The main chamber contained a hemispherical four-port bottom flange, which held four custom-built electron beam evaporators arranged linearly and directed at the centre of the chamber with a 16$^{o}$ angle between adjacent evaporators. All four evaporators were simultaneously controlled using a LabVIEW program that was written in collaboration with Ramsdale Software. A quartz crystal microbalance (QCM) could be translated in and out of the centre of the chamber to measure deposition rates from individual evaporators using a QCM controller (INFICON SQM-160). Substrates were moved between the main chamber and load-lock chamber using a sample holder attached to a magnetically-coupled rotary-linear motion translator.

Prior to deposition, fluorine doped tin oxide (FTO) coated glass substrates (Pilkington, TEC15) were washed with detergent (CONTREX) and water followed by washing in ethyl alcohol (PHARMC0-AAPER, 99.5%), ultrasonically cleaned for 15 min in ethyl alcohol (BRANSON 1210), and rinsed with de-mineralized water. The clean substrates were transferred through the load-lock into the main chamber. In the main chamber the substrate to be deposited on was held approximately 6 inches away from each evaporating component and the deposition angle ($\gamma$) was adjusted to a fixed angle (0-90$^{o}$) between the direction normal to the surface of the substrate and the plane of the evaporators (see Figure 3.1).

Each of the four evaporators contained either bismuth granules (Alfa Aesar, 99.997% purity) in a molybdenum crucible, a 0.25 inch diameter vanadium rod (ESPI, 3N purity), a 0.125 inch molybdenum rod (Alfa Aesar, 99.95%), or a 0.125 inch diameter

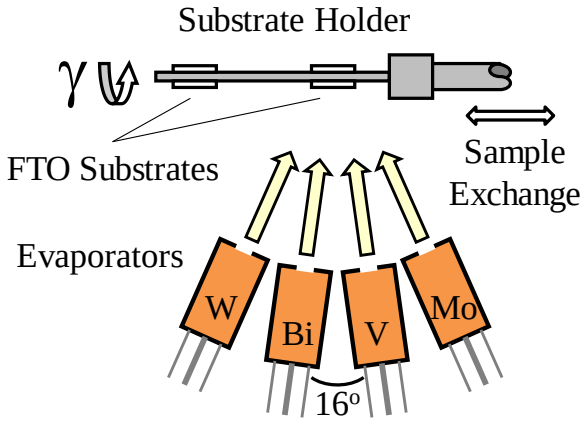


Figure 3.1. Films were grown on FTO substrates. This schematic illustrates how the FTO substrate was orientated above the evaporators during deposition. The substrate holder could hold up to four substrates and rotate to any deposition angle (γ), defined as the angle between the plane of evaporators and the vector normal to the FTO substrate surface.

tungsten rod (Alfa Aesar, 99.95%). Before depositing on a substrate, the deposition rate of each component was measured using the QCM. Adjustments were made to the evaporation rates in order to achieve the target atomic percentage of each component and the film thickness was determined by the QCM measured deposition rate, deposition angle (γ), and total deposition time. The majority of the films synthesized for this study were deposited in vacuum at pressures on the order of $5 \times 10^{-8}$ Torr or lower. For films grown by reactive ballistic deposition (RBD), a leak valve was used to backfill the chamber with oxygen (Matheson, UHP grade) to approximately $5 \times 10^{-6}$ Torr where it was held during deposition. Deposition was done at the ambient temperature of the chamber which was warmer than room temperature due to heat from the evaporators. After deposition the films were annealed in air at 500 °C for 2 hours using a muffle furnace (Neytech) with a temperature ramp rate of 10 °C $min^{-1}$. For photo-deposition of Pt the films were placed in a beaker with freshly made 10 mM $H_2PtCl_6 \cdot 6H_2O$ (Alfa Aesar,

99.95%) and 0.2 M methanol (Fischer) and illuminated from the backside with approximately 140 mW $cm^{-2}$ of white light for 1 hour.

**Measurement Techniques**

Photoelectrochemical measurements were conducted using a 3-electrode photoelectrochemical cell, which had a main compartment for the working electrode and two branched compartments separated by fritted disks (Ace Glass, 10-20 μm porosity) for the counter electrode and reference electrode. The working electrode was the $BiVO_4$ film which was pressed against an o-ring on the main compartment. It had a backside mask so that the active area was approximately 0.212 $cm^2$ for both frontside and backside illumination. The distance between the film surface and the light source was the same for frontside and backside illumination measurements. The counter electrode was a 1 mm diameter Pt wire (Alfa Aesar, 99.95%) and the reference electrode was Ag/AgCl (CH Instruments, CH111). Each compartment of the cell was filled from the same stock of electrolyte solution, which was made using $Na_2SO_4$ or $Na_2SO_3$ anhydrous, sodium phosphate monobasic monohydrate, and sodium phosphate dibasic anhydrous (Fisher) in de-mineralized water. To make 0.1 M $Na_2SO_4$ or 0.1 M $Na_2SO_3$ and 0.1 M phosphate buffer solution (pH 6.8), equal parts 0.2 M phosphate monobasic and 0.2 M phosphate dibasic were mixed and then $Na_2SO_4$ or $Na_2SO_3$ was added to the mixture. The pH of the solution was checked using a bench top pH meter (OAKTON). The pH increased slightly to 7 when 0.1 M $Na_2SO_3$ was added to the 0.1 M phosphate buffer (pH 6.8). An electrochemical analyzer/workstation (CH Instruments CH660D) was used to control the cell potential. All potentials were converted to the reversible hydrogen electrode (RHE) scale. For linear sweep voltammetry (LSV) and constant potential measurements the illumination source was a filtered (Newport, Schott KG3) 100 W xenon lamp (Newport,

Model 66452). For white light measurements the lamp was positioned to provide approximately 73 mW $cm^{-2}$ irradiation on the film. For visible light measurements an additional filter (Newport, Cut-on 420 nm) was added to the light source. IPCE measurements were conducted using a full spectrum solar simulator (Newport, Model 9600, 150 W xenon lamp) with an AM 1.5 filter (Newport) and a motorized monochrometer (Oriel Cornerstone 130 1/8 m). The monochrometer slit size was adjusted to 0.75 mm x 2 mm in order to provide between 5 and 160 μW $cm^{-2}$ of irradiation for wavelengths between 350 and 520 nm. See Appendix B (Figure B.1) for a typical light power density spectrum used for IPCE measurements. Light power was measured using a handheld optical power meter with a UV enhanced silicon photo-detector (Newport, Models 1916C and 818-UV). IPCE values were calculated using the following equation:

$$IPCE\ (\lambda) = \frac{1240\, j_p\,(\lambda)}{\lambda\, E_\lambda\,(\lambda)}$$

where $j_P(\lambda)$ is the measured photocurrent density (mA $cm^{-2}$) and $E_\lambda(\lambda)$ is the incident light power density (mW $cm^{-2}$) for each wavelength, $\lambda$ (nm). UV-vis transmission measurements were performed on a Cary 5000 spectrophotometer. Transmission-reflectance measurements were conducted using a Cary 500 spectrophotometer with an integrating sphere (Labsphere). For Tauc plots the absorption coefficient ($\alpha$) was determined by:

$$\alpha = \frac{-\ln\left(10^{-Absorbance}\right)}{z}$$

where z is the film thickness. Electrochemical impedance spectroscopy (EIS) measurements were conducted using the CH Instruments CH660D and the built in software was used to measure space charge capacitance, $C_{sc}$ (F), vs. applied potential, $E$ (V). Mott-Schottky plots were created based on ideal semiconductor behavior:[31]

$$\frac{1}{C_{sc}^2} = \frac{2}{e\ \varepsilon\ \varepsilon_0\ N_D}\left(E - E_{fb} - \frac{k\ T}{e}\right)$$

where $e$ is the electronic charge (C), $\varepsilon$ is the dielectric constant of the semiconductor, $\varepsilon_0$ is the permittivity of free space, $N_D$ is the donor density ($cm^{-3}$), $E_{fb}$ is the flat band potential (V), $k$ is the Boltzmann constant, and T is the temperature (K). Scanning electron microscope (SEM) images were acquired using a Zeiss Supra 40 VP SEM. X-ray diffraction (XRD) measurements were taken on a Bruker-Nonius D8 diffractometer. The Cu Kα radiation source was operated at 40 kV and 40 mA and measurements were carried out in the θ/2θ mode with an incident angle of 5°. X-ray photoelectron spectroscopy (XPS) measurements were performed on a Kratos AXIS Ultra DLD spectrometer with Mg Kα radiation. The concentration of Bi, V, Mo, W, O, and C were calculated from the integrated peak areas obtained after subtracting the background from each peak using the Shirley method.[32] Inductively coupled plasma mass spectrometry (ICP-MS) measurements were performed using an Agilent 7500ce Quadrupole ICP-MS. To prepare ICP-MS samples films were dissolved in 3 ml of 20% $HNO_3$ (v/v) (Fischer) inside a 23 ml acid digester vessel at 160°C for 2 hours.

## RESULTS AND DISCUSSION

### Optimal Synthesis Parameters

Mo and W containing $BiVO_4$ films were synthesized with varying deposition parameters such as the deposition angle, Bi:V:Mo:W atomic ratio, background gas pressure, and deposition time (film thickness). Evaporation at high angles of incidence, i.e., glancing angle deposition (GLAD) can be used to control the morphology of the material being synthesized.[33,34] Evaporation in vacuum onto a substrate without any background gas is a form of ballistic deposition. The addition of background gas during deposition can be used to alter the chemical composition of the material being

synthesized via a process known as reactive ballistic deposition (RBD).[35-39] For $BiVO_4$, we found that ballistic deposition followed by annealing in air to form an oxide resulted in higher photocurrents than RBD in $5x10^{-6}$ Torr of oxygen followed by the same annealing conditions. The stoichiometric $BiVO_4$ films (Bi/V atomic ratio of 1) synthesized by ballistic deposition in this study showed much higher photocurrents than the stoichiometric films deposited by RBD in our previous study.[40] Unless otherwise indicated the photoelectrochemical results in this study are for films deposited by ballistic deposition (no background gas). For these films, the deposition angle had an obvious affect on the film morphology, but not the photoactivity. Films deposited at normal incidence ($\gamma=0^o$) had slightly lower photocurrent than films deposited at more glancing angles, but there was not a significant difference in photocurrent for films deposited at angles between $45^o$ and $75^o$. Therefore, a constant deposition angle of $\gamma=55^o$ was chosen for comparing the photoelectrochemical performance of films. SEM images of a film deposited with a Bi:V:Mo:W atomic ratio of 46:46:6:2 (6% Mo, 2% W) at a deposition angle of $\gamma=55^o$ are shown in Figure 3.2. The images were taken right after deposition (Figure 3.2a) and after annealing in air at $500^oC$ for 2 hours (Figure 3.2b). For a constant deposition angle of $\gamma=55^o$, SEM images of films having different Bi:V:Mo:W atomic ratios appeared the same; i.e., Mo and W incorporation did not change the surface structure and morphology. SEM images for films grown at different deposition angles are included in Appendix B (Figure B.4). Several researchers have studied the effect of deposition angle on materials deposited by ballistic deposition.[33,34,41] During the initial stages of ballistic deposition incoming atoms randomly land on the substrate surface, creating clusters of topographically elevated points. With continued deposition at high angles of incidence the topographically elevated points have a self-shadowing effect that promotes an inclined nanocolumnar structure. As shown in Appendix B, Mo and W

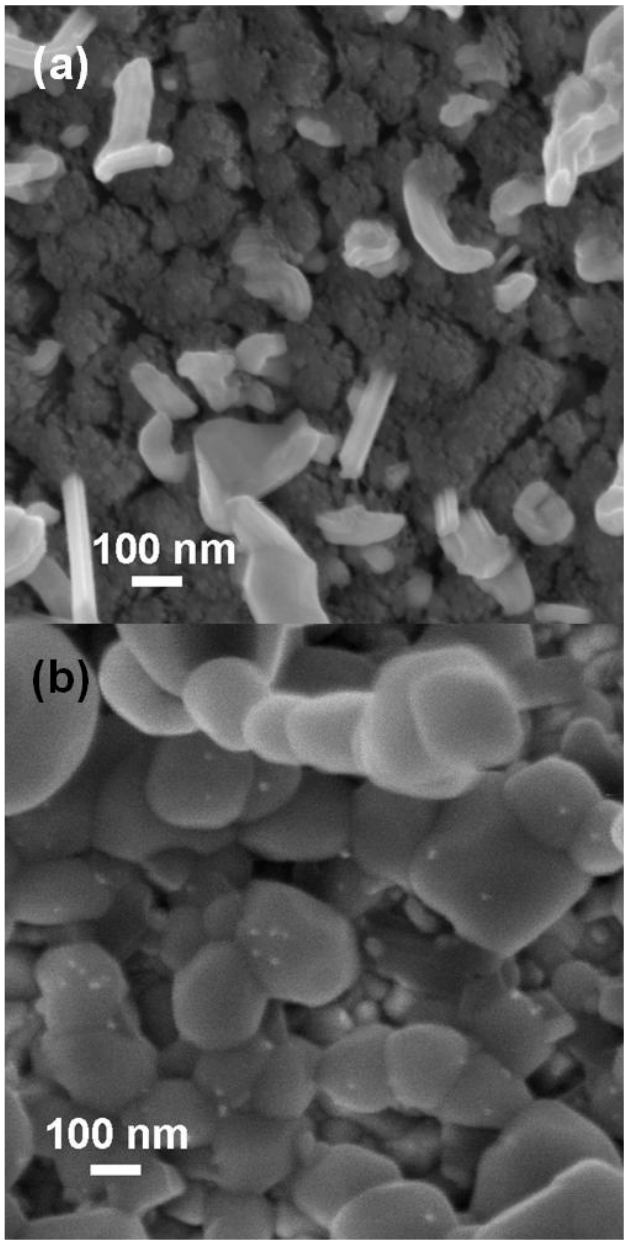


Figure 3.2. Top view SEM images of a 6% Mo, 2% W $BiVO_4$ film deposited in vacuum at a deposition angle of $\gamma=55^{o}$ (a) as deposited and (b) after annealing in air at 500$^{o}$C for 2 hours.

containing $BiVO_4$ films deposited at lower angles of incidence ($\gamma$=0-25°) had bundles of nanowires spread over the surface, which can be attributed to surface diffusion and segregation of bismuth atoms during deposition.[40] At higher angles of incidence ($\gamma$=45-75°) self-shadowing hindered nanowire growth, resulting in a more directional, columnar film structure. Nevertheless, some intermittent nanowires were still present on the surface as can be seen in Figure 3.2a. Upon annealing to 500°C, the finer features of the film sintered together into slightly larger, irregular crystal structures as shown in Figure 3.2b. Figure 3.3 shows a cross-sectional view SEM image of a 6% Mo, 2% W $BiVO_4$ film deposited at $\gamma$=55° and annealed in air at 500°C for 2 hours. The exact film thickness could not be measured because of the uneven surface structure and protruding wires. The

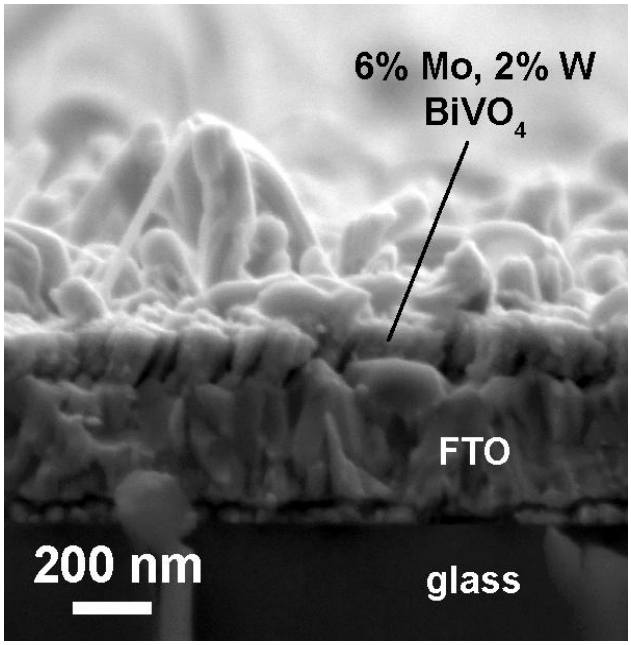


Figure 3.3. Cross-sectional view SEM image of a 6% Mo, 2% W $BiVO_4$ film deposited in vacuum at a deposition angle of $\gamma$=55° and annealed in air at 500°C for 2 hours.

nominal thickness of the film was estimated to be approximately 140 nm, which is the approximate thickness that resulted in the highest photoactivity.

For individual Mo and W incorporation, films with Bi:V:Mo:W atomic ratios of 47.5:47.5:5:0 (5% Mo) and 48.75:48.75:0:2.5 (2.5% W) had the highest photoactivity. Figure 3.4a shows the steady-state photocurrent density for films incorporated with various concentrations of Mo or W under visible and white light illumination in 0.1 M $Na_2SO_4$ and 0.1 M phosphate buffer solution (pH 6.8) at 1.1 V vs. RHE. For all levels of incorporation, Mo was more effective than W at improving the photoelectrochemical performance. Our results for $Na_2O_4$ and phosphate buffer without a sacrificial reagent are slightly different from a recent scanning electrochemical microscopy (SECM) study of Mo and W doped $BiVO_4$ arrays that found 6% W resulted in higher photocurrent than 4% Mo when tested at 0.4 V vs. NHE in 0.1 M $Na_2SO_3$ and 0.1 M $Na_2SO_4$ under white light illumination.[28] The SECM study was supported by DFT calculations that suggested W is more efficient than Mo at donating electrons to the host lattice. A separate DFT study of doped $BiVO_4$ concluded that under Bi-rich/O-poor growth conditions Mo is a more promising dopant than W for $BiVO_4$ because Mo doping does not result in significant Fermi level pinning while W doping pins the Fermi level ~0.3 V below the conduction band minimum.[42] Neither DFT study accounted for all of the factors that can contribute to PEC water oxidation such as the activity of catalytic sites created by Mo or W incorporation. Upon annealing above 397-497 $^oC$ monoclinic $BiVO_4$ adopts a scheelite crystal structure.[19] It was found that scheelites with molybdate defects were slightly better than those with tungstate defects for selective oxidation and ammoxidation of propylene.[43] To rule out differences in catalytic activity for water oxidation we performed PEC testing of the highest photoactivity Mo and W incorporated $BiVO_4$ films in 0.1 M phosphate buffer (6.8) with $Na_2SO_3$ added as a sacrificial electron donor. In this solution

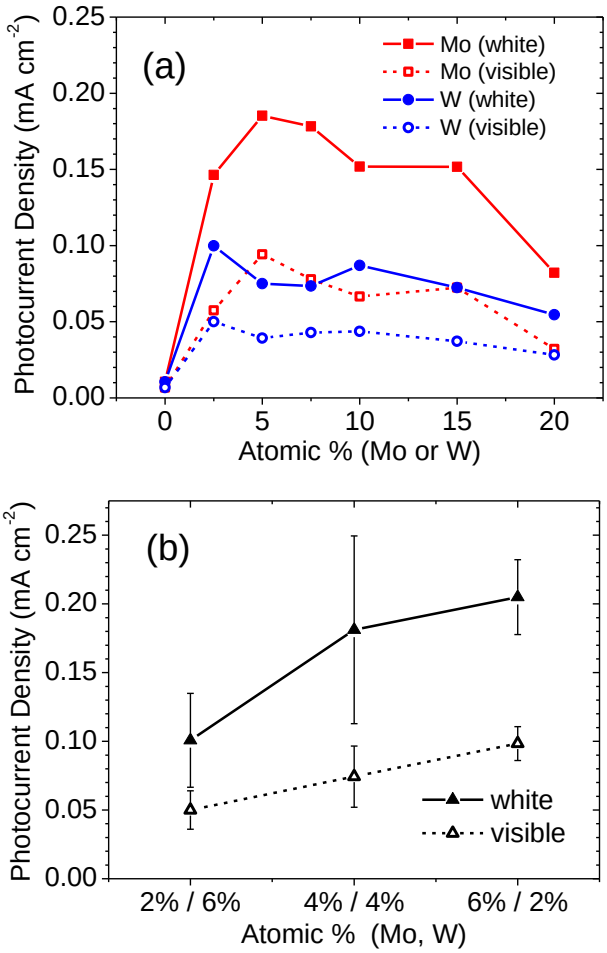


Figure 3.4. Steady-state photocurrent density values under visible and white light illumination (frontside) at 1.1 V vs. RHE in 0.1 M $Na_2SO_4$ and 0.1 M phosphate buffer solution (pH 6.8) for $BiVO_4$ films with (a) incorporation of Mo or W individually and (b) co-incorporation of Mo and W. The atomic % is relative to the total amount of Bi, V, Mo, and W (excluding oxygen content). The white light illumination power density was 73 mW $cm^{-2}$. Error bars represent one standard deviation.

at relatively low potentials (0.4 to 0.8 V vs. RHE) vacuum deposited 2.5% W $BiVO_4$ films showed slightly better photoactivity than 5% Mo $BiVO_4$ films, which is consistent with the SECM study.[28] However, at higher potentials the 5% Mo $BiVO_4$ films were more photoactive in both $Na_2SO_4$ and $Na_2SO_3$. Another factor that contributes to photoactivity

for PEC water oxidation is the minority carrier diffusion length, which has been shown to decrease with heavy doping of semiconductor materials.[44,45] At low potentials a decrease in minority carrier diffusion length in $BiVO_4$ would be expected to reduce photoactivity, but at higher applied potentials increased band bending can help drive minority carriers to the reaction site at the film-electrolyte interface.

Films with co-incorporation of Mo and W were synthesized with Bi:V:Mo:W atomic ratios of 46:46:2:6 (2% Mo, 6% W), 46:46:4:4 (4% Mo, 4% W), and 46:46:6:2 (6% Mo, 2% W). The steady-state photocurrent densities for these films under visible and white light illumination at 1.1 V vs. RHE are shown in Figure 3.4b. Photoactivity increased along with increasing Mo/W ratio and films with a Bi:V:Mo:W ratio of 46:46:6:2 showed the best performance for PEC water oxidation out of all films tested. In summary, photoactivity increased according to the following trend: pure $BiVO_4$ < 2.5% W < 5% Mo < 6% Mo, 2% W. Figure 3.5 shows a comparison of the optimal films with chopped (dark and white light) linear sweep voltammetry (LSV) scans in (a) 0.1 M $Na_2SO_4$ and 0.1 M phosphate buffer solution (pH 6.8) and (b) 0.1 M $Na_2SO_3$ and 0.1 M phosphate buffer solution (pH 6.8). Figure 3.5 shows backside illumination results for the 6% Mo, 2% W $BiVO_4$ film only, but backside illumination resulted in higher photocurrents for all levels of Mo and W incorporation.

When pure $BiVO_4$ is illuminated in $Na_2SO_4$ for long periods of time the photocurrent tends to decrease as the material photo-corrodes and vanadium dissolves into solution.[30,40] For short term PEC scans the Mo and W incorporated films showed higher stability than pure $BiVO_4$ and during the first 1-2 minutes of illumination at constant potential the photocurrent actually increased. In addition the photoactivity of Mo and W containing films tended to improve with age after annealing (see Figure B.5 in Appendix B). This increase in photocurrent ranged from 20% to 50% and leveled off

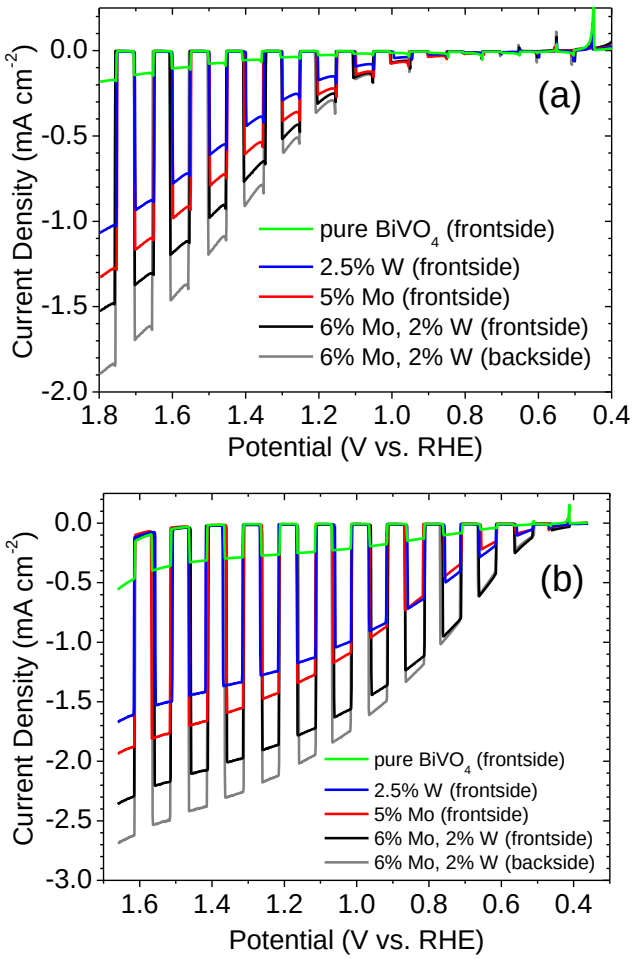


Figure 3.5. Chopped (dark and white light) LSV scans for $BiVO_4$ films with varying atomic percentages of Mo and W (relative to the total Bi, V, Mo, and W) with frontside or backside illumination as indicated. Measurements were conducted in (a) 0.1 M $Na_2SO_4$ and 0.1 M phosphate buffer solution (pH 6.8) or (b) 0.1 M $Na_2SO_3$ and 0.1 M phosphate buffer (pH 6.8). The illumination power density at the film surface was 73 mW $cm^{-2}$ and the scan rate was 0.025 V $s^{-1}$.

after 40 to 80 days of aging. Between measurements the films were simply left in a plastic container in the laboratory at normal atmospheric conditions. To rule out the aging effect when comparing different films, all the previous constant potential and LSV scans in Section 3.1 were done within 24 hours of annealing. After 1-2 hours of illumination at

constant potential the Mo and W containing $BiVO_4$ films remained fairly stable. Figure 3.6 shows an amperometric i-t scan of a 6% Mo, 2% W $BiVO_4$ film at 1.1 V vs. RHE in 0.1 M $Na_2SO_4$ and 0.1 M phosphate buffer solution (pH 6.8) done 14 days after annealing. The figure shows an initial increase in photocurrent (Figure 3.6 inset) followed by a decay. A large portion of the decay seemed to be caused by an electrolyte concentration gradient and bubble formation at the film surface because most of the photocurrent could be restored by temporarily blocking the light and flushing the film surface with fresh electrolyte. Long term there was still a net decrease in photocurrent that may have been due to photo-corrosion.

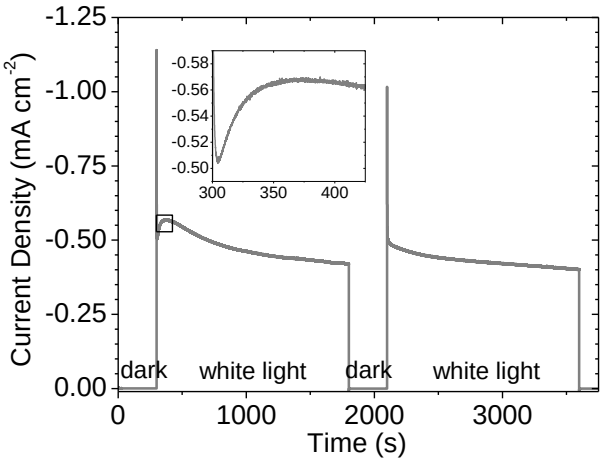


Figure 3.6. Amperometric i-t curve for a 6% Mo, 2% W $BiVO_4$ at a constant applied potential of 1.1 V vs. RHE in 0.1 M $Na_2SO_4$ and 0.1 M phosphate buffer solution (pH 6.8). The film was measured 14 days after annealing. Backside illumination was used and the power density at the film surface was 73 mW $cm^{-2}$. At 1800 s the light was blocked and the film surface was flushed with fresh electrolyte. Material Characterization

**X-Ray Diffraction**

X-ray diffraction (XRD) measurements were taken immediately after deposition and after annealing in air at 500°C for 2 hours. Immediately after deposition no peaks

were observed for V, Mo, or W, but there were peaks for crystalline Bi (PDF#00-044-1246) and $SnO_2$ (PDF#00-046-1088) from the FTO. Interestingly, films deposited by RBD in 5 x $10^{-6}$ Torr showed higher intensity peaks for crystalline Bi than films deposited without any background gas. In our previous study we found that Bi was not reactive towards background oxygen, while V reacted readily to form vanadium oxide.[40] When Bi and V are deposited together in 5 x $10^{-6}$ Torr of oxygen the reaction between V and oxygen impedes mixing of Bi and V, which increases Bi segregation. After annealing, all films showed XRD peaks which closely resembled the reference patterns for monoclinic $BiVO_4$ (PDF#00-014-0688) and $SnO_2$ (PDF#00-046-1088). Films deposited by RBD generally showed lower intensity $BiVO_4$ peaks and occasionally showed additional peaks for $Bi_4V_2O_{11}$ at 28.3° and 32°. Figure 3.7a shows the XRD pattern for pure, 5% Mo, and 6% Mo, 2% W $BiVO_4$ films deposited by ballistic deposition along with the reference patterns. Similar to Park et al., we observed merging of the (2 0 0) peak at 34.5° and (0 0 2) peak at 35.2° into a single peak at 34.9° for 5% Mo incorporation and for 6% Mo, 2% W co-incorporation.[28] The merging of peaks was attributed to a deformation of the scheelite crystal structure from monoclinic to tetragonal symmetry, which had previously been reported for Mo and W incorporation in a variety of scheelite-type materials including $BiVO_4$.[46] Figure 3.7b shows that for 2.5% W incorporation only partial merging of the peaks occurred. At 5% W the two peaks had fully merged at 34.9°, but an additional peak appeared at 24°, which matches the strongest peak in the reference pattern for $WO_3$ (PDF#00-041-0905). This implies that phase segregation begins to occur when ballistic deposition is used to incorporate more than 2.5% W into $BiVO_4$, and this may be another factor contributing to the decrease in photocurrent for higher amounts of W incorporation above 2.5% (see Figure 3.4a).

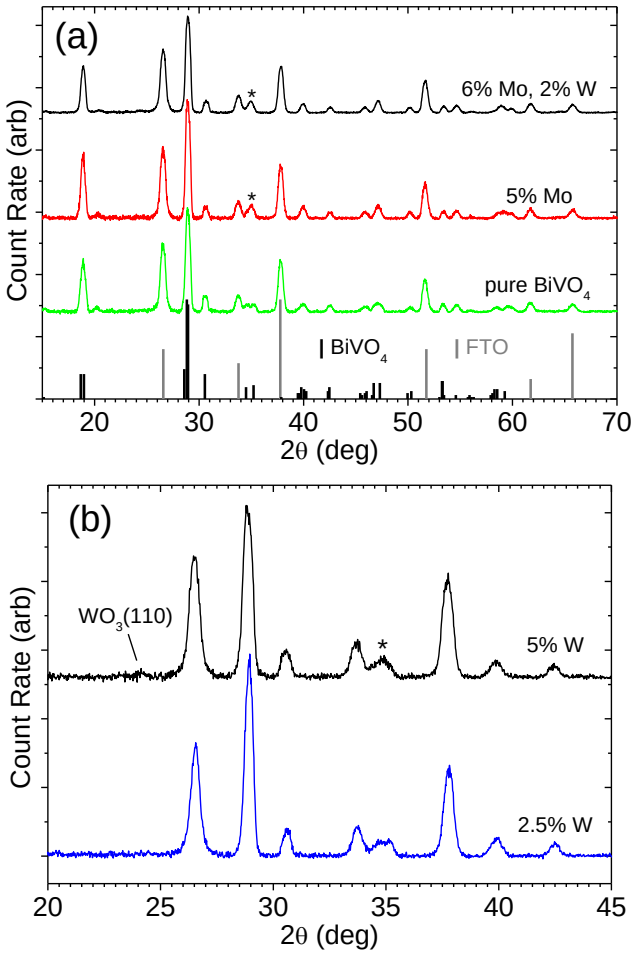


Figure 3.7. (a) XRD spectra for pure, 5% Mo, and 6% Mo, 2% W $BiVO_4$ with JCPDS peak intensities and locations plotted below the data for monoclinic $BiVO_4$ (PDF#00-014-0688) and $SnO_2$ (PDF#00-046-1088. (b) XRD spectra for 2.5% W and 5% W $BiVO_4$ with the highest intensity JCPDS peak for $WO_3$ (PDF#00-041-0905) labelled at 24°. In both (a) and (b) the * symbol indicates a single peak at 34.9° after Mo and W incorporation rather than two peaks at 34.5° and 35.2° for pure $BiVO_4$

**Transmission-Reflectance and Electrical Impedance Spectroscopy**

Initially, we measured the Mo and W incorporated $BiVO_4$ films using UV-vis transmission spectroscopy, but the spectra showed absorption tails that extended to energies as low as 2.0 eV. This was most likely caused by diffuse scattering off the

irregular surface structure of the films (see SEM images in Figures 3.2 and 3.3). In order to obtain more accurate absorption spectra we measured the films using transmission-reflectance spectroscopy with an integrating sphere to capture all of the light. The absorption data was converted to a Tauc plot (see Figure 3.8) with the assumption that the $BiVO_4$ films had a direct band gap.[47] Regardless of the amount of Mo and W incorporation, all of the films had approximately the same x-axis intercept of ~2.5 eV from extrapolation of the linear portions of the curves. This value is in line with a band gap of 2.4-2.5 eV reported for $BiVO_4$ synthesized by other techniques indicating that Mo and W incorporation does not alter the band gap of $BiVO_4$.[18-21,27,28]

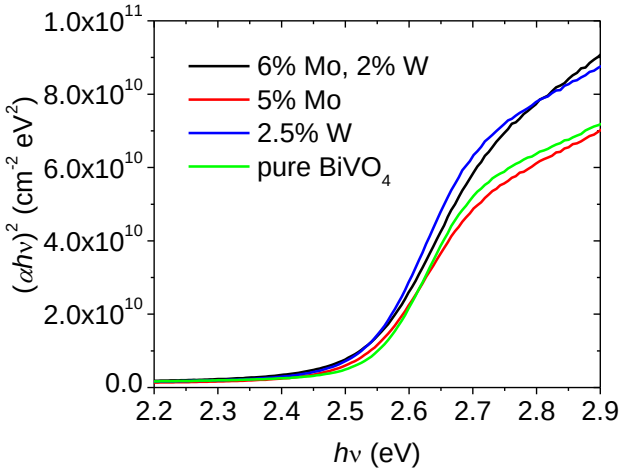


Figure 3.8. Tauc plots for $BiVO_4$ films with varying atomic percentages of Mo and W calculated from transmission spectroscopy data.

We performed electrochemical impedance spectroscopy (EIS) measurements to better understand the effect of Mo and W incorporation on carrier concentration. Mott-Schottky plots for pure $BiVO_4$ and 6% Mo, 2% W $BiVO_4$ films are included in Appendix B (Figure B.6). The slopes of the plots indicate that the flat band potentials are in the range of 0.0 - 0.05 V vs. RHE for pure $BiVO_4$ and 0.12 - 0.15 V vs. RHE for 6% Mo, 2%

W $BiVO_4$. The plot for 6% Mo, 2% W $BiVO_4$ has a lower slope, which is expected for a higher carrier concentration or doping level ($N_D$).[31] It should be noted that nanostructure has a significant impact on the impedance behaviour of a material.[48-50] EIS was used for comparison of the pure and 6% Mo, 2% W $BiVO_4$ films because they appeared to have the same surface structure and morphology when viewed by SEM.

**X-ray Photoelectron Spectroscopy and Inductively Coupled Plasma Mass Spectroscopy**

X-ray photoelectron spectroscopy (XPS) measurements were taken to verify the concentration and oxidation states of elements in the films and to help understand the increase in photocurrent with age after annealing. The XPS data for a single 6% Mo, 2% W $BiVO_4$ film taken both one day and 41 days after annealing is shown in Table 3.1 and Figure 3.9. Additional XPS spectra are included in Appendix B (Figure B.7). One day after annealing, the binding energy locations for the peaks were at 159.0 eV for Bi 4f 7/2, 516.8 eV for V 2p 3/2, 529.9 eV for O 1s, 232.2 for eV Mo 3d 5/2, and 35.1 eV for W 4f 7/2, which corresponds to oxidation states of $Bi^{3+}$, $V^{5+}$, $O^{2-}$, $Mo^{6+}$, and $W^{6+}$.[51] The XPS measured Bi:V:Mo:W atomic ratio of 41:50:3.8:5.5 did not match up with the expected ratio of 46:46:6:2 based on QCM measurements prior to starting deposition. We could not use XPS to accurately measure below the surface because the films where nanoporous and the argon sputter etch gun on the XPS instrument was mounted with an incident angle of 45° so even after sputter etching a considerable amount of surface remained exposed to the x-rays. To verify the bulk composition we dissolved a film in acid and used inductively coupled plasma mass spectroscopy (ICP-MS) to measure the concentration of cations in the solution.The ICP-MS measured atomic ratio was 46.6:45.8:6.0:1.6, which closely matched the QCM measurements indicating that the surface concentration was different from the bulk material. Mo and W have similar

atomic radii, but W may be more likely to segregate. As observed in by XRD, W began to segregate out of $BiVO_4$ and form $WO_3$ at concentrations higher than 2.5%. Mo and W incorporation may have caused a reduction in the oxidation state of Bi or V below the surface, which also could not be detected by XPS surface measurements. For the repeat measurement 41 days after annealing, the peaks were at same binding energy locations (within ± 0.1 eV) but the FWHM of the V 2p 3/2, Mo 3d 5/2, and W 4f 7/2 peaks had decreased slightly. In addition the O 1s peak developed a shoulder between 531 and 535 eV (see Figure 3.9). XPS measurements for 2.5% W $BiVO_4$ and 5% Mo $BiVO_4$ also showed a slight decrease in the FWHM for the V 2p 3/2, Mo 3d 5/2, and W 4f 7/2 peaks and development of a shoulder on the O 1s peak. Surface science studies of other metal oxides such as MgO and $TiO_2$ have demonstrated that dissociative water adsorption can lead to a high binding energy shoulder at ~532 eV on the O 1s peak.[52,53] It can be attributed to the oxygen in hydroxyls binding at defect sites.[54] The development of the shoulder on Mo and W incorporated $BiVO_4$ films is noteworthy because it suggests that the Mo and W incorporated $BiVO_4$ films have surface defects or O vacancies. These surface defects might be passivated over time reducing the number of electron-hole traps on the surface and improving the photoactivity for PEC water oxidation. Passivation of surface defects may also occur when the films are held at a positive potential in solution leading to the initial increase in photocurrent observed during amperometric i-t scans (see Figure 3.6 inset).

| 1 day after annealing | | | | |
|---|---|---|---|---|
| Element | Peak | BE [eV] | FWHM | Atomic % |
| Bi | Bi 4f 7/2 | 159.0 | 0.87 | 41 |
| V | V 2p 3/2 | 516.8 | 1.13 | 50 |
| Mo | Mo 3d 5/2 | 232.2 | 1.18 | 3.8 |
| W | W 4f 7/2 | 35.1 | 0.84 | 5.5 |
| 41 days after annealing | | | | |
| Element | Peak | BE [eV] | FWHM | Atomic % |

| | | | | |
|---|---|---|---|---|
| Bi | Bi 4f 7/2 | 159.1 | 0.87 | 43 |
| V | V 2p 3/2 | 516.8 | 1.09 | 47 |
| Mo | Mo 3d 5/2 | 232.3 | 1.11 | 4.0 |
| W | W 4f 7/2 | 35.2 | 0.81 | 6.0 |

Table 3.1. XPS data for 6% Mo, 2% W $BiVO_4$ film taken 1 day and 41 days after annealing.

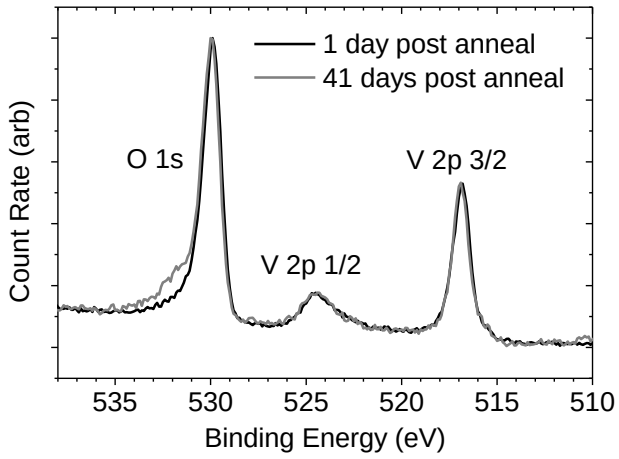


Figure 3.9. XPS spectra for a single 6% Mo, 2% W $BiVO_4$ film taken 1 day and 41 days after annealing, which shows the development of a shoulder on the O 1s peak.

**PHOTOELECTROCHEMICAL PERFORMANCE**

It has been suggested that poor charge transport is a major limiting factor for the photocatalytic activity of $BiVO_4$ based materials.[29,55] Poor charge transport in $BiVO_4$ can lead to electron-hole recombination in the bulk material, across particulate networks, and at the $BiVO_4$-FTO interface.[29,55-57] One way to improve charge transport through the bulk $BiVO_4$ material is with incorporation of impurities such as Mo and W. Experimental data from Hoffart et al. showed that 5% Mo doped $BiVO_4$ had a total conductivity at least an order of magnitude higher than $BiVO_4$ at 600 $^oC$.[58] DFT calculations suggest that doping Mo and W into $BiVO_4$ results in better separation of the excited electron-hole pairs and enhanced charge carrier mobility.[28] Recombination across particulate networks can be

overcome by synthesis techniques that result in a film with a continuous conduction path from the film surface to the FTO, such as ballistic deposition at a deposition angle of $\gamma=55^{o}$. As shown in the cross-sectional SEM images (Figure 3.3), the 6% Mo, 2% W $BiVO_4$ films were composed of continuous columns that extend all the way to the $BiVO_4$-FTO interface. The pores between columns allow the electrolyte to penetrate deeply into the film reducing the cumulative charge transport length between the location of electron-hole generation and the $BiVO_4$-electrolyte interface. Problems with recombination near the $BiVO_4$-FTO interface can be assessed by comparing frontside illumination (light source facing the electrolyte-$BiVO_4$ interface) with backside illumination (light source facing the $BiVO_4$-FTO interface). When a semiconductor film is irradiated the higher energy wavelengths will usually be absorbed at shorter depths; i.e., closer to the light source. Thus, for backside illumination the higher energy electron-hole pairs will be generated closer to the film-FTO interface. If recombination at the film-FTO interface is a major problem then backside illumination should lead to lower IPCE values than frontside illumination for higher energy wavelengths in the range of 350-425 nm (the FTO rather than the film will likely absorb light wavelengths below 350 nm). This behavior has been observed for $\alpha$-$Fe_2O_3$ films, which appear to have excessive electron-hole recombination near the film-FTO interface.[59,60] For pure and Mo and W incorporated $BiVO_4$ we observed higher overall photocurrent densities and IPCE values for backside illumination compared to frontside for nearly all wavelengths of light including 360-425 nm. The frontside and backside illumination chopped LSV scans for a 6% Mo, 2% W $BiVO_4$ film are included in Figure 3.6 and the IPCE values are included in Figure 3.10.

The higher IPCE values for backside illumination for nearly all wavelengths of light suggests that recombination at the $BiVO_4$-FTO interface is not the most significant

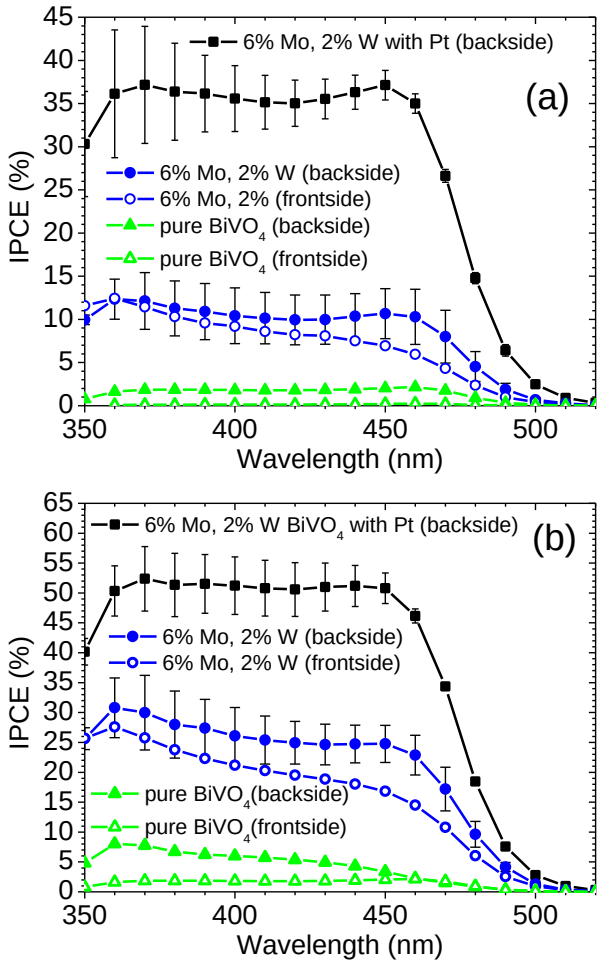


Figure 3.10. IPCE measurements conducted at (a) 1.1 V vs. RHE and (b) 1.6 V vs. RHE in 0.1 M $Na_2SO_4$ and 0.1 M phosphate buffer solution (pH 6.8) with white light illumination (frontside and backside). The films were pure $BiVO_4$, 6% Mo, 2% W $BiVO_4$, and 6% Mo, 2% W $BiVO_4$ with Pt photo-deposited on the surface. The error bars represent one standard deviation.

limiting factor for the photoactivity. Moreover, the results reveal another unique aspect of Mo and W containing $BiVO_4$ films synthesized by ballistic deposition. The lower photocurrent densities and IPCE values for frontside illumination are most likely caused diffuse scattering of incident light by the uneven surface structure at the electrolyte-$BiVO_4$ interface, which blocks light from being absorbed. For backside illumination, light

is not diffusely scattered until it travels all the way through the film, and some of this light will actually be scattered back into the film giving it another chance at being absorbed. To verify this we conducted frontside and backside illumination PEC tests on a 6% Mo, 2% W film. Then we brushed the front of the film with a clean latex glove to remove some of the irregular surface structure and repeated the frontside and backside measurements. After brushing the film surface the photocurrent density increased for frontside illumination but decreased for backside. In addition, SEM images reveal fewer wires and intermittent features protruding out of the film surface after it was brushed. Chopped LSV scans, SEM images, and UV-vis absorbance spectra for the brushed film are included in Appendix B (Figures B.8, B.9, and B.10).

Even after addressing the poor charge transport issues associated with $BiVO_4$, another significant limiting factor remains. As demonstrated by the chopped LSV scans in Figure 3.5, both pure and Mo and W containing $BiVO_4$ films suffered from slow water oxidation kinetics and recombination at the surface (electrolyte-$BiVO_4$ interface). Pure $BiVO_4$ did not show a significant increase in photocurrent until potentials were more positive than 1.0 V vs. RHE, which is well beyond the estimated flat band potential of 0.0 - 0.05 V vs. RHE. Mo and W incorporation improved the onset potential slightly and resulted in a steeper slope for the white light portion of the chopped LSV, but the photocurrent still did not reach saturation, even at potentials more positive than 1.23 V vs. RHE where water oxidation is thermodynamically possible even without illumination. One method for overcoming the slow kinetics and surface recombination of $BiVO_4$ is with the addition of an electrocatalyst. Ye et al. recently conducted an SECM study of W doped $BiVO_4$ comparing the effectiveness of different electrocatalysts including $IrO_x$, Pt, $Co_3O_4$, and cobalt-phosphate (Co-Pi).[61] Other groups recently explored the use of Co-Pi on doped $BiVO_4$ films.[62-64] Of these catalysts Pt and Co-Pi appeared to be the most

effective. Optically transparent Pt layers can be photo-deposited onto semiconductor films using a variety of solutions containing $H_2PtCl_6$[61,65,66] As a final test of the 6% Mo, 2% W $BiVO_4$ film, we photo-deposited a layer of Pt onto the surface by immersing it in a solution of 10 mM $H_2PtCl_6$ and 0.2 M methanol under backside illumination. The IPCE values and chopped LSV scans for this film are included in Figures 3.10 and 3.11. The chopped LSV scans for 6% Mo, 2% W $BiVO_4$ with Pt show a sharp increase in anodic photocurrent at 0.6 V vs. RHE. Between 0.6 and 1.23 V vs. RHE the photocurrents are drastically higher than for the film without an electrocatalyst in $Na_2SO_4$. The photocurrent for the film with Pt photo-deposited on the surface in $Na_2SO_4$ was only about 10% lower than the photocurrent observed for the film without an electrocatalyst in $Na_2SO_3$ solution, which can be used to estimate the obtainable photocurrent after overcoming the slow kinetics of water oxidation. In addition, the IPCE values for the film with Pt were much higher than for the film without an electrocatalyst (Figure 3.10). The 6% Mo, 2% $BiVO_4$ film with Pt photo-deposited on the surface had IPCE values above 37% at 1.1 V vs. RHE and above 50% at 1.6 V vs. RHE for light wavelengths between 360 and 450 nm. Integration of the IPCE values over the AM1.5 solar spectrum results in current densities of 1.7 mA $cm^{-2}$ at 1.1 V vs. RHE and 2.3 mA $cm^{-2}$ at 1.6 V vs. RHE, which is on par with other benchmark materials used for photoelectrochemical water oxidation.[13,67] Previously it was reported that drop-cast $BiVO_4$ films with Pt photo-deposited remained stable for at least 6 hours.[61] Our vacuum deposited 6% Mo, 2% W $BiVO_4$ with Pt did not appear to be stable when illuminated in electrolyte for long periods of time and the use of Pt would not be ideal in a large scale water splitting system since Pt is a rare metal. Nevertheless, these PEC results show the potential of Mo and W incorporated $BiVO_4$ films when combined with a suitable electrocatalyst material. After we completed our study J.A. Seabold et al. demonstrated that photo-deposited FeOOH is a highly active and stable water oxidation

catalyst for pure $BiVO_4$.[68] It would be interesting to test Mo and W incorporated $BiVO_4$ films with additional electrocatalysts such as FeOOH.

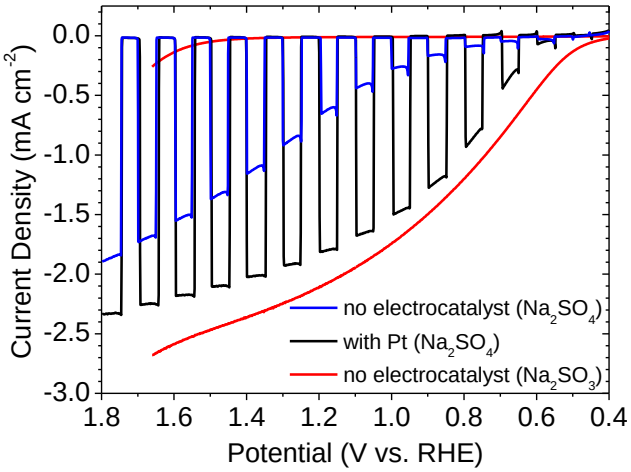


Figure 3.11. Chopped (dark and white light) LSV scans for a 6% Mo, 2% W $BiVO_4$ film without an electrocatalyst and with Pt deposited on the surface in 0.1 M $Na_2SO_4$ and 0.1 M phosphate buffer solution (pH 6.8). LSV scans (dark and white light) for a 6% Mo, 2% W $BiVO_4$ film without an electrocatalyst in 0.1 M $Na_2SO_3$ and 0.1 M phosphate buffer solution (pH 6.8). Measurements were conducted with backside illumination at 73 mW cm$^{-2}$ and a scan rate of 0.025 V s$^{-1}$.

**Conclusions**

We have incorporated Mo and W into porous, nanostructured $BiVO_4$ films to improve the performance for photoelectrochemical (PEC) water oxidation. For ballistic deposition of Bi, V, Mo and W at a deposition angle of 55° the optimal levels for individual incorporation were 2.5% W $BiVO_4$ and 5% Mo $BiVO_4$, which resulted in photocurrent densities that were 7 and 8 times higher than for pure $BiVO_4$, respectively. Further improvement was observed for co-incorporation of Mo and W. The optimal level for co-incorporation was found to be 6% Mo, 2% W $BiVO_4$, which had photocurrent densities that were 10 times higher than for pure $BiVO_4$ and higher than has been

previously reported for Mo and W incorporated $BiVO_4$. The 6% Mo, 2% W $BiVO_4$ films remained fairly stable throughout photoelectrochemical testing and improved in performance with age. The films consisted of a porous, nanocolumnar layer beneath an irregular surface structure that scattered light. Backside illumination could be used to reflect some of this scattered light back into the film for utilization, which resulted in 30-45% higher photocurrent densities than frontside illumination. The films showed some kinetic limitations for the water oxidation reaction as the maximum photocurrent densities could only be achieved at potentials well positive of the flat band potential. This was overcome by photo-deposition of Pt onto the surface as an electrocatalyst. For 450 nm light the 6% Mo, 2% W $BiVO_4$ film with Pt on the surface achieved quantum efficiencies of 37% at 1.1 V vs. RHE and 50% at 1.6 V vs. RHE. However, the films with Pt did not show long term stability and continued research is needed to optimize the photoactivity and stability of $BiVO_4$ based materials for us in a practical water splitting system.

**References**


(1) Bard, A. J.; Fox, M. A. *Accounts of Chemical Research* **1995**, *28*, 141-145.

(2) Kudo, A.; Miseki, Y. *Chemical Society Reviews* **2009**, *38*, 253-278.

(3) Osterloh, F. E. *Chemistry of Materials* **2007**, *20*, 35-54.

(4) Bak, T.; Nowotny, J.; Rekas, M.; Sorrell, C. C. *International Journal of Hydrogen Energy* **2002**, *27*, 991-1022.

(5) Maeda, K.; Domen, K. *The Journal of Physical Chemistry C* **2007**, *111*, 7851-7861.

(6) Walter, M. G.; Warren, E. L.; McKone, J. R.; Boettcher, S. W.; Mi, Q.; Santori, E. A.; Lewis, N. S. *Chemical Reviews* **2010**, *110*, 6446-6473.

(7) Zou, Z.; Arakawa, H. *Journal of Photochemistry and Photobiology A: Chemistry* **2003**, *158*, 145-162.

(8) Woodhouse, M.; Parkinson, B. A. *Chemical Society Reviews* **2009**, *38*, 197-210.

(9) Chen, X.; Shen, S.; Guo, L.; Mao, S. S. *Chemical Reviews* **2010**, *110*, 6503-6570.

(10) Irie, H.; Watanabe, Y.; Hashimoto, K. *Chemistry Letters* **2003**, *32*, 772-773.

(11) Asahi, R.; Morikawa, T.; Ohwaki, T.; Aoki, K.; Taga, Y. *Science* **2001**, *293*, 269-271.

(12) Umebayashi, T.; Yamaki, T.; Itoh, H.; Asai, K. *APPLIED PHYSICS LETTERS* **2002**, *81*, 454-456.

(13) Kay, A.; Cesar, I.; Grätzel, M. *Journal of the American Chemical Society* **2006**, *128*, 15714-15721.

(14) Hahn, N. T.; Mullins, C. B. *Chemistry of Materials* **2010**, *22*, 6474-6482.

(15) Jang, J. S.; Lee, J.; Ye, H.; Fan, F.-R. F.; Bard, A. J. *The Journal of Physical Chemistry C* **2009**, *113*, 6719-6724.

(16) Jorand Sartoretti, C.; Alexander, B. D.; Solarska, R.; Rutkowska, I. A.; Augustynski, J.; Cerny, R. *The Journal of Physical Chemistry B* **2005**, *109*, 13685-13692.

(17) Hoang, S.; Berglund, S. P.; Hahn, N. T.; Bard, A. J.; Mullins, C. B. *Journal of the American Chemical Society* **2012**, *134*, 3659-3662.

(18) Kudo, A.; Omori, K.; Kato, H. *Journal of the American Chemical Society* **1999**, *121*, 11459-11467.

(19) Tokunaga, S.; Kato, H.; Kudo, A. *Chemistry of Materials* **2001**, *13*, 4624-4628.

(20) Sayama, K.; Nomura, A.; Zou, Z.; Abe, R.; Abe, Y.; Arakawa, H. *Chemical Communications* **2003**, 2908-2909.

(21) Liu, H.; Nakamura, R.; Nakato, Y. *Journal of The Electrochemical Society* **2005**, *152*, G856-G861.

(22) Long, M.; Cai, W.; Cai, J.; Zhou, B.; Chai, X.; Wu, Y. *The Journal of Physical Chemistry B* **2006**, *110*, 20211-20216.

(23) Liu, H.; Nakamura, R.; Nakato, Y. *ChemPhysChem* **2005**, *6*, 2499-2502.

(24) Liu, H.; Nakamura, R.; Nakato, Y. *Electrochemical and Solid-State Letters* **2006**, *9*, G187-G190.

(25) Yao, W.; Ye, J. *The Journal of Physical Chemistry B* **2006**, *110*, 11188-11195.

(26) Yao, W.; Iwai, H.; Ye, J. *Dalton Transactions* **2008**, 1426-1430.

(27) Ye, H.; Lee, J.; Jang, J. S.; Bard, A. J. *The Journal of Physical Chemistry C* **2010**, *114*, 13322-13328.

(28) Park, H. S.; Kweon, K. E.; Ye, H.; Paek, E.; Hwang, G. S.; Bard, A. J. *The Journal of Physical Chemistry C* **2011**, *115*, 17870-17879.

(29) Liang, Y.; Tsubota, T.; Mooij, L. P. A.; van de Krol, R. *The Journal of Physical Chemistry C* **2011**, *115*, 17594-17598.

(30) Sayama, K.; Nomura, A.; Arai, T.; Sugita, T.; Abe, R.; Yanagida, M.; Oi, T.; Iwasaki, Y.; Abe, Y.; Sugihara, H. *The Journal of Physical Chemistry B* **2006**, *110*, 11352-11360.

(31) Bard, A. J.; Faulkner, L. R. *Electrochemical Methods: Fundamentals and Applications*; Second ed.; John Wiley & Sons, Inc.: New Jersey, 2001.

(32) Shirley, D. A. *Physical Review B* **1972**, *5*, 4709.

(33) Robbie, K.; Sit, J. C.; Brett, M. J. *Advanced techniques for glancing angle deposition*; AVS, 1998; Vol. 16.

(34) Hawkeye, M. M.; Brett, M. J. *Journal of Vacuum Science & Technology A* **2007**, *25*, 1317-1335.

(35) Dohnálek, Z.; Kimmel, G. A.; McCready, D. E.; Young, J. S.; Dohnálková, A.; Smith, R. S.; Kay, B. D. *The Journal of Physical Chemistry B* **2002**, *106*, 3526-3529.

(36) Flaherty, D. W.; Dohnálek, Z.; Dohnálková, A.; Arey, B. W.; McCready, D. E.; Ponnusamy, N.; Mullins, C. B.; Kay, B. D. *The Journal of Physical Chemistry C* **2007**, *111*, 4765-4773.

(37) Flaherty, D. W.; Hahn, N. T.; Ferrer, D.; Engstrom, T. R.; Tanaka, P. L.; Mullins, C. B. *The Journal of Physical Chemistry C* **2009**, *113*, 12742-12752.

(38) Flaherty, D. W.; May, R. A.; Berglund, S. P.; Stevenson, K. J.; Mullins, C. B. *Chemistry of Materials* **2009**, *22*, 319-329.

(39) Flaherty, D. W.; Hahn, N. T.; May, R. A.; Berglund, S. P.; Lin, Y.-M.; Stevenson, K. J.; Dohnalek, Z.; Kay, B. D.; Mullins, C. B. *Accounts of Chemical Research* **2011**.

(40) Berglund, S. P.; Flaherty, D. W.; Hahn, N. T.; Bard, A. J.; Mullins, C. B. *The Journal of Physical Chemistry C* **2011**, *115*, 3794-3802.

(41) Abelmann, L.; Lodder, C. *Thin Solid Films* **1997**, *305*, 1-21.

(42) Yin, W.-J.; Wei, S.-H.; Al-Jassim, M. M.; Turner, J.; Yan, Y. *Physical Review B* **2011**, *83*, 155102.

(43) Aykan, K.; Halvorson, D.; Sleight, A. W.; Rogers, D. B. *Journal of Catalysis* **1974**, *35*, 401-406.

(44) H. C. Casey, Jr.; Miller, B. I.; Pinkas, E. *Journal of Applied Physics* **1973**, *44*, 1281-1287.

(45) Leonid, C.; Andrei, O.; Henryk, T.; Yang, J. W.; Chen, Q.; Khan, M. A. *APPLIED PHYSICS LETTERS* **1996**, *69*, 2531-2533.

(46) Sleight, A. W.; Aykan, K.; Rogers, D. B. *Journal of Solid State Chemistry* **1975**, *13*, 231-236.

(47) Walsh, A.; Yan, Y.; Huda, M. N.; Al-Jassim, M. M.; Wei, S.-H. *Chemistry of Materials* **2009**, *21*, 547-551.

(48) Bisquert, J.; Garcia-Belmonte, G.; Fabregat-Santiago, F.; Ferriols, N. S.; Bogdanoff, P.; Pereira, E. C. *The Journal of Physical Chemistry B* **2000**, *104*, 2287-2298.

(49) Fabregat-Santiago, F.; Garcia-Belmonte, G.; Bisquert, J.; Zaban, A.; Salvador, P. *The Journal of Physical Chemistry B* **2001**, *106*, 334-339.

(50) Fabregat-Santiago, F.; Garcia-Belmonte, G.; Bisquert, J.; Bogdanoff, P.; Zaban, A. *Journal of The Electrochemical Society* **2003**, *150*, E293-E298.

(51) Wagner, C. D.; Naumkin, A. V.; Kraut-Vass, A.; Allison, J. W.; Powell, C. J.; John R. Rumble, J.; August 15, 2007 ed.; National Institute of Standards and Technology, Gaithersburg.

(52) Lazarov, V. K.; Plass, R.; Poon, H. C.; Saldin, D. K.; Weinert, M.; Chambers, S. A.; Gajdardziska-Josifovska, M. *Physical Review B* **2005**, *71*, 115434.

(53) Yamamoto, S.; Bluhm, H.; Andersson, K.; Ketteler, G.; Ogasawara, H.; Salmeron, M.; Nilsson, A. *Journal of Physics-Condensed Matter* **2008**, *20*, 14.

(54) Bluhm, H. *Journal of Electron Spectroscopy and Related Phenomena* **2010**, *177*, 71-84.

(55) Ng, Y. H.; Iwase, A.; Kudo, A.; Amal, R. *The Journal of Physical Chemistry Letters* **2010**, *1*, 2607-2612.

(56) Chatchai, P.; Murakami, Y.; Kishioka, S.-y.; Nosaka, A. Y.; Nosaka, Y. *Electrochemical and Solid-State Letters* **2008**, *11*, H160-H163.

(57) Chatchai, P.; Murakami, Y.; Kishioka, S.-y.; Nosaka, A. Y.; Nosaka, Y. *Electrochimica Acta* **2009**, *54*, 1147-1152.

(58) Hoffart, L.; Heider, U.; Jörissen, L.; Huggins, R. A.; Witschel, W. *Solid State Ionics* **1994**, *72, Part 2*, 195-198.

(59) Cesar, I.; Sivula, K.; Kay, A.; Zboril, R.; Grätzel, M. *The Journal of Physical Chemistry C* **2008**, *113*, 772-782.

(60) Hahn, N. T.; Ye, H.; Flaherty, D. W.; Bard, A. J.; Mullins, C. B. *ACS Nano* **2010**, *4*, 1977-1986.

(61) Ye, H.; Park, H. S.; Bard, A. J. *The Journal of Physical Chemistry C* **2011**, *115*, 12464-12470.

(62) Zhong, D. K.; Choi, S.; Gamelin, D. R. *Journal of the American Chemical Society* **2011**, *133*, 18370-18377.

(63) Pilli, S. K.; Furtak, T. E.; Brown, L. D.; Deutsch, T. G.; Turner, J. A.; Herring, A. M. *Energy & Environmental Science* **2011**, *4*, 5028-5034.

(64) Wang, D.; Li, R.; Zhu, J.; Shi, J.; Han, J.; Zong, X.; Li, C. *The Journal of Physical Chemistry C* **2012**, *116*, 5082-5089.

(65) Heller, A.; Aspnes, D. E.; Porter, J. D.; Sheng, T. T.; Vadimsky, R. G. *The Journal of Physical Chemistry* **1985**, *89*, 4444-4452.

(66) Yang, J. C.; Kim, Y. C.; Shul, Y. G.; Shin, C. H.; Lee, T. K. *Applied Surface Science* **1997**, *121-122*, 525-529.

(67) Santato, C.; Ulmann, M.; Augustynski, J. *The Journal of Physical Chemistry B* **2001**, *105*, 936-940.

(68) Seabold, J. A.; Choi, K.-S. *Journal of the American Chemical Society* **2012**, *134*, 2186-2192.

# Chapter 4: Screening of Transition and Post-Transition Metals to Incorporate Into Copper Oxide and Copper Bismuth Oxide for Photoelectrochemical Hydrogen Evolution

## INTRODUCTION

In theory, efficient photoelectrochemical (PEC) water splitting to produce hydrogen and oxygen by solar irradiation of a semiconductor material in water is an ideal method for renewable energy production. When it is produced by solar energy hydrogen is a carbon neutral fuel with no harmful combustion products. Less than 1% of the sun's incident power and only about $2x10^{-6}$ % of the earth's ocean water is required to produce enough hydrogen to meet the current world power demand using solar energy.[1] In practice, economical hydrogen production by PEC water splitting remains a tremendous challenge. We have not yet discovered a semiconductor material that demonstrates high solar-to-hydrogen (STH) efficiency, remains stable in electrolyte indefinitely, and is composed of abundant elements. For this reason the identification of new materials is crucial to the advancement of PEC water splitting. The first economical PEC water splitting system will likely be a multi-component device, such as a tandem PEC cell which utilizes both a p-type photocathode and n-type photoanode, since multi-component devices allow for higher theoretical efficiencies.[2-4]

Several p-type semiconductor materials with reasonable STH efficiencies (>5 %) have already been discovered. In 1982 p-InP (Rh-H alloy) and p-InP (Re-H alloy) photocathodes were tested for the photo-reduction of hydrogen with solar-to-chemical efficiencies calculated at 13.3 % and 11.4 %, respectively.[5] p-Si, when coated with electrocatalysts such as discontinuous Pt islands, can also achieve relatively high efficiencies for photo-reduction reactions.[6-8] Recently, attempts have been made to improve p-Si further by altering the nanostructure. For example nanoporous black silicon

photocathodes showed IPCE values around 90% in 0.5 M $H_2SO_4$ at -1.0 V vs. Ag/AgCl (-0.8 V vs. RHE) for 500 to 700 nm light.[9] Thin film photovoltaic materials such as $CuGaSe_2$ (CGS) and $Cu(In,Ga)Se_2$ (CIGS) have also shown reasonably high efficiencies when used as photocathodes. $CuGaSe_2$ achieved a photocurrent of 10.5 mA/cm$^2$ in 0.5 M $H_2SO_4$ at -0.9 V vs. SCE (-0.7 V vs. RHE) under AM1.5 illumination.[10] $Cu(In,Ga)Se_2$ with Pt as an electrocatalyst achieved a quantum efficiency of 19% at -0.24 V vs. RHE.[11] There is one major shortcoming with all of the previously mentioned p-type materials. They all require a large negative bias to reach the limiting photocurrent. In some cases the potential applied is even more negative than the thermodynamic $H^+$ reduction potential, which defeats the purpose of using light to drive the hydrogen evolution reaction (HER). The addition of precious metals such a Pt helps, but the maximum cathodic photocurrent is still not achieved until potentials more negative than 0.4 V vs. RHE. This makes these materials less useful for a tandem PEC device because the overlap in photocurrent of both the photocathode and photoanode at a single potential determines the operating current of such a device.[4]

Two alternative p-type semiconductor materials that have much more positive cathodic photocurrent onset potentials are CuO and $CuBi_2O_4$. CuO is reported to have a band gap energy between 1.35 and 1.7 eV.[12-16] It has been shown to have an onset potential near 0.28 V vs. SCE in 0.25 $Na_2SO_4$ at pH 6.72 (0.9 V vs. RHE) and is capable of reaching photocurrents on the order of 1 mA/cm$^2$.[17] Unfortunately, the electrochemical potential for the reduction of CuO to $Cu_2O$ in aqueous solutions is less negative than both the potential for proton reduction and the conduction band of CuO, which makes the material highly unstable in aqueous electrolytes under illumination.[17,18] Moreover, the potential for reducing $Cu_2O$ to pure Cu is more positive than both the potential for proton reduction and the conduction band of $Cu_2O$ so it is also unstable.[18] On the other hand,

$CuBi_2O_4$ has been reported to be stable as an electrode.[19] It has a light absorption threshold between 1.55 and 1.8 eV and a cathodic photocurrent onset between 1.0 and 1.1 V vs. RHE.[19,20] However, the photo-conversion efficiency of $CuBi_2O_4$ appears to be low and it may not be stable for all synthesis techniques.[20] If the stability of CuO and the efficiency of $CuBi_2O_4$ can be improved then these materials show promise for use as photocathodes in a tandem PEC device. One method for improving the stability and efficiency of materials for PEC water splitting is through incorporation of additional elements or doping.[21-24] This paper describes a combinatorial chemistry study of transition and post-transition metals for incorporation into CuO and $CuBi_2O_4$ to improve the PEC performance for photo-reduction reactions.

Combinatorial chemistry is a methodology that involves rapid synthesis of a large number of related molecules or materials, which can be screened for a specific application. It is often referred to as high-throughput screening. Pioneering work in combinatorial chemistry began in the 1960's with automated synthesis of peptides and continued research in the field of drug discovery.[25,26] Combinatorial chemistry wasn't applied to materials research until the 1990's, when it was used to investigate large magnetoresistance materials, luminescent materials, heterogeneous catalysts, and polymer thin-films.[27-32] Even more recently, combinatorial techniques have been applied to the field of photocatalysis and photo-electrochemistry. Lettmann et al. were the first to report a combinatorial technique for investigating photocatalysts in 2001.[33] They used a sol-gel method to dope $TiO_2$, $SnO_2$, and $WO_3$ with various metal salts and assessed the photocatalytic activity for water purification by measuring the degradation of a model pollutant (4-chlorophenol) under illumination. Since then other research groups have demonstrated a variety of techniques for high-throughput screening of photocatalytic materials. Nakayama et al. used molecular beam epitaxy (MBE) combined with a mask to

deposit $TiO_2$ films doped with cobalt.[34] The photocatalytic activity was assessed by reducing ferric ions and oxidizing water resulting in an increase in protons that were detected by 2-dimensional pH measurements.[34] Jaramillo et al. used automated electrochemical deposition to create libraries of mesoporous ZnO and varying composition $Zn_{1-x}Co_xO$ thin films, which were measured using a photo-electrochemical cell with a moveable probe.[35,36] Goldsmith et al., synthesized heteroleptic iridium complexes using a variety of precursor solutions.[37] The complexes were placed in vials containing triethanolamine (TEOA) as the sacrificial reductant and illuminated while measuring $H_2$ production with a hydrogen sensor. Dai et al., mixed a variety of metal nitrate solutions with a $TiCl_4$ precursor solution and silica to synthesize doped $TiO_2$ on $SiO_2$ supports.[38] They reacted 1,6-hexamethylenediamine with fluorescamine, measured the fluorescence, and correlated it to the photocatalytic activity of each material. Arai et al. developed an automated system for dispensing precursor solutions onto FTO glass for material synthesis by metal organic decomposition (MOD).[19] Photoactivity was tested in a 3-electrode PEC. Seyler used the sol-gel method to make photocatalyst materials and measured the hydrogen production under illumination using gas chromatography.[39] Other researchers have used inkjet printers to synthesize mixed-metal oxide arrays on FTO followed by PEC testing in 2 and 3-electrode PEC cells.[23,40,41] Lee et al. dispensed metal nitrate precursor solutions with a single piezoelectric dispenser onto FTO.[42] The FTO was annealed creating mixed metal oxide arrays, which were scanned by placing them in a 3-electrode cell and using a scanning electrochemical microscope (SECM) to raster a fiber optic tip across the surface while measuring the photocurrent. This approach has been used successfully to identify several high photoactivity n-type materials such as Sn/Ti doped $Fe_2O_3$, W doped $BiVO_4$ and Mo/W doped $BiVO_4$ for use as photoanodes.[43-47] We have taken a similar approach and developed a new array dispenser and scanner system

capable of screening arrays with a larger number of chemical components at a much faster rate. More details of the array scanner and dispenser system are given in the Experimental section below.

## EXPERIMENTAL

### Array Dispenser and Scanner System

Figure 4.1 shows a schematic of the array dispenser that we developed and used for this study. The array dispenser consisted of a printhead assembly (MicroFab, PH046H-AT), which held up to four 2-ml fluid reservoirs and four piezoelectric microdispensing devices (MicroFab, MJ-AT-01-80). The pressure in each reservoir was varied by a pneumatic controller (MicroFab, CP-PT4), which was connected to a vacuum / pressure pump (Thermo Scientific, 420-1901). Each reservoir contained a precursor solution that was fed to one of the four microdispensing devices. The printhead assembly was mounted on a 3-dimensional positioner (CH Instruments). The positioner and microdispensing devices were connected to a 3-dimensional positioner controller / piezo jet device controller (CH Instruments, 1560A), which was connected to a standard PC and user workstation. CH Instruments software was used to control the array dispenser system. Each microdispensing device had an orifice diameter of 80 μm and was capable of dispensing individual drops in the range of 150 to 350 pL depending on the solvent used for the precursor solution and the voltage pulse applied. Based on measurements of the mass dispensed we estimate that the drop size varied by approximately ±14% from device to device when using the same voltage pulse. To create an array, varying amounts of each precursor solution was dispensed in a pattern on a hydrophobic fluorine doped tin oxide (FTO) substrate. To make the FTO substrates hydrophobic they were cleaned and sonicated in reagent alcohol (PHARMCO-AAPER, 99.5 %), soaked in 3:50

dichlorodimethylsilane (ACROs, 99+ %) : n-hexane (ACROS, 95%), rinsed in n-hexane, and then heated at 60 ºC in a vacuum oven for 1-2 hours. Arrays were dispensed onto the cleaned FTO substrates, which were placed in a vacuum oven at 80 ºC for 15 minutes to flatten the spots for adherence and then annealed at 500 ºC for 2 hours to form mixed metal oxides.

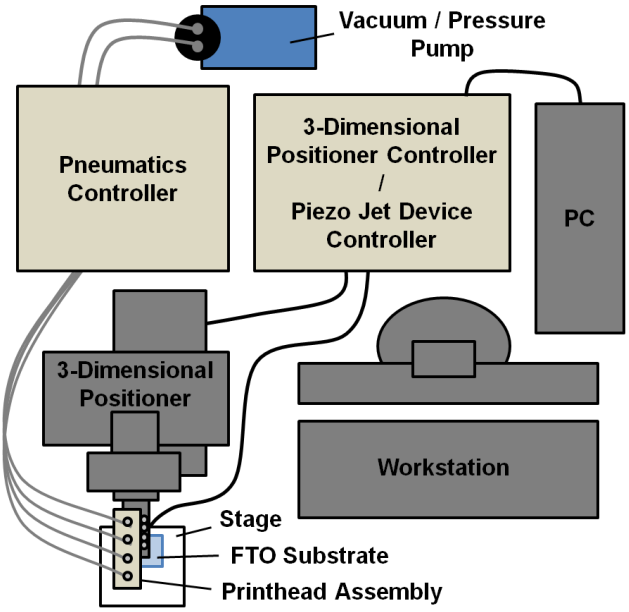


Figure 4.1. Schematic of array dispenser.

Figure 4.2 shows a schematic of the array scanner that we developed. It consisted of a Teflon 3-electrode electrochemical cell with the array in the bottom as the working electrode (WE), a platinum wire (Alfa Aesar, 0.6 mm diameter, 99.95 % purity) counter electrode (CE), and a Ag/AgCl (CH Instruments, CHI111) reference electrode (RE). The electrochemical cell was filled with an electrolyte and connected to an electrochemical analyzer (CH Instruments, CHI601D). A polished optical fiber with a 400 μm diameter core (Thorlabs, BFH48-400) was used to illuminate the array during scans. One end of the fiber was illuminated with a 100 W xenon lamp (Newport, Model 66452) with a filter

(Newport, Schott KG3) and the fiber tip at the opposite end was held in electrolyte approximately 150 μm above the array by a 3-dimensional positioner (CH instruments). A custom LabVIEW program was used to control both the electrochemical analyzer and 3- dimensional positioner. During a scan the electrochemical cell was held at a constant potential and the optical fiber tip was rastered over the array at a rate of 250-500 μm/sec while the current was recorded through a data acquisition (DAQ) board (National Instruments, USB-6009).

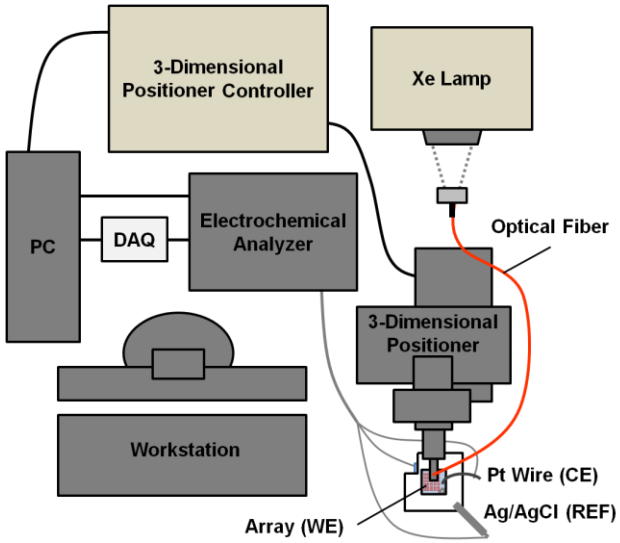


Figure 4.2. Schematic of array scanner.

**Array Synthesis and Measurement Parameters**

For this study, 22 different metals (Ag, Cd, Zn, Al, Ga, In, La, Sc, Y, Sn, Ti, Zr, Nb, Ta, V, Cr, Mo, W, Mn, Co, Fe, Ni) were dispensed along with Bi and Cu onto arrays. Each precursor solution consisted of a metal ion dissolved at a concentration of 0.15 M in ethylene glycol. Metal nitrates ($AgNO_3$, $Cu(NO_3)_2 \cdot xH_2O$, $Cd(NO_3)_2 \cdot 4H_2O$, $Zn(NO_3)_2 \cdot xH_2O$, $Al(NO_3)_3 \cdot xH_2O$, $Ga(NO_3)_3 \cdot xH_2O$, $In(NO_3)_3 \cdot xH_2O$, $La(NO_3)_2 \cdot 6H_2O$,

$Ga(NO_3)_3 \cdot xH_2O$, $Y(NO_3)_3 \cdot xH_2O$, $Bi(NO_3)_3 \cdot xH_2O$, $Cr(NO_3)_3 \cdot xH_2O$, $Mn(NO_3)_2 \cdot xH_2O$, $Co(NO_3)_2 \cdot 6H_2O$, $Fe(NO_3)_3 \cdot 9H_2O$, $N_2NiO_6 \cdot 6H_2O$) were dissolved in ethylene glycol (ACROS, 99+%). Metal chlorides ($SnCl_4 \cdot xH_2O$, $TiCl_4$, $ZrCl_4$, $NbCl_5$, $TaCl_5$, $VCl_3$) were dissolved in anhydrous ethylene glycol (Sigma-Aldrich, 99.8%) inside a glove box. $(NH_4)_6Mo_7O_{24} \cdot 4H_2O$ and $(NH_4)_{10}W_{12}O_{41} \cdot 5H_2O$ were dissolved in ethylene glycol (Fischer, certified). A complete list of chemical suppliers and purities is included in Appendix C.

For the initial screening we dispensed and scanned 22 different 19 x 19 Bi-M-Cu arrays on 3 cm x 3 cm FTO substrates (Hartford Glass, TEC15, 2.3 mm thick) according to the pattern shown in Figure 4.3. Dispensing was done with a spot spacing of 550 - 650 μm, pulse amplitude of 90 V, pulse width of 25 μs, and pulse period of 10 ms. Each spot consisted of a total of 18 drops (18 voltage pulses) with varying amounts from each precursor solution allowing concentration increments of 5.6 %. The arrays consisted of a repeat pattern (symmetric across the diagonal) so that the 153 unique Bi:M:Cu atomic ratios could be scanned twice with a single array. The corners were pure components (18 drops of a single precursor solution) and four pure Cu spots were placed in the upper/lower left corner as standards (Cu oxide standard). The spot with an atomic ratio of Bi:M:Cu=12:0:6 in the diagonal of the array was also used as a standard (Bi-Cu oxide standard). With the above settings it took 16 minutes to complete a 19 x 19 Bi-M-Cu array (6786 dispensed drops).

Initial scans were done at a constant potential of -0.1 V vs. Ag/AgCl in 0.1 M $Na_2SO_4$ (pH 5.9) with an optical fiber tip scan rate of 300 - 500 μm/sec without purging the electrolyte with nitrogen. After the initial 19 x 19 Bi-M-Cu array screening we designed fine increment Bi-M-Cu arrays for the metals that showed acceptable photo-activity relative to the Cu oxide and Bi-Cu oxide standards. Example patterns are shown later in the Results and Discussion. These arrays were dispensed onto 1.5 cm x 1.5 cm

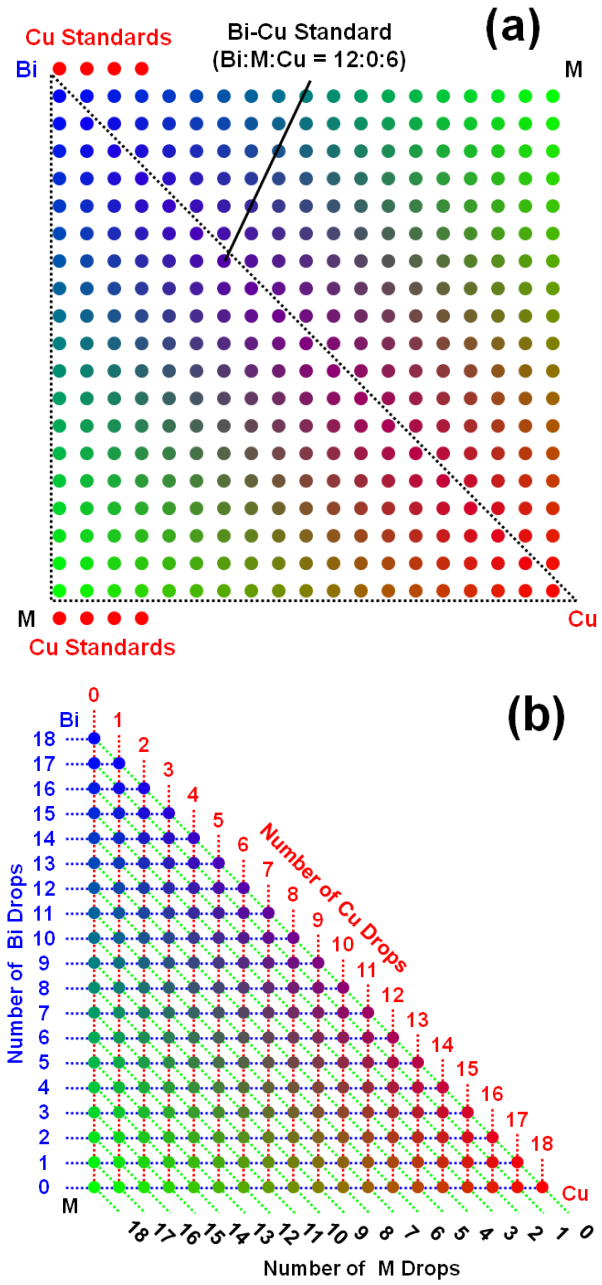


Figure 4.3. Pattern used for the initial 19 x19 Bi-M-Cu arrays. Bi and Cu were kept constant while M represents one of the 22 transition or post-transition metals. (a) Shows the entire pattern with two repeat triangles symmetric about the diagonal. (b) Indicates the number of drops from each component in the triangle adding up to 18 drops per spot.

substrates using a spot spacing of 1000 μm, pulse amplitude of 90 V, pulse width of 25 μs, and pulse period of 10 ms. Each spot consisted of a total of 36 drops for concentration increments of 2.78 %. Before each fine increment scan the electrolyte was purged for 15 minutes with nitrogen (Matheson). Next the electrochemical cell was covered with a silicone elastomer tent and nitrogen was allowed to continuously flow through the tent over the electrolyte. These scans were done at constant potential of -0.1 V vs. Ag/AgCl in 0.1 M $Na_2SO_4$ (pH 5.9) with an optical fiber tip scan rate of 250 μm/sec.

**Materials Scale-up and Characterization**

After completing the array scans the most photo-active Bi:M:Cu atomic ratios were used to make scaled-up films for materials characterization and PEC testing. Pre-cursor solutions were mixed in the desired Bi:M:Cu atomic ratios and diluted to 30 mM. Next 150 μL of the 30 mM pre-mixed solutions were drop-cast onto 1.5 x 1.5 cm substrates that had been cleaned and sonicated with reagent alcohol (PHARMCO-AAPER, 99.5 %). The drop-cast films were dried in air at 120 $^oC$ for 1 hour and then annealed in air at 500$^oC$ for 2 hours. PEC measurements of the scaled-up films were done using a 3-electrode PEC cell, electrochemical workstation/analyzer (CH Instruments 660D), and a full spectrum solar simulator (Newport, Model 9600, 150 W xenon lamp) with an AM 1.5 filter (Newport). The film was the WE, a Pt wire (Alfa Aesar, 1 mm diameter, 99.95%) was the CE, and the RE was a Ag/AgCl electrode (CH Instruments, CH111). Electrolyte solutions were prepared using $Na_2SO_4$, sodium phosphate monobasic monohydrate, sodium phosphate dibasic anhydrous (Fisher), and de-mineralized water. Non-aqueous solutions containing NaI (Fisher) and $I_2$ (Fisher, crystalline, 99.99+%) in acetonitrile (Fisher, ACS) were also prepared. Potentials were converted to reversible

hydrogen electrode (RHE) and normal hydrogen electrode (NHE) for aqueous and non-aqueous solutions, respectively. X-ray diffraction (XRD) measurements were taken on a Bruker-Nonius D8 diffractometer. The Cu Kα radiation source was operated at 40 kV and 40 mA and measurements were carried out in the θ/2θ mode with an incident angle of 1°. UV-vis transmission measurements were done on a Cary 5000 spectrophotometer. Scanning electron microscope (SEM) images were acquired using a Zeiss Supra 40 VP SEM. Energy dispersive X-ray spectroscopy (EDS) was performed using a Quanta FEG 650 SEM with a Bruker XFlash 5010 EDS detector. X-ray photoelectron spectroscopy (XPS) measurements were performed on a Kratos AXIS Ultra DLD spectrometer with Mg Kα radiation. Hydrogen measurements were done using a 3-electrode cell with the film as the WE in a sealed compartment and an evacuated port for gas collection. Prior to measurements the cell was purged with Ar (PRAXAIR). The cell was controlled using an electrochemical analyzer (CH Instruments Model 630) and illuminated with a 100 W xenon lamp (Newport, Model 66452). Gas samples were collected using a syringe and immediately injected into a gas chromatograph (GC) (SHIMADZU, CG-2014). Pt was deposited onto the surface of some films as an electrocatalyst. This was done by holding the films in 10 mM $H_2PtCl_6 \cdot 6H_2O$ (Alfa Aesar, 99.95%) and 0.1 M phosphate buffer (pH 6.8) at 0.0 V vs. Ag/AgCl until a total charge of 10 mC/cm$^2$ had passed.

## RESULTS AND DISCUSSION

### Photoactive M-Cu Oxides and Bi-M-Cu Oxides

From the array scans we found that 10 of the 22 transition and post-transition metals (M) formed a M-Cu oxide compound with higher photocurrent than the Cu oxide standard. For each M we determined the most photoactive M:Cu atomic ratio by averaging the results from three to six different fine increment arrays (2.78 %

concentration increments). Figure 4.4 shows a Pareto plot of the most photoactive M:Cu atomic ratios for each M. Photocurrent percent difference values were calculated from the M-Cu oxide and the Cu oxide standard on a single array. In Figure 4.4 each point is the average of at least three different arrays while the vertical bars are the minimum and maximum.

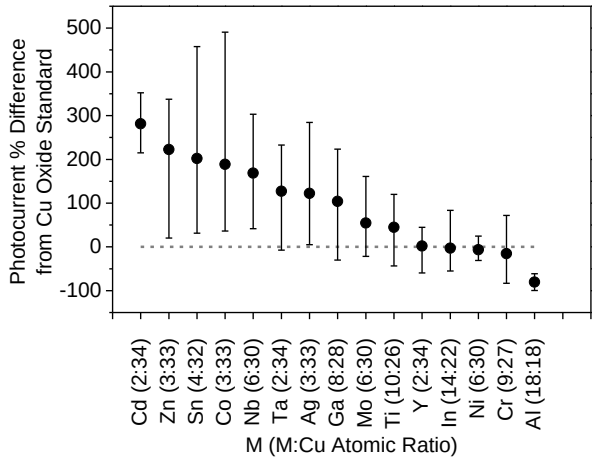


Figure 4.4. Pareto plot of the percent difference in photocurrent of the M-Cu oxide compounds from the Cu oxide standard. Each point is the average of at least three arrays while the vertical bars are the maximum and minimum. Arrays were scanned in 0.1 M $Na_2SO_4$ (pH 5.9) at a potential of -0.1 V vs. Ag/AgCl (0.45 V vs. RHE).

To our knowledge this is the first direct comparison of these M-Cu oxide compounds for PEC performance using a single measurement apparatus. In the literature few reports of Cu based ternary oxide materials for photo-reduction reactions exist. Trari et al. demonstrated $H_2$ evolution from illumination of $CuYO_2$ in electrolyte solutions containing $S^{2-}$ or $SO_3^{2-}$ species, but did not compare $CuYO_2$ with other Cu oxide compounds.[48] Saadi et al. compared $H_2$ evolution from p-type spinel materials of the form

$CuM_2O_4$ (M = Al, Cr, Mn, Fe and Co) in 0.025 M $S^{2-}$ / 1 M KOH and found that $CuCo_2O_4$ was the most photoactive of these materials.[49] Mor et al. fabricated CuO rich p-type Cu-Ti-O nanotubes as the photocathode material in a photoelectrochemical diode, but they did not investigate different Ti:Cu ratios or incorporation of other metals besides Ti.[50] From our results we found that the most photoactive M-Cu oxide materials were composed primarily of Cu (at least 72.2% Cu metals basis). The five most effective metals (Cd, Zn, Sn, and Co) for improving photoactivity compared to the Cu oxide standard are all capable of forming monoxides (CdO, ZnO, SnO, CoO, and NbO) which may allow for easier substitution into CuO, although they form different monoxide crystal structures on their own. CuO forms a monoclinic crystal system, CdO and CoO are cubic, ZnO is most commonly hexagonal (Wurzite) but also cubic, SnO is tetragonal, and NbO has a cubic structure similar to rock salt.

We synthesized scaled-up films by drop-casting and performed materials characterization to determine if incorporation of these metals altered the crystal structure from that of CuO. The XRD spectra for drop-cast Cu, Cd:Cu=2:34, Zn:Cu=3:33, and Sn:Cu=4:32 oxide films are included in Appendix C (Figure C.1). The strongest peaks for all of these films matched the reference pattern for CuO (PDF#00-048-1548) without any additional peaks for Cd, Zn, or Sn oxides. We also performed UV-vis measurements to determine if incorporation of the metals changed the light absorption of CuO (Figure C.2 in Appendix C). The Cu, Cd:Cu=2:34, Zn:Cu=3:33, and Sn:Cu=4:32 oxide films all had similar absorbance. These results suggest that incorporation of Cd, Zn, and Sn (at 11.1% or less metals basis) improves the charge transport and/or photo-reduction kinetics of CuO without modifying the crystal structure or light absorbance.

Similar to the approach used for M-Cu oxide compounds, we compared the most photoactive Bi-M-Cu oxide compounds with the Bi-Cu oxide standard (Bi:Cu=2:1). 10

out of the 22 elements resulted in a Bi-M-Cu oxide compound with higher photocurrent than the Bi-Cu oxide standard on the same array. Figure 4.5 shows a Pareto plot for these photoactive materials.

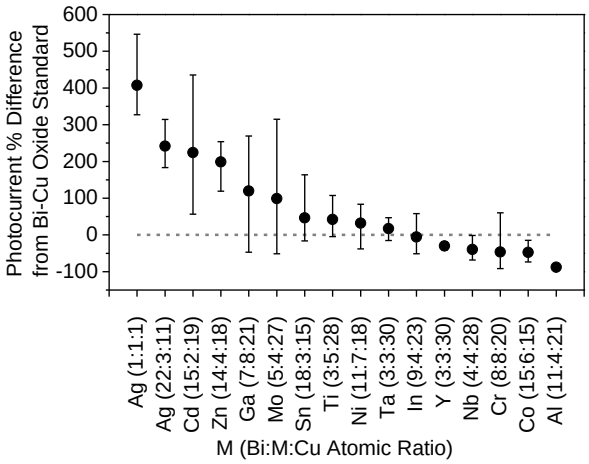


Figure 4.5. Pareto plot of the percent difference in photocurrent of Bi-M-Cu oxide compounds from the Bi-Cu oxide standard. Each point is the average of at least three arrays while the vertical bars are the maximum and minimum. Arrays were scanned in 0.1 M $Na_2SO_4$ (pH 5.9) at a potential of -0.1 V vs. Ag/AgCl (0.45 V vs. RHE).

For the majority of metals the most photoactive Bi-M-Cu oxide did not have a Bi:Cu atomic ratio close to 2:1 (ratio for $CuBi_2O_4$). Rather, the combinations with the highest photocurrent contained an excess amount of Cu over Bi (e.g. Bi:Ga:Cu=7:8:21, Bi:Mo:Cu=5:4:27, and Bi:Ti:Cu=3:5:28). In effect these materials were like Bi and M co-doped Cu oxide rather than M doped $CuBi_2O_4$. However, the three most effective metals (Ag, Cd, Zn) for improving photoactivity over Cu-Bi oxide showed high photoactivity compounds with a Bi:Cu ratio closer to 1:1 (e.g. Bi:Ag:Cu=1:1:1, Bi:Cd:Cu=15:2:19, and Bi:Zn:Cu=14:4:18).

**Cd-Cu Oxide Results**

Because of the effectiveness of Cd at enhancing photoactivity as Cd-Cu and Bi-Cd-Cu oxide it was studied in more detail. Figure 4.6 shows the initial 19 x 19 Bi-Cd-Cu array scan, which was carried out in 0.1 M $Na_2SO_4$ (pH 5.9) at -0.1 V vs. Ag/AgCl. The figure shows that 1 - 6 drops of Cd (5.56% - 33.3% metals basis) with the remaining drops Cu resulted in higher photocurrents than the Cu oxide standards. It also shows that 1 - 3 drops of Cd (5.56% - 16.7% metals basis) in the Bi-Cd-Cu areas of the array had relatively high photocurrent compared to the Cu and Cu-Bi oxide standards. These photoactive areas were used to design the fine increment array and narrow in on the most photoactive Cd:Cu and Bi:Cd:Cu atomic ratios. Figure 4.7a shows the pattern that was used for the fine increment Bi-Cd-Cu array. The array contained Bi-Cu and Cu oxide standards on the left, a square with Bi-Cd-Cu oxides in the upper right and a row of Cd-

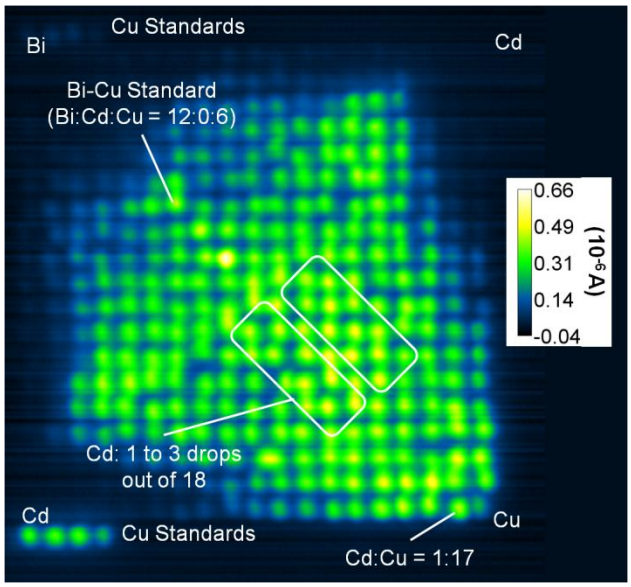


Figure 4.6. 19 x 19 Bi-Cd-Cu array scan results. The spot spacing was 550 µm. The measurement was carried out in 0.1 M $Na_2SO_4$ (pH 5.9) at a potential of -0.1 V vs. Ag/AgCl (0.45 V vs. RHE) with an optical fiber tip scan rate of 500 µm/s.

Cu oxides on the bottom. Figure 4.7b shows the scan results for this array. The entire Cd-Cu oxide row had 2-3 times higher photocurrent than the Cu oxide standard and a range of Bi-Cd-Cu oxides with 1 - 4 drops of Cd (2.78% to 11.1% metals basis) had 1.5 - 2.5 times higher photocurrent than the Bi-Cu and Cu oxide standards. The optimal atomic ratios of Cd:Cu=2:34 and Bi:Cd:Cu=15:2:19 were determined by dispensing and scanning several repeat arrays.

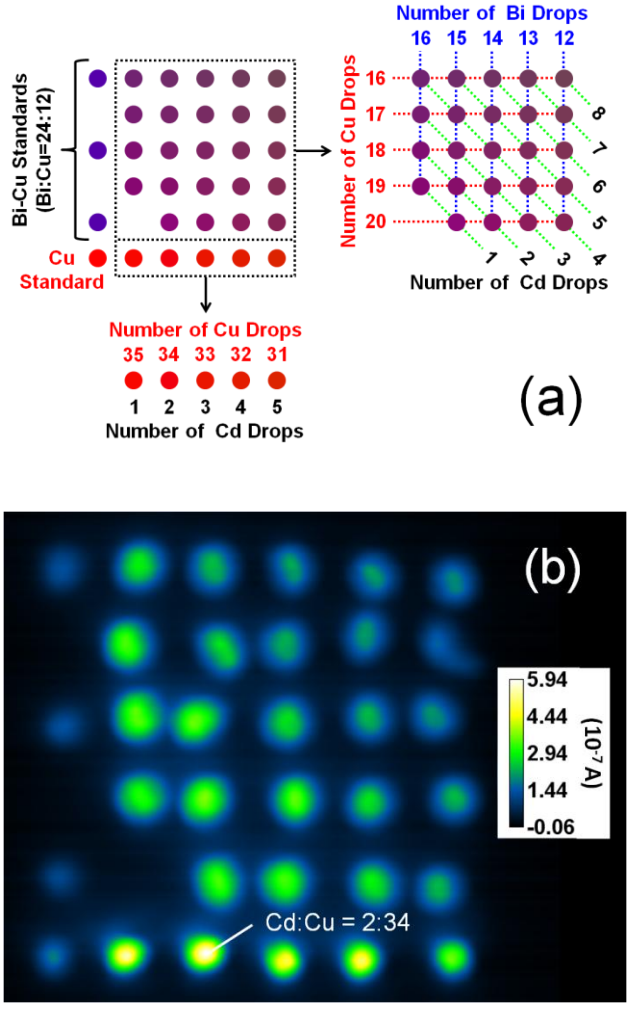


Figure 4.7. Fine increment Bi-Cd-Cu (a) array pattern and (b) scan results. Each spot had a total of 36 drops with a spot spacing was 1000 μm. Scanned at a potential of -0.1 V vs. Ag/AgCl (0.45 V vs. RHE) with an optical fiber tip scan rate of 250 μm/s.

Scaled-up Cd:Cu=2:34 oxide films synthesized by drop-casting were tested in 0.1 M $Na_2SO_4$ along with 0.1 M phosphate buffer (pH 6.8) to maintain a constant pH. Electrochemical impedance spectroscopy (EIS) was performed to determine the effect of Cd incorporation on the flat band potential ($V_{FB}$) and carrier donor density ($N_D$). A Mott-Schottky plot for the CuO and Cd:Cu=2:34 oxide film is included in Appendix C (Figure C.3). The line for the CuO film had an x-axis intercept of $V_{FB} \approx$ 1.24 V vs. RHE, which is consistent with other reports for CuO in the literature.[14,16] The Cd:Cu=2:34 oxide film had a similar x-axis intercept ($V_{FB} \approx$ 1.21 V vs. RHE) but a lower slope indicating a higher $N_D$ and possibly better conductivity than the CuO film. Figure 4.8a shows a chopped (dark/white) LSV scan for the CuO and Cd:Cu=2:34 oxide films in 0.1 M $Na_2SO_4$ and 0.1 M phosphate buffer. Consistent with the array scan results, the scaled-up Cd:Cu=2:34 oxide films showed higher photocurrent than CuO.

To test the Cd:Cu=2:34 oxide film stability an illuminated amperometric i-t measurement was run for several minutes at a constant potential of 0.6 V vs. RHE in buffered electrolyte (see Figure C.4a in Appendix C). Regrettably, incorporation of Cd into CuO did not protect the material from photo-corrosion in the aqueous solution. The photocurrent dropped by about 90% of the initial value after 20 minutes of illumination. The same measurement was conducted for other M-Cu oxide films (Cd:Cu=2:34, Zn:Cu=3:33, and Sn:Cu=4:32) as well and they all showed a large drop in photocurrent. To rule out the presumption that the higher photocurrent of the M-Cu oxide films was merely due to higher photo-corrosion we repeated the PEC tests in a non-aqueous solution containing the iodide/triiodide redox couple. The solution was prepared by dissolving 10 mM $I_2$ and 50 mM NaI in acetonitrile, which leads to an iodide:triiodide ratio of 4:1.[51] Figure 4.8b shows a chopped (dark/white) LSV scan for the CuO and Cd:Cu=2:34 oxide films in this solution with the Cd:Cu=2:34 oxide film reaching higher

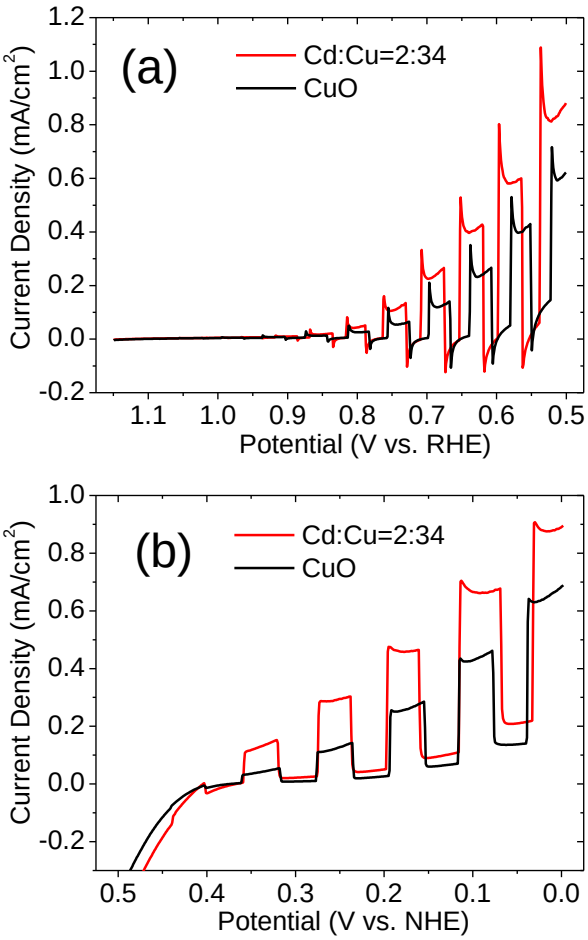


Figure 4.8. Chopped (dark/light) LSV scans for CuO and Cd:Cu=2:34 oxide films in (a) 0.1 M $Na_2SO_4$ and 0.1 M phosphate buffer (pH 6.8) and (b) 10 mM $I_2$, 50 mM NaI in acetonitrile. Measurements were done using backside illumination (100 mW/cm$^2$) and a scan rate of 0.025 V/s.

photocurrent and also remaining stable. Amperometric i-t measurements at 0.2 V vs. NHE were conducted in the iodide/triiodide solution corroborating the improved photoactivity of Cd:Cu=2:34 oxide over CuO and stability in the non-aqueous electrolyte (see Figure C.4b in Appendix C). These results confirm that incorporation of transition and post-transition metals into CuO can improve the performance for photo-reduction reactions. This may be useful if future work leads to methods for stabilizing CuO in

aqueous solutions. It has already been demonstrated that $Cu_2O$ can be protected from photo-corrosion to an extent with nanolayers of Al-doped ZnO and $TiO_2$.[52] A similar technique may be effective for CuO based materials.

**Bi-Ag-Cu Oxide Results**

Out of the 22 metals tested Ag was certainly the most effective at producing photoactive Bi-M-Cu oxide compounds. Figure 4.9 shows the initial 19 x 19 Bi-Ag-Cu array scan with several areas having drastically higher photocurrent than the Bi-Cu and Cu oxide standards, especially for Bi:Ag:Cu atomic ratios near 1:1:1 (6:6:6). Also worth mentioning is that in the Bi-Cu diagonal an excess amount of Cu compared to the Bi-Cu oxide standard (e.g. Bi:Ag:Cu=10:0:8 compared to Bi:Cu=12:6) produced a higher photocurrent. Similarly, for the Bi-Cd-Cu array results in Figure 4.6, the Bi:Cd:Cu=10:0:8 spot shows more photocurrent than the Bi-Cu oxide standard. Initially

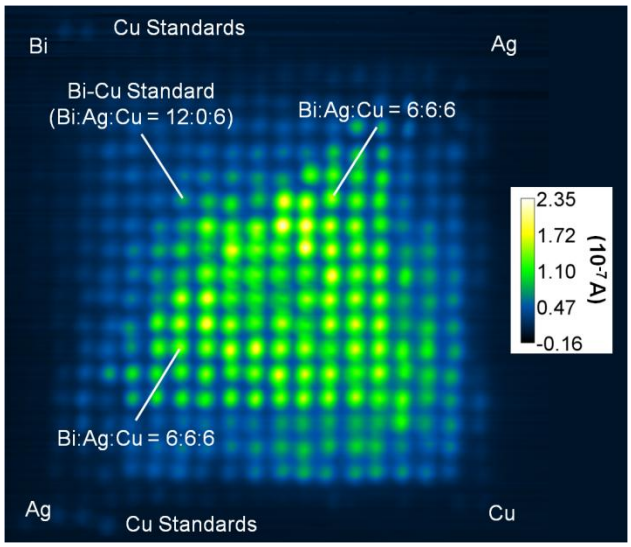


Figure 4.9. 19 x 19 Bi-Ag-Cu array scan results. The spot spacing was 550 μm. The measurement was carried out in 0.1 M Na2SO4 (pH 5.9) at a potential of -0.1 V vs. Ag/AgCl (0.45 V vs. RHE) with an optical fiber tip scan rate of 500 μm/s.

this led us to prepare scaled-up Bi-M-Cu oxide films with excess Cu by drop-casting. However, PEC measurements of the films with excess Cu (e.g. Bi:Ag:Cu=1:1:1, Bi:Cd:Cu=15:2:19, and Bi:Zn:Cu=14:4:18) tended to show more dark current and less long-term stability than films synthesized with a Bi:Cu atomic ratio closer to 2:1. In addition the excess Cu did not result in any new compounds other than $CuBi_2O_4$, which is apparent from XRD measurements. Figure 4.10 shows the XRD spectra for films synthesized by drop- casting with atomic ratios of Bi:Cu=2:1, Bi:Ag:Cu=22:3:11, and Bi:Ag:Cu=1:1:1. Even when excess Cu was added, as in the case of Bi:Ag:Cu=1:1:1, the largest XRD peaks matched the reference pattern for kusachiite, $CuBi_2O_4$ (PDF# 00-042-0334) which has a Bi:Cu ratio of 2:1 and there were no additional peaks related to a Cu compound. This suggests that the excess Cu is incorporated into the interstitial sites of $CuBi_2O_4$, which may contribute to the instability during PEC measurements. Previously we showed that $BiVO_4$ films synthesized with excess V (Bi:V=1:2) had much higher initial photocurrents than $BiVO_4$ synthesized with stoichiometric Bi and V (Bi:V=1:1); however, much of the initial photocurrent was due to photo-corrosion and dissolution of excess V into solution.[53] For this reason we focused on materials characterization and PEC testing of scaled-up films with a Bi:Cu atomic ratio of 2:1 (e.g. $CuBi_2O_4$ and Bi:Ag:Cu=22:3:11). Interestingly, Ag was not incorporated into $CuBi_2O_4$ as an oxide but rather segregated primarily as reduced Ag. The XRD patterns for both Bi:Ag:Cu=22:3:11 and Bi:Ag:Cu 1:1:1 showed the emergence of peaks at 2θ values of 38.1° and 44.3° corresponding to the (111) and (200) peaks in the reference pattern for Ag (PDF#00-004-0783). Incorporation of Ag did not result any shifting of the $CuBi_2O_4$ peaks.

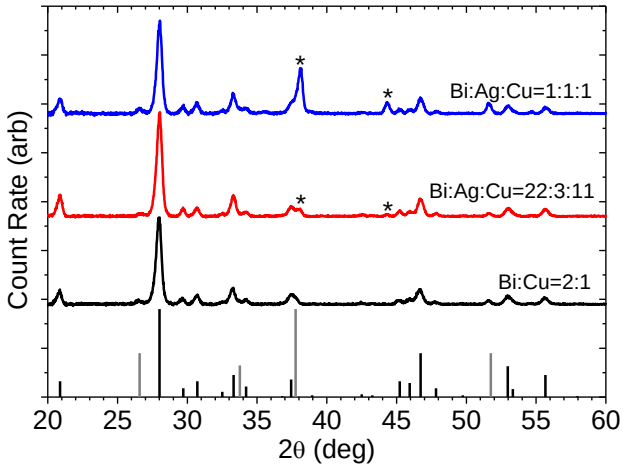


Figure 4.10. XRD spectra for bulk films drop-cast with atomic ratios of Bi:Cu=2:1, Bi:Ag:Cu=22:3:11, and Bi:Ag:Cu=1:1:1. Grey vertical lines (|) represent the cassiterite, $SnO_2$ reference pattern (PDF# 00-042-0334). Black vertical lines (|) represent the kusachiite, $CuBi_2O_4$ reference pattern (PDF# 00-042-0334). Asterisks marks (*) indicate the silver, Ag (111) and (200) peaks at 2θ values of 38.1° and 44.3°, respectively (PDF#00-004-0783).

Figure 4.11a shows the fine increment Bi-Ag-Cu array pattern and Figure 4.11b shows the array scan results for this pattern. The fine increment array scans demonstrated that a range of Ag concentrations (8.3 % to 19.4 % metals basis) improved the photocurrent compared to $CuBi_2O_4$. After dispensing and scanning several different arrays the optimal Bi:Ag:Cu atomic ratio was determined to be 22:3:11 (8.3% Ag metals basis), which consistently showed 2.5 times higher photocurrent than $CuBi_2O_4$. The improvement in photocurrent of Bi:Ag:Cu=22:3:11 oxide films over $CuBi_2O_4$ was confirmed by PEC testing of scaled-up films. Figure 4.12a shows the chopped (dark/white) LSV scan for these films in 0.1 M $Na_2SO_4$ and 0.1 M phosphate buffer. At 0.6 V vs. RHE the photocurrent for the Bi:Ag:Cu=22:3:11 oxide film was about 4 times higher than that of $CuBi_2O_4$. In addition the $CuBi_2O_4$ film showed significantly larger transient spikes in the photocurrent traces. For n-type semiconductors large anodic and

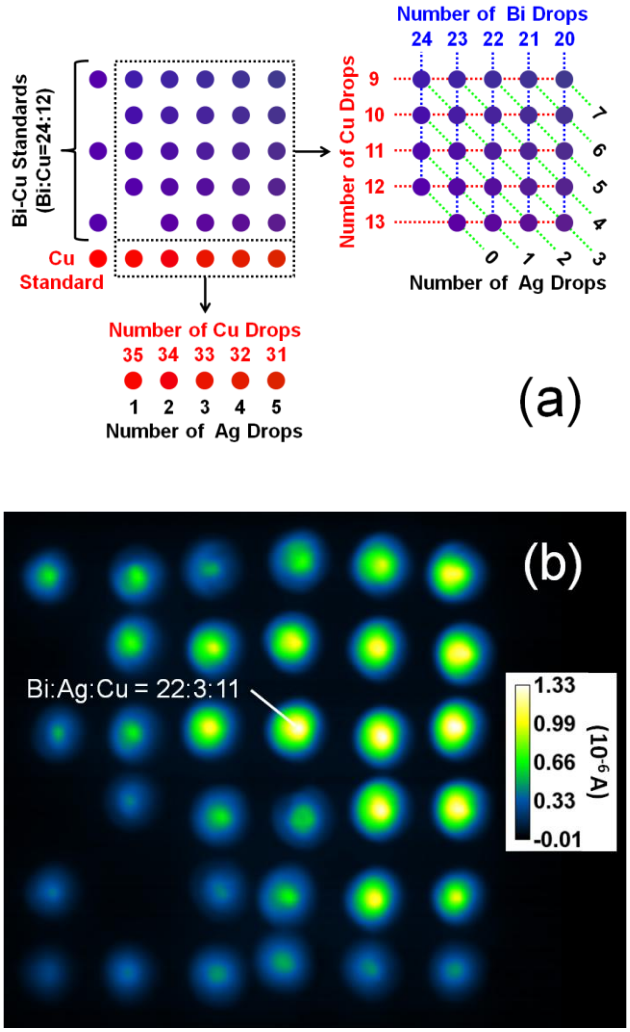


Figure 4.11. Fine increment Bi-Ag-Cu (a) array pattern and (b) scan results. Each spot had a total of 36 drops with a spot spacing was 1000 μm. Scanned at a potential of -0.1 V vs. Ag/AgCl (0.45 V vs. RHE) with an optical fiber tip scan rate of 250 μm/s.

cathodic spikes are often attributed to recombination or back reactions of the photogenerated species on the surface of the semiconductor.[17,54,55] The large transient spikes imply that the $CuBi_2O_4$ surface has slower reaction kinetics for the photo-reduction reaction. To further assess differences in kinetics we tested the $CuBi_2O_4$ and Bi:Ag:Cu=22:3:11 oxide films in the non-aqueous iodide/triiodide electrolyte prepared

from 10 mM $I_2$ and 50 mM NaI, in acetonitrile. The triiodide species is expected to undergo a fast reduction lessening the influence of reaction kinetics on the overall photoactivity. Figure 4.12b shows the chopped (dark/light) LSV scans. In the iodide/triiodide electrolyte the $CuBi_2O_4$ and Bi:Ag:Cu=22:3:11 oxide films had very similar photo-currents without significant transient spikes. The relative differences in

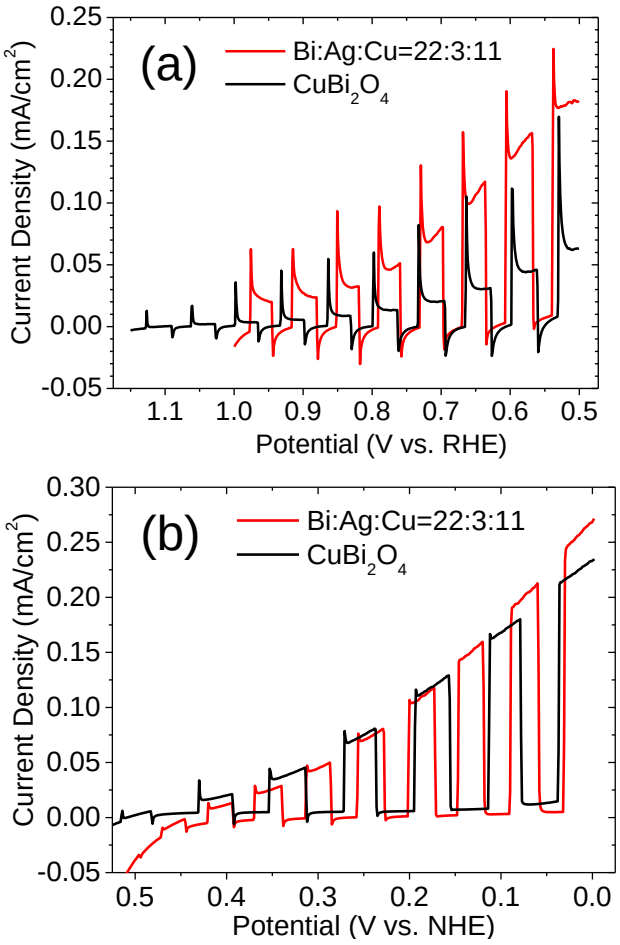


Figure 4.12. Chopped (dark/light) LSV scans for $CuBi_2O_4$ and Bi:Ag:Cu=22:3:11 oxide films synthesized by drop-cast in (a) 0.1 M $Na_2SO_4$ and 0.1 M phosphate buffer (pH 6.8) and (b) 10 mM $I_2$, 50 mM NaI in acetonitrile. Measurements were done using backside illumination (100 mW/cm$^2$) and a scan rate of 0.025 V/s.

photocurrents for $CuBi_2O_4$ and Bi:Ag:Cu=22:3:11 oxide in the aqueous and iodide/triiodide electrolytes confirm that Bi:Ag:Cu=22:3:11 oxide has better reaction kinetics for the photo-reduction reactions in the aqueous solution, which likely includes $H^+$ reduction. Ag is not regarded as an effective electrocatalyst for HER, but computational studies have suggested that surface alloys can be much more active for HER than the individual elements from which the alloys are composed.[56] We also tested Bi:Ag:Cu=22:3:11 oxide films with Pt electrodeposited on the surface. This increased the dark current but did not significantly increase the photocurrent for chopped LSV scans in electrolyte that had not been purged with an inert gas (see Figure C.5a in Appendix C).

To uncover more reasons that Ag incorporation improved the photocurrent of $CuBi_2O_4$ we performed materials characterization of the scaled-up films. UV-Vis measurements showed that Ag incorporation did not change the absorption significantly (see Figure C.6 in Appendix C). SEM images revealed slight differences in surface structures and morphologies for $CuBi_2O_4$ and Bi:Ag:Cu=22:3:11 oxide films. Figure 4.13 shows high and low magnification SEM images of the $CuBi_2O_4$ and Bi:Ag:Cu=22:3:11 spots in a fine detail array and SEM images of the drop-cast films are included in the Appendix C (Figure C.7). The images show that the Bi:Ag:Cu=22:3:11 oxide contains a mix of lager features (50-250 nm coalesced particles) and much smaller particles (<10 nm diameter) while the $CuBi_2O_4$ contained a more dense layer with less variation in feature sizes (<100 nm coalesced particles). The larger features of the Bi:Ag:Cu=22:3:11 oxide my improve charge transport through the film while the smaller particles on the surface might act as reaction sites to improve the kinetics of the surface reaction.

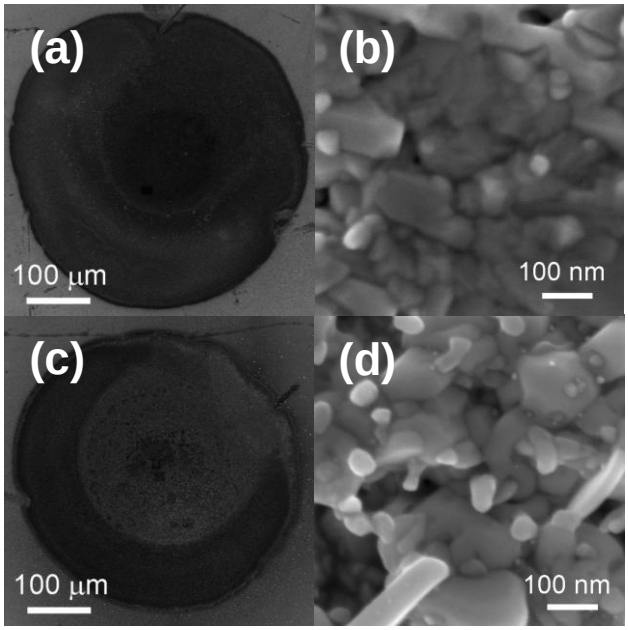


Figure 4.13. SEM images of a fine detail Bi-Ag-Cu array. (a) Entire Bi:Cu=2:1 spot, (b) area in centre of Bi:Cu=2:1 spot, (c) entire Bi:Ag:Cu=22:3:11 spot, and (c) area in centre of Bi:Ag:Cu=22:3:11 spot.

Both EDS and XPS were used to analyze the chemical composition of the $CuBi_2O_4$ and Bi:Ag:Cu=22:3:11 oxide films. EDS mapping of a Bi-Ag-Cu array spot showed that Bi, Ag, and Cu were distributed throughout the entire spot and quantification of the EDS spectra from several spots confirmed that the dispensed atomic ratios were within ±1 drop of the expected values. The EDS data is included in Appendix C (Figure C.8 and Table C.1). Figure 4.14 shows the XPS spectra for scaled-up $CuBi_2O_4$ and Bi:Ag:Cu=22:3:11 oxide films. The Bi 4f, Cu 2p, and O 1s regions were similar for both compositions with the main Bi 4f 7/2, Cu 2p 3/2, and O 1s peaks at 158.4 eV, 934.0 eV, and 529.3 eV, respectively. This corresponds to oxidation states of $Bi^{3+}$, $Cu^{2+}$, and $O^{2-}$ and matches the stoichiometry of the films.[57] As mentioned previously, Ag appeared to be incorporated in the reduced form based on XRD measurements. The XPS spectra for the

Bi:Ag:Cu=22:3:11 oxide film showed a Ag 3d 5/2 peak at 368.1 eV, which is in range of the experimentally reported binding energies for pure Ag at 368.0 - 368.4 eV.[57-59] But distinguishing the oxidation state of Ag by XPS is a challenge because the reported binding energies of $Ag_2O$ and AgO overlap at 367.6 – 368.4 eV and 367.2 – 368.1 eV, respectively.[57,58] As further proof that Ag is incorporated in the reduced form we ran CV scans in the dark on the films between 0.6 to 1.3 V vs. RHE (Figure C.10 in Appendix C). The CV scan for the $CuBi_2O_4$ film was perfectly flat while that for Bi:Ag:Cu=22:3:11 oxide showed a large anodic spike for the oxidation of Ag when scanning more positive than 1.0 V vs. RHE. Ag metal is known for exceptionally low contact resistance and very high electrical conductivity while Ag oxides have relatively low conductivity.[58,60] Incorporation of reduced Ag into $CuBi_2O_4$ likely improves the conductivity and charge transport through the film, which is another possible reason for the improvement in photoactivity. The improvement may also be related to spectral sensitization by surface

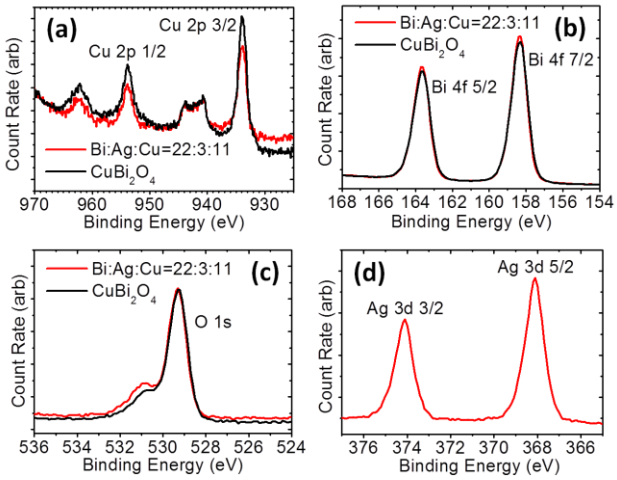


Figure 4.14. XPS spectra for $CuBi_2O_4$ and Bi:Ag:Cu=22:3:11 oxide films. (a) Cu 2p (b) Bi 4f (c) O 1s and (d) Ag 3d regions.

plasmon resonance of dispersed Ag nanoparticles. This was proposed for a study in which 50% Ag incorporation into $Fe_2O_3$ resulted in 5 nm Ag nanoparticles that were observed by transmission electron microscopy (TEM).[61]

Because the Ag in the Bi:Ag:Cu=22:3:11 oxide films were easily oxidized at potentials more positive than 1.0 V vs. RHE the films were kept between 0.5 and 1.0 V vs. RHE during PEC testing. Within this range both $CuBi_2O_4$ and Bi:Ag:Cu=22:3:11 oxide films appeared to be relatively stable in neutral aqueous electrolyte. Long-term PEC testing was also performed. Figure 4.15 shows the illuminated amperometric i-t measurement for $CuBi_2O_4$ and Bi:Ag:Cu=22:3:11 oxide films and a Bi:Ag:Cu=22:3:11 oxide film with Pt electrodeposited on the surface. Initially the films showed a drop in photocurrent, but afterwards the photocurrents remained fairly constant for 45 minutes. As mentioned previously, Pt did not improve the photocurrent significantly for chopped LSV scans, but as shown in Figure 4.15 it did enhance the photocurrent for long-term testing at a constant potential.

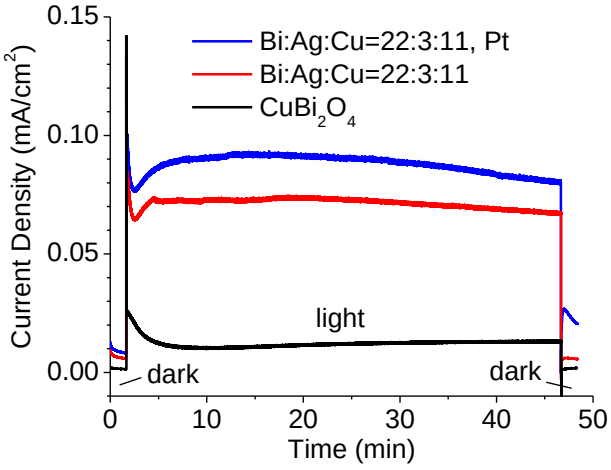


Figure 4.15. Amperometric i-t curve for $CuBi_2O_4$ and Bi:Ag:Cu=22:3:11 oxide films. Measurements done in 0.1 M $Na_2SO_4$ and 0.1 M phosphate buffer solution (pH 6.8) at constant potential of 0.6 V vs. RHE.

Unless otherwise indicated the PEC testing of scaled-up films was done without purging the electrolyte with an inert gas so a portion of the photocurrent came from the reduction of species other than $H^+$. When the electrolyte was purged with an inert gas such as Ar or $N_2$ the photocurrent was lower, even with the addition of Pt. This is seen by comparing Figures C.5a and C.5b in Appendix C. To confirm that the films were actually capable of reducing $H^+$ and evolving $H_2$ we performed qualitative $H_2$ detection measurements for Bi:Ag:Cu=22:3:11 oxide films with and without Pt deposited on the surface. The films were placed in a sealed PEC cell with 0.1 M $Na_2SO_4$ and 0.1 M phosphate buffer (pH 6.8) that had been purged with Ar for 30 minutes. Then the films were held at a constant potential of 0.6 V vs. RHE and illuminated with a 100 W Xe lamp for about 5 hours. We observed formation of small (~1 mm) bubbles on the films with and without Pt on the surface. The gas above the electrolyte was collected and measured by GC. A significant amount of $H_2$ was detected for the film with Pt but not for the film without Pt. Since 0.6 V vs. RHE is well positive of the thermodynamic $H^+$ reduction potential, the $H_2$ must have been produced photoelectrochemically.

## CONCLUSIONS

We have designed a new array dispenser and scanner system for materials research by combinatorial chemistry. The system was used to study the incorporation of 22 different transition and post-transition metals (M) into CuO and $CuBi_2O_4$ to improve the PEC performance for photo-reduction reactions including hydrogen evolution. We identified 10 metals that produced M-Cu oxide compounds with higher photoactivity than CuO. The most photoactive M-Cu oxide materials contained 2.78 to 11.1 % M incorporated into CuO (metals basis). Cd, Zn, and Sn were the most effective at improving the photocurrent of CuO and with optimal atomic ratios of Cd:Cu=2:34,

Zn:Cu=3:33, and Sn:Cu=4:32. Unfortunately incorporation of these elements into CuO did not prevent photo-corrosion in aqueous solutions, but it did enhance the photocurrent with stability in non-aqueous iodide/triiodide solutions. For Bi-M-Cu oxides we found 10 metals that increased the photocurrent relative to $CuBi_2O_4$. Ag was the most effective element at improving the photoactivity of $CuBi_2O_4$ while also maintaining the stability in neutral electrolyte solutions. Films with a Bi:Ag:Cu atomic ratio of 22:3:11 produced photocurrents up to 5 times higher than $CuBi_2O_4$ between 1.0 and 0.5 V vs. RHE, which is a reasonable operating range for a tandem PEC cell. With the addition of a HER electrocatalyst such as Pt, these films were capable of evolving hydrogen under illumination in a neutral electrolyte solution at a potential of 0.6 V vs. RHE.

## REFERENCES


(1) van de Krol, R.; Grätzel, M. *Photoelectrochemical Hydrogen Production*; Springer: New York Dordrecht Heidelberg London, 2012.

(2) Weber, M. F.; Dignam, M. J. *International Journal of Hydrogen Energy* **1986**, *11*, 225-232.

(3) Bolton, J. R.; Strickler, S. J.; Connolly, J. S. *Nature* **1985**, *316*, 495-500.

(4) Walter, M. G.; Warren, E. L.; McKone, J. R.; Boettcher, S. W.; Mi, Q.; Santori, E. A.; Lewis, N. S. *Chemical Reviews* **2011**, *111*, 5815-5815.

(5) Aharon-Shalom, E.; Heller, A. *Journal of The Electrochemical Society* **1982**, *129*, 2865-2866.

(6) Nakato, Y.; Tonomura, S.; Tsubomura, H. *Berichte der Bunsengesellschaft für physikalische Chemie* **1976**, *80*, 1289-1293.

(7) Dominey, R. N.; Lewis, N. S.; Bruce, J. A.; Bookbinder, D. C.; Wrighton, M. S. *Journal of the American Chemical Society* **1982**, *104*, 467-482.

(8) Nakato, Y.; Yano, H.; Nishiura, S.; Ueda, T.; Tsubomura, H. *Journal of Electroanalytical Chemistry and Interfacial Electrochemistry* **1987**, *228*, 97-108.

(9) Oh, J.; Deutsch, T. G.; Yuan, H.-C.; Branz, H. M. *Energy & Environmental Science* **2011**, *4*, 1690-1694.

(10) Marsen, B.; Cole, B.; Miller, E. L. *Solar Energy Materials and Solar Cells* **2008**, *92*, 1054-1058.

(11) Yokoyama, D.; Minegishi, T.; Maeda, K.; Katayama, M.; Kubota, J.; Yamada, A.; Konagai, M.; Domen, K. *Electrochemistry Communications* **2010**, *12*, 851-853.

(12) Nakaoka, K.; Ueyama, J.; Ogura, K. *Journal of The Electrochemical Society* **2004**, *151*, C661-C665.

(13) Ghijsen, J.; Tjeng, L. H.; van Elp, J.; Eskes, H.; Westerink, J.; Sawatzky, G. A.; Czyzyk, M. T. *Physical Review B* **1988**, *38*, 11322-11330.

(14) Koffyberg, F. P.; Benko, F. A. *Journal of Applied Physics* **1982**, *53*, 1173-1177.

(15) Chaudhary, Y. S.; Agrawal, A.; Shrivastav, R.; Satsangi, V. R.; Dass, S. *International Journal of Hydrogen Energy* **2004**, *29*, 131-134.

(16) Chauhan, D.; Satsangi, V. R.; Dass, S.; Shrivastav, R. *Bulletin of Materials Science* **2006**, *29*, 709-716.

(17) Hardee, K. L.; Bard, A. J. *Journal of The Electrochemical Society* **1977**, *124*, 215-224.

(18) Gerischer, H. *Journal of Electroanalytical Chemistry and Interfacial Electrochemistry* **1977**, *82*, 133-143.

(19) Arai, T.; Konishi, Y.; Iwasaki, Y.; Sugihara, H.; Sayama, K. *Journal of Combinatorial Chemistry* **2007**, *9*, 574-581.

(20) Hahn, N. T.; Holmberg, V. C.; Korgel, B. A.; Mullins, C. B. *The Journal of Physical Chemistry C* **2012**, *116*, 6459-6466.

(21) Zou, Z.; Ye, J.; Sayama, K.; Arakawa, H. *Nature* **2001**, *414*, 625-627.

(22) Asahi, R.; Morikawa, T.; Ohwaki, T.; Aoki, K.; Taga, Y. *Science* **2001**, *293*, 269-271.

(23) Woodhouse, M.; Parkinson, B. A. *Chemistry of Materials* **2008**, *20*, 2495-2502.

(24) Chen, X.; Shen, S.; Guo, L.; Mao, S. S. *Chemical Reviews* **2010**, *110*, 6503-6570.

(25) Merrifield, R. B. *Science* **1965**, *150*, 178-185.

(26) Gallop, M. A.; Barrett, R. W.; Dower, W. J.; Fodor, S. P. A.; Gordon, E. M. *Journal of Medicinal Chemistry* **1994**, *37*, 1233-1251.

(27) Briceño, G.; Chang, H.; Sun, X.; Schultz, P. G.; Xiang, X. D. *Science* **1995**, *270*, 273-275.

(28) Danielson, E.; Golden, J. H.; McFarland, E. W.; Reaves, C. M.; Weinberg, W. H.; Wu, X. D. *Nature* **1997**, *389*, 944-948.

(29) Senkan, S. M. *Nature* **1998**, *394*, 350-353.

(30) Jandeleit, B.; Schaefer, D. J.; Powers, T. S.; Turner, H. W.; Weinberg, W. H. *Angewandte Chemie International Edition* **1999**, *38*, 2494-2532.

(31) Meredith, J. C.; Smith, A. P.; Karim, A.; Amis, E. J. *Macromolecules* **2000**, *33*, 9747-9756.

(32) Maier, W. F.; Stöwe, K.; Sieg, S. *Angewandte Chemie International Edition* **2007**, *46*, 6016-6067.

(33) Lettmann, C.; Hinrichs, H.; Maier, W. F. *Angewandte Chemie International Edition* **2001**, *40*, 3160-3164.

(34) Nakayama, A.; Suzuki, E.; Ohmori, T. *Applied Surface Science* **2002**, *189*, 260-264.

(35) Jaramillo, T. F.; Baeck, S.-H.; Kleiman-Shwarsctein, A.; McFarland, E. W. *Macromolecular Rapid Communications* **2004**, *25*, 297-301.

(36) Jaramillo, T. F.; Baeck, S.-H.; Kleiman-Shwarsctein, A.; Choi, K.-S.; Stucky, G. D.; McFarland, E. W. *Journal of Combinatorial Chemistry* **2004**, *7*, 264-271.

(37) Goldsmith, J. I.; Hudson, W. R.; Lowry, M. S.; Anderson, T. H.; Bernhard, S. *Journal of the American Chemical Society* **2005**, *127*, 7502-7510.

(38) Dai, Q. X.; Xiao, H. Y.; Li, W. S.; Na, Y. Q.; Zhou, X. P. *Applied Catalysis A: General* **2005**, *290*, 25-35.

(39) Seyler, M.; Stoewe, K.; Maier, W. F. *Applied Catalysis B: Environmental* **2007**, *76*, 146-157.

(40) Woodhouse, M.; Herman, G. S.; Parkinson, B. A. *Chemistry of Materials* **2005**, *17*, 4318-4324.

(41) Katz, J. E.; Gingrich, T. R.; Santori, E. A.; Lewis, N. S. *Energy & Environmental Science* **2009**, *2*, 103-112.

(42) Lee, J.; Ye, H.; Pan, S.; Bard, A. J. *Analytical Chemistry* **2008**, *80*, 7445-7450.

(43) Jang, J. S.; Lee, J.; Ye, H.; Fan, F.-R. F.; Bard, A. J. *The Journal of Physical Chemistry C* **2009**, *113*, 6719-6724.

(44) Ye, H.; Lee, J.; Jang, J. S.; Bard, A. J. *The Journal of Physical Chemistry C* **2010**, *114*, 13322-13328.

(45) Park, H. S.; Kweon, K. E.; Ye, H.; Paek, E.; Hwang, G. S.; Bard, A. J. *The Journal of Physical Chemistry C* **2011**, *115*, 17870-17879.

(46) Hahn, N. T.; Mullins, C. B. *Chemistry of Materials* **2010**, *22*, 6474-6482.

(47) Berglund, S. P.; Rettie, A. J. E.; Hoang, S.; Mullins, C. B. *Physical Chemistry Chemical Physics* **2012**, *14*, 7065-7075.

(48) Trari, M.; Bouguelia, A.; Bessekhouad, Y. *Solar Energy Materials and Solar Cells* **2006**, *90*, 190-202.

(49) Saadi, S.; Bouguelia, A.; Trari, M. *Renewable Energy* **2006**, *31*, 2245-2256.

(50) Mor, G. K.; Varghese, O. K.; Wilke, R. H. T.; Sharma, S.; Shankar, K.; Latempa, T. J.; Choi, K.-S.; Grimes, C. A. *Nano Letters* **2008**, *8*, 1906-1911.

(51) Macagno, V. A.; Giordano, M. C.; Arvía, A. J. *Electrochimica Acta* **1969**, *14*, 335-357.

(52) Paracchino, A.; Laporte, V.; Sivula, K.; Grätzel, M.; Thimsen, E. *Nat Mater* **2011**, *10*, 456-461.

(53) Berglund, S. P.; Flaherty, D. W.; Hahn, N. T.; Bard, A. J.; Mullins, C. B. *The Journal of Physical Chemistry C* **2010**, *115*, 3794-3802.

(54) Iwanski, P.; Curran, J. S.; Gissler, W.; Memming, R. *Journal of The Electrochemical Society* **1981**, *128*, 2128-2133.

(55) Anderman, M.; Kennedy, J. H. *Journal of The Electrochemical Society* **1984**, *131*, 21-26.

(56) Greeley, J.; Jaramillo, T. F.; Bonde, J.; Chorkendorff, I.; Norskov, J. K. *Nat Mater* **2006**, *5*, 909-913.

(57) Wagner, C. D.; Naumkin, A. V.; Kraut-Vass, A.; Allison, J. W.; Powell, C. J.; John R. Rumble, J.; August 15, 2007 ed.; National Institute of Standards and Technology, Gaithersburg.

(58) Rivers, S. B.; Bernhardt, G.; Wright, M. W.; Frankel, D. J.; Steeves, M. M.; Lad, R. J. *Thin Solid Films* **2007**, *515*, 8684-8688.

(59) Barrie, A.; Christensen, N. E. *Physical Review B* **1976**, *14*, 2442-2447.

(60) Smith, D. R.; Fickett, F. R. *Journal of Research of the National Institute of Standards and Technology* **1995**, *100*, 119-171.

(61) Jang, J. S.; Yoon, K. Y.; Xiao, X.; Fan, F.-R. F.; Bard, A. J. *Chemistry of Materials* **2009**, *21*, 4803-4810.

# Chapter 5: p-Si/$W_2C$ and p-Si/$W_2C$/Pt Photocathodes for the Hydrogen Evolution Reaction

## INTRODUCTION

Photoelectrochemical (PEC) water splitting is a potential processing route for hydrogen production using water and solar energy.[1,2] The hydrogen that is produced can be captured and utilized as a clean burning fuel or chemical feedstock. Practical implementation of PEC water splitting requires the development of PEC materials that are efficient, stable, and earth abundant. Two main types of materials are used for PEC water splitting. n-type semiconductors are used as photoanodes for the oxygen evolution reaction (OER) and p-type semiconductors are used as photocathodes for the hydrogen evolution reaction (HER). One well known p-type semiconductor material, p-type silicon (p-Si), can produce relatively high photocurrent densities for the HER, but it requires the addition of an electrocatalyst such as Pt to produce photocurrent at potentials more positive than 0 V vs. RHE.[3-5] Unfortunately, Pt is an extremely scarce resource, making it expensive to use on a large scale for hydrogen production technologies.[6]

A more earth abundant alternative to Pt, is tungsten carbide, which has shown similar electronic and catalytic properties to Pt for certain chemical reactions.[7,8] Both tungsten carbide (WC) and tungsten semicarbide ($W_2C$) have demonstrated relatively high activity as electrocatalysts for the HER along with good stability in neutral and acid solutions, although the exchange current densities ($j_0$) reported for tungsten carbide for the HER are lower than the values for Pt so tungsten carbide may not be sufficient to replace Pt entirely.[9-13] Nevertheless, tungsten carbide can be used as a support for Pt allowing for a reduction in Pt loading while retaining or improving activity for the HER.[14-17] For this reason, Pt loaded tungsten carbide may be a useful electrocatalyst for p-type semiconductor photocathodes. Recently, tungsten carbide was tested as a co-catalyst

on particulate photocatalysts such as p-type CdS and n-type Na-doped $SrTiO_3$.[18,19] We are unaware of any published results for WC or $W_2C$ as electrocatalysts on p-type photocathodes for the HER. In this work we present the PEC results for p-Si photocathodes with a thin film of tungsten semicarbide ($W_2C$) on the surface. In addition we show that $W_2C$ is an effective support for Pt nanoparticles on p-Si photocathodes and can be used to reduce Pt loading by a factor of 9 while improving the PEC activity for the HER.

## EXPERIMENTAL

### Photocathode Synthesis

Photocathodes were prepared using p-type Si(111) substrates from two different suppliers (Addison Engineering, 540 μm thick, single-side polish, B doped, 0.1 – 10 ohm cm; EL-Cat Inc., 525 mm thick, double-side polish, B doped, 0.2 – 1.0 ohm cm). $W_2C$ was deposited onto the polished side of the p-Si substrates using a technique known as reactive ballistic deposition (RBD), in which metal is evaporated onto a substrate inside a high vacuum chamber containing a reactant gas ambient.[20-24] For $W_2C$ synthesis the evaporant source was a 0.125 inch diameter tungsten rod (Alfa Aesar, 99.95%) and the reactant gas was ethylene. The high vacuum chamber used for this study has been described previously.[25] Prior to deposition, the p-Si substrates were cleaned according to the following procedure. First they were rinsed and sonicated in reagent alcohol (PHARMCO-AAPER, 99.5%) for 15 min. Next they were rinsed with de-ionized water (DIW, <18 MΩ cm) and submerged in a freshly prepared solution of DIW : hydrogen peroxide (Fisher, 30%): sulfuric acid (Fisher, ACS, 95.0 to 98.0 w/w %) = 1 : 2 : 6 for 15 min. Then they were rinsed with DIW and etched in a solution of 5 w/w% hydrofluoric acid (Sigma-Aldrich, ACS) for 5 min. Finally, they were rinsed with DIW, dried, and

quickly loaded into the high vacuum chamber for deposition. The vacuum chamber was pumped down to a pressure of 5 x $10^{-8}$ Torr or lower. Deposition was done at ambient temperature using a W deposition rate of approximately 1.25 ML/min and a background ethylene pressure of 1 x $10^{-6}$ Torr resulting in an ethylene flux that was about 48 times higher than that of W. This was done to ensure an excess amount of carbon for the carburization reaction; however, x-ray diffraction and x-ray photoemission spectroscopy measurements revealed that these conditions resulted in the formation of $W_2C$ rather than WC. Various thicknesses of $W_2C$ were deposited onto the p-Si substrates. $W_2C$ was also deposited onto fluorine doped tin oxide (FTO) coated glass substrates using the same conditions. The resulting photocathodes and electrodes are referred to as p-Si/$W_2C$ and FTO/$W_2C$. After deposition some of the p-Si/$W_2C$ photocathodes and FTO/$W_2C$ electrodes were annealed in a tube furnace (MTI, OTF-1200X) as follows. The tube furnace was pumped to a pressure of 500 mTorr and then filled with Ar (Matheson Tri-Gas, 99.995%) to a pressure of 760 Torr. Next Ar was allowed to continuously purge the tube at 100 SCCM while the tube was heated with a temperature ramp rate of 10$^{o}$C/min and held at the desired temperature (350, 450, 550, 650 $^{o}$C) for 2 hours. For comparison purposes, Ni-Mo films were deposited onto p-Si substrates by co-evaporation of nickel and molybdenum in the high vacuum chamber at pressures less than 5 x $10^{-8}$ Torr. The evaporant sources were a 0.25 inch diameter nickel rod (Alfa Aesar, 99.95%) and a 0.125 inch diameter molybdenum rod (Alfa Aesar, 99.95%).

Pt nanoparticles were deposited onto some of the p-Si and p-Si/$W_2C$ photocathodes to make p-Si/Pt and p-Si/$W_2C$/Pt photocathodes using a current controlled pulsed deposition technique in a solution of 1g/L $H_2PtCl_6$•$6H_2O$ (Alfa Aesar, 99.95%).[26] During deposition the photocathodes were illuminated. The pulse sequence was 5 mA/cm$^2$ cathodic current for 10 ms followed by 5 mA/cm$^2$ anodic current for 2 ms

followed by zero current for 100 ms, which was repeated for the desired deposition time. An example of the current controlled pulsed deposition sequence is included in Appendix (Figure D.1). Pt nanoparticles were deposited onto FTO/$W_2C$ to make FTO/$W_2C$/Pt electrodes using the same technique but without illumination. Dense Pt films were synthesized by drop-casting 225 μL of 1g/L $H_2PtCl_6 \bullet 6H_2O$ onto 1.5 cm x 1.5 cm FTO substrates, which were then annealed in the tube furnace at 350°C for 2 hrs under 100 SCCM flow of 5% $H_2$ / 95% Ar.

**Photocathode Characterization**

When not in use, the p-Si/$W_2C$ photocathodes were stored under vacuum (< 1 x $10^{-7}$ Torr) to avoid unwanted oxidation. Bare p-Si photocathodes were cleaned, etched with 5 w/w% hydrofluoric acid, and rinsed with DIW immediately before PEC measurements using the procedure described above. The backside of each photocathode was scratched, painted with gallium indium eutectic (Alfa Aesar, 99.99%), and adhered to a piece of copper foil to create an ohmic contact. PEC measurements were conducted using a 3-electrode photoelectrochemical cell with a main compartment and two branched compartments separated by fritted disks (Ace Glass, 10-20 μm porosity). The cell was controlled using an electrochemical analyzer/workstation (CH Instruments CH660D). The working electrode (WE) was connected to the p-Si/$W_2C$ photocathode or FTO/$W_2C$ film, which was pressed onto the main compartment of the cell with an o-ring having an active area of 0.22 $cm^2$. The counter electrode (CE) was a 1 mm diameter Pt wire (Alfa Aesar, 99.95%) and the reference electrode (REF) was saturated Ag/AgCl (CH Instruments, CH111). The CE and REF were placed in the branched compartments of the cell. The cell was filled with 1 N sulfuric acid (Fisher, Certified 0.995 – 1.005 N, pH 0.3) that was continuously bubbled with nitrogen starting at least 30 min prior to

measurements. The light source was a full spectrum solar simulator (Newport, Model 9600, 150 W xenon lamp) with an AM 1.5 global filter (Newport). A thermopile sensor (Newport, Model 818P-020-12) was used to set the illumination power density to 100 $mW/cm^2$. Measured potentials were converted to the reversible hydrogen electrode (RHE) scale via the Nernst equation.

The material properties of the photocathodes were characterized using a variety of analytical instruments. X-ray diffraction (XRD) spectra were obtained using a Spider R-Axis diffractometer with an incident angle of 6 deg, a rotation speed of 6 deg/sec, and Cu Kα radiation at 40 kV and 40 mA. UV-vis transmission and UV-vis transmission-reflectance measurements were taken on a Cary 5000 spectrophotometer and a Cary 500 spectrophotometer with an integrating sphere (Labsphere). A Zeiss Supra 40 VP scanning electron microscope (SEM) was used to capture SEM images. X-ray photoelectron spectroscopy (XPS) measurements were performed on a Kratos AXIS Ultra DLD spectrometer with Mg Kα radiation. Time-of-Flight Secondary Ion Mass Spectrometer (TOF-SIMS) information was acquired using a TOF.SIMS 5 (ION-TOF GMBH). Atomic force microscopy (AFM) was performed on an Asylum Research MFP3D.

## RESULTS AND DISCUSSION

### Photoelectrochemical Results

Figure 5.1 shows a linear sweep voltammetry (LSV) scan for p-Si and p-Si/$W_2C$ photocathodes with and without Pt nanoparticles deposited on the surface in the dark and under white light illumination. The p-Si/$W_2C$ photocathode had a $W_2C$ film thickness of approximately 49 Å as determined by QCM measurements during deposition and cross-sectional SEM images. Before PEC testing, the p-Si/$W_2C$ photocathode was annealed under Ar flow at 450 $^oC$ for 2 hours to improve the stability. The p-Si/Pt(90s) and p-

Si/$W_2C$/Pt(10s) photocathodes had Pt nanoparticles deposited by current controlled pulsed deposition with total deposition times of 90 sec and 10 sec, respectively. These deposition times resulted in the most positive photocurrent onset potentials and highest limiting photocurrent densities for p-Si and p-Si/$W_2C$. Also included in Figure 5.1, is the LSV scan for a dense Pt film on FTO. The LSV scans confirm that bare p-Si by itself is a poor photocathode for the HER since it did not show noticeable photocurrent until potentials more negative than -0.1 V vs. RHE and the photocurrent density was always lower than the current density for the dense Pt film. The LSV scans demonstrate that $W_2C$ is an effective electrocatalyst for p-Si since the p-Si/$W_2C$ photocathode had a photocurrent onset potential near 0.2 V vs. RHE and it remained higher than the current

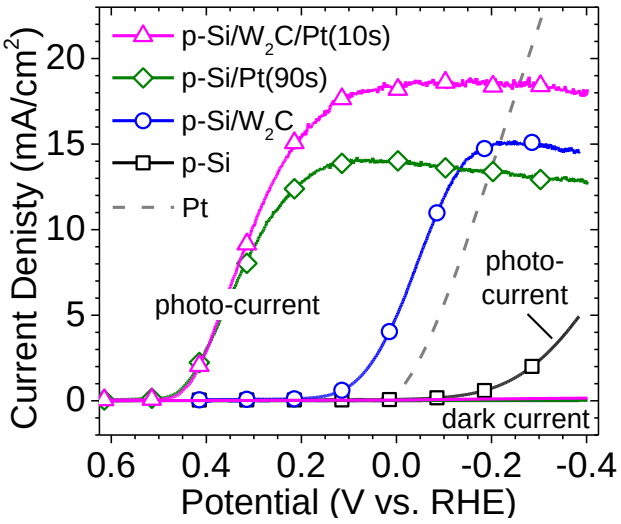


Figure 5.1. LSV scans (dark and white light) for p-Si and p-Si/$W_2C$ photocathodes with and without Pt nanoparticles deposited on the surface. Current controlled pulsed deposition was used to deposit the Pt nanoparticles (total deposition times shown in parentheses). Before PEC measurements and Pt nanoparticle deposition, the p-Si/$W_2C$ photocathode was annealed in Ar at 450°C for 2 hrs. The LSV scan for a dense Pt film on FTO is included. Measurements were conducted in $N_2$ purged 1 N $H_2SO_4$ using a scan rate of 25 mV/s and white light intensity of 100 mW/cm$^2$.

density of the dense Pt film until -0.22 V vs. RHE. As previously mentioned, Pt is more active than tungsten carbide for the HER. The addition of Pt nanoparticles to the p-Si and p-Si/$W_2C$ photocathodes improved the photocurrent onset potentials to about 0.5 V vs. RHE. The p-Si/$W_2C$/Pt(10s) photocathode showed a slightly higher limiting photocurrent of 18.6 mA/cm$^2$ compared that of p-Si/Pt(90s) at 14.0 mA/cm$^2$.

The optimal Pt deposition times of 90 and 10 sec for p-Si and p-Si/$W_2C$ were determined by varying the Pt deposition time and measuring the PEC activity. Figure 5.2 shows the average photocurrent density at 0.215 V vs. RHE for p-Si and p-Si/$W_2C$ photocathodes following different Pt deposition times. The p-Si/$W_2C$ photocathodes reached the maximum photocurrent density after 10 sec of Pt deposition compared to 90 sec for p-Si. Since the pulsed deposition sequence is current controlled, the p-Si/$W_2C$

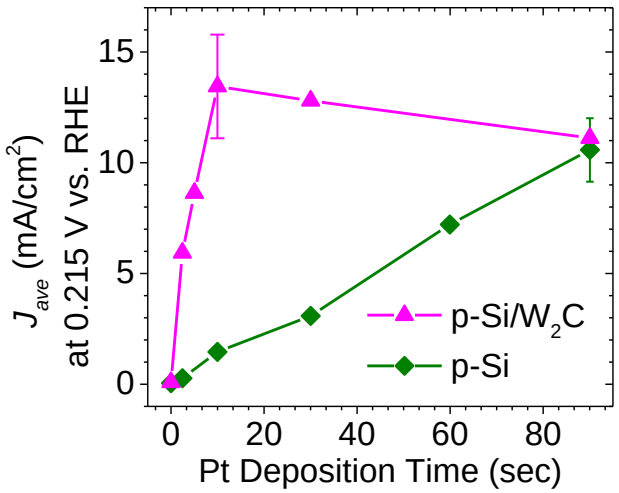


Figure 5.2. Average photocurrent density ($J_{ave}$) at 0.215 V vs. RHE for p-Si and p-Si/$W_2C$ photocathodes for various Pt current controlled pulsed deposition times. Before PEC measurements and Pt deposition the p-Si/$W_2C$ photocathodes were annealed in Ar at 450°C for 2 hrs. The photocurrent density values were obtained from LSV scans under white light illumination in $N_2$ purged 1 N $H_2SO_4$ using a scan rate of 25 mV/s and white light intensity of 100 mW/cm$^2$. The error bars signify one standard deviation.

photocathodes reach the maximum values after passing 1/9 as much charge as the p-Si photocathodes, and perhaps after depositing 1/9 as much Pt.

To qualitatively compare the amount of Pt deposited on the p-Si/Pt(90s) and p-Si/$W_2C$/Pt(10s) photocathodes we imaged them by SEM. Figure 5.3a shows that the p-Si/Pt(90s) photocathodes were covered with Pt flakes on the order of 100 nm and Pt nanoparticles that were 10 – 50 nm in diameter. The p-Si/$W_2C$/Pt(10s) photocathodes in Figure 5.3b consist of a rough layer of $W_2C$ with scattered nanowires that were about 100 nm in length and a sparse coverage of Pt particles that were less than 50 nm in diameter. Clearly there was less Pt on the p-Si/$W_2C$/Pt(10s) photocathodes compared to p-Si/Pt(90s). Collectively, the PEC results and SEM images demonstrate that depositing a thin film of $W_2C$ onto p-Si is an effective means of reducing the required Pt loading while retaining PEC activity for the HER.

The effect of Pt overlayers ($Pt_{ML}$) on top of WC(0001) and $W_2C$(0001) surfaces has been studied from a theoretical perspective via density functional theory (DFT) calculations.[17,27,28] Esposito et al. calculated that $Pt_{ML}$/WC(0001) and $Pt_{ML}$/$W_2C$(0001) possess hydrogen binding energies (HBEs) of -0.43 and -0.24 eV, which are close to the value of -0.46 eV for Pt(111).[17] Ma et al. concluded that for certain reaction sites the activation energy for hydrogen dissociation was similar for $Pt_{ML}$/W(0001) and Pt(111) at 5.28 and 4.93 kJ/mol, respectively.[27] In addition, a strong intermetallic interaction between the Pt and WC(0001) was calculated involving the interfacial W and Pt d-states.[27,28] The HER activity of $Pt_{ML}$/WC(0001) was found to match the activity of Pt(111) rather than exceed it and no synergistic effect between Pt and WC(0001) was identified, but the possibility of hydrogen spill-over was mentioned.[28] Hydrogen spill-over has been validated for a variety of catalytic reactions on supports containing defective insulators, graphitic carbon, or reducible metal oxides such as $WO_3$, but spill-over to a defect-free

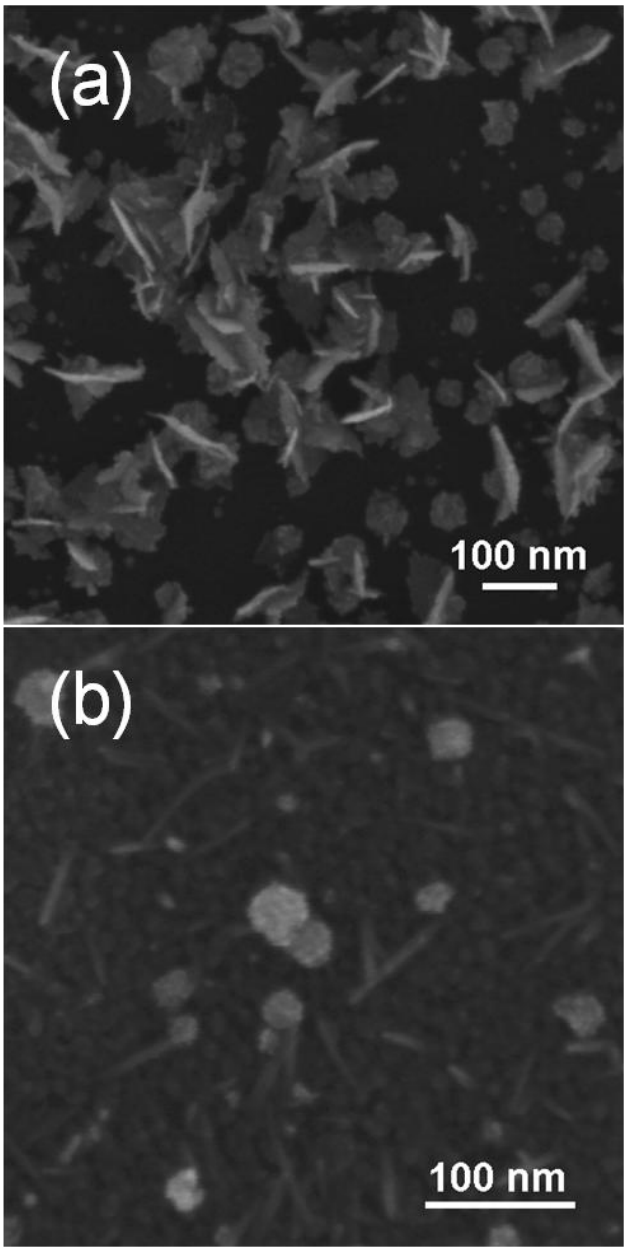


Figure 5.3. SEM images of (a) p-Si/Pt(90s) and (b) p-Si/$W_2C$/Pt(10s) photocathodes.

support such as $SiO_2$ has been calculated to be energetically unfavorable.[29-31] This implies that hydrogen spill-over would not occur on the crystalline p-Si/Pt(90s) photocathodes. Though a recent study demonstrated hydrogen spill-over from Pt metal to high quality

silicon oxide for p-Si based metal insulator semiconductor (MIS) photocathodes.[32] The high activity of the Si/$W_2C$/Pt(10s) photocathodes with reduced Pt loading is likely the result of a strong Pt and $W_2C$ intermetallic interaction combined with a reaction mechanism involving hydrogen mobility on both the Pt and $W_2C$ surfaces.

To optimize the p-Si/$W_2C$ photocathodes, we performed PEC measurements on photocathodes with different $W_2C$ thicknesses (25, 49, 99, and 148 Å) and annealing temperatures (as deposited, 350, 450, 550 $^oC$). The LSV scans for these films are included in Appendix (Figure D.2 and S3). The p-Si/$W_2C$ photocathodes with $W_2C$ thicknesses of 25 and 49 Å showed similar limiting photocurrent densities. As the thickness increased to 99 and 148 Å the limiting photocurrent density decreased, presumably due to increased reflection by the thicker films. p-Si/$W_2C$ photocathodes with a $W_2C$ thickness of 49 Å showed similar photocurrent onset potentials and photocurrent densities regardless of the annealing temperature (as deposited, 350, 450, 550 $^oC$). However, annealing in Ar improved the stability of the p-Si/$W_2C$ photocathodes and resulted in higher photocurrents after depositing Pt nanoparticles. The photocathodes that were not annealed may have oxidized during the anodic segment of the current controlled pulsed deposition. Other research groups have reported that transition metal carbides can be passivated and stabilized for certain chemical reactions by annealing in oxygen following synthesis.[33,34] We chose an annealing temperature of 450 $^oC$ for further characterization because there appeared to be a loss of crystalline $W_2C$ after annealing to temperatures of $\geq$ 550 $^oC$ as explained in the X-ray diffraction results later.

**Electrochemical Results**

Electrochemical measurements were performed on the FTO/$W_2C$ electrodes to test their resistance to oxidation and further assess $W_2C$ as a support for Pt nanoparticles.

Figure 5.4a shows a cyclic voltammetry (CV) scan for FTO/$W_2C$ electrodes with a $W_2C$ thickness of 148 Å as deposited and after annealing in Ar at 450 °C for 2 hrs. The initial

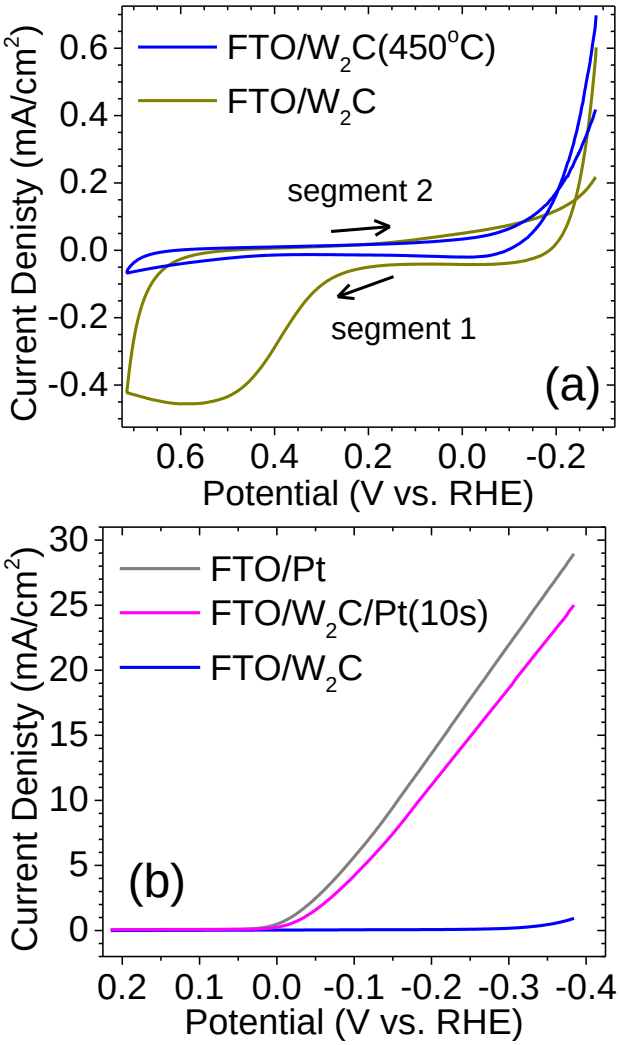


Figure 5.4. (a) CV scans of FTO/$W_2C$ electrodes as deposited and annealed in Ar flow at 450 °C for 2 hrs. The initial scan direction (segment 1) was from negative to positive potentials followed by a scan in the reverse direction (segment 2). (b) LSV scans of FTO/$W_2C$ electrodes that were both annealed at 450° C in Ar with and without Pt nanoparticles deposited on the surface for 10 sec along with an LSV scan of a dense Pt film on FTO. The FTO/$W_2C$ electrodes had a $W_2C$ thickness of 148 Å. Measurements were conducted in $N_2$ purged 1 N $H_2SO_4$ using a scan rate of 25 mV/s without iR compensation.

scan direction was from negative to positive potentials (segment 1) followed by a scan in the opposite direction (segment 2). The FTO/$W_2C$ electrode that was not annealed produced a peak in anodic current at potentials more positive than 0.2 V vs. RHE, which can be attributed to oxidation of the $W_2C$ film. After CV testing the $W_2C$ film was visibly transparent where it had been in contact with the electrolyte. In contrast, the FTO/$W_2C$ that was annealed did not produce significant anodic current during the CV scan or change noticeably in appearance after testing. Weidemen et al., used chronopotentiometric (CP) titrations to create potential vs. pH stability maps for WC, $W_2C$, $Mo_2C$.[35] In acid environments (pH <1), WC and $W_2C$ did not undergo surface oxidation / dissolution as long as the potentials were more negative than 0.86 and 0.46 V vs RHE, respectively. The $W_2C$ films deposited by RBD and annealed in Ar appear to be stable with a similar potential range in 1 N $H_2SO_4$. Figure 5.4b shows a LSV scan for FTO/$W_2C$ electrodes annealed in Ar flow at 450 $^oC$ with and without Pt nanoparticles deposited on the surface for 10 sec along with the LSV scan for a dense Pt film on FTO. At potentials more positive than 0 V vs. RHE, the FTO/$W_2C$/Pt(10s) electrode showed a much faster increase in current density than FTO/$W_2C$ and behaved similar to the dense Pt film. A Tafel plot was constructed from LSV scans a slower scan rate of 1 mV/sec (see Figure D.4 in Appendix). The Tafel plot shows that the FTO/$W_2C$/Pt/(10s) electrodes and Pt films have nearly identical exchange current densities (log(Current Density) at 0 V vs. RHE) and slopes. This result is consistent with previous reports for Pt monolayers on $W_2C$ (ML Pt–$W_2C$).[17]

**X-Ray Diffraction Results**

The p-Si and p-Si/$W_2C$ photocathodes were measured by XRD to determine the crystallinity of the $W_2C$ films following synthesis by RBD and annealing in Ar. To obtain

an adequate XRD count rate the $W_2C$ films were deposited to a thickness of 148 Å. Figure 5.5 shows XRD spectra for p-Si and p-Si/$W_2C$ photocathodes as deposited and after annealing in Ar at 450 °C for 2 hrs. The reference patterns for Si (PDF#00-027-1402) and $W_2C$ (PDF#00-035-0776) are also included. The spectrum for bare p-Si(111) contained peaks for different lattice planes because the sample was rotated during the measurement and all peaks matched the reference pattern for Si. The p-Si/$W_2C$ photocathode as deposited showed one additional peak besides the Si peaks. It was a broad peak at a two theta value of 39.6 deg, which matched the highest intensity line in the reference pattern for $W_2C$ corresponding to the (101) plane. This confirms that the $W_2C$ films possessed some level of $W_2C$ crystallinity even when deposited at ambient temperatures. After annealing the p-Si/$W_2C$ photocathode in Ar at 450 °C the main peak

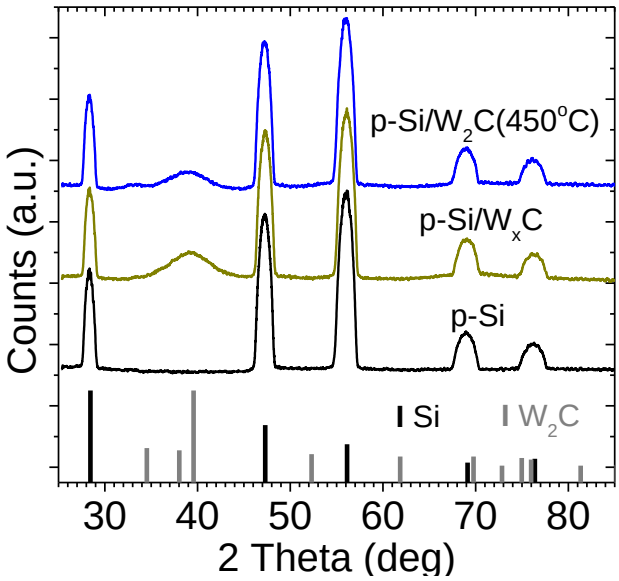


Figure 5.5 XRD spectra for p-Si and p-Si/$W_2C$ as deposited and after annealing at 450 °C in Ar flow for 2 hrs. The $W_2C$ layer was 148 Å thick. The black vertical lines are the reference pattern for Si (PDF#00-027-1402) and the grey vertical lines are the reference pattern for $W_2C$ (PDF#00-035-0776).

at 39.6 deg became smaller and another peak began to emerge at a 2 theta value of about 33 deg. Additional XRD spectra for p-Si/$W_2C$ photocathodes annealed in Ar at various temperatures (as deposited, 350, 450, 550 $^oC$) are displayed in Figure D.5 in Appendix. After annealing the p-Si/$W_2C$ photocathode at 550 $^oC$ the peak at 33 deg became much more prominent and the $W_2C$(101) peak at 39.6 deg was nearly gone suggesting that the film no longer contained crystalline $W_2C$.

One advantage of synthesizing thin films by RBD isthat crystalline materials can be deposited at relatively low substrate temperatures because the evaporated metal atoms are in a highly reactive state when they strike the surface of the substrate. RBD was previously used to grow crystalline MgO at -73 to 63 $^oC$ with Mg as the evaporant source in an ambient of oxygen ($1x10^{-6}$ - $1x10^{-5}$ Torr).[20] Crystalline TiC was also deposited by RBD at 35 $^oC$ using Ti in a background of ethylene (~$2x10^{-7}$ Torr).[22] In this work the p-Si(111) substrate temperature was not controlled during deposition although the e-beam evaporator provided some radiative heating. The temperature of the stainless steel substrate holder was measured to be about 50 $^oC$ during deposition. This is noteworthy because synthesis of transition metal carbides by thermal cracking in ethylene typically requires annealing temperatures above 600 K.[36] To fully carburize tungsten to WC, annealing temperatures above 1000 K are often needed.[37] Vapor phase synthesis techniques can be used to lower the formation temperature of $W_2C$ and WC. With magnetron sputtering from a WC target, the substrate temperature, reactant gases, and post annealing conditions can be adjusted to control the W to C ratio.[8,17,38] At a substrate temperature of 400 $^oC$, magnetron sputtering in pure Ar will result in $W_2C$, while leaking in hydrogen and ethylene ($H_2$:$C_2H_4$ ratio of 2:1) can produce WC.[17] Although we synthesized $W_2C$ films using a single temperature, it may be possible to synthesize WC by evaporation of W in ethylene at slightly higher substrate temperatures.

**X-Ray Photoelectron Spectroscopy**

The p-Si/$W_2C$ photocathodes were measured using XPS to investigate the elemental composition. XPS spectra were obtained for the W 4f, C 1s, Si 2s, and O 1s binding energy regions and Ar sputtering was used to probe below the $W_2C$ surface. Figure 5.6 shows XPS spectra for a p-Si/$W_2C$ photocathode that was annealed in Ar at 450 $^oC$ for 2 hours. The measurements were performed after Ar sputter times of 0, 1, and 10 sec as indicated. Figure 5.6a shows that the W $4f_{5/2}$ and W $4f_{7/2}$ peaks were located at binding energies of 33.8 and 31.6 eV, respectively, which is 0.2 to 0.8 eV positive of the binding energies for W metal.[39] Ar sputtering increased the W 4f peak heights but did not shift their locations. Figure 5.6b shows the C 1s spectra and reveals that before Ar sputtering the $W_2C$ films were covered with a layer of adventitious carbon because the C 1s peak was located at 284.3 eV. After 1 sec of Ar sputtering the C 1s peak broadened due to overlap in signal from the adventitious carbon and the carbon bonded to tungsten in the $W_2C$ film and after 10 sec there was a single C 1s peak at 283.2 eV. This is the expected peak location for $W_2C$ rather than WC, which typically shows a C 1s peak at a slightly lower binding energy.[17] Figure 5.6c shows the XPS spectra for the O 1s. Before Ar sputtering there was an O 1s peak centered a 530.5 eV with a small shoulder at higher binding energy. After 10 sec of Ar sputtering the O 1s signal was diminished indicating that the $W_2C$ films are mainly oxidized on the surface. We discovered that the $W_2C$ surface oxidized readily even at low partial pressures of oxygen and water ($\leq 10^{-5}$ Torr). An additional p-Si/$W_2C$ photocathode was measured by XPS after transferring from the high vacuum deposition chamber ($5x10^{-8}$ Torr) into a vacuum tight capsule and then from the capsule into the XPS chamber. This photocathode still showed a significant O 1s signal on the surface.

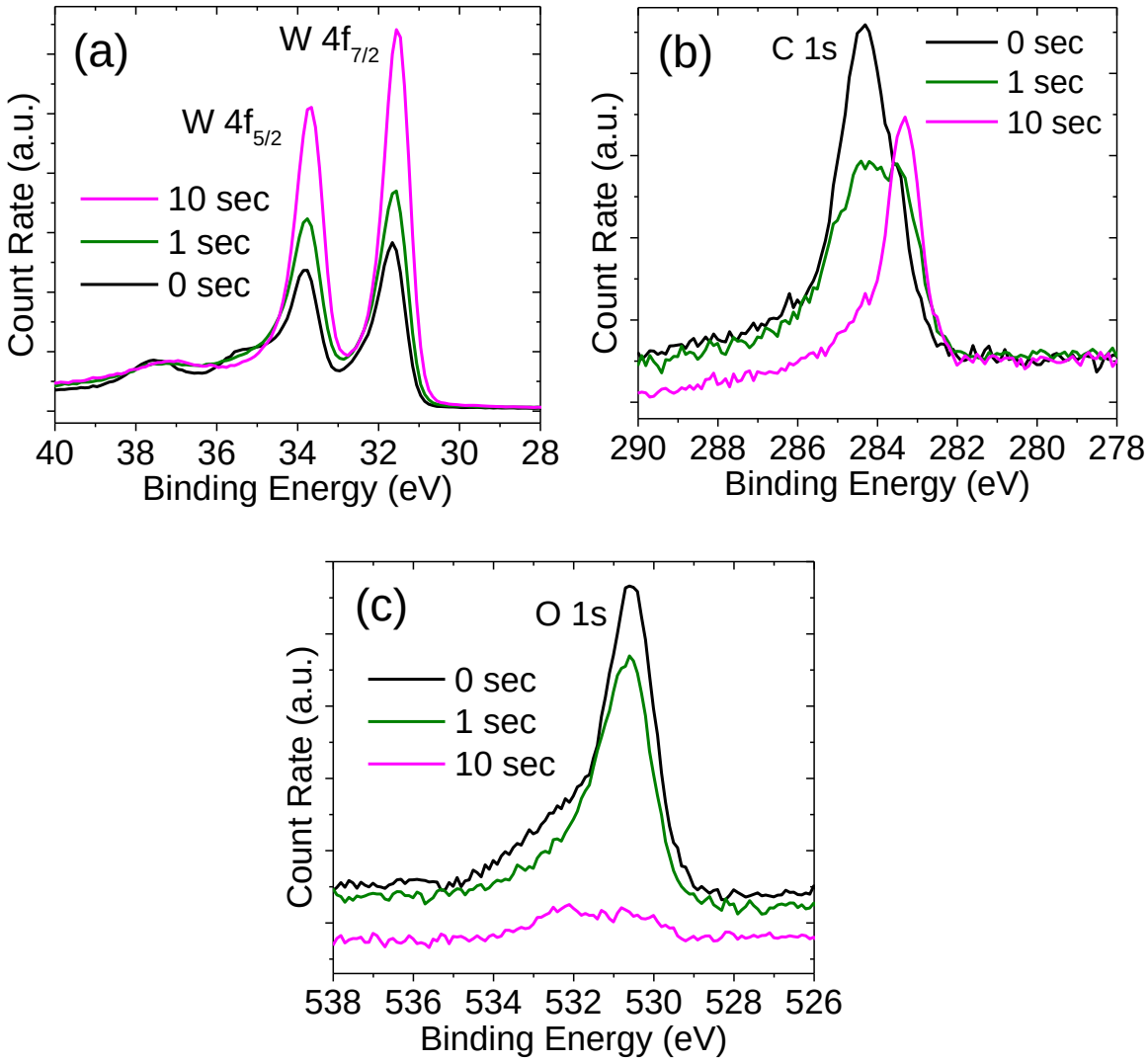


Figure 5.6. XPS spectra for showing (a) W 4f, (b) C 1s, and (c) O 1s regions after various Ar sputter times (0, 1, and 10 sec) for a p-Si/$W_2C$ photocathode that was annealed in Ar at 450 $^{o}$C for 2 hrs.

XPS was used to create concentration depth profiles for the p-Si/$W_2C$ photocathodes and determine the bulk W:C atomic ratio below the surface. The atomic concentration of W, C, O, and Si were calculated by integrating the areas under the XPS spectra and subtracting the background using the Shirley method.[40] To distinguish

between adventitious surface carbon and carbon in the $W_2C$ films, the C 1s peaks located at 284 – 285 eV were not used in the calculations. Concentration depth profiles for p-Si/$W_2C$ photocathodes as deposited and after annealing at 450 $^oC$ in Ar for 2 hours are shown in Figure D.6 in Appendix. The shapes of the concentration depth profiles were slightly different. The annealed p-Si/$W_2C$ photocathode had a broader distribution of W and C, which trailed off after longer Ar sputtering times. This may have been due to a slower Ar sputtering rate for the annealed $W_2C$ film. As shown in the electrochemical results above, the annealed $W_2C$ film was more stable in electrolyte and less susceptible to damage by oxidation. Additionally the W and C may have diffused into the p-Si substrate during annealing. After 7 seconds of Ar sputtering the p-Si/$W_2C$ photocathodes as deposited and annealed both showed W:C atomic ratios of approximately 1.8:1, which is close to the expected ratio of 2:1 for $W_2C$. Nevertheless, the films may contain a slight excess of carbon in addition to the crystalline $W_2C$ that was revealed by XRD.

XPS was also performed on p-Si and p-Si/$W_2C$ photocathodes with Pt nanoparticles on the surface. Figure 5.7 shows the Pt 4f region XPS spectra for p-Si/(90s), p-Si/$W_2C$/Pt(10s), and p-Si/$W_2C$/Pt(90s) photocathodes that had been used for PEC measurements. The p-Si/Pt and p-Si/$W_2C$/Pt(90s) photocathodes had Pt $4f_{5/2}$ and $4f_{7/2}$ peaks at binding energies of 73.9-74.1 and 70.5-70.8 eV, respectively which is characteristic of Pt metal.[39] The p-Si/$W_2C$/Pt(10s) photocathode produced a much lower XPS count rate (signal multiplied by 50 in the figure), which is reasonable considering that it contained perhaps 1/9 as much Pt and smaller Pt nanoparticles. The p-Si/$W_2C$/Pt(10s) photocathode also showed a shift in the Pt 4f peak locations to higher binding energies with two peaks at 75.7 and 72.4 eV and a third peak at 79.8 eV. This may have been the result surface oxidation of the Pt nanoparticles as well as an electronic interaction between the Pt nanoparticles and the $W_2C$ film. As mentioned earlier, DFT

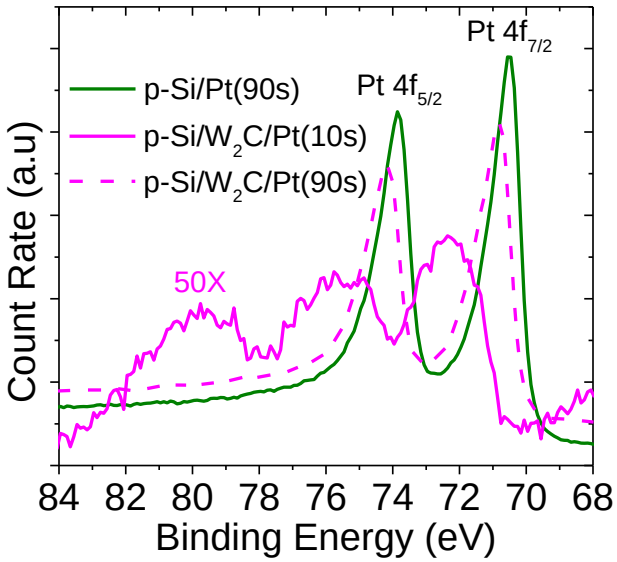


Figure 5.7. XPS spectra of the Pt 4f region for p-Si/(90s), p-Si/$W_2C$/Pt(10s), and p-Si/$W_2C$/Pt(90s) photocathodes after PEC testing and Pt deposition. The p-Si/$W_2C$/Pt photocathodes had a $W_2C$ thickness of 49 Å and had been annealed in Ar at 450 °C for 2 hours. The count rate for the p-Si/$W_2C$/Pt(10s) was multiplied by 50.

calculations predicted a strong interfacial interaction between W and Pt d-states for Pt monolayers on WC.[27,28] The DFT calculations did not consider Pt f-states, but XPS produces a higher signal for the Pt 4f region compared to other Pt regions.

**Time-of-Flight Secondary Ion Mass Spectrometry**

Time of flight secondary ion mass spectrometry (TOF-SIMS) was employed to investigate the chemical composition of the $W_2C$ films and the corresponding $W_2C$-Si interfaces. In order to attain a reasonable depth resolution while resolving the very thin $W_2C$ layers the depth profiles were acquired in a special SIMS dynamic profiling mode with a low current (~3 pA) primary ion beam ($Bi_1^+$ at 30 keV), which was used for both probing and sputtering.[41] Due to edge sputtering effects all depth profiles were reconstructed from the initial raw data by using an identical region of interest centered

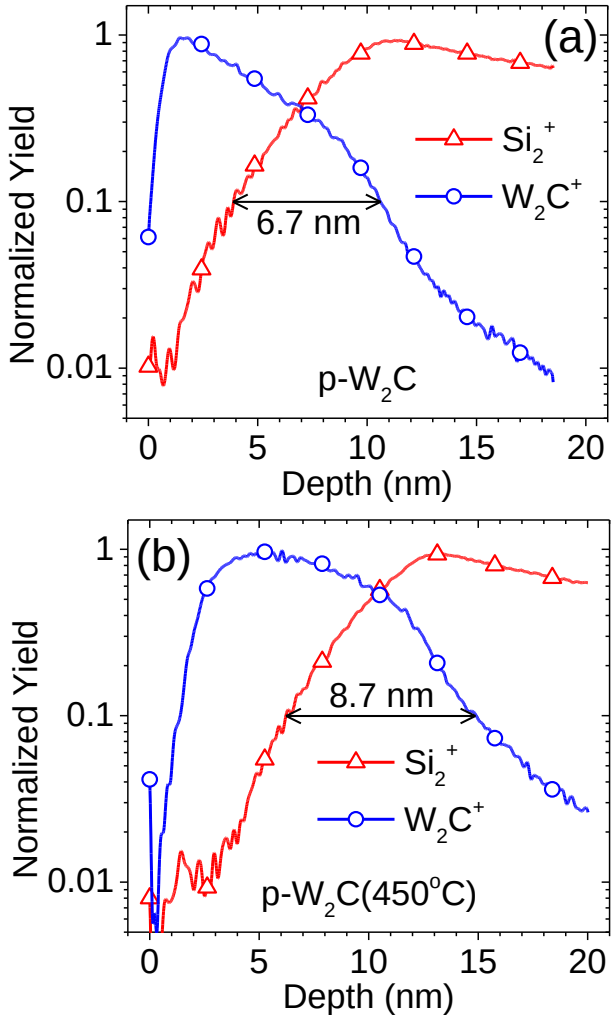


Figure 5.8. Dynamic depth profiles of $W_2C^+$ and $Si_2^+$ markers for the p-Si/$W_2C$ samples (a) as deposited and (b) after annealing in Ar at 450 °C for 2 hours.

within the primary ion beam raster area of 20 μm x 20 μm. All detected secondary ions had positive polarity and a mass resolution better than 3000 (m/δm). The sputtering rates of $W_2C$ (~0.31 Å/s) and Si (~0.042 Å/s) were determined based on knowledge of the $W_2C$ thickness and a previously sputtered Si wafer. An improved interfacial rate model was used to convert the sputtering time into depth.[42] The normalized secondary ion yields of $W_2C^+$ (marker for the $W_2C$ film) and $Si_2^+$ (marker for the Si substrate) are shown in

Figure 5.8a and 8b for a p-Si/$W_2C$ photocathode as deposited and after annealing in Ar at 450 °C, respectively. The dynamic profile of the p-Si/$W_2C$ photocathode that was annealed showed larger levels of contaminants (Na, K) and oxygen at the surface. AFM measurements indicated a $W_2C$ surface corrugation of less than 3 Å for both photocathodes (see Figure D.7 in Appendix). The atomic intermixing between the $W_2C$ overlayer and the Si substrate (calculated at 10% of the $W_2C^+$ and $Si_2^+$ signals and corrugation deconvoluted[42,43]) were ~6.7 and ~8.7 nm, as deposited and after annealing, respectively. Thus the annealing process induces the growth of a thin layer contamination and thicker oxide at the $W_2C$ surface and additional atomic intermixing (2 nm) at the $W_2C$-Si interface. It is possible that a new material, such as tungsten silicide ($WSi_x$), forms at the interface. Amorphous $WSi_x$ films have been shown to undergo crystallization when annealed in Ar at 450 °C.[44] This may contribute to the increased stability of the annealed p-Si/$W_2C$ photocathodes during Pt deposition and could potentially improve charge transport at the $W_2C$-Si interface.

**Transmission and Reflection Spectroscopy**

Since $W_2C$ is a reflective material, it will reduce light transmission when deposited onto a photocathode as an electrocatalyst. To confirm this, we measured the transmission and reflectance of the p-Si and p-Si/$W_2C$ photocathodes with a $W_2C$ thickness of 49 Å as deposited and after annealing in Ar at 450 °C using a UV-Vis instrument with an integrating sphere. Figure 5.9a shows the transmission- reflectance (%T + %R) and transmission (%T) spectra for the photocathodes. %T + %R was obtained with the photocathodes inside the integrating sphere and %T was acquired with the photocathodes in front of the integrating sphere so the measurement does not distinguish between %R and light that is absorbed. Nevertheless, all of the spectra show a

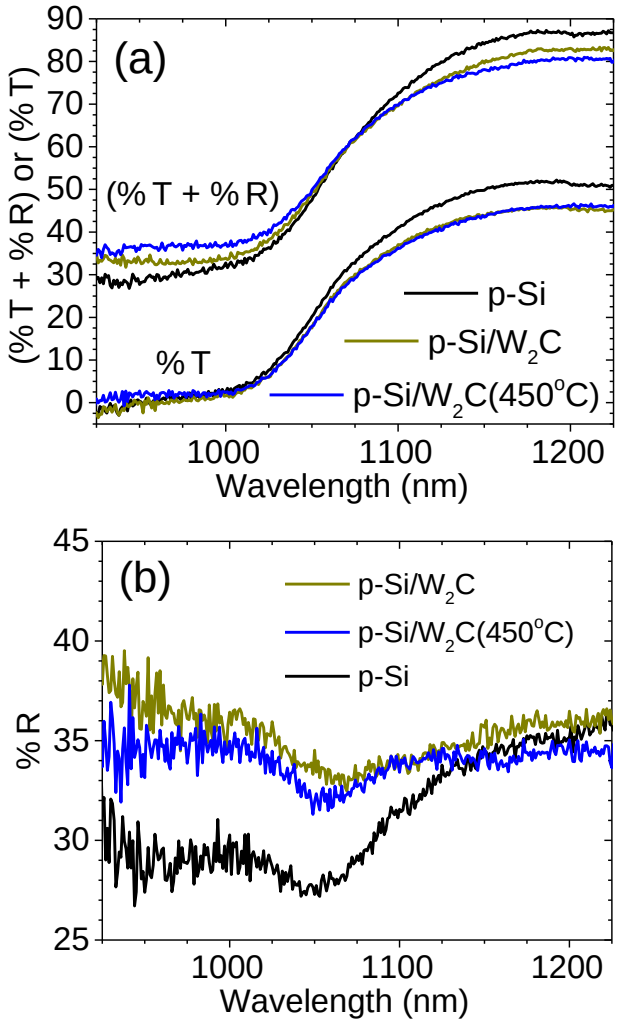


Figure 5.9. Transmission-reflectance spectra for p-Si and p-Si/$W_2C$ photocathodes as deposited and annealed in Ar flow at 450 °C. The $W_2C$ thickness was 49 Å. (a) Shows the measured (% T + % R) and % T. (b) Shows (% T + % R) - % T calculated from the data in (a).

decrease in %T for light wavelengths less than 1150 nm corresponding to light absorption by the p-Si substrate, which has an indirect bandgap of 1.12 eV.[2] %R can be estimated by subtracting the %T spectrum from the %T + %R spectrum for each photocathode (Figure 5.9b). The %R spectra show that the p-Si/$W_2C$ photocathodes reflect 20-30% more light than the bare p-Si photocathodes for light wavelengths less than 1150 nm. We

also measured %T for bare FTO and FTO/$W_2C$ electrodes as deposited and after annealing (see Figure D.9 in Appendix). The FTO/$W_2C$ electrodes transmitted 20-40% less light than bare FTO at light wavelengths less than 1150 nm. So even while absorbing less light, the p-Si/$W_2C$ photocathodes remain more photoactive than the p-Si photocathodes.

**Photoelectrochemical Stability and Comparison with Ni-Mo**

We checked the stability of the annealed p-Si/$W_2C$ and p-Si/$W_2C$/Pt(10s) photocathodes and the p-Si/Pt(90s) photocathodes by performing long-term amperometric i-t scans as (see Figure 5.10). The photocathodes were held at a constant potential of 0.015 V vs. RHE under a light intensity of 100 mW/cm$^2$ for 60 min while $N_2$

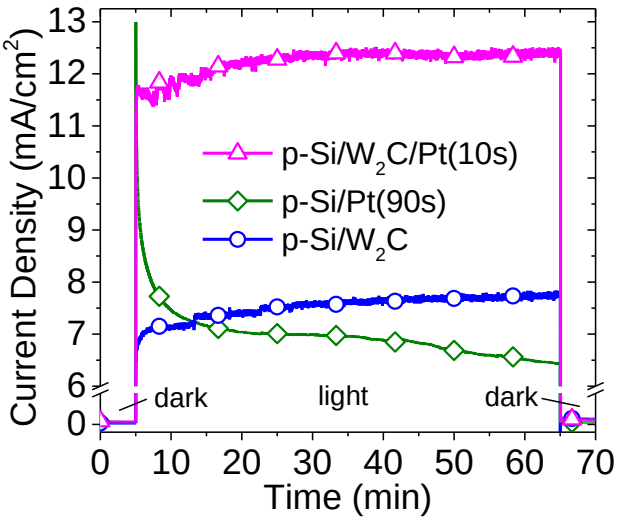


Figure 5.10. Amperometric i-t curve at a constant potential of 0.015 V vs. RHE for a p-Si/$W_2C$ photocathode, a p-Si/Pt photocathode with 90 sec of pulsed Pt deposition, and a p-Si/$W_2C$ photocathode with 10 sec of pulsed Pt deposition. The $W_2C$ thickness was 49 Å and the p-Si/$W_2C$ photocathodes were annealed under Ar flow at 450 $^oC$ for 2 hrs. Measurements were conducted in $N_2$ purged 1 N $H_2SO_4$ with the film surface continuously flushed using a peristaltic pump and a white light intensity of 100 mW/cm$^2$.

was bubbled through the cell and the surfaces of the photocathodes were continuously flushed with electrolyte using a peristaltic pump. The p-Si/$W_2C$ and p-Si/$W_2C$/Pt(10s) photocathodes showed good stability over the course of 60 min with the photocurrent density increasing slightly. The increase may have been the result of oxygen production by OER at the Pt counter electrode, which diffused to the photocathodes faster than it could be purged by $N_2$. On the contrary, p-Si/Pt(90s) photocathodes did not show photocurrent densities that were as repeatable and stable over 60 min as demonstrated by the decay in photocurrent for p-Si/Pt(90s).

Lastly, we compared the PEC performance of $W_2C$ to Ni-Mo, another earth abundant material that has been studied as an electrocatalyst for HER on electrodes and Si based photocathodes.[45-48] We tested four different Ni:Mo atomic ratios (7:1, 3:1, 1:1, and 3:5) and found that p-Si/Ni-Mo photocathodes with a Ni:Mo atomic ratio of 1:1 resulted in the highest photocurrent densities. A Ni:Mo atomic ratio of 1:1 has been suggested as the most catalytic atomic ratio for the HER.[49] Figure 5.11 shows the LSV scans for the p-Si/$W_2C$ and p-Si/Ni-Mo photocathodes with equivalent $W_2C$ and Ni-Mo film thicknesses of 49 Å. The p-Si/$W_2C$ photocathodes were annealed in Ar at 450 $^oC$ but the p-Si/Ni-Mo photocathodes were not. The p-Si/Ni-Mo photocathodes produced a photocurrent onset potential of about 0.3 V vs. RHE, which was slightly more positive than the p-Si/$W_2C$ photocathode and more positive than previously reported for electrodeposition of Ni-Mo onto p-Si.[47] However, the p-Si/Ni-Mo photocathodes produced considerable anodic current at more positive potentials and the photocurrent decreased with repeated testing so they were not stable. Ni-Mo has been reported to be stable in alkaline solutions for long periods but stability and passiviation requirements for Ni-Mo in acidic solutions are less substantiated.[50] We attempted to passivate the p-Si/Ni-Mo photocathodes by annealing in Ar flow at 450 $^oC$ but it worsened the photocurrent

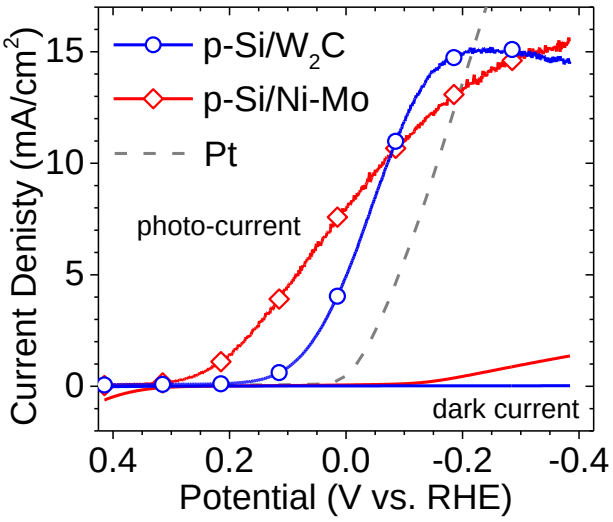


Figure 5.11. LSV scans (dark and white light) for p-Si/Ni-Mo and p-Si/$W_2C$ photocathodes and a dense Pt film. The Ni-Mo and $W_2C$ thicknesses were both estimated to be 49 Å. The p-Si/$W_2C$ photocathodes were annealed under argon flow at 450 $^oC$ for 2 hrs. Measurements were conducted in $N_2$ purged 1 N $H_2SO_4$ with a scan rate of 25 mV/s and white light intensity of 100 $mW/cm^2$.

density. In summary, the p-Si/$W_2C$ photocathodes showed a comparable photocurrent density to p-Si/Ni-Mo at 0.0 V vs. RHE along with better stability in acidic solution making $W_2C$ another earth abundant option to use as an electrocatalyst for solar hydrogen production.

**Conclusions**

We have synthesized p-Si/$W_2C$ photocathodes by reactive ballistic deposition (RBD) and reported the photoelectrochemical (PEC) activity for the HER. X-ray diffraction (XRD) revealed that the $W_2C$ films contained crystalline $W_2C$ when deposited at ambient temperatures while x-ray photoemission spectroscopy (XPS) indicated a W:C atomic ratio of approximately 1.8:1. The $W_2C$ film surface was passivated by annealing in Ar flow at 450 $^oC$, which improved stability in 1 N sulfuric acid. p-Si/$W_2C$ photocathodes demonstrated cathodic photocurrent onset potentials more positive than 0

v vs. RHE while the p-Si photocathode did not. The $W_2C$ film was an effective support for Pt nanoparticles deposited by current controlled pulsed deposition allowing for a factor of 9 reduction in Pt loading. p-Si/$W_2C$ photocathodes with Pt nanoparticles showed comparable photocurrent onset potentials and limiting photocurrent densities and better stability than p-Si photocathodes with 9 times as much Pt.

## REFERENCES


(1) Bard, A. J.; Fox, M. A. *Accounts of Chemical Research* **1995**, *28*, 141-145.

(2) Walter, M. G.; Warren, E. L.; McKone, J. R.; Boettcher, S. W.; Mi, Q.; Santori, E. A.; Lewis, N. S. *Chemical Reviews* **2010**, *110*, 6446-6473.

(3) Nakato, Y.; Tonomura, S.; Tsubomura, H. *Berichte der Bunsengesellschaft für physikalische Chemie* **1976**, *80*, 1289-1293.

(4) Dominey, R. N.; Lewis, N. S.; Bruce, J. A.; Bookbinder, D. C.; Wrighton, M. S. *Journal of the American Chemical Society* **1982**, *104*, 467-482.

(5) Nakato, Y.; Yano, H.; Nishiura, S.; Ueda, T.; Tsubomura, H. *Journal of Electroanalytical Chemistry and Interfacial Electrochemistry* **1987**, *228*, 97-108.

(6) Yang, C.-J. *Energy Policy* **2009**, *37*, 1805-1808.

(7) Levy, R. B.; Boudart, M. *Science* **1973**, *181*, 547-549.

(8) Hwu, H. H.; Chen, J. G. *Chemical Reviews* **2004**, *105*, 185-212.

(9) Sokolsky, D. V.; Palanker, V. S.; Baybatyrov, E. N. *Electrochimica Acta* **1975**, *20*, 71-77.

(10) Armstrong, R. D.; Bell, M. F. *Electrochimica Acta* **1978**, *23*, 1111-1115.

(11) Nikolov, I.; Petrov, K.; Vitanov, T.; Guschev, A. *International Journal of Hydrogen Energy* **1983**, *8*, 437-440.

(12) Harnisch, F.; Sievers, G.; Schröder, U. *Applied Catalysis B: Environmental* **2009**, *89*, 455-458.

(13) Chen, W.-F.; Muckerman, J. T.; Fujita, E. *Chemical Communications* **2013**, *49*, 8896-8909.

(14) Ma, C.; Sheng, J.; Brandon, N.; Zhang, C.; Li, G. *International Journal of Hydrogen Energy* **2007**, *32*, 2824-2829.

(15) Ham, D. J.; Ganesan, R.; Lee, J. S. *International Journal of Hydrogen Energy* **2008**, *33*, 6865-6872.

(16) Wu, M.; Shen, P. K.; Wei, Z.; Song, S.; Nie, M. *Journal of Power Sources* **2007**, *166*, 310-316.

(17) Esposito, D. V.; Hunt, S. T.; Kimmel, Y. C.; Chen, J. G. *Journal of the American Chemical Society* **2012**, *134*, 3025-3033.

(18) Garcia-Esparza, A. T.; Cha, D.; Ou, Y.; Kubota, J.; Domen, K.; Takanabe, K. *ChemSusChem* **2013**, *6*, 168-181.

(19) Jang, J. S.; Ham, D. J.; Lakshminarasimhan, N.; Choi, W. y.; Lee, J. S. *Applied Catalysis A: General* **2008**, *346*, 149-154.

(20) Dohnálek, Z.; Kimmel, G. A.; McCready, D. E.; Young, J. S.; Dohnálková, A.; Smith, R. S.; Kay, B. D. *The Journal of Physical Chemistry B* **2002**, *106*, 3526-3529.

(21) Flaherty, D. W.; Dohnálek, Z.; Dohnálková, A.; Arey, B. W.; McCready, D. E.; Ponnusamy, N.; Mullins, C. B.; Kay, B. D. *The Journal of Physical Chemistry C* **2007**, *111*, 4765-4773.

(22) Flaherty, D. W.; May, R. A.; Berglund, S. P.; Stevenson, K. J.; Mullins, C. B. *Chemistry of Materials* **2009**, *22*, 319-329.

(23) Berglund, S. P.; Flaherty, D. W.; Hahn, N. T.; Bard, A. J.; Mullins, C. B. *The Journal of Physical Chemistry C* **2010**, *115*, 3794-3802.

(24) Flaherty, D. W.; Hahn, N. T.; May, R. A.; Berglund, S. P.; Lin, Y.-M.; Stevenson, K. J.; Dohnalek, Z.; Kay, B. D.; Mullins, C. B. *Accounts of Chemical Research* **2012**, *45*, 434-443.

(25) Berglund, S. P.; Rettie, A. J. E.; Hoang, S.; Mullins, C. B. *Physical Chemistry Chemical Physics* **2012**, *14*, 7065-7075.

(26) He, H.; Xiao, P.; Zhou, M.; Zhang, Y.; Jia, Y.; Yu, S. *Catalysis Communications* **2011**, *16*, 140-143.

(27) Ma, C. a.; Liu, T.; Chen, L. *Applied Surface Science* **2010**, *256*, 7400-7405.

(28) Vasić, D. D.; Pašti, I. A.; Mentus, S. V. *International Journal of Hydrogen Energy* **2013**, *38*, 5009-5018.

(29) Benson, J. E.; Kohn, H. W.; Boudart, M. *Journal of Catalysis* **1966**, *5*, 307-313.

(30) Tseung, A. C. C.; Chen, K. Y. *Catalysis Today* **1997**, *38*, 439-443.

(31) Prins, R. *Chemical Reviews* **2012**, *112*, 2714-2738.

(32) Esposito, D. V.; Levin, I.; Moffat, T. P.; Talin, A. A. *Nature Materials* **2013**, *12*, 562-568.

(33) Santos, J. B. O.; Valença, G. P.; Rodrigues, J. A. J. *Journal of Catalysis* **2002**, *210*, 1-6.

(34) Patt, J.; Moon, D.; Phillips, C.; Thompson, L. *Catalysis Letters* **2000**, *65*, 193-195.

(35) Weidman, M. C.; Esposito, D. V.; Hsu, Y.-C.; Chen, J. G. *Journal of Power Sources* **2012**, *202*, 11-17.

(36) Chen, J. G. *Chemical Reviews* **1996**, *96*, 1477-1498.

(37) Benziger, J. B.; Ko, E. I.; Madix, R. J. *Journal of Catalysis* **1978**, *54*, 414-425.

(38) Zellner, M. B.; Chen, J. G. *Catalysis Today* **2005**, *99*, 299-307.

(39) Wagner, C. D.; Naumkin, A. V.; Kraut-Vass, A.; Allison, J. W.; Powell, C. J.; John R. Rumble, J.; August 15, 2007 ed.; National Institute of Standards and Technology, Gaithersburg.

(40) Shirley, D. A. *Physical Review B* **1972**, *5*, 4709.

(41) Nayak, A. P.; Dolocan, A.; Lee, J.; Chang, H.-Y.; Pandhi, T.; Tao, L. I.; Holt, M.; Akinwande, D. *Nano* **2013**, *0*, 1450002.

(42) Zimmerman, J. D.; Lassiter, B. E.; Xiao, X.; Sun, K.; Dolocan, A.; Gearba, R.; Vanden Bout, D. A.; Stevenson, K. J.; Wickramasinghe, P.; Thompson, M. E.; Forrest, S. R. *ACS Nano* **2013**, *7*, 9268-9275.

(43) Hofmann, S. *Thin Solid Films* **2001**, *398â€“399*, 336-342.

(44) Tsai, M. Y.; d'Heurle, F. M.; Johnson, R. W. *Journal of Applied Physics* **1981**, *52*, 5350-5355.

(45) Raj, I. A. *Journal of Materials Science* **1993**, *28*, 4375-4382.

(46) Fan, C. L.; Piron, D. L.; Sleb, A.; Paradis, P. *Journal of The Electrochemical Society* **1994**, *141*, 382-387.

(47) McKone, J. R.; Warren, E. L.; Bierman, M. J.; Boettcher, S. W.; Brunschwig, B. S.; Lewis, N. S.; Gray, H. B. *Energy & Environmental Science* **2011**, *4*, 3573-3583.

(48) Lin, Y.; Battaglia, C.; Boccard, M.; Hettick, M.; Yu, Z.; Ballif, C.; Ager, J. W.; Javey, A. *Nano Letters* **2013**.

(49) Jakšić, J. M.; Vojnović, M. V.; Krstajić, N. V. *Electrochimica Acta* **2000**, *45*, 4151-4158.

(50) Brown, D. E.; Mahmood, M. N.; Man, M. C. M.; Turner, A. K. *Electrochimica Acta* **1984**, *29*, 1551-1556.

# Chapter 6: Investigation of 35 Elements as Single Metal Oxides, Mixed Metal Oxides, or Dopants for Titanium Dioxide for Dye-Sensitized Solar Cells

## INTRODUCTION

Dye-Sensitized solar cells (DSCs) are photo-electrochemical (PEC) devices that can be used to convert solar energy into electrical energy. DSCs consist of a reversible redox couple placed between a counter electrode and a thin layer of dye molecules that are anchored to a wide bandgap metal oxide semiconductor.[1] During light absorption, the dye molecules rapidly inject photo-excited electrons into the conduction band of the semiconductor while the redox species continuously regenerate the oxidized dye molecules to the ground state and transport charge to the counter electrode. In the seminal DSC paper by O'Regan and Grätzel, published in 1991, a ruthenium based dye was anchored to nanostructured $TiO_2$ and iodide/triiodide was used as the redox couple.[2] The use of nanometer scale $TiO_2$ particles was a key breakthrough as it significantly increased the surface area available for dye adsorption and resulted in an order of magnitude increase in efficiency up to 7.1-7.9%. Since then, there has been an exponential growth in the number of research publications related to DSCs. With the aim of improving DSC efficiency and reducing cost, hundreds of metal complex and organic dyes have been tested along with a variety of redox couples and electrolytes.[3] However, relatively few metal oxide semiconductors have been tested. Besides $TiO_2$ the only metal oxides that have received considerable attention are ZnO, $SnO_2$, $Nb_2O_5$, $Zn_2SnO_4$, and $SrTiO_3$.[3-5] In contrast a vast number of metal oxides have been studied for other PEC applications such as water splitting and pollutant photodegradation.[6-8] Some of these metal oxides have also been incorporated with extra elements or dopants to improve their PEC performance.[9-13] There have been some recent reports of improved DSC performance for doped $TiO_2$, but

only for a small number of dopants including Al, W, Cr, Ta, Nb, Cu, Sm, Eu, Zn, and Sb.[14-25] This leaves a large pool of elements yet to be tested.

One technique that has been used to rapidly test large groups of materials for PEC applications is high throughput testing.[26-29] In our study we have applied this approach to investigate new materials for use in DSCs, which has not previously been done. We utilized an array dispenser and scanner system to test 35 different elements as single component metal oxides and as dopants for $TiO_2$. This includes 4 alkali metals (Na, K, Rb, and Cs), 4 alkaline earth metals (Mg, Ca, Sr, Ba), 17 transition metals (Sc, Y, Zr, V, Nb, Ta, Cr, Mo, W, Mn, Fe, Co, Ni, Cu, Ag, Zn, Cd), 8 post-transition metals (Al, Ga, In, Ge, Sn, Pb, Sb, Bi), and 2 lanthanides (La, Ce). From the array scans we identified new compositions for use in DSCs including 6% In $TiO_2$, 6% Sn $TiO_2$, 6% Sb $TiO_2$, and 2% Cr, 6% Sb $TiO_2$ . We used these compositions to synthesize scaled-up films for detailed characterization and DSC device testing.

## EXPERIMENTAL

### Array Synthesis and DSC Scans

In order to rapidly synthesize a large number of metal oxides and dopants for $TiO_2$ we created mixed metal oxide arrays using an array dispenser system that has been described previously.[29,30] Briefly, the system consisted of four microdispensing devices, each connected to a separate fluid reservoir that could be filled with a metal salt solution. This provided the capability of dispensing four different components simultaneously. The system used a 3-dimensional positioner to dispense a varying number of drops from each microdispensing device in an array pattern on top of fluorine doped tin oxide coated glass (FTO substrates). The chemical composition of each spot in the array was controlled by

the concentration of the metal salt solutions and number of drops dispensed from each microdispensing device.

The metal salt solutions were prepared using the following metal salts and chlorides: $NaNO_3$, $KNO_3$, $RbNO_3$, $CsNO_3$, $Mg(NO_3)_2 \cdot xH_2O$, $Ca(NO_3)_2 \cdot 4H_2O$, $N_2O_6Sr$, $BaN_2O_6$, $Sc(NO_3)_3 \cdot xH_2O$, $Y(NO_3)_3 \cdot xH_2O$, $La(NO_3)_3 \cdot 6H_2O$, $Ce(NO_3)_3 \cdot 6H_2O$, $TiCl_4$, $ZrCl_4$, $VCl_3$, $NbCl_5$, $TaCl_5$, $Cr(NO_3)_3 \cdot xH_2O$, $(NH_4)_6Mo_7O_{24} \cdot 4H_2O$, $(NH_4)_{10}W_{12}O_{41} \cdot 5H_2O$, $Mn(NO_3)_2 \cdot xH_2O$, $Fe(NO_3)_3 \cdot 9H_2O$, $Co(NO_3)_2 \cdot 6H_2O$, $N_2NiO_6 \cdot 6H_2O$, $Cu(NO_3)_2 \cdot xH_2O$, $AgNO_3$, $Zn(NO_3)_2 \cdot xH_2O$, $Cd(NO_3)_2 \cdot 4H_2O$, $Al(NO_3)_3 \cdot xH_2O$, $Ga(NO_3)_3 \cdot xH_2O$, $In(NO_3)_3 \cdot xH_2O$, $GeCl_4$, $SnCl_4 \cdot xH_2O$, $Pb(NO_3)_2$, $SbCl_3$, $Bi(NO_3)_3 \cdot xH_2O$. A complete list of chemical suppliers and purities is included in Appendix E. Each metal salt solution had a metal ion concentration of 0.15 M dissolved in ethylene glycol (Fisher, Certified) except for $TaCl_5$, which had a concentration of 0.03 M because it was insoluble at 0.15 M.

Figure 6.1 shows a diagram of the Ti-M array pattern that was used for this study. M is a variable for the metals that were tested in the array patterns (except for Ta which had a slightly different pattern). In the diagram, the blue and red numbers represent the number of Ti and M drops, respectively, that were dispensed at each location. Since the Ti and M metal salt solutions had equal molar concentrations, the numbers also represent the Ti:M atomic ratios. Considering all 35 arrays, a total 596 unique Ti:M atomic ratios were dispensed for this study. 50 drops were dispensed at spot allowing for concentration increments of 1/50 or 2%. The spacing between spots was 1 mm. The pulse amplitude of each microdispensing device was adjusted to decrease the variation in ethylene glycol dispensed per drop to within ±5%. The pulse width and pulse period were set to 25 μs and 10 ms, respectively.

The arrays were dispensed onto hydrophobic 1.9 cm x 1.9 cm FTO substrates (Hartford Glass, TEC15, 2 mm thick). To make the FTO substrates hydrophobic they

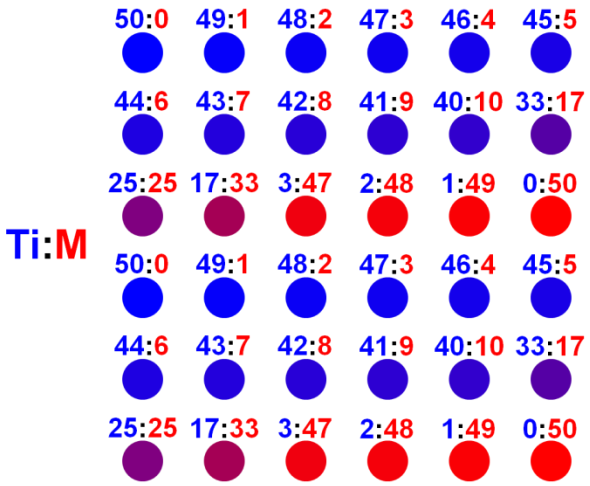


Figure 6.1. Diagram of the Ti-M array pattern used during dispensing as viewed through the FTO substrate. M is a variable representing the metal that was tested on a particular array (Na, K, Rb, Cs, Mg, Ca, Sr, Ba, Sc, Y, La, Ce, Zr, V, Nb, Cr, Mo, W, Mn, Fe, Co, Ni, Cu, Ag, Zn, Cd, Al, Ga, In, Ge, Sn, Pb, Sb, and Bi). The blue and red numbers represent the number of Ti and M drops that were dispensed at each location, respectively i.e. the Ti:M atomic ratios.

were cleaned and sonicated in reagent ethanol (PHARMCO-AAPER, 99.5 %), dried, soaked in 3:50 dichlorodimethylsilane (ACROS, 99+%) : n-hexane (ACROS, 95%), rinsed with n-hexane, and then heated at 60 $^{o}$C in a vacuum oven for 1-2 hours. Just before dispensing each substrate was cleaned with de-mineralized water and dried. After dispensing the substrates were placed in a vacuum oven at 80 $^{o}$C for 15 minutes to flatten the array spots for better adherence and then annealed at 500 $^{o}$C in air for 2 hours to form metal oxide spots. The arrays were allowed to cool naturally to ~100$^{o}$C and then placed in N719 dye solution, which was 0.5 mM cis-diisothiocyanato-bis(2,2'-bipyridyl-4,4'-dicarboxylato) ruthenium(II) bis(tetrabutylammonium) (Solaronix, Ruthenizer 535-bisTBA) in ethyl alcohol (ACROS, anhydrous, 99.5+%). The arrays were allowed to soak in the dye solution in the dark for at least 10 hours. Prior to scanning, the arrays were removed from the dye solution, rinsed with acetonitrile (Fisher, HPLC grade), and

dried in air. Next a 60 μm thick Surlyn gasket (Solaronix, 74301) with a 0.8 cm x 0.8 cm opening was placed around the array spots. The inside of the gasket was filled with 50 mM iodide/triiodide in acetonitrile with additives of ionic liquid, lithium salt, and pyridine (Solaronix, Iodolyte AN-50). A 2 cm x 2 cm piece of Pt coated glass (Solaronix, 74201) was placed over the gasket to complete the array assembly, which was held together using steel clips.

Figure 6.2a shows a schematic of a completed array assembly. The array scanner used to measure the arrays has previously been described for three-electrode PEC

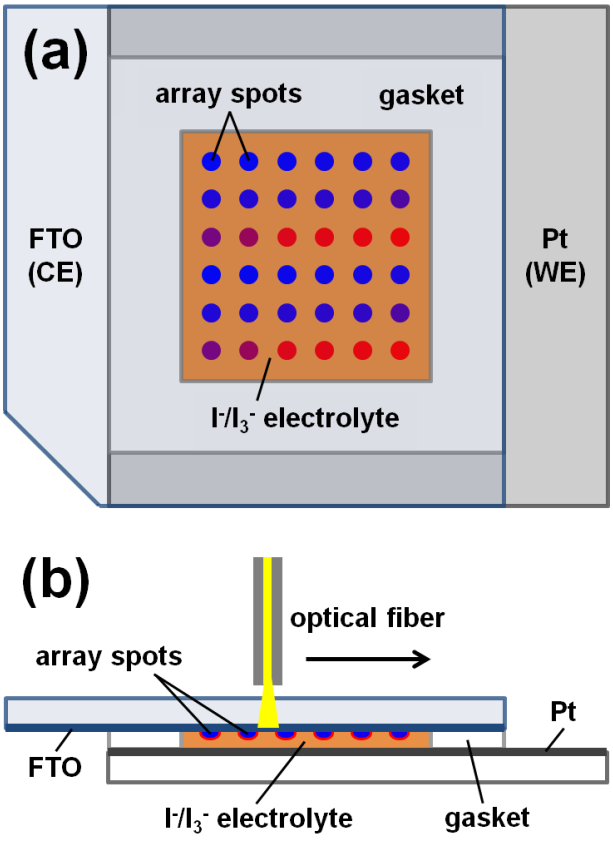


Figure 6.2. Schematic of the array assembly as viewed (a) through the FTO substrate and (b) by cross-section with the optical fiber rastering across the backside of the FTO substrate.

measurements.[29] For DSC measurements, the array assembly was connected to the potentiostat with the working electrode (WE) on the Pt coated glass and the reference (REF) and counter electrode (CE) connected together on the array. The array spots were scanned by rastering an optical fiber tip across the backside of the array while applying a constant voltage between the Pt coated glass and the array as illustrated in Figure 6.2b. For this study the optical fiber had a 0.22 numerical aperture and a 200 μm core (Thorlabs, BFH22-200) and it was illuminated by a 100 W xenon lamp (Newport, Model 66452). To obtain the light induced current and account for shunting caused by bare FTO in contact with the electrolyte, the background current (bare FTO current) of each raster scan was subtracted from the instantaneous current.

**Drop-Cast Film Synthesis and DSC Measurements**

After using the array scans to identify promising dopants for $TiO_2$, we synthesized scaled-up films by drop-casting and assembled them into DSCs according to the following procedure. Precursor solutions were pre-mixed and diluted to a total concentration of 30 mM in ethylene glycol. 265 μL of the pre-mixed solution was drop-cast onto the surface of a 1.9 cm x 1.9 cm FTO substrate that had been cleaned, sonicated, and rinsed with reagent alcohol. The drop-cast solutions on FTO were annealed in air at 120 $^{o}$C for 1 hr followed by 500 $^{o}$C for 2 hrs with a temperature ramp rate of 10 $^{o}$C/min. After annealing the films were removed from the oven at ~100 $^{o}$C and placed in the N719 dye solution in the dark for at least 10 hours. We used the same N719 dye solution and DSC assembly materials that were described above for the Ti-M arrays. Prior to DSC measurements, the drop-cast films were rinsed with acetonitrile, dried in air, and assembled into DSC devices using the thick Surlyn gasket, iodide/triiodide electrolyte, and Pt coated glass. In addition, the glass on the backside of the drop-cast

film was masked to an opening of 0.8 cm x 0.8 cm. The DSC device was connected to an electrochemical workstation/analyzer (CH Instruments 660D) with the WE on the Pt coated glass and the REF and CE connected together on the drop-cast film. A full spectrum solar simulator (Newport, Model 9600, 150 W xenon lamp) with an AM 1.5 global filter (Newport) was used to illuminate the DSC device at 100 mW/cm$^2$ through the backside of the film. The electrochemical workstation/analyzer controlled the voltage of the DSC device and recorded current density vs. voltage (J-V) and electrochemical impedance spectroscopy (EIS) data.

**Materials Characterization**

To acquire images of the array spots and drop-cast films we used a Zeiss Supra 40 VP scanning electron microscope (SEM) with ATLAS software. For X-ray diffraction (XRD) measurements, we synthesized the drop-cast films inside glass vials instead of on FTO substrates. The films inside the vials were scraped into powders, which were then measured on a Spider R-Axis diffractometer with the Cu Kα radiation source at 40 kV and 40 mA. Energy dispersive X-ray spectroscopy (EDS) was performed using a Quanta FEG 650 SEM with a Bruker XFlash 5010 EDS detector and X-ray photoelectron spectroscopy (XPS) measurements were acquired using a Kratos AXIS Ultra DLD spectrometer with Mg Kα radiation. A Cary 5000 spectrophotometer was used for UV-Vis transmission measurements. For Tauc plots the absorption coefficient (α) was determined by:

$$\alpha = \frac{-\ln\left(10^{-A_\lambda}\right)}{z}$$

where $A_\lambda$ is measured absorbance and $z$ is the film thickness. Aqueous electrolyte measurements were performed using the electrochemical workstation/analyzer with a 3-

electrode cell. The WE was the drop-cast film, the CE was a Pt wire (Alfa Aesar, 1 mm diameter, 99.95%), and the REF was saturated Ag/AgCl. The electrolyte was prepared from NaOH (Fisher, certified ACS) and de-mineralized water. Mott-Schottky plots were created based on ideal semiconductor behavior:[31,32]

$$\frac{1}{C_{SC}^2} = \frac{2}{e\ \varepsilon\ \varepsilon_0\ N_D}\left(E - E_{FB} - \frac{k\ T}{e}\right)$$

where $C_{SC}$ is the space charge capacitance (F), $e$ is the electronic charge (C), $\varepsilon$ is the dielectric constant of the semiconductor, $\varepsilon_0$ is the permittivity of free space, $N_D$ is the donor density ($cm^{-3}$), $E$ is potential (V), $E_{FB}$ is the flat band potential (V), $k$ is the Boltzmann constant, and T is the temperature (K). For dye adsorption measurements, the drop-cast films were submerged in the N719 dye solution in the dark for 20 hours, rinsed with acetonitrile, and then soaked in 3.55 ml of 0.1 M NaOH in 1:1 ethanol:water (by volume) for 1 hour. Next the absorbance of each soaking solution was measured by UV-Vis and the dye concentration was calculated according to Beer's law.[33] We used an extinction coefficient of 1.7 x $10^4$ $M^{-1}$ $cm^{-1}$ at 510 nm, which had been determined by UV-Vis measurements of known concentrations of N719 in 0.1 M NaOH in 1:1 ethanol:water.

## RESULTS AND DISCUSSION

### Array DSC Scan Results

The typical figures of merits used to benchmark DSC performance are the short circuit current ($I_{SC}$) or short circuit current density ($J_{SC}$), open circuit voltage ($V_{OC}$), and maximum power point ($|IV|_{max}$ or $|JV|_{max}$).[3,5] These values can be used to calculate the fill-factor ($FF$) and overall efficiency ($\eta$) as follows:

$$FF = \frac{|JV|_{max}}{J_{SC}V_{OC}}$$

$$\eta = \frac{J_{SC}V_{OC}FF}{P_{in}}$$

where $P_{in}$ is the power density of the incident light. To estimate $I_{SC}$, $V_{OC}$, and $|IV|_{max}$ we measured each Ti-M array at 0, 0.2, 0.4, 0.5, 0.6, and 0.7 V. $I_{SC}$ was simply the current measured at 0 V while $V_{OC}$ was estimated by fitting a line through the current values at 0.4, 0.5, 0.6, and 0.7 V and then extrapolating or interpolating the voltage that produced zero current. Power was calculated by multiplying the current by the voltage and $|IV|_{max}$ was identified for the set of voltages that were measured (0.2, 0.4, 0.5, 0.6, and 0.7 V). $|IV|_{max}$ always occurred at 0.5 V for Ti oxide spots (Ti:M=50:0), but varied for other Ti-M oxide spots (Ti:M≠ 50:0). We attempted to select the Ti-M oxide on each array with the highest nominal $|IV|_{max}$ to compare with the Ti oxide spots on the same array. Comparisons were made within arrays so that synthesis conditions and dye adsorption times were equivalent. We synthesized and scanned two to five repeat arrays for each Ti-M combination. Since each array consisted of two identical patterns (see Figure 6.1), this resulted in 4 to 10 measurements of each of the 596 unique Ti-M compositions. The repeat scans were used to calculate the average $I_{SC}$, $V_{OC}$, $|IV|_{max}$ for the optimal Ti-M oxide spots relative to the Ti oxide spots on the same arrays.

Figure 6.3 shows an example of the scan results for a Ti-Sb array at voltages of 0, 0.2, 0.4, 0.5, 0.6, and 0.7 V. The Ti:Sb atomic ratio of each spot can be identified according to the Ti-M array pattern shown in Figure 6.1, using M=Sb. The light induced current of each spot can be quantified according to the color calibration bar on the right side of the figure. Note that the array spots with more than 66% Sb were not visible in the scans because they did not produce sufficient current. The $I_{SC}$ of each spot can be

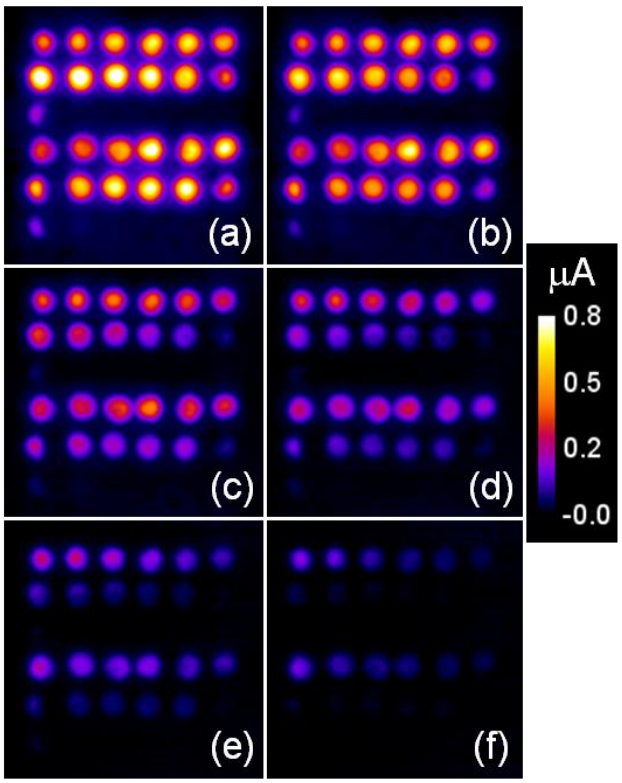


Figure 6.3. Ti-Sb array scans at (a) 0 V, (b) 0.2 V, (c) 0.4 V, (d) 0.5 V, (e) 0.6 V, and (f) 0.7 V. The composition of each spot can be identified according to the Ti-M array pattern shown in Figure 6.1, using M=Sb for this scan.

determined from Figure 6.3a since it was measured at 0 V. In the figure, all the spots containing 2 – 20 % Sb (metals basis) show higher current than the Ti oxide spots indicating that a wide range of Sb incorporation increases the $I_{SC}$. At the higher voltages of 0.4, 0.5, 0.6, and 0.7 V (Figures 6.3a, 6.3c, 6.3d, 6.3e, 6.3f) the current drops off faster for spots containing higher amounts of Sb and by 0.6 V the Ti oxide spots show the highest current. This indicates that incorporation of Sb decreases the $V_{OC}$ to an extent that is inversely proportional to the amount of Sb incorporation. On average, the highest $|IV|_{max}$ was observed at 0.4 V for a Ti:Sb atomic ratio of 47:3 (6% Sb metals basis). Numerous Ti-Sb arrays were synthesized and scanned in order to obtain the average

current values at each voltage and produce I-V curves for Ti oxide and 6% Sb as shown in Figure 6.4. From the I-V curve it is clear that 6% Sb has a higher $I_{SC}$ than Ti oxide. However, the current for 6% Sb drops off much faster with increasing voltages and points to a lower $V_{OC}$. Also plotted in Figure 6.4 is the power curve. For 6% Sb it shows a $|IV|_{max}$ of 0.14 μW at 0.4 V, which is 25% higher than the $|IV|_{max}$ of 0.11 μW at 0.5 V for Ti oxide.

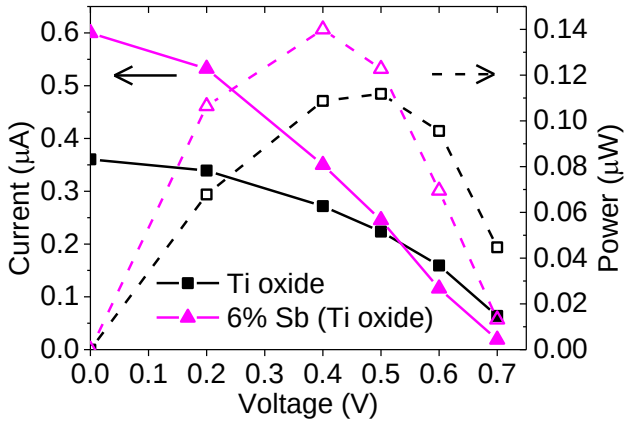


Figure 6.4. I-V curve produced by averaging the Ti-Sb array scans for 6% Sb and Ti oxide.

One disadvantage of preparing metal oxides by dispensing and annealing metal salt solutions is that there is little control over the surface structure and morphology of the final material. The amount of surface area a material has available for dye adsorption has a tremendous influence on the overall DSC device performance. We imaged the spots by SEM to qualitatively compare their surface area. Figures 6.5a and 6.5b show SEM images of a Ti oxide spot under low and high magnification. The Ti oxide array spots were mostly flat and dense with random cracks and pores less than 20 nm wide. In fact, the Ti oxide appeared to fill in the peaks and valleys of underlying FTO, which is evident from the high magnification image of bare FTO (Figure 6.5c). Adding a relatively small

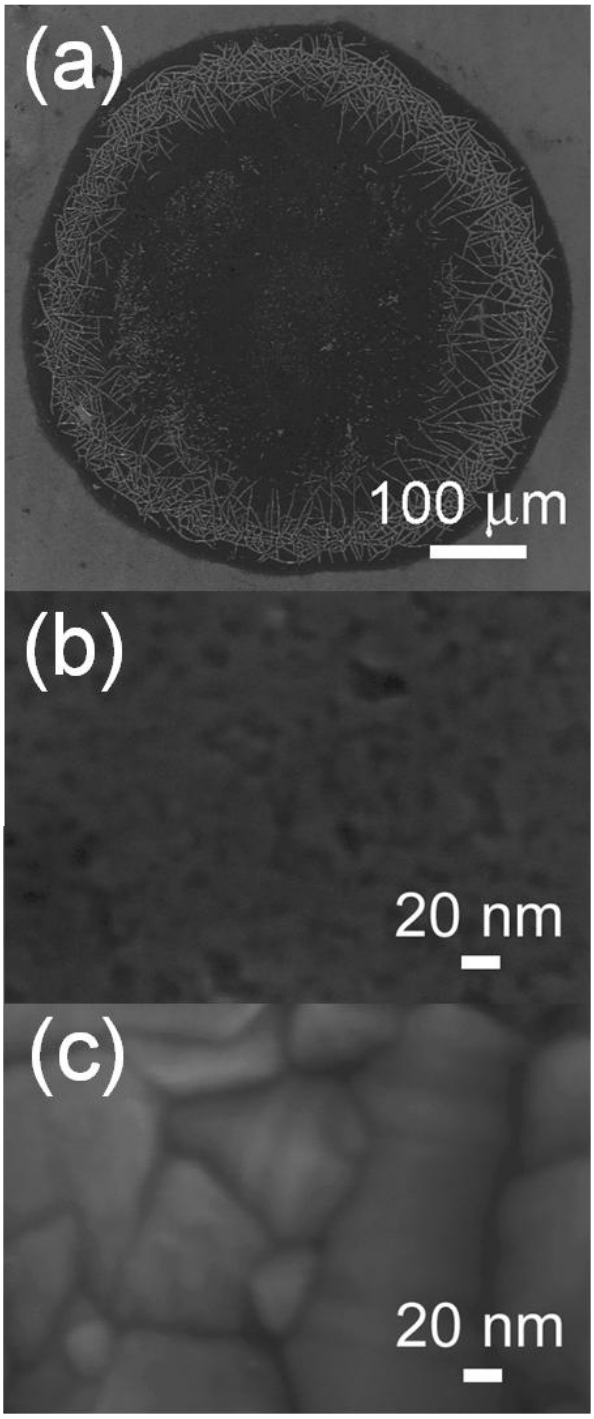


Figure 6.5. SEM images of a Ti-M array showing (a) the entire Ti oxide array spot at low magnification and (b) the middle of the Ti oxide array spot and (b) bare FTO near the array spots at high magnification.

amount of foreign metal salt to the $TiCl_4$ precursor solution to make 2 – 10 % doped Ti oxide did not have a significant impact on the resulting surface structure and morphology of the arrays spots. A mosaic SEM image of the Ti-Sb array and a close up SEM image of the 6% Sb spot are included in Appendix E (Figures E.1, E.2g, and E.2h). Similar to pure Ti oxide, the 6% Sb array spots were mostly flat and dense with porous features smaller than 20 nm.

To identify the optimal Ti:M ratios (% M values) for each of the 35 values of M, all of the Ti-M arrays were analyzed in a manner similar to the Ti-Sb array above. The results are summarized in Figure 6.6, which shows a scatter plot of the average $I_{SC}$ and $V_{OC}$ percent difference between the % M spots and the Ti oxide spots. To account for variation from array to array, the % M spots were only compared with Ti oxide spots on the same array. The scatter plot in Figure 6.6 has four quadrants: (I) positive $I_{SC}$ % difference, positive $V_{OC}$ % difference, (II) positive $I_{SC}$ % difference, negative $V_{OC}$ % difference, (III) negative $I_{SC}$ % difference, negative $V_{OC}$ % difference, and (IV) negative $I_{SC}$ % difference, positive $V_{OC}$ % difference. Dopant metal concentrations in quadrant (I) are the most promising candidates for improving the $|IV|_{max}$ $TiO_2$ for DSCs. Metals in quadrants (II) and (IV) are less likely to result in higher current than $TiO_2$ for all voltages, but they may be useful for improving DSC performance depending on whether a higher $I_{SC}$ or $V_{OC}$ is desired. Metals in quadrant (III) are most likely detrimental to DSC performance.

The results in Figure 6.6 are specific to the synthesis method that we used to make the arrays, which involved dispensing and annealing metal salts with $TiCl_4$ in ethylene glycol; however, the results are consistent with most known results obtained employing other synthesis techniques. For example, 1 – 2 % W was reported to improve $I_{SC}$ but decrease $V_{OC}$.[14,34] 2% Cu showed a significant drop in $I_{SC}$ but a positive 6.4% change in

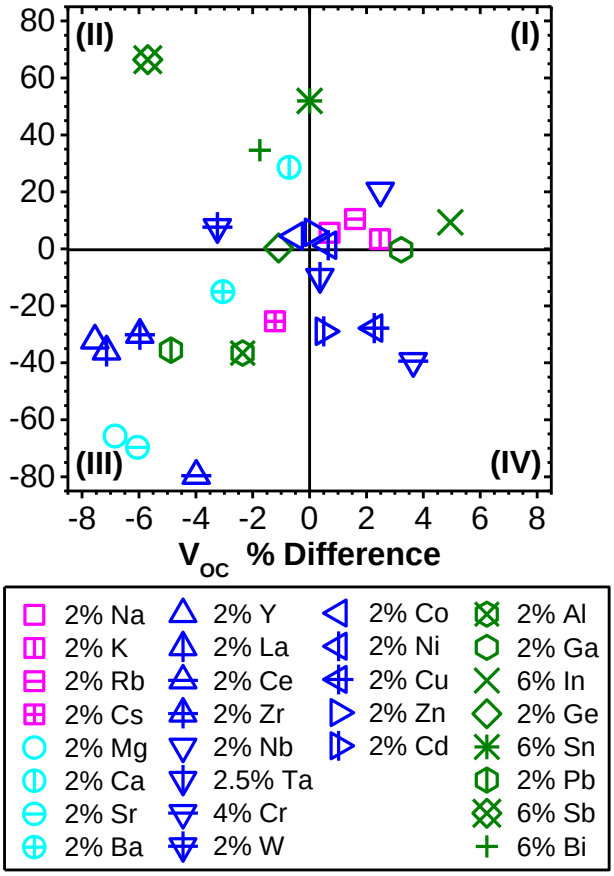


Figure 6.6. Scatter plot of average *Isc* and *Voc* % differences relative to Ti oxide for the optimal compositions of % M doped Ti oxide (metals basis), which were obtained from the Ti-M array scans.

*Voc*.[14,21,34] 1.7 – 2.7 mol % Nb $TiO_2$ resulted in improvements in *Jsc* and *Voc* up to 32.6% and 5.7%, respectively.[19,35] Zn doping has also been shown to improve both *Isc* and *Voc* to an extent, particularly under low intensity illumination.[18,23] Some of the results shown in Figure 6.6 have not previously been reported. For example, numerous post-transition metals (Ga, Ge, In, Sn, Sb and Bi) appear to maintain or increase *Isc* when incorporated into Ti oxide, but there is limited literature related to post-transition metals as dopants for $TiO_2$ for DSCs. One study showed an increase in *Isc* and decrease in *Voc* for incorporation of 1-3% Sb in $TiO_2$, but it did not include results for higher concentrations of Sb.[24] Recall

that we observed the highest $|IV|_{max}$ for 6% Sb incorporation. Figure 6.6 shows that 6% Sb resulted in the highest $I_{SC}$ of all dopants, but a significant decrease in $V_{OC}$. 6% Sn showed the next highest $I_{SC}$ and a reasonable $V_{OC}$, and 6% In showed the highest $V_{OC}$ and a reasonable $I_{SC}$. After completing the single dopant array scans we searched for metals to co-incorporate with Sb in an effort to increase $I_{SC}$ without decreasing the $V_{OC}$. We tested arrays containing 0 – 14 % Sb with 0 – 8% Na, K, Rb, Cs, Cr, and Al separately. They all showed some improvement in $|IV|_{max}$ but co-incorporation of Cr and Sb was the most consistent. 2% Cr, 6% Sb resulted in even higher $I_{SC}$ than 6% Sb along with a smaller drop in $V_{OC}$.

Some elements that were tested are not included in 6.6. Metals, such as scandium, vanadium, and iron, are not included because they were outside the range of the scatter plot. 2% V and 2% Sc decreased $J_{SC}$ and $V_{OC}$ by more than 85% and 8.5%, respectively. 2% Fe improved $J_{SC}$ by 50%, but decreased $V_{OC}$ by 29%. Molybdenum and silver were not included because array spots containing Mo or Ag were not consistent and tended to flake off the FTO substrate during annealing.

In addition to testing the 35 elements as dopants for titanium oxide, we tested them all as single component metal oxides. When sensitized with N719 dye, most of them did not show a measureable current or $V_{OC}$ during the array scans. The materials that did are summarized in Figure 6.7 according to $I_{SC}$ and $V_{OC}$ % difference. The only single component metal oxide that ended up in quadrant (I) was Zn oxide, which had a relatively high $I_{SC}$ and $V_{OC}$ compared to Ti oxide. In terms of DSC research publications, ZnO is second most studied metal oxide behind $TiO_2$.[3] It has a similar bandgap and conduction band energy level to $TiO_2$, but it is more susceptible to photo-corrosion.[3,31] All of the remaining single component metal oxides lie within quadrants (II) and (III)

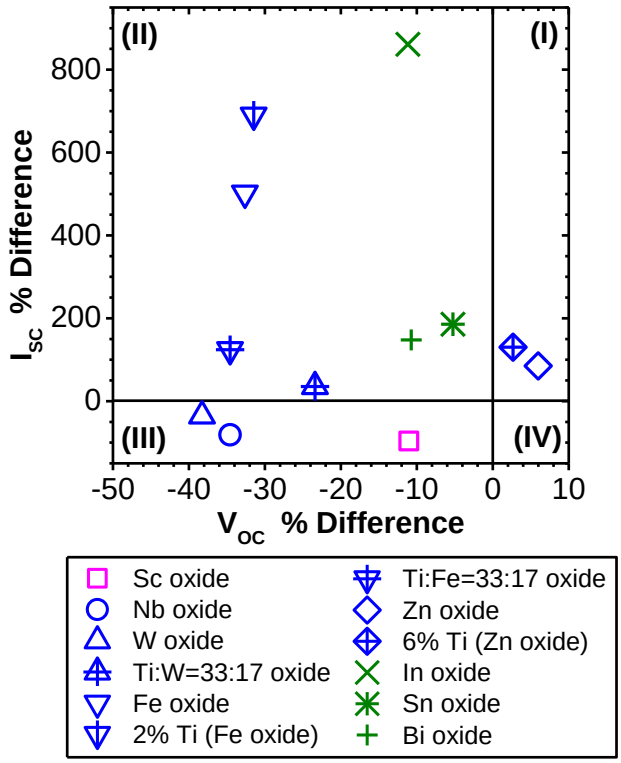


Figure 6.7. Scatter plot of average $I_{SC}$ and $V_{OC}$ % differences relative to Ti oxide for the single component M oxides that showed sufficient current during the Ti-M array scans.

because they have lower $V_{OC}$ values than Ti oxide. Some single component metal oxides (Fe, In, Sn, and Bi oxide) and two mixed metal oxides (Ti:W=33:17 and Ti:Fe=33:17 oxide) showed very high $I_{SC}$ values. The higher *Isc* and lower $V_{OC}$ of these metal oxides is partially due to the energy band positions. For common n-type metal oxide semiconductors used in photo-electrochemistry, the Fermi level ($E_F$) is typically about 0.1 eV below the conduction band ($E_{CB}$) and the location of $E_F$ can be estimated by measuring the flat band ($E_{FB}$) potential and taking into account the potential drop across the Hemholtz layer ($\Delta_{pH}$).[36] At the pH value where the potential drop across the Hemholtz layer is zero ($\Delta_{pH}$ =0), the point of zero zeta potential (PZZP), there is a linear correlation between the $E_{CB}$ and $E_{FB}$.[36,37] Thus $E_{FB}$ can be used to estimate $E_{CB}$. $Fe_2O_3$, $FeTiO_3$, $In_2O_3$,

$SnO_2$, and $Bi_2O_3$ all have $E_{FB}$ values that are at least 0.5 V more positive than the $E_{FB}$ of $TiO_2$.[31,36-38] The more positive $E_{FB}$ values result in a larger potential difference between the $E_{CB}$ of these metal oxides and the HOMO of the adsorbed dye resulting in a larger driving force for $I_{SC}$. At the same time the $V_{OC}$ of these single component metal oxides is constrained since the maximum obtainable $V_{OC}$ is the voltage difference between the $E_F$ of the metal oxide and the potential of the redox species.[3-5] Another contributing factor to the higher *Isc* of the Zn, In, Sn, Bi, and Ti:W=33:17 oxides, is the surface area of the array spots. These single component metal oxides appeared to have more complicated surface structure than Ti oxide, which likely resulted in adsorption of more dye, and hence more light absorption. Figure E.3 in Appendix E shows comparison SEM images for Ti, Fe, Zn, In, Sn, Bi, and Ti:W=33:17 oxide array spots.

**Drop-cast Film DSC Results**

Scaled-up films were synthesized by drop-casting with the following compositions: Ti only ($TiO_2$), Ti:In=47:3 (6% In $TiO_2$), and Ti:Sn=47:3 (6% Sn $TiO_2$), Ti:Sb=47:3 (6% Sb $TiO_2$), Ti:Cr=47:3 (6% Cr $TiO_2$), and Ti:Cr:Sb=46:1:3 (2% Cr, 6% Sb $TiO_2$). We performed XRD measurements to reveal which crystal phases of $TiO_2$ were formed by oxidation of the metal salts and $TiCl_4$ in ethylene glycol. The XRD spectra are shown in Figures 6.8a and 6.8b along with the reference pattern for anatase $TiO_2$ (PDF # 00-021-1272) with Miller indices for anatase labeled by the letter A. All of the compositions formed $TiO_2$, primarily in the anatase phase. Figure 6.8a shows that the pure Ti oxide films matched the reference pattern for anatase $TiO_2$ almost exactly. Close inspection of the spectra for 6% In $TiO_2$ and 6% Sn $TiO_2$ reveals slight negative shifts of 0.14 – 0.16 deg for the (200) peak near two theta of 48 deg and 0.06 – 0.09 for the (211) peak near 55 deg. A similar negative shift was observed for 5 – 10 % Nb incorporation

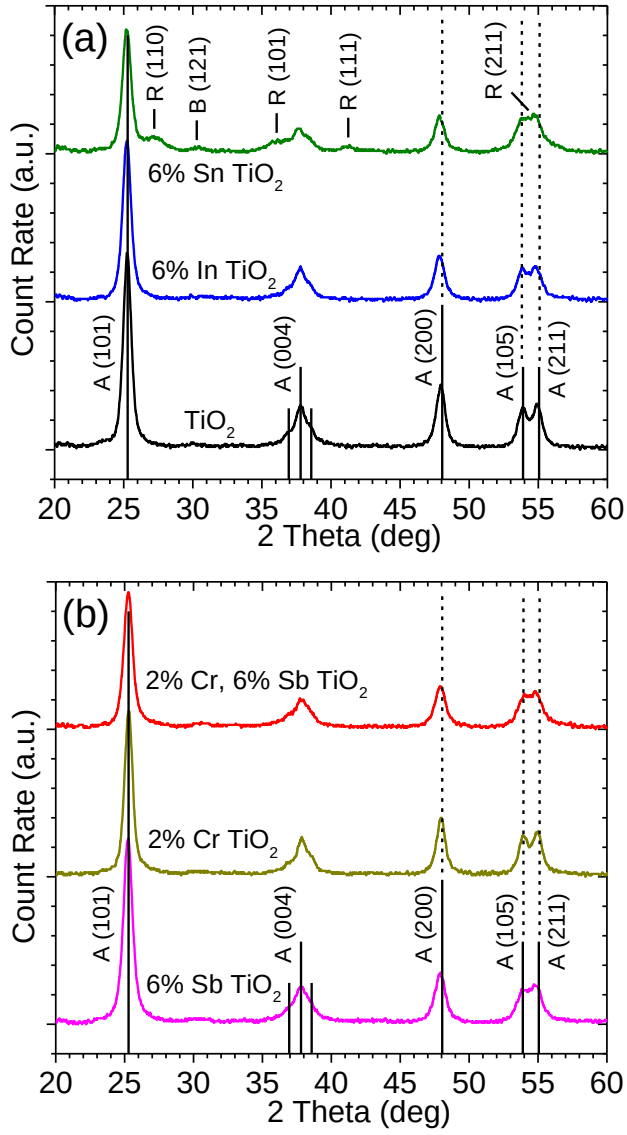


Figure 6.8. XRD spectra for material synthesized by drop-cast composed with compositions of (a) Ti only ($TiO_2$), Ti:In=47:3 (6% In $TiO_2$), and Ti:Sn=47:3 (6% Sn $TiO_2$) and (b) Ti:Sb=47:3 (6% Sb $TiO_2$), Ti:Cr=49:1 (2% Cr $TiO_2$), and Ti:Cr:Sb=46:1:3 (2% Cr, 6% Sb $TiO_2$). The reference pattern is for anatase (A) $TiO_2$ (PDF # 00-021-1272). Peaks for rutile (R) $TiO_2$ (PDF # 00-021-1276) and brookite (B) $TiO_2$ (PDF# 00-029-1360) are also indicated.

into $TiO_2$, which was attributed to the larger ionic radius of $Nb^{5+}$ compared to $Ti^{4+}$.[19] In and Sn likely incorporated with larger ionic radii as well. Using a coordination

number of 6 for $TiO_2$, some possible oxidation state (ionic radius) values for In, Sn, Sb, and Cr doped anatase $TiO_2$ are as follows: $In^{3+}$ (0.80 Å) , $Sn^{4+}$ (0.69 Å), $Sb^{5+}$ (0.60 Å), $Cr^{3+}$ (0.615 Å), and $Ti^{4+}$ (0.605 Å).[39] Along with the anatase peak shifts, 6% Sn $TiO_2$ also showed the emergence of extra peaks, which matched the references for rutile $TiO_2$ (PDF # 00-021-1276) and possibly the second largest peak for brookite $TiO_2$ (PDF# 00-029-1360) at two theta of 30.8 deg. The Miller indices of these peaks are labeled with the letters R and B. For 6% Sn $TiO_2$ the relative peak intensities for anatase (101) and rutile (110) were 93% and 7%, respectively, indicating a low percentage of rutile $TiO_2$. In Figure 6.8b, the XRD spectrum for 2% Cr $TiO_2$ did not stray appreciably from the anatase $TiO_2$ reference pattern. The spectra for 6% Sb $TiO_2$ and 2% Cr, 6% Sb $TiO_2$ did not show noticeable shifts for the anatase (200) and (211) peaks but they did show merging of the (105) and (211) peaks near 54 and 55 degrees. In addition to XRD, the chemical compositions of the drop-cast films were verified using XPS and EDS. The results are summarized in Appendix E (Table S1). EDS showed atomic percentages that were slightly above and below the expected values for the incorporated metals while XPS revealed atomic percentages that were mostly above the expected values. This suggests that synthesis favors segregation of the metals to the surface of the $TiO_2$. Surface effects can be important for dye adsorption and charge transport, which is discussed later.[3]

The drop-cast films were imaged by SEM to determine if incorporation of dopants altered the surface structure and morphology. Figure 6.9 shows SEM images of a typical $TiO_2$ film synthesized by drop-casting. The drop-cast $TiO_2$ films (Figure 6.9a) were similar in appearance to the Ti oxide array spots (Figure 6.5b). They consisted of a compact agglomerate of particulates that were less than 20 nm in diameter. SEM images for 6% In $TiO_2$, 6% Sn $TiO_2$, 6% Sb $TiO_2$, and 2% Cr, 6% Sb $TiO_2$ were equally unremarkable and are included in Appendix E (Figure E.4). Based on the high

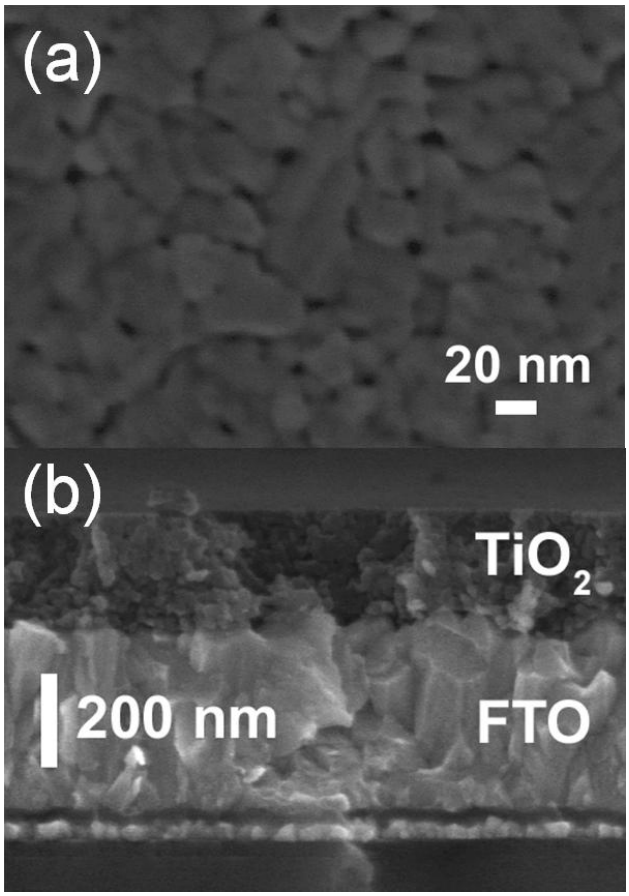


Figure 6.9. SEM image of a scaled-up $TiO_2$ film synthesized by drop-cast from (a) top view and (b) cross-sectional view.

magnification SEM images, up to 6% incorporation of In, Sn, or Sb did not appear to alter the surface area significantly. We also used dye desorption measurements to estimate the amount of dye adsorbed by each composition and the results are included in Table 6.1. All of the compositions adsorbed about 4 nmol/cm$^2$ of N719 dye, which is quite low compared to high efficiency DSCs. For instance, in the 1991 breakthrough paper, the $TiO_2$ nanoparticle DSC had an adsorption of 130 nmol/cm$^2$ for the ruthenium based dye.[2] Nevertheless, these low surface area films synthesized by drop-casting are useful for comparing the effect of doping, especially since the different compositions

| Film | Total Samples | *Dye Adsorption* (nmol/cm$^2$) |
|---|---|---|
| $TiO_2$ | 3 | 4.1 ± 0.5 |
| 6% In $TiO_2$ | 3 | 3.5 ± 0.5 |
| 6% Sn $TiO_2$ | 3 | 3.9 ± 0.2 |
| 6% Sb $TiO_2$ | 3 | 4.4 ± 0.3 |
| 2% Cr, 6% Sb $TiO_2$ | 3 | 3.8 ± 0.5 |

Table 6.1. Dye adsorption estimates for drop-cast films. Calculated from UV-Vis measurements of solution used to desorb N719 dye from sensitized films. Values are listed as the average ± one standard deviation.

show the same level of dye adsorption.

In order to compare the light absorption of different compositions, UV-vis measurements were performed. Figure 6.10 shows the UV-Vis spectra for various drop-cast films. Between 320 and 460 nm, the light response was essentially the same for all compositions. The Tauc plot (Figure E.5) suggests an indirect bandgap energy of about 3.2 eV, which is typical for anatase $TiO_2$.[3,5,40] It is worth mentioning that the drop-cast 2% Cr $TiO_2$ and 2% Cr, 6% Sb $TiO_2$ were mostly transparent in the middle, but had an orange tint around the edge of the FTO. For Cr and Cr,Sb co-doped $TiO_2$ synthesized by other methods, researchers have observed a visible orange hue along with absorption spectra shoulders extending beyond 550 nm.[11,41,42] From the cross-sectional SEM images (Figure 6.9b) we estimate the thickness of our drop-cast films to be approximately 200 nm. At this thickness, the films only absorbed a fraction of the incident light, even at wavelengths well below 380 nm. Perhaps thicker 2% Cr $TiO_2$ and 2% Cr, 6% Sb $TiO_2$ films would show light absorption features at higher wavelengths. However, extension of the visible light response of $TiO_2$ is not necessary for DSCs because the task of visible light absorption is accomplished by the dye molecules.

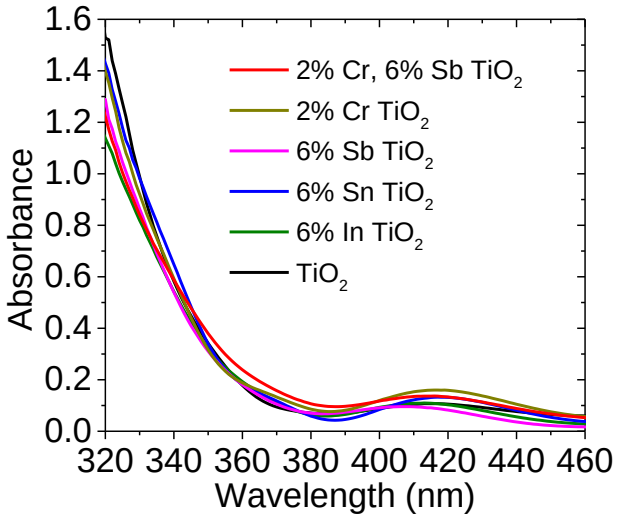


Figure 6.10. UV-Vis absorbance spectrum for films synthesized by drop-casting with various compositions.

To ensure reproducibility of the DSC devices, we synthesized and tested numerous repeat films of each composition. The average $J_{SC}$, $V_{OC}$, $|JV|_{max}$, and $FF$ of each composition are listed in Table 6.2 and typical I-V curves for each composition are shown in Figures 6.11a and 6.11b. The general trends in $J_{SC}$ and $V_{OC}$ are consistent with the array scan results, although the $J_{SC}$ and $V_{OC}$ percent differences relative to $TiO_2$ are

| Film | Total Samples | $J_{SC}$ (mA/cm$^2$) | $V_{OC}$ (V) | $\|JV\|_{max}$ (mW/cm$^2$) | $FF$ |
|---|---|---|---|---|---|
| $TiO_2$ | 10 | 0.312 ± 0.10 | 0.649 ± 0.04 | 0.110 ± 0.03 | 0.547 ± 0.04 |
| 6% In $TiO_2$ | 8 | 0.327 ± 0.09 | 0.679 ± 0.03 | 0.138 ± 0.04 | 0.621 ± 0.04 |
| 6% Sn $TiO_2$ | 7 | 0.355 ± 0.05 | 0.639 ± 0.06 | 0.135 ± 0.03 | 0.588 ± 0.04 |
| 6% Sb $TiO_2$ | 7 | 0.428 ± 0.11 | 0.552 ± 0.02 | 0.114 ± 0.03 | 0.476 ± 0.03 |
| 2% Cr $TiO_2$ | 5 | 0.268 ± 0.08 | 0.651 ± 0.04 | 0.105 ± 0.05 | 0.586 ± 0.03 |
| 2% Cr, 6% Sb $TiO_2$ | 10 | 0.559 ± 0.10 | 0.593 ± 0.04 | 0.150 ± 0.03 | 0.452 ± 0.03 |

Table 6.2. Comparison of parameters for scaled-up DSC devices. Values are listed as the average ± one standard deviation.

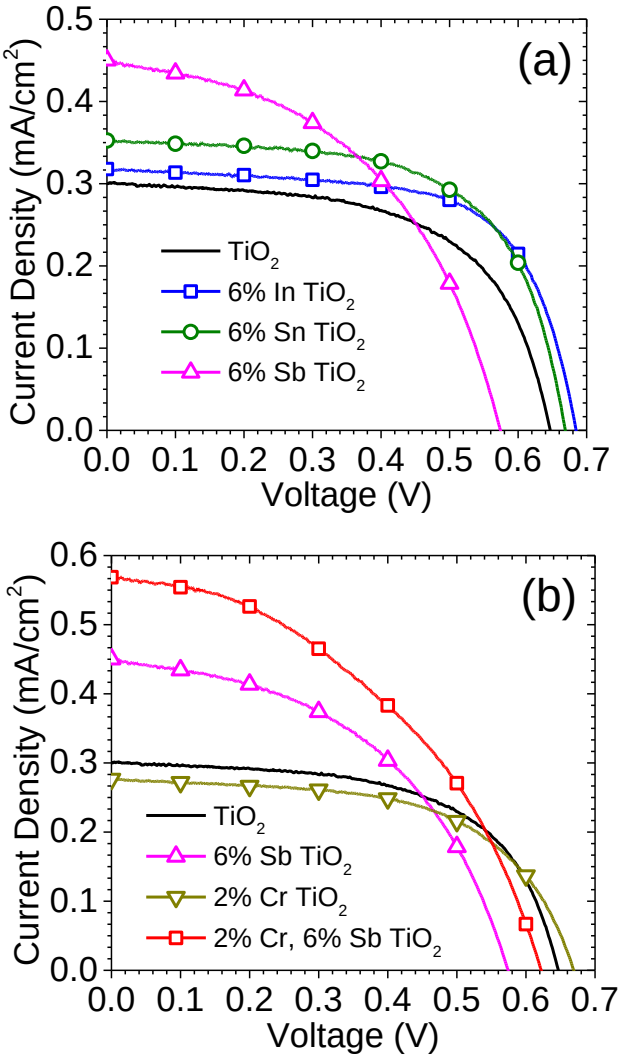


Figure 6.11. I-V curves for typical DSC devices containing films synthesized by drop-cast composed of (a) $TiO_2$, 6% In $TiO_2$, 6% Sn $TiO_2$, and 6% Sb $TiO_2$ and (b) $TiO_2$, 6% Sb $TiO_2$, 2% Cr $TiO_2$, and 2% Cr, 6% Sb $TiO_2$. The lamp power was 100 mW/cm$^2$.

smaller. According to the drop-cast film results, 6% Sb increased $J_{SC}$ by 31% but decreased $V_{OC}$ by 15%, 6% Sn increased $J_{SC}$ by 14% and maintained $V_{OC}$ to within 1.5%, and 6% In increased $V_{OC}$ by 4.5% along with a slight increase in $J_{SC}$ of 4.8% giving it the highest $FF$ at 0.62. For the array scans, 4% Cr was the optimal amount of Cr

incorporation for improving $V_{OC}$, but 2% Cr $TiO_2$ films were made by drop-casting to compare with 2% Cr, 6% Sb $TiO_2$. 2% Cr resulted in a 14% decrease in $J_{SC}$, but slight increase in $V_{OC}$. Adding 2% Cr along with 6% Sb resulted in the largest increase in $J_{SC}$ at 79% and a decrease in $V_{OC}$ of 8.6%, which was an improvement relative to 6% Sb alone. 2% Cr, 6% Sb $TiO_2$ had a relatively poor *FF* at 0.45, but had the highest $|JV|_{max}$ due to the high current.

The improvements observed for co-incorporation of 2% Cr and 6% Sb relative to 6% Sb by itself suggest that Cr and Sb play complementary roles when incorporated together in $TiO_2$. In photocatalysis research, improved photoactivity for Cr, Sb co-doped rutile $TiO_2$ for $O_2$ evolution has been attributed in part to an enhancement in visible light response.[11] Based on our UV-Vis measurements of the drop-cast 2% Cr, 6% Sb $TiO_2$ films, which were anatase, the improvement in DSC performance does not appear to be caused by improved light absorption. Instead it is more likely related to improved charge transport properties. A recent study used density function theory (DFT) calculations to analyze the combined roles of Cr and Sb when co-doped in anatase $TiO_2$.[43] It was theorized that substitutional doping with Cr could result in either $Cr^{4+}$ sites or $Cr^{3+}$ along with oxygen vacancies while substitutional doping with Sb would likely result in $Sb^{5+}$ and $Ti^{3+}$ sites. Substitutional doping of Cr and Sb together would allow for an electron transfer from Sb to Cr without the need to create defects such as oxygen vacancies or $Ti^{3+}$ sites, reducing the rate of electron-hole recombination. Indeed, if $Sb^{5+}$ and $Cr^{3+}$ were equally substituted for $Ti^{4+}$ in $TiO_2$, then the charge would be fully compensated and there would be no need for oxygen vacancies or $Ti^{3+}$ species. However, we found that a Cr:Sb ratio of 1:3 resulted in the highest currents for DSCs. One possibility is that higher Sb concentrations result in both $Sb^{5+}$ and $Sb^{3+}$ species. Researchers have shown that Sb incorporation into $SnO_2$ reduces resistivity and deconvoluted XPS spectra suggest a mix

of $Sb^{5+}$ and $Sb^{3+}$ at higher concentrations of Sb.[44] Nb doping of $TiO_2$ , most likely as $Nb^{5+}$, has also been shown to reduce resistivity, which was one of the factors attributed to improved DSC performance.[19] In general, metal oxides have poor conductivity compared to non-oxide semiconductors and electron transport through $TiO_2$ is one of the slowest electronic processes during DSC operation. The typical time constant for electron transport through nanocrystalline $TiO_2$ films in DSCs has been estimated to be on the order of $10^{-3}$-$10^{0}$ s, which is quite slow compared to the typical time constants for injection of photo-excited electrons by the dye ($10^{-12}$-$10^{-10}$ s) and regeneration of the oxidized dye molecules by the redox couple ($10^{-8}$ s for iodide/triiodide).[3,45-48] It is expected that an improvement in the conductivity of $TiO_2$ would be beneficial to reducing current losses in a DSC device.

EIS is one method that can be used to estimate the internal resistances of DSC materials. It involves the application of minute AC voltage amplitudes to elucidate an equivalent internal circuit. We performed EIS measurements on typical DSC devices at open circuit potential under illumination to produce the Nyquist plots shown in Figure 6.12 (the same DSC devices that were used for Figure 6.11). There is some disagreement in the literature as to the equivalent circuit assignment for every point in the Nyquist plots for DSCs, but it is commonly accepted that the semi-circle ($Z_2$) in the middle frequency range 10 – 100 Hz can be assigned to electron transfer through the $TiO_2$/dye/electrolyte.[49-53] This is the frequency range for the largest semi-circles shown in Figures 6.12a and 6.12b. For each composition, the high frequency ohmic resistance (Rh) was similar at about 30 ohms, but $Z_2$ varied. We used ZView software to model each $Z_2$ as a resistor ($R_2$) in series with a capacitor ($C_2$). For $TiO_2$, 6% In $TiO_2$, and 6% Sn $TiO_2$, and 2% Cr $TiO_2$, the model predicted a similar $C_2$ value of about 5 x $10^{-5}$ F and varying $R_2$ values of 216, 183, 172, and 327 ohms, respectively. 6% Sb $TiO_2$ and 2% Cr, 6% Sb $TiO_2$ were

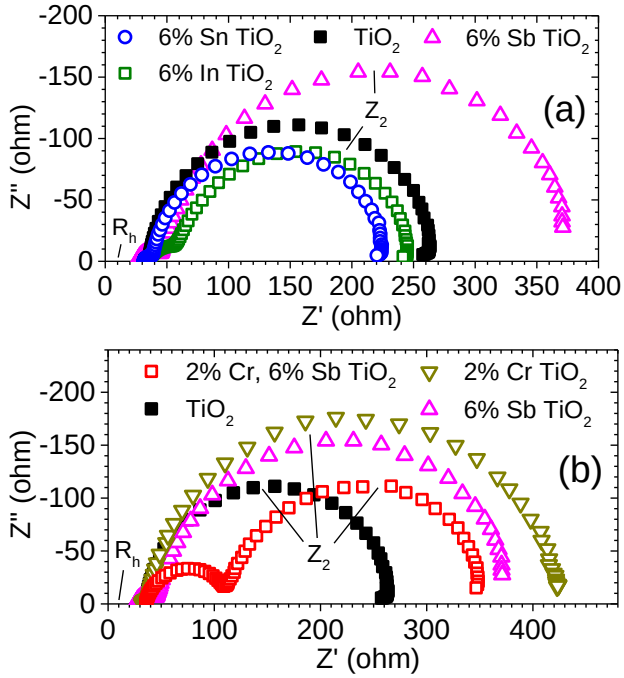


Figure 6.12. Nyquist plots for typical DSC devices containing films synthesized by drop-cast composed of (a) $TiO_2$, 6% In $TiO_2$, 6% Sn $TiO_2$, and 6% Sb $TiO_2$ and (b) $TiO_2$, 6% Sb $TiO_2$, 2% Cr $TiO_2$, and 2% Cr, 6% Sb $TiO_2$. The EIS measurements were conducted at open circuit potential under illumination.

also similar to each other in $C_2$ at about ~3 x $10^{-4}$ F but had differing $R_2$ values of 311 and 231 ohms, respectively. The large reduction in $R_2$ for 2% Cr, 6% Sb $TiO_2$ compared to 2% Cr $TiO_2$ and 6% Sb $TiO_2$ suggests that the complementary interaction between Cr and Sb helps decrease resistance to charge transport in the DSC device. The incorporated metals may improve charge transport by passivating surface trap states and suppressing recombination between electrons in the metal oxide and the dye or electrolyte. Such an effect has been observed for ultrathin films of $Al_2O_3$, $Nb_2O_5$, $SiO_2$, and $ZrO_2$ applied to the surface of $TiO_2$.[3,5,54,55] A more detailed EIS analysis utilizing varying steady states can be used to probe the surface kinetics of DSC materials and determine the rate of interfacial charge transfer.[52,53] On the other hand the incorporated metals may increase the

rate of recombination within the bulk material. Excess doping of metal oxide semiconductors can create trap states, which can decrease the carrier lifetime even though conductivity and photoactivity increases.[18,56,57] A decrease in carrier lifetime might lead to lower photoactivity for doped $TiO_2$ films that are thicker than the 200 nm films that we synthesized by drop-casting.

Lastly, we performed 3-electrode PEC measurements for each composition with the film as the WE and aqueous 1 M NaOH as the electrolyte. This included chopped (light/dark) J-V measurements and EIS measurements using a voltage amplitude of 5 mV and a frequency of 10 kHz between -0.2 and -1.0 V vs. Ag/AgCl. Figures for these measurements are included in Appendix E (S6, S7, and S8). Mott-Schottky analysis of the EIS data was used to estimate the $E_{FB}$ of each composition. Figure 6.13 shows the average $V_{OC}$ values obtained from DSC device measurements versus the $E_{FB}$ values estimated by Mott-Schottky. The $V_{OC}$ and $E_{FB}$ values show a linear correlation. This is

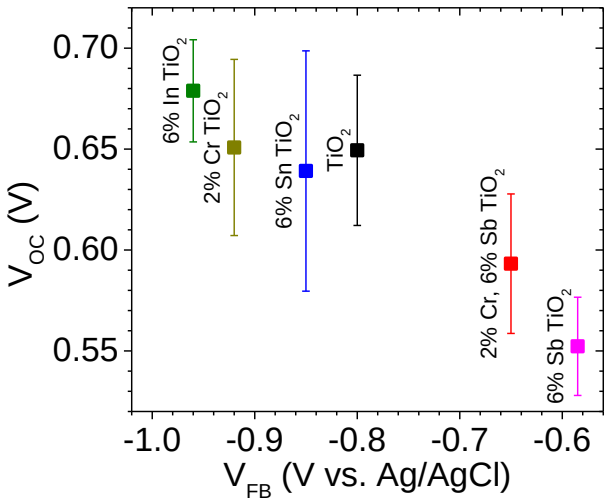


Figure 6.13. Plot of the average $V_{OC}$ obtained from DSC devices versus the $V_{FB}$ estimated from Mott-Schottky analysis of typical drop-cast films with various compositions.

expected since the maximum obtainable $V_{OC}$ is constrained by the difference in the $E_F$ of the metal oxide and the potential of the redox species. The slightly more negative $E_{FB}$ of 2% Cr, 6% Sb $TiO_2$ compared to that 6% Sb $TiO_2$ is consistent with the slightly higher $V_{OC}$. Along with the higher $J_{SC}$ of 2% Cr, 6% Sb $TiO_2$, this is further evidence that Cr and Sb have a combined effect that improves charge transport in the DSC device.

## CONCLUSIONS

We have used an array dispenser and scanner system to investigate 35 different elements as single component metal oxides and as dopants for $TiO_2$ for use in DSC devices with N179 as the dye and iodide/triiodide as the redox species. When incorporated as dopants, each element showed a unique influence on $I_{SC}$ and $V_{OC}$. Changes in $I_{SC}$ and $V_{OC}$ were consistent with known results for doping $TiO_2$ with 2% W, 2% Cu, 2% Nb, and 2% Zn. In addition, new dopants were discovered including several post-transition metals with optimal dopant levels of 6% In, 6% Sn, and 6% Sb along with co-incorporation of 2% Cr and 6% Sb. Single component metal oxides, such as Fe, In, Sn, and Bi oxide, showed considerably higher $I_{SC}$ values than Ti oxide but lower $V_{OC}$ values. This was attributed to the array spots having more surface area and more positive $E_{CB}$ values than $TiO_2$.

Scaled-up films of $TiO_2$, 6% In $TiO_2$, 6% Sn $TiO_2$, 6% Sb $TiO_2$, 2% Cr $TiO_2$, and 2% Cr, 6% Sb $TiO_2$ were synthesized by drop-casting for materials characterization and DSC device measurements. From XRD measurements the films were confirmed to be primarily anatase $TiO_2$. They all had similarly low surface area and dye adsorption, which resulted in low DSC device efficiency, but allowed for fair comparison of their DSC performance. Incorporation of $TiO_2$ with 6% In increased $V_{OC}$ by 4.5% and $J_{SC}$ by 5% resulting in a *FF* at 0.62, which was the highest of all the compositions. 6% Sb increased

$J_{SC}$ by 31% but decreased $V_{OC}$ by 15%. The addition of 2% Cr along with 6% Sb increased the $J_{SC}$ even more by 79% and lessened the decrease in $V_{OC}$ to 8.6%. As a result 2% Cr, 6% Sb $TiO_2$ had the highest $|JV|_{max}$ of all the compositions even though the *FF* was relatively low at 0.42. The increase in current for 2% Cr, 6% $TiO_2$ was the result of a complementary interaction between Cr and Sb, possibly involving charge compensation. For EIS measurements 2% Cr, 6% Sb $TiO_2$ showed a lower resistance to charge transport relative to 2% Cr $TiO_2$ and 6% Sb $TiO_2$. The various compositions showed a linear relation between the $V_{OC}$ values obtained from DSC operation and the $E_{FB}$ values estimated by Mott-Schottky. These compositions may be useful in making high efficiency DSC devices if they can be synthesized by other methods that result in significantly higher surface area for dye adsorption. Additionally the $I_{SC}$ and $V_{OC}$ of these compositions might be maximized using dyes other than N719 and electrolyte species having more positive redox potentials.

## REFERENCES


(1) Grätzel, M. Journal of Photochemistry and Photobiology C: Photochemistry Reviews **2003**, 4, 145-153.

(2) O'Regan, B.; Grätzel, M. Nature **1991**, 353, 737-740.

(3) Hagfeldt, A.; Boschloo, G.; Sun, L.; Kloo, L.; Pettersson, H. Chemical Reviews **2010**, 110, 6595-6663.

(4) Sayama, K.; Sugihara, H.; Arakawa, H. Chemistry of Materials **1998**, 10, 3825-3832.

(5) Jose, R.; Thavasi, V.; Ramakrishna, S. Journal of the American Ceramic Society **2009**, 92, 289-301.

(6) Osterloh, F. E. Chemistry of Materials **2007**, 20, 35-54.

(7) Kudo, A.; Miseki, Y. Chemical Society Reviews **2009**, 38, 253-278.

(8) Chen, X.; Shen, S.; Guo, L.; Mao, S. S. Chemical Reviews **2010**, 110, 6503-6570.

(9) Zou, Z.; Ye, J.; Sayama, K.; Arakawa, H. Nature **2001**, 414, 625-627.

(10) Asahi, R.; Morikawa, T.; Ohwaki, T.; Aoki, K.; Taga, Y. Science **2001**, 293, 269-271.

(11) Kato, H.; Kudo, A. The Journal of Physical Chemistry B **2002**, 106, 5029-5034.

(12) Zou, Z.; Arakawa, H. Journal of Photochemistry and Photobiology A: Chemistry **2003**, 158, 145-162.

(13) Woodhouse, M.; Parkinson, B. A. Chemistry of Materials **2008**, 20, 2495-2502.

(14) Ko, K. H.; Lee, Y. C.; Jung, Y. J. Journal of Colloid and Interface Science **2005**, 283, 482-487.

(15) Kim, C.; Kim, K.-S.; Kim, H. Y.; Han, Y. S. Journal of Materials Chemistry **2008**, 18, 5809-5814.

(16) Iwamoto, S.; Sazanami, Y.; Inoue, M.; Inoue, T.; Hoshi, T.; Shigaki, K.; Kaneko, M.; Maenosono, A. ChemSusChem **2008**, 1, 401-403.

(17) Feng, X.; Shankar, K.; Paulose, M.; Grimes, C. A. Angewandte Chemie International Edition **2009**, 48, 8095-8098.

(18) Wang, K.-P.; Teng, H. Physical Chemistry Chemical Physics **2009**, 11, 9489-9496.

(19) Lü, X.; Mou, X.; Wu, J.; Zhang, D.; Zhang, L.; Huang, F.; Xu, F.; Huang, S. Advanced Functional Materials **2010**, 20, 509-515.

(20) Tsvetkov, N.; Larina, L.; Shevaleevskiy, O.; Ahn, B. T. Energy & Environmental Science **2010**, 4, 1480-1486.

(21) Navas, J.; Fernández-Lorenzo, C.; Aguilar, T.; Alcántara, R.; Martín-Calleja, J. physica status solidi (a) **2011**, 209, 378-385.

(22) Hafez, H.; Saif, M.; Abdel-Mottaleb, M. S. A. Journal of Power Sources **2011**, 196, 5792-5796.

(23) Zhang, Y.; Wang, L.; Liu, B.; Zhai, J.; Fan, H.; Wang, D.; Lin, Y.; Xie, T. Electrochimica Acta **2011**, 56, 6517-6523.

(24) Wang, M.; Bai, S.; Chen, A.; Duan, Y.; Liu, Q.; Li, D.; Lin, Y. Electrochimica Acta **2012**, 77, 54-59.

(25) Hoang, S.; Ngo, T. Q.; Berglund, S. P.; Fullon, R. R.; Ekerdt, J. G.; Mullins, C. B. ChemPhysChem **2013**, 14, 2270-2276.

(26) Lettmann, C.; Hinrichs, H.; Maier, W. F. Angewandte Chemie International Edition **2001**, 40, 3160-3164.

(27) Nakayama, A.; Suzuki, E.; Ohmori, T. Applied Surface Science **2002**, 189, 260-264.

(28) Jaramillo, T. F.; Baeck, S.-H.; Kleiman-Shwarsctein, A.; McFarland, E. W. Macromolecular Rapid Communications **2004**, 25, 297-301.

(29) Berglund, S. P.; Lee, H. C.; Nunez, P. D.; Bard, A. J.; Mullins, C. B. Physical Chemistry Chemical Physics **2013**, 15, 4554-4565.

(30) Fosdick, S. E.; Berglund, S. P.; Mullins, C. B.; Crooks, R. M. Analytical Chemistry **2013**, 85, 2493-2499.

(31) Maruska, H. P.; Ghosh, A. K. Solar Energy **1978**, 20, 443-458.

(32) Bard, A. J.; Faulkner, L. R. Electrochemical Methods: Fundamentals and Applications; Second ed.; John Wiley & Sons, Inc.: New Jersey, 2001.

(33) Beer Annalen der Physik **1852**, 162, 78-88.

(34) Zhang, X.; Liu, F.; Huang, Q.-L.; Zhou, G.; Wang, Z.-S. The Journal of Physical Chemistry C **2011**, 115, 12665-12671.

(35) Tsvetkov, N.; Larina, L.; Shevaleevskiy, O.; Ahn, B. T. Journal of the Electrochemical Society **2011**, 158, B1281-B1285.

(36) Butler, M. A.; Ginley, D. S. Journal of the Electrochemical Society **1978**, 125, 228-232.

(37) Xu, Y.; Schoonen, M. A. A. American Mineralogist **2000**, 85, 543-556.

(38) Scaife, D. E. Solar Energy **1980**, 25, 41-54.

(39) Shannon, R. D. Acta Crystallographica Section A **1976**, 32, 751-767.

(40) Tang, H.; Prasad, K.; Sanjines, R.; Schmid, P. E.; Levy, F. Journal of Applied Physics **1994**, 75, 2042-2047.

(41) Herrmann, J.-M.; Disdier, J.; Pichat, P. Chemical Physics Letters **1984**, 108, 618-622.

(42) Serpone, N.; Lawless, D.; Disdier, J.; Herrmann, J.-M. Langmuir **1994**, 10, 643-652.

(43) Valentin, C. D.; Pacchioni, G.; Onishi, H.; Kudo, A. Chemical Physics Letters **2009**, 469, 166-171.

(44) Terrier, C.; Chatelon, J. P.; Berjoan, R.; Roger, J. A. Thin Solid Films **1995**, 263, 37-41.

(45) Tachibana, Y.; Moser, J. E.; Grätzel, M.; Klug, D. R.; Durrant, J. R. The Journal of Physical Chemistry **1996**, 100, 20056-20062.

(46) Frank, A. J.; Kopidakis, N.; Lagemaat, J. v. d. Coordination Chemistry Reviews **2004**, 248, 1165-1179.

(47) Ardo, S.; Meyer, G. J. Chemical Society Reviews **2009**, 38, 115-164.

(48) Koops, S. E.; O'Regan, B. C.; Barnes, P. R. F.; Durrant, J. R. Journal of the American Chemical Society **2009**, 131, 4808-4818.

(49) Hoshikawa, T.; Yamada, M.; Kikuchi, R.; Eguchi, K. Journal of the Electrochemical Society **2005**, 152, E68-E73.

(50) Han, L.; Koide, N.; Chiba, Y.; Mitate, T. Applied Physics Letters **2004**, 84, 2433-2435.

(51) Adachi, M.; Sakamoto, M.; Jiu, J.; Ogata, Y.; Isoda, S. The Journal of Physical Chemistry B **2006**, 110, 13872-13880.

(52) Fabregat-Santiago, F.; García-Cañadas, J.; Palomares, E.; Clifford, J. N.; Haque, S. A.; Durrant, J. R.; Garcia-Belmonte, G.; Bisquert, J. Journal of Applied Physics **2004**, 96, 6903-6907.

(53) Fabregat-Santiago, F.; Garcia-Belmonte, G.; Mora-Sero, I.; Bisquert, J. Physical Chemistry Chemical Physics **2011**, 13, 9083-9118.

(54) Zaban, A.; Chen, S. G.; Chappel, S.; Gregg, B. A. Chemical Communications **2000**, 2231-2232.

(55) Palomares, E.; Clifford, J. N.; Haque, S. A.; Lutz, T.; Durrant, J. R. Chemical Communications **2002**, 1464-1465.

(56) Choi, W.; Termin, A.; Hoffmann, M. R. The Journal of Physical Chemistry **1994**, 98, 13669-13679.

(57) Abdi, F. F.; Savenije, T. J.; May, M. M.; Dam, B.; van de Krol, R. The Journal of Physical Chemistry Letters **2013**, 4, 2752-2757.

# Chapter 7: Concluding Remarks and Future Research

## Overview of Completed Work

This dissertation presented the results for numerous scientific studies of mixed metal oxides and electrocatalyst materials for use in solar energy conversion. Chapter 1 introduced the sustainable energy challenge and different methods of solar energy conversion including photovoltaic electricity generation and photo-electrochemical (PEC) water splitting. Various methods for improving the photo-conversion efficiency of PEC materials were discussed including nanostructuring, incorporation of additional elements or doping, and the application of electrocatalysts.

Chapter 2 presented a study in which reactive ballistic deposition (RBD) was used to synthesize nanostructured $BiVO_4$ films as photoanodes for the water oxidation reaction. Synthesis conditions were adjusted to optimize the PEC performance. $BiVO_4$ films deposited with excess vanadium (V/Bi=2) at incident angles of 65° showed IPCE values above 21% for light wavelengths of 340-460 nm (in 0.5 M $Na_2SO_4$ at 1.0 V vs. Ag/AgCl). The films were not completely stable and the photocurrent density dropped by 60-75% before reaching steady-state. The steady-state IPCE values were above 14% for 340-460 nm light. Chapter 3 explained efforts to improve the PEC performance of $BiVO_4$ further by incorporation of Mo and W using ballistic deposition (BD) in vacuum. Synthesis parameters such as the Bi:V:Mo:W atomic ratio and deposition angle were optimized and films synthesized with a Bi:V:Mo:W atomic ratio of 46:46:6:2 (6% Mo, 2% W) at an incident angle of 55° produced the highest photocurrent densities. These films achieved quantum efficiencies of 37% at 1.1 V vs. RHE and 50% at 1.6 V vs. RHE for 450 nm light when Pt was deposited on the surface as an electrocatalyst.

Chapter 4 described the screening of metals to incorporate into copper oxide and copper bismuth oxide as photocathodes for proton reduction. A dispenser and scanner

system ws used to create and screen Bi-M-Cu oxide arrays for cathodic photoactivity, where M represented 1 of 22 different transition and post-transition metals. Over 3,000 unique Bi:M:Cu atomic ratios were screened. Several photoactive M-Cu oxides and Bi-M-Cu oxides were identified with photocurrents that were 200% - 300% higher than CuO and 200% - 400% higher than $CuBi_2O_4$. Most notable was a Bi-Ag-Cu oxide (Bi:Ag:Cu atomic ratio of 22:3:11) which showed 4 times higher photocurrent than $CuBi_2O_4$. With Pt as an electrocatalyst, the Bi-Ag-Cu oxide evolved hydrogen under illumination in neutral electrolyte at 0.6 V vs. RHE.

Chapter 5 discussed the use of $W_2C$ as an electrocatalyst for p-type silicon (p-Si) for proton reduction or the hydrogen evolution reaction (HER). $W_2C$ thin films synthesized by RBD demonstrated catalytic activity for the HER and were an effective support for Pt nanoparticles allowing for a significant reduction in Pt loading. p-Si/$W_2C$/Pt photocathodes with Pt nanoparticles achieved photocurrent onset potentials and limiting photocurrent densities that were comparable to p-Si/Pt photocathodes a Pt loading that was nine times higher.

Chapter 6 described utilization of the array scanner and dispenser to screen new materials for dye-sensitized solar cells. 35 elements were investigated as single component metal oxides and as dopants for $TiO_2$ for use in DSCs. Several new DSC materials were identified including 6% In $TiO_2$, 6% Sn $TiO_2$, 6% Sb $TiO_2$, and 2% Cr, 6% Sb $TiO_2$ (metals basis). When co-incorporated, Cr and Sb showed a complimentary interaction, which reduced the resistance to charge transport in the DSC device and increased the short circuit current. The fill-factor for 2% Cr, 6% Sb $TiO_2$ was relatively low, but it showed a higher maximum power than $TiO_2$ due to the higher currents.

Each of the scientific studies described in this dissertation were successful in that a new synthesis technique was demonstrated and/or new photoactive materials were

identified. In some instances the new synthesis techniques and material combinations resulted in improvements in PEC performance. The materials were thoroughly assessed and characterized to futher understand their nanostructure, chemical composition, light absorption, charge transport properties, catalytic activity, and stability. Hopefully the results will be helpful to others conducting research in the field of photo-electrochemistry.

## ONGOING AND FUTURE WORK

In recent years, significant progress has been made in the development of PEC materials for water oxidation and proton reduction. Nanostructuring and electrocatalysts have been applied to $\alpha$-$Fe_2O_3$ to obtain a photocurrent density of ~3 mA/cm$^2$ under AM 1.5.[1] Incorporation of Mo and W into $BiVO_4$ along with various electrocatalyst has produced IPCE above 50% corresponding to photocurrent densities above 2 mA/cm$^2$ when integrated over AM 1.5.[2-4] These are good achievements; however, the photocurrent densities remain well below the predicted maximum values of ~12.5 and ~7.5 mA/cm$^2$ for $\alpha$-$Fe_2O_3$ and $BiVO_4$, respectively.[5]

One problem with fractal and nanorod morphology of metal oxide photoelectrodes is that the nanostructure is usually composed entirely of the metal oxide. Thus, the majority carriers (electrons for photoanodes) still need to traverse the entire length of the metal oxide nanostructure, which is typically much longer than the electron diffusion length. This can result in charge carrier recombination. A more methodical approach would involve coating a metal oxide shell around a highly conductive core or scaffold as shown in Figure 7.1. This may allow for improved charge transport of both the majority and minority carriers. There are relatively few publications related to highly conductive, nanosctructured scaffolds. Recently $\alpha$-$Fe_2O_3$ was coated onto $TiSi_2$ nanonets

for PEC water oxidation.[6] α-$Fe_2O_3$ was also deposited onto conducting Nb doped $SnO_2$ on top of a $TiO_2$ scaffold.[7] Perhaps further improvements can be achieved using a well-defined conducting scaffold – metal oxide photoanode with a greater overall surface area and various combinations of metal oxides ($TiO_2$, $Fe_2O_3$, $WO_3$, $BiVO_4$, etc.).

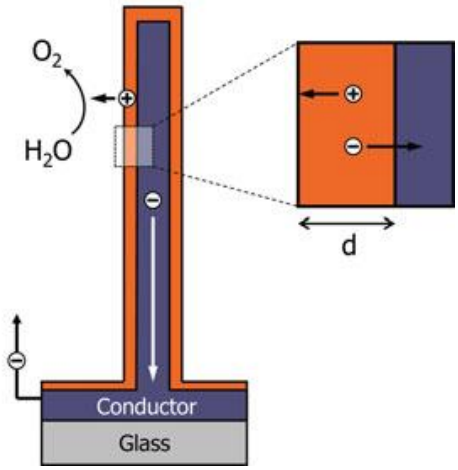


Figure 7.1 Schematic of a metal oxide shell around a highly conductive shell or core.[8] The nanorods shorten the travel distance of photo-generated holes (+) in the radial direction and electrons (-) in the co-axial direction while still allowing for adequate light absorption in the co-axial direction.

The lack of earth abundant and long lasting electrocataysts for PEC materials is also a problem and a more thorough understanding of the interactions between electrocatalysts and absorber materials is needed. In chapter 5 it was shown $W_2C$ deposited onto p-Si is an effective support for Pt nanoparticles for improving the photocurrent onset potential, but the exact reaction mechanism leading to the improvement has not yet been fully characterized and understood. Other earth abundant materials should be explored as electrocatalysts for PEC materials as well. Ni-Mo is a well-known electrocatalyst for HER, which has been tested on p-Si for PEC proton reduction.[9-11] Perhaps there are Ni-Mo-M combinations (where M represents a third

transition metal) that posess lower overpotentials and better stability than Ni-Mo. We are currently collaborating with Fosdick and Crooks to screen Ni-Mo-M combinations for the HER using bipolar electrode arrays.[12]

## REFERENCES


(1) Tilley, S. D.; Cornuz, M.; Sivula, K.; Grätzel, M. Angewandte Chemie International Edition 2010, 49, 6405-6408.

(2) Pilli, S. K.; Furtak, T. E.; Brown, L. D.; Deutsch, T. G.; Turner, J. A.; Herring, A. M. Energy & Environmental Science 2011, 4, 5028-5034.

(3) Berglund, S. P.; Rettie, A. J. E.; Hoang, S.; Mullins, C. B. Physical Chemistry Chemical Physics 2012, 14, 7065-7075.

(4) Abdi, F. F.; Firet, N.; van de Krol, R. Chemcatchem 2013, 5, 490-496.

(5) Chen, Z. B.; Jaramillo, T. F.; Deutsch, T. G.; Kleiman-Shwarsctein, A.; Forman, A. J.; Gaillard, N.; Garland, R.; Takanabe, K.; Heske, C.; Sunkara, M.; McFarland, E. W.; Domen, K.; Miller, E. L.; Turner, J. A.; Dinh, H. N. Journal of Materials Research 2010, 25, 3-16.

(6) Lin, Y.; Zhou, S.; Sheehan, S. W.; Wang, D. Journal of the American Chemical Society 2011, 133, 2398-2401.

(7) Stefik, M.; Cornuz, M.; Mathews, N.; Hisatomi, T.; Mhaisalkar, S.; Grätzel, M. Nano Letters 2012, 12, 5431-5435.

(8) van de Krol, R.; Grätzel, M. Photoelectrochemical Hydrogen Production; Springer: New York Dordrecht Heidelberg London, 2012.

(9) Raj, I. A. Journal of Materials Science 1993, 28, 4375-4382.

(10) Fan, C.; Piron, D. L.; Paradis, P. Electrochimica Acta 1994, 39, 2715-2722.

(11) McKone, J. R.; Warren, E. L.; Bierman, M. J.; Boettcher, S. W.; Brunschwig, B. S.; Lewis, N. S.; Gray, H. B. *Energy & Environmental Science* **2011**, *4*, 3573-3583.

(12) Fosdick, S. E.; Berglund, S. P.; Mullins, C. B.; Crooks, R. M. Analytical Chemistry 2013, 85, 2493-249

# Appendix A: Supplemental Information for Photoelectrochemical Oxidation of Water Using Nanostructured $BiVO_4$ Films

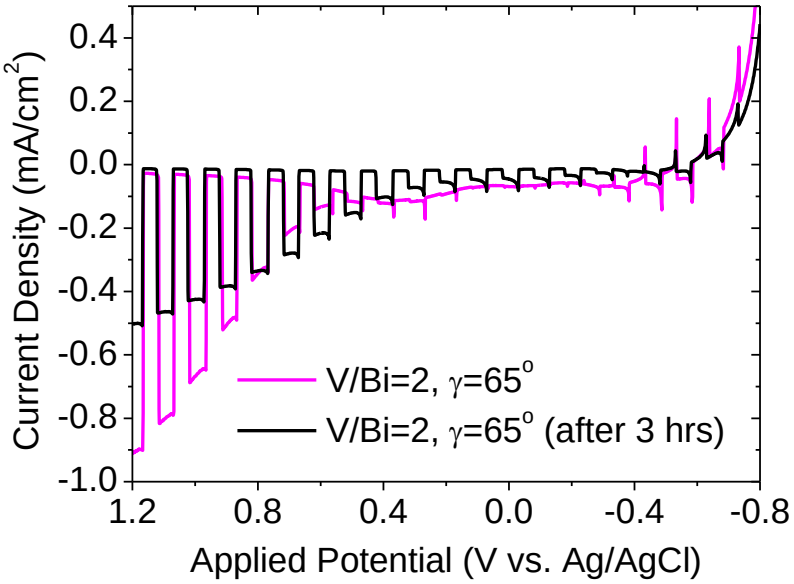


Figure A.1. Chopped (dark and white light) LSV scans for a $BiVO_4$ film synthesized by RBD (V/Bi=2, $\gamma$=65°, thickness=0.5 μm) in 0.5 M $Na_2SO_4$. The film was measured initially (magenta) and after illumination for 3 hours at a constant potential of 1.0 V vs. Ag/AgCl (black). The scan rate was 0.025 V/s.

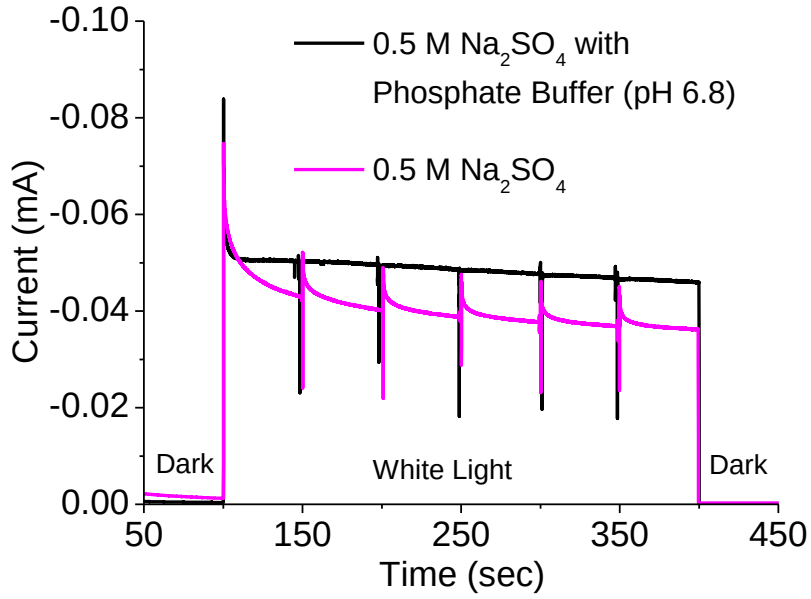


Figure A.2. Amperometric i-t curve for a $BiVO_4$ film synthesized by RBD (V/Bi=2, $\gamma$=65°, thickness=0.5 μm) in 0.5 M $Na_2SO_4$ (magenta) and 0.5 M $Na_2SO_4$ with 0.5 M phosphate buffer solution (pH 6.8) (black) at a constant applied potential of 1.0 V vs. Ag/AgCl. During white light illumination the film was flushed with fresh electrolyte every 50 seconds causing the spikes in photocurrent. For non-buffered 0.5 M $Na_2SO_4$ local pH changes near the film surface caused by the water oxidation reaction resulted in gradual photocurrent decay after each flush.

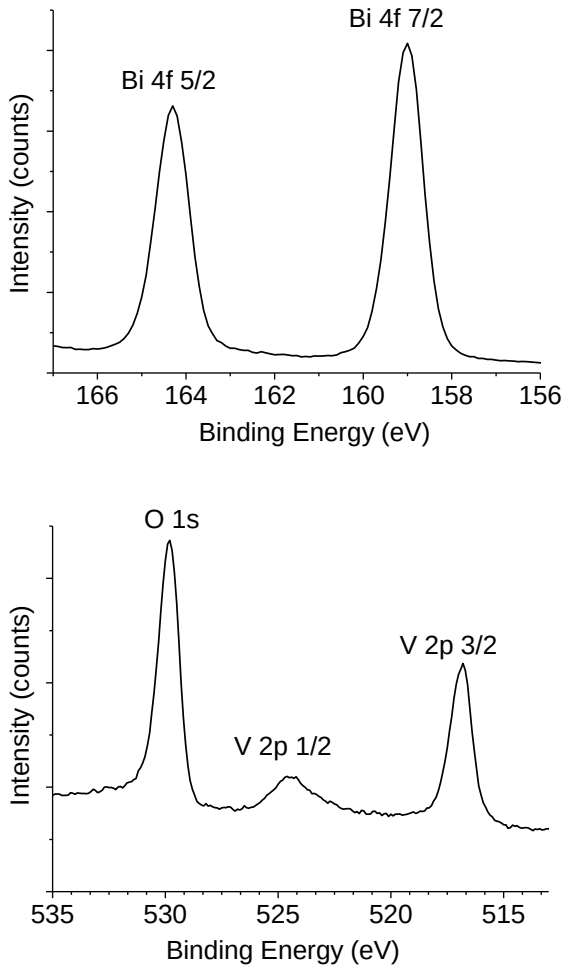


Figure A.3. XPS spectra for $BiVO_4$ film synthesized by RBD (V/Bi=2, $\gamma$=65°, thickness=0.5 μm) obtained before PEC testing. Binding energies of 159.0 eV for Bi 4f 7/2, 516.8 eV for V 2p 3/2, and 529.8 eV for O 1s imply oxidation states of $Bi^{3+}$, $V^{5+}$, and $O^{2-}$.

| Film Deposition Parameters and Surface Treatments | Ion Concentrations (ppb) in Unused Electrolyte | | Ion Concentrations (ppb) in Used Electrolyte (3 hrs of illumination at 1.0V vs. Ag/AgCl) | |
|---|---|---|---|---|
| | Bi | V | Bi | V |
| V/Bi=2, $\gamma=65^{o}$ | 0.1 | 1.2 | 0.3 | 247 |
| V/Bi=1, $\gamma=65^{o}$ (Co surface) | 0.4 | 0.9 | 0.4 | 0.9 |

Table A.1. ICP-MS results for electrolyte solutions used with two different $BiVO_4$ films synthesized by RBD. A batch of 0.1 M $Na_2SO_4$ was prepared for each film and measured to obtain the ion concentrations in unused electrolyte. About 25 mL of each 0.1 M $Na_2SO_4$ solution was used for PEC testing (over 3 hours of illumination at constant applied bias of 1.0 V vs. Ag/AgCl) and measured to obtain the ion concentrations in used electrolyte. All values were below the detection limits of the ICP-MS system except for the V concentration in used electrolyte from the V/Bi=2 film.

# Appendix B: Supplemental Information for Incorporation of Mo and W into Nanostructured $BiVO_4$ Films for Efficient Photoelectrochemical Water Oxidation

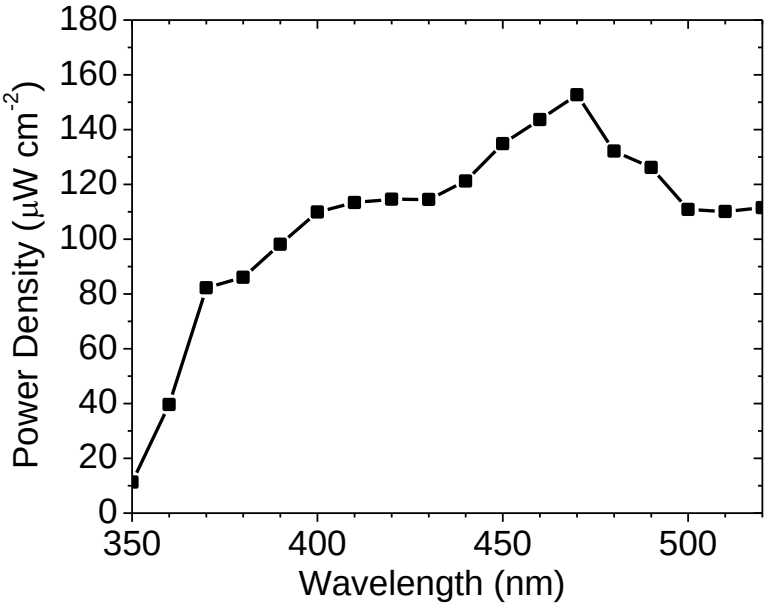


Figure B.1. Typical power density spectrum for light that was incident on the film during IPCE measurements. The power was measured using a UV enhanced silicon photo-detector.

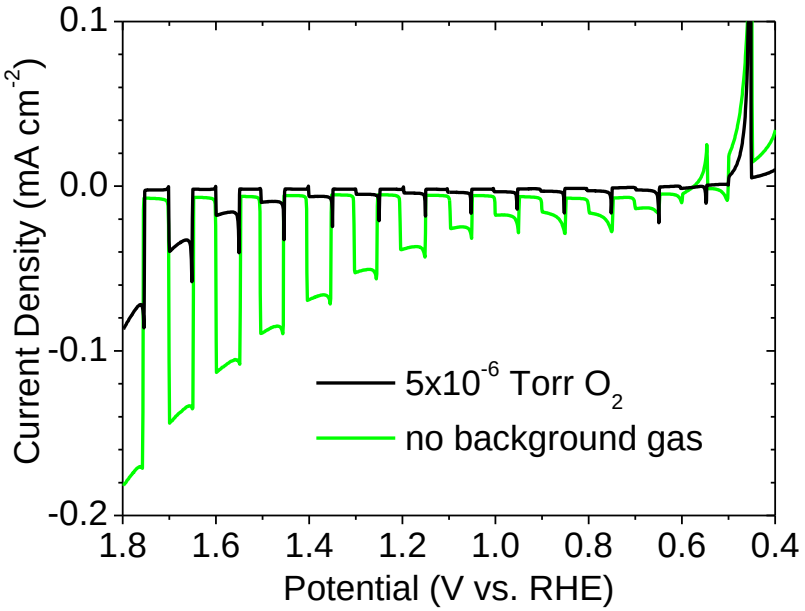


Figure B.2. Chopped (dark and white light) LSV scans for $BiVO_4$ films deposited in vacuum with no background gas and with $5x10^{-6}$ Torr of $O_2$. After deposition both films were annealed in air at 500°C in for 2 hours. Measurements were conducted in mixture of 0.1 M $Na_2SO_4$ and 0.1 M phosphate buffer solution (pH 6.8) with a scan rate of 0.025 V $s^{-1}$.

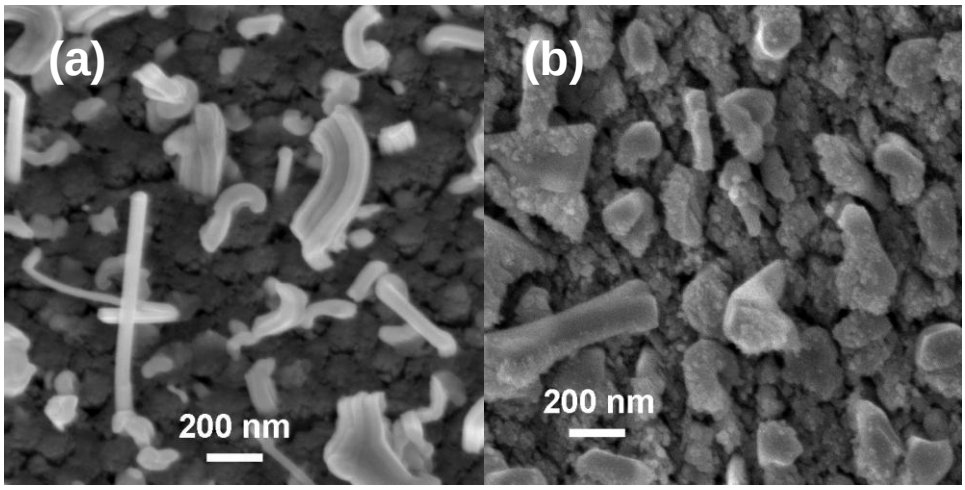


Figure B.3. SEM images of films with a Bi:V:Mo:W atomic ratio of 50:50:0:0 deposited at $\gamma=55^{o}$ (a) in vacuum with no background gas and (b) with $5x10^{-6}$ Torr of $O_2$. The films have not been annealed.

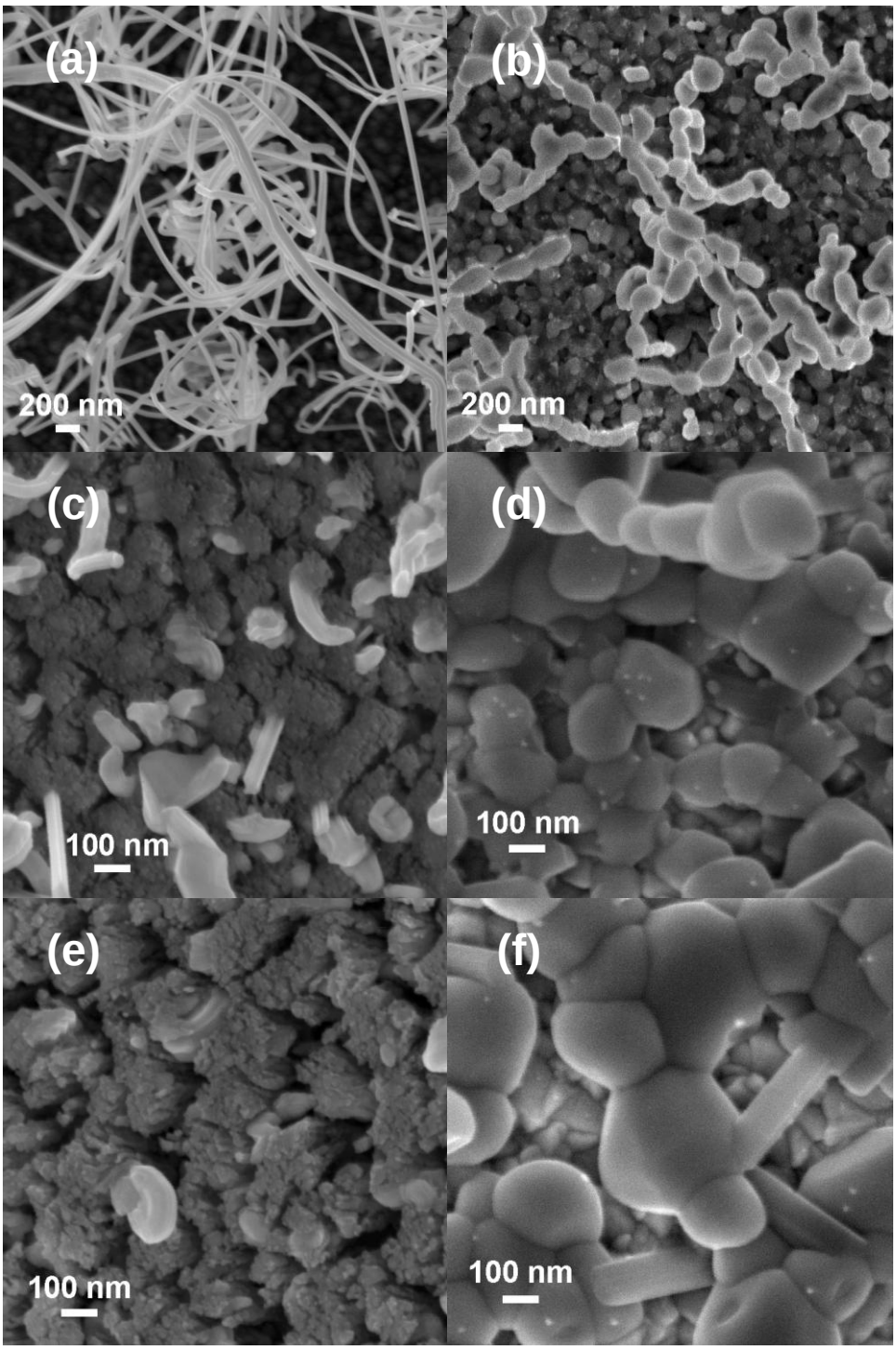
(a)
200 nm
(b)
200 nm
(c)
100 nm
(d)
100 nm
(e)
100 nm
(f)
100 nm

Figure B.4. SEM images of films with Bi:V:Mo:W atomic ratios of 46:46:6:2 deposited in vacuum at different deposition angles (γ) taken before and after annealing in air at 500 °C for 2 hours: (a) γ=0°, before annealing (b) γ=0°, after annealing (c) γ=55°, before annealing (d) γ=55°, after annealing (e) γ=75°, before annealing (f) γ=75°, after annealing.

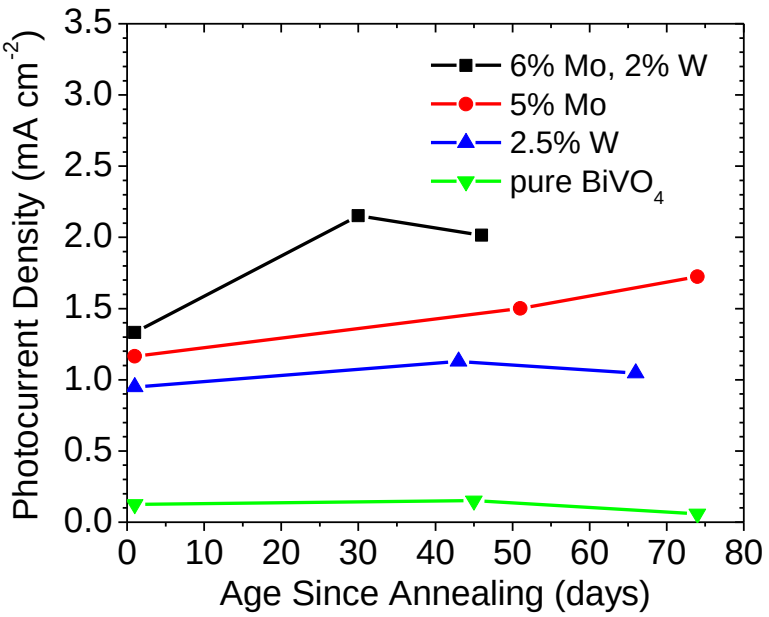


Figure B.5. Trends showing improvement in photocurrent density with age since annealing for $BiVO_4$ films with varying atomic percentages of Mo and W (relative to the total Bi, V, Mo, and W). The photocurrent density values were taken from LSV scans (value at 1.6 V vs. RHE) in 0.1 M $Na_2SO_4$ and 0.1 M phosphate buffer solution (pH 6.8) with a scan rate of 0.025 V $s^{-1}$. Between measurements the films were simply left in plastic container in the laboratory at normal atmospheric conditions.

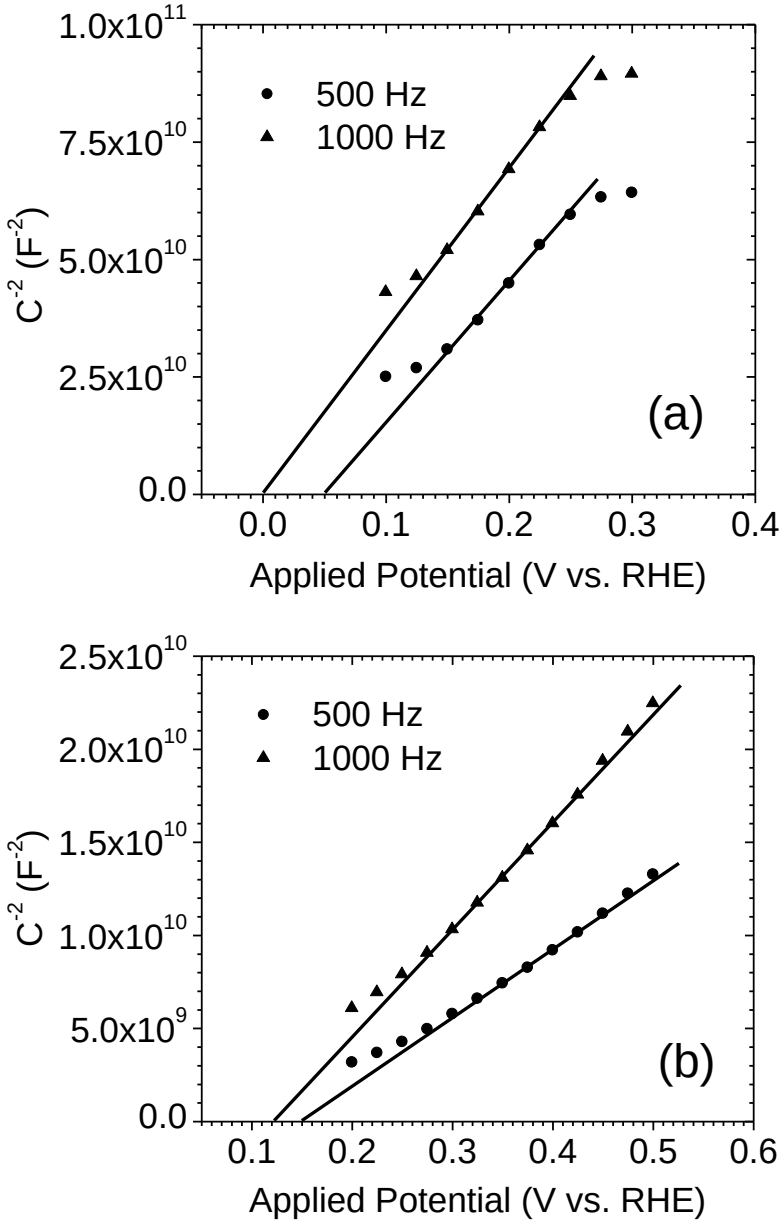


Figure B.6. Mott-Schottky plot for (a) pure $BiVO_4$ and (b) 6% Mo, 2% W $BiVO_4$ films conducted in 0.1 M $Na_2SO_4$ and 0.1 M phosphate buffer solution (pH 6.8).

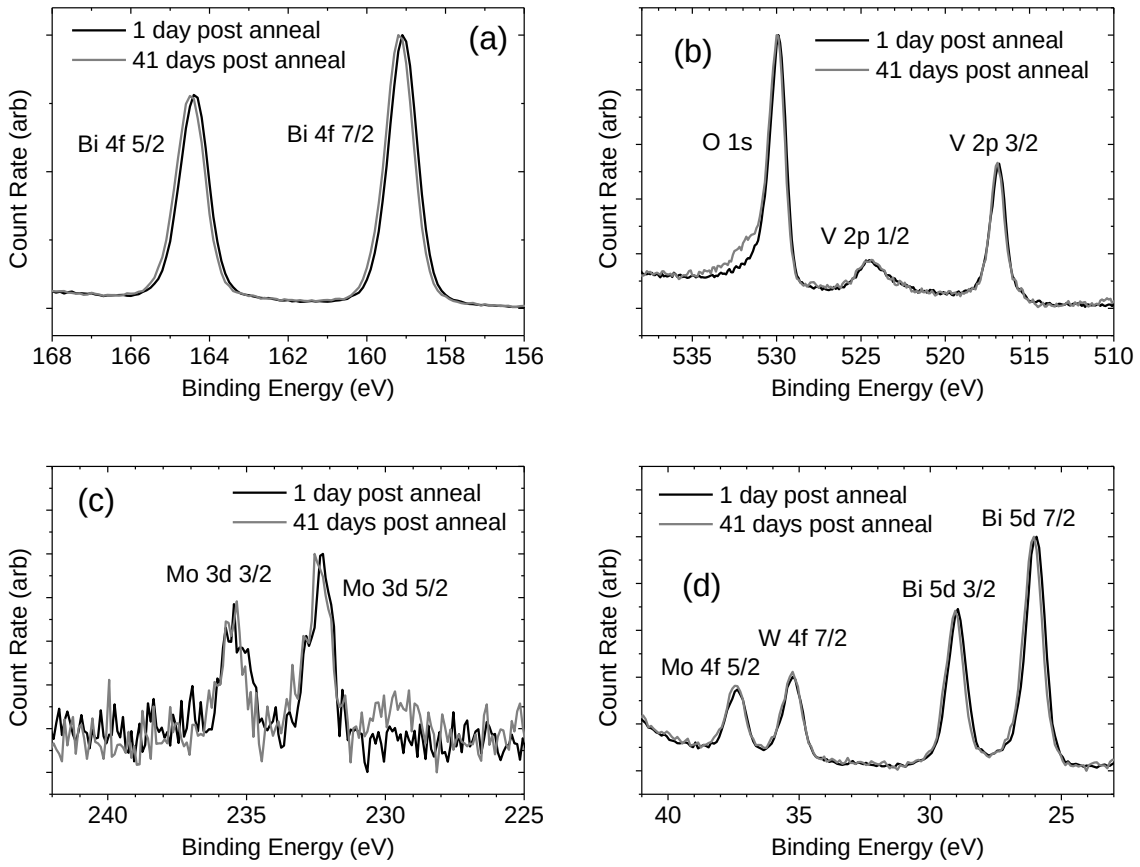


Figure B.7. XPS spectra for a single 6% Mo, 2% W $BiVO_4$ film taken 1 day and 41 days after annealing.

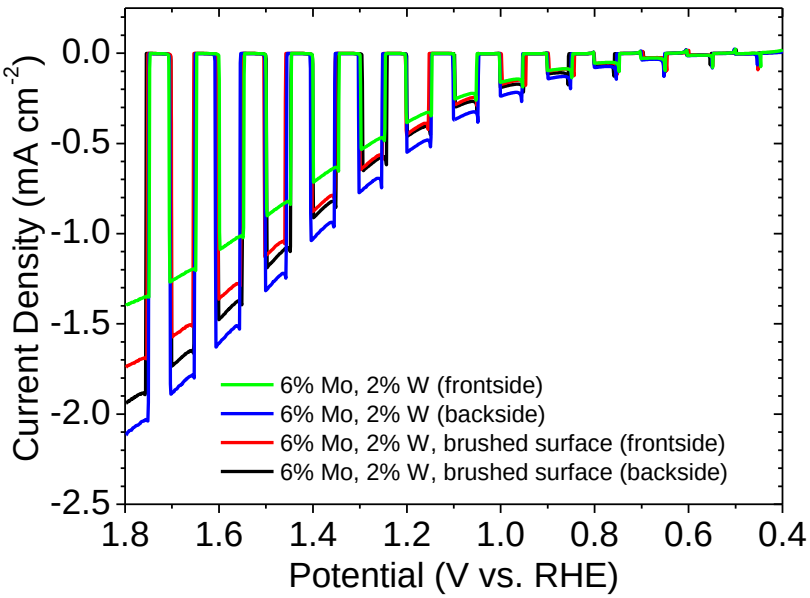


Figure B.8. Chopped (dark and white light) LSV scans for a 6% Mo, 2% W $BiVO_4$ film before brushing the film surface (frontside and backside illumination) and after brushing the film surface and rinsing it with de-mineralized water to remove irregular surface structures (frontside and backside illumination). Measurements were conducted in mixture of 0.1 M $Na_2SO_4$ and 0.1 M phosphate buffer solution (pH 6.8) with a scan rate of 0.025 V $s^{-1}$.

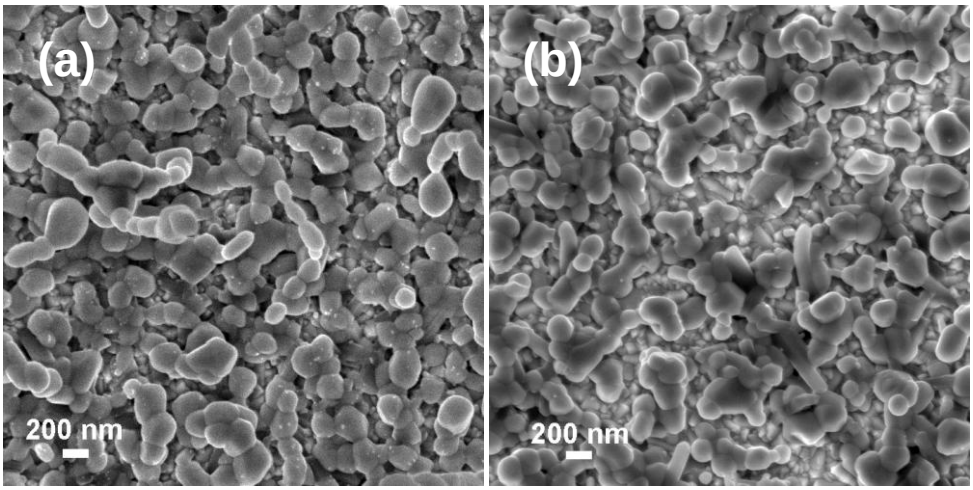


Figure B.9. Top view SEM images of a 6% Mo, 2% W BiVO4 film (a) before brushing the film surface and (b) after brushing the film surface and rinsing it with de-mineralized water.

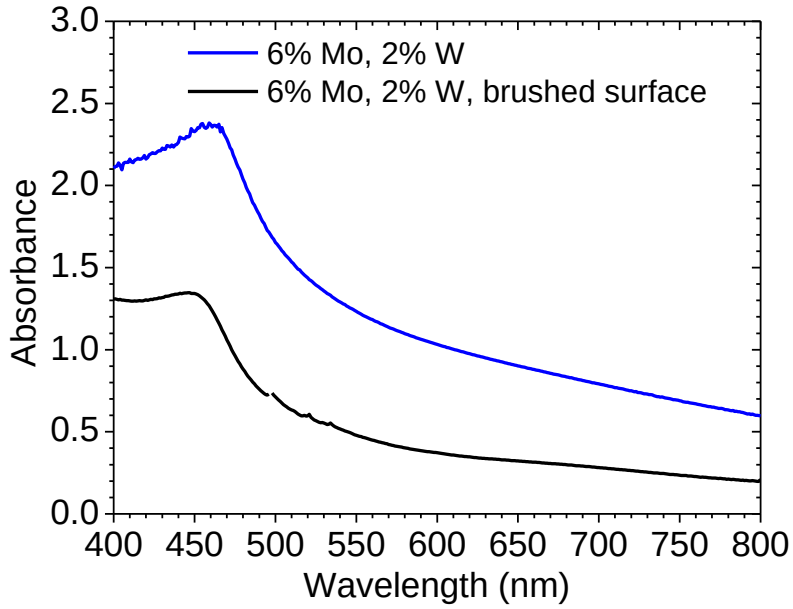


Figure B.10. UV-Vis absorbance spectrum for a 6% Mo, 2% W $BiVO_4$ film taken before and after brushing the film surface and rinsing it with de-mineralized water. The measurements were taken using a Cary 5000 spectrophotometer in transmission mode so any diffusely scattered light contributed to the measured absorbance.

# Appendix C: Supplementary Information for Screening of Transition and Post-Transition Metals to Incorporate Into Copper Oxide and Copper Bismuth Oxide for Photoelectrochemical Hydrogen Evolution

## CHEMICALS

The following metal salts and chlorides were used to make arrays and films:

$AgNO_3$ (ACROS, p.a.)
$Cu(NO_3)_2 \cdot xH_2O$ (Alfa Aesar, 99.999%)
$Cd(NO_3)_2 \cdot 4H_2O$ (Alfa Aesar, 99.999%)
$Zn(NO_3)_2 \cdot xH_2O$ (Sigma-Aldrich, 99.999%)
$Al(NO_3)_3 \cdot xH_2O$ (Alfa Aesar, 99.999%)
$Ga(NO_3)_3 \cdot xH_2O$ (Alfa Aesar, 99.999%)
$In(NO_3)_3 \cdot xH_2O$ (Alfa Aesar, 99.999%)
$La(NO_3)_2 \cdot 6H_2O$ (Alfa Aesar, 99.999%)
$Ga(NO_3)_3 \cdot xH_2O$ (Alfa Aesar, 99.99%)
$Y(NO_3)_3 \cdot xH_2O$ (Alfa Aesar, 99.99%)
$Bi(NO_3)_3 \cdot xH_2O$ (Alfa Aesar, 99.999%)
$SnCl_4 \cdot xH_2O$ (Alfa Aesar, 98%)
$TiCl_4$ (Alfa Aesar, 99.99%)
$ZrCl_4$ (Alfa Aesar, 99.5+%)
$NbCl_5$ (Sigma-Adrich, 99.995%)
$TaCl_5$ (Alfa Aesar 99.99%)
$VCl_3$ (Sigma Aldrich, 97%)
$Cr(NO_3)_3 \cdot xH_2O$ (Alfa Aesar, 99.999%)
$(NH_4)_6Mo_7O_{24} \cdot 4H_2O$ (Sigma-Aldrich, 99.98%)
$(NH_4)_{10}W_{12}O_{41} \cdot 5H_2O$ (Sigma-Aldrich, 99.99%)
$Mn(NO_3)_2 \cdot xH_2O$ (Alfa Aesar, 99.999%)
$Co(NO_3)_2 \cdot 6H_2O$ (Alfa Aesar, 99.999%)
$Fe(NO_3)_3 \cdot 9H_2O$ (Sigma Aldrich, 99.999%)
$N_2NiO_6 \cdot 6H_2O$ (Alfa Aesar, 99.9985%)

## ADDITIONAL FIGURES

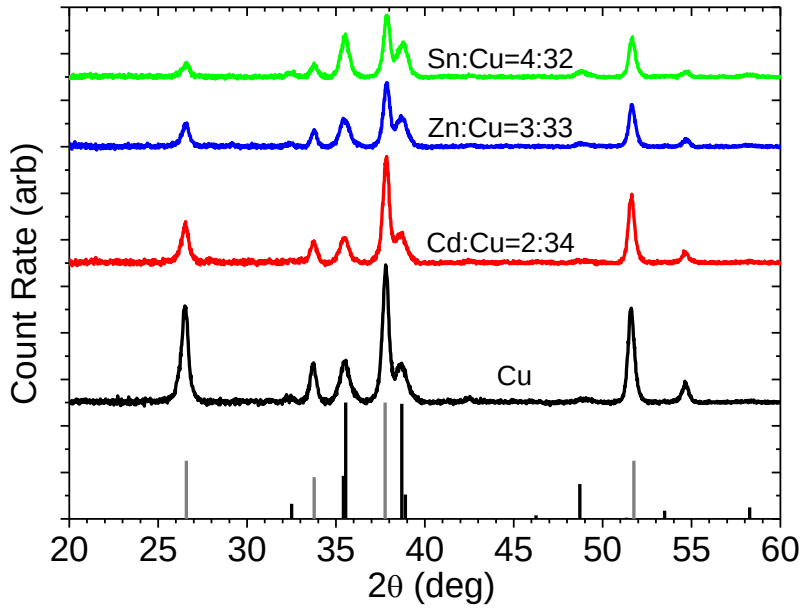


Figure C.1. XRD spectra for Cu oxide and M-Cu oxide films synthesized by drop-cast with atomic ratios of Cd:Cu=2:34, Zn:Cu=3:33, and Sn:Cu=4:32. Grey vertical lines (|) represent the cassiterite, $SnO_2$ reference pattern (PDF# 00-042-0334). Black vertical lines (|) represent the CuO reference pattern (PDF#00-048-1548).

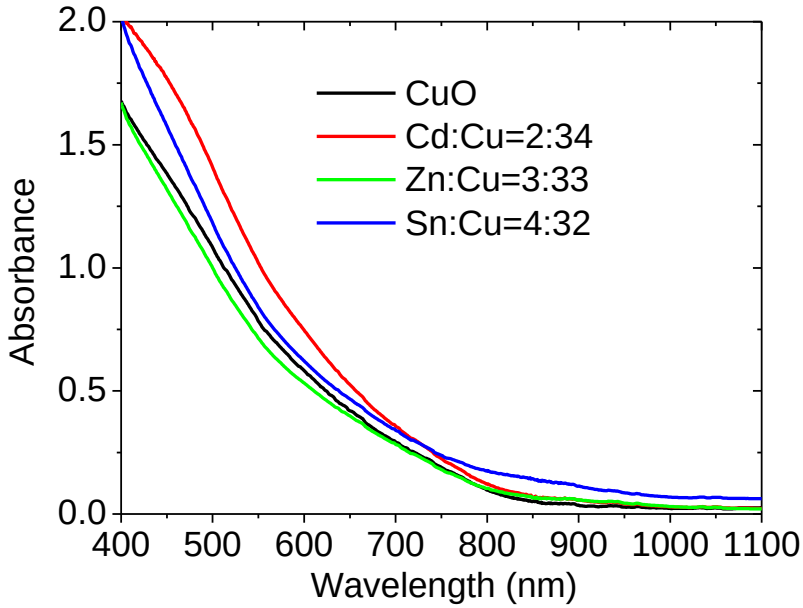


Figure C.2. UV-Vis absorbance spectra for CuO and M-Cu oxide films with atomic ratios of Cd:Cu=2:34, Zn:Cu=3:33, and Sn:Cu=4:32.

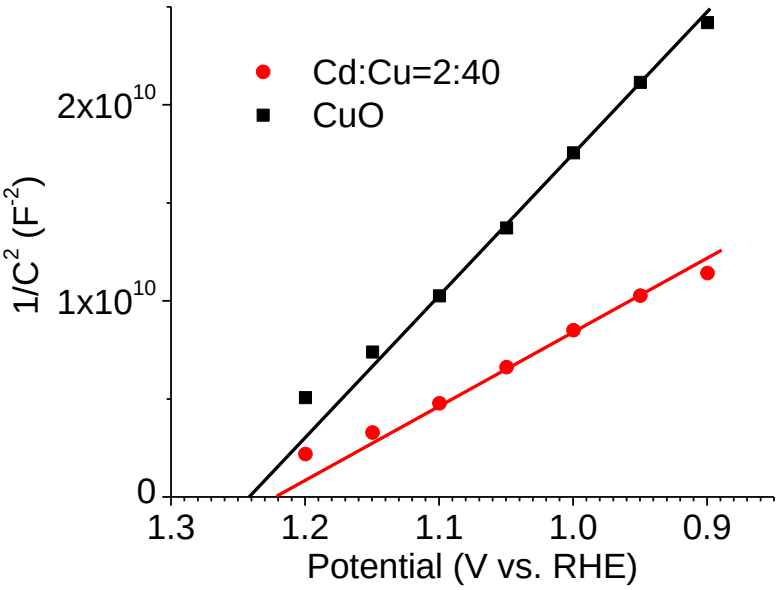


Figure C.3. Mott-Schottky plot for CuO and Cd:Cu=2:34 oxide films. Measurements were conducted in 0.1 M $Na_2SO_4$ and 0.1 M phosphate buffer (pH 6.8) using a frequency of 1000 Hz.

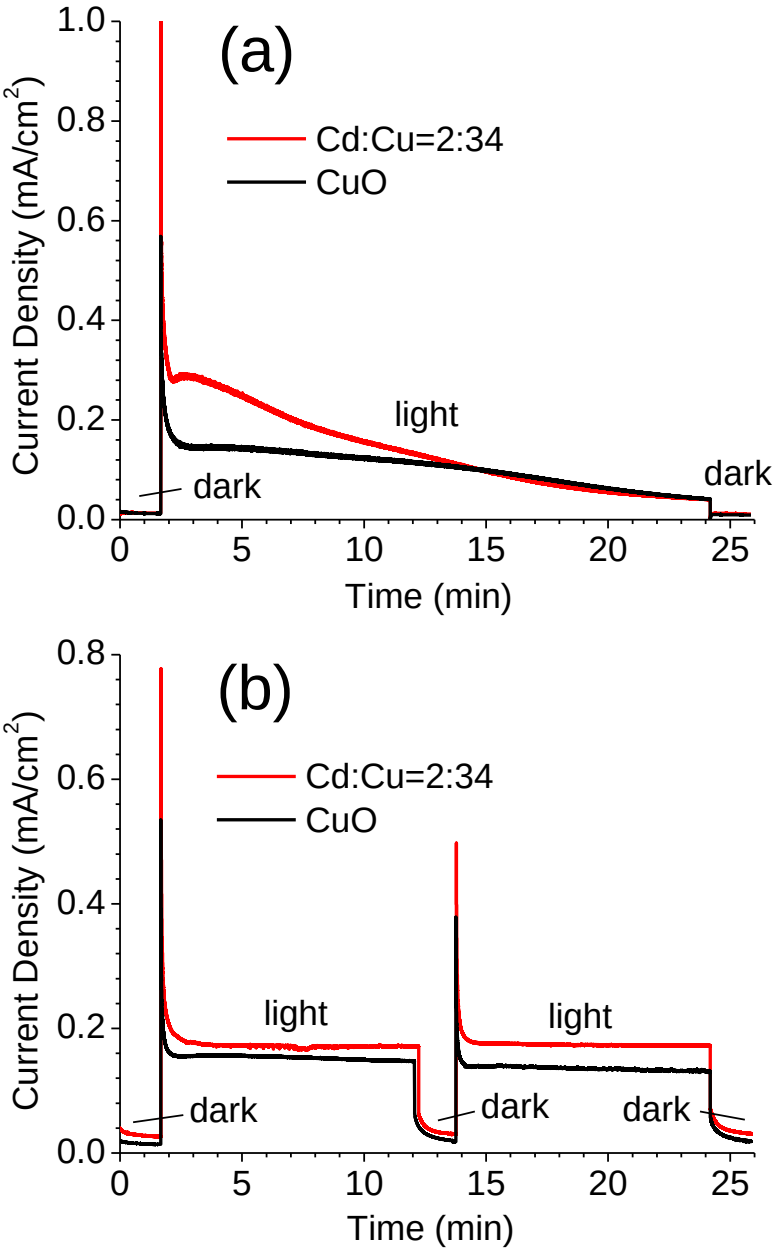


Figure C.4. Amperometric i-t measurement for CuO and Cd:Cu=2:34 oxide films. Measurements were done in (a) 0.1 M $Na_2SO_4$ and 0.1 M phosphate buffer solution (pH 6.8) at 0.6 V vs. RHE and (b) 10 mM $I_2$, 50 mM NaI in acetonitrile at 0.2 V vs. NHE. The films were illuminated from the backside with 100 mW/cm$^2$.

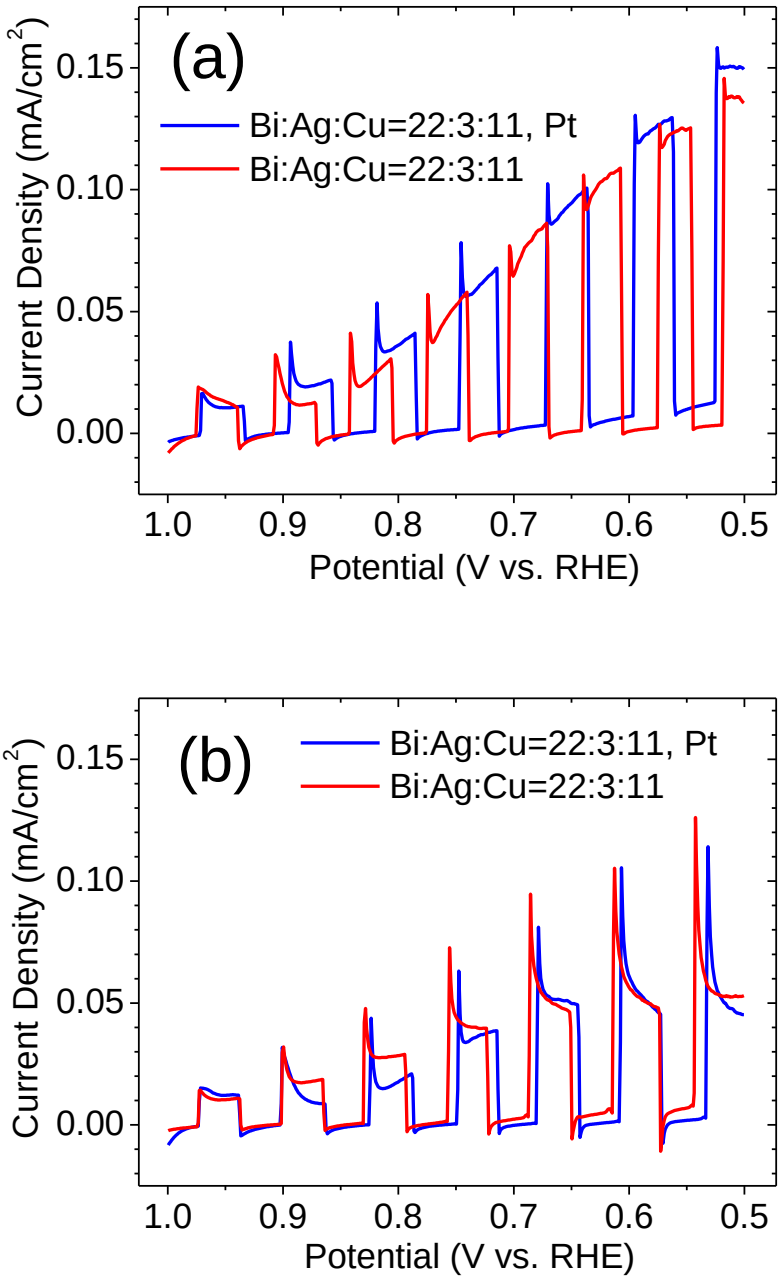


Figure C.5. Chopped (dark/light) LSV scans for Bi:Ag:Cu=22:3:11 oxide films as synthesized by drop-cast and after depositing Pt on the surface. Measurements were done in 0.1 M $Na_2SO_4$ and 0.1 M phosphate buffer (pH 6.8) using backside illumination (100 mW/cm$^2$) and a scan rate of 0.025 V/s. The electrolyte was used (a) as prepared and (b) after purging with $N_2$ for 30 minute prior to the measurements.

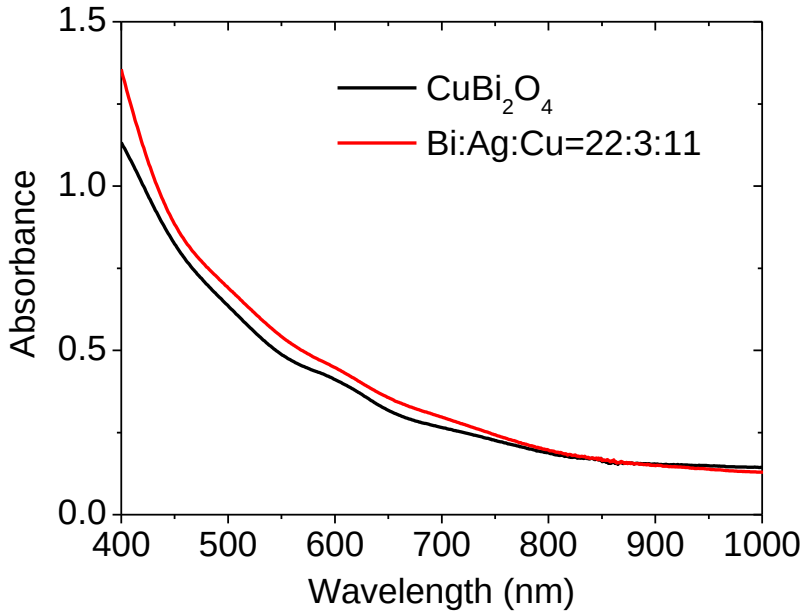


Figure C.6. UV-Vis absorbance spectra for CuO and Bi:Ag:Cu=22:3:11 oxide films.

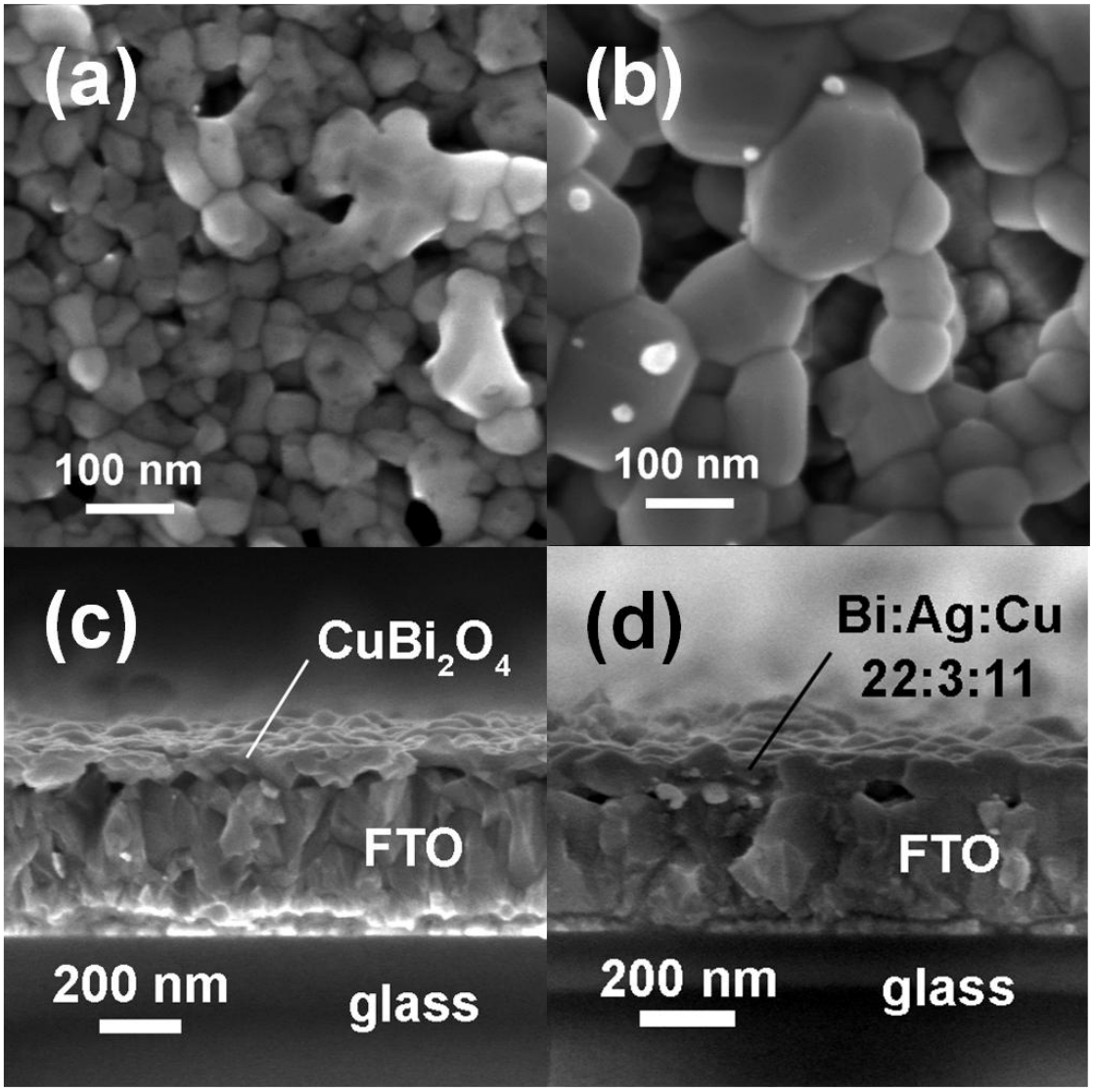


Figure C.7. SEM images of films synthesized by drop-cast. On the left are (a) top-view and (c) cross section view images of a $CuBi_2O_4$ film. On the right are (b) top view and (d) cross-section images of a Bi:Ag:Cu=22:3:11 oxide film.

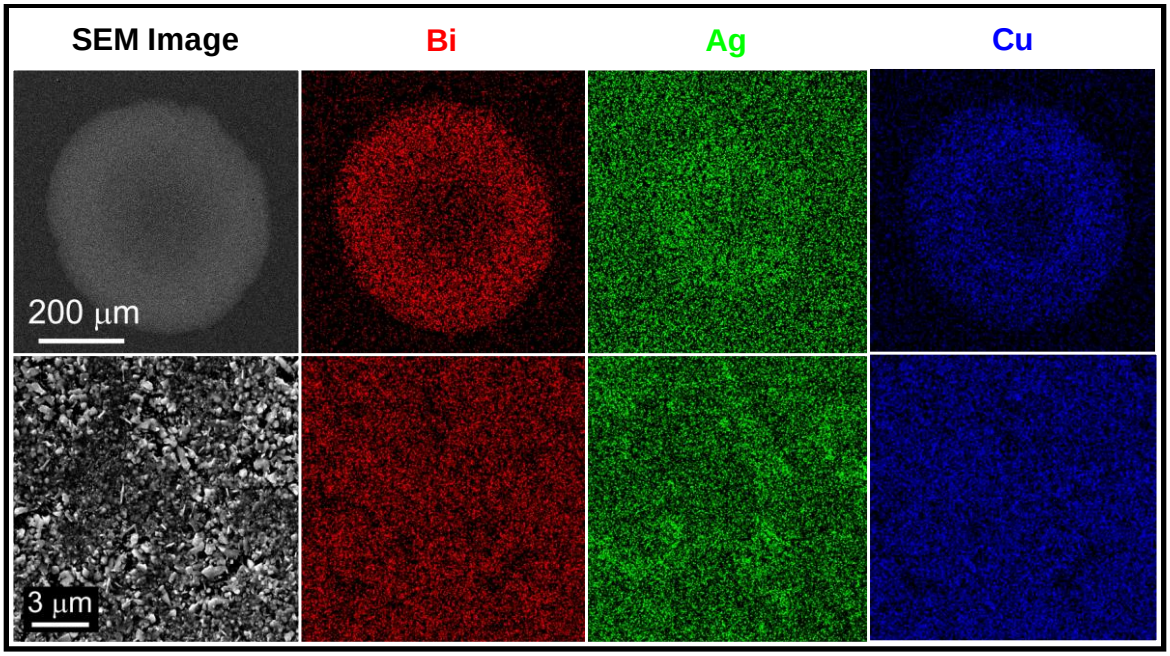


Figure C.8. EDS mapping data for a Bi:Ag:Cu=22:3:11 spot on a fine detail Bi-Ag-Cu array. The top row shows mapping data for the entire spot and the bottom row shows data for a smaller area near the centre of the spot. Ag mapping data shows up on the FTO substrate around the spot due to overlap in signal from the Ag L series (2.983 keV) and the Sn L series (3.444 keV) peaks.

| Array Pattern | Total Number of Drops | Expected Atomic Ratio | EDS Measured Atomic Ratio |
|---|---|---|---|
| Initial 19 x 19 | 18 | Bi:Cu = 12:6 | Bi:Cu = 12.8:5.2 |
| Fine Detail | 36 | Bi:Cu = 24:12 | Bi:Cu = 24.1:11.9 |
| Fine Detail | 36 | Bi:Ag:Cu = 22:3:11 | Bi:Ag:Cu = 22.6:1.8:11.5 |

Table C.1. EDS quantification results for various array spots. The expected atomic ratios are based on the number of drops dispensed for the array pattern (Figures 3 and 11). The EDS measured atomic ratios were calculated by averaging three different locations per spot. The voltage setting was 20 keV and the following peaks were used for quantification: Bi K series (10.839 keV), Ag L series (2.983 keV), Cu K series (8.046 keV), Sn L series (3.444 keV), and O K series (0.525 keV). There was significant overlap in the signal from the Ag and Sn peaks near 3 keV resulting in error for Ag quantification.

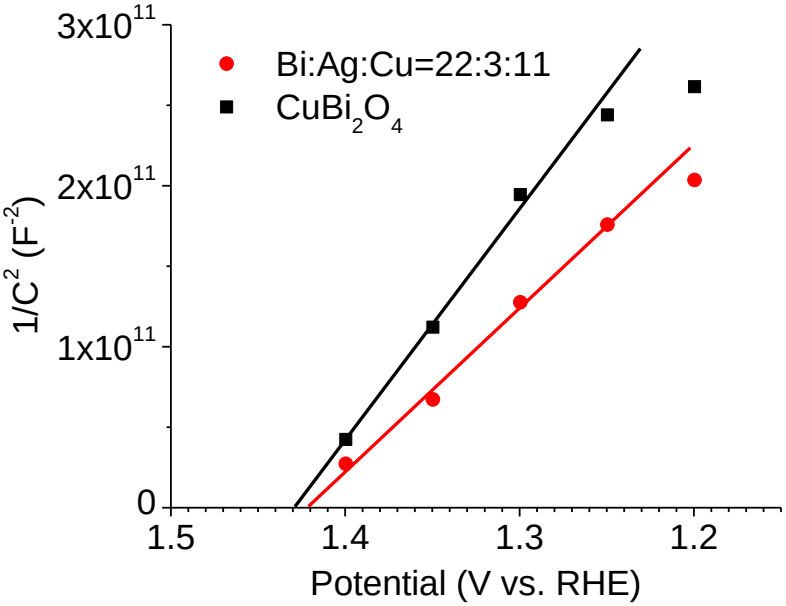


Figure C.9. Mott-Schottky plot for $CuBi_2O_4$ and Bi:Ag:Cu=22:3:11 oxide films. Measurements were conducted in 0.1 M $Na_2SO_4$ and 0.1 M phosphate buffer (pH 6.8) using a frequency of 1000 Hz.

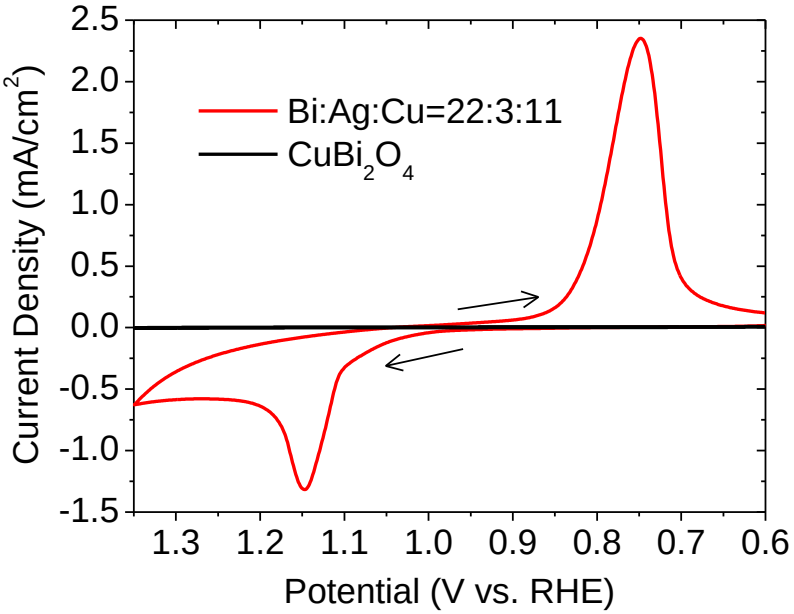


Figure C.10. CV measurements of $CuBi_2O_4$ and Bi:Ag:Cu=22:3:11 oxide films. Measurements were done in 0.1 M $Na_2SO_4$ and 0.1 M phosphate buffer (pH 6.8) with a scan rate of 0.05 V/s.

# Appendix D: Supplemental Information for p-Si/$W_2C$ and p-Si/$W_2C$/Pt Photocathodes for the Hydrogen Evolution Reaction

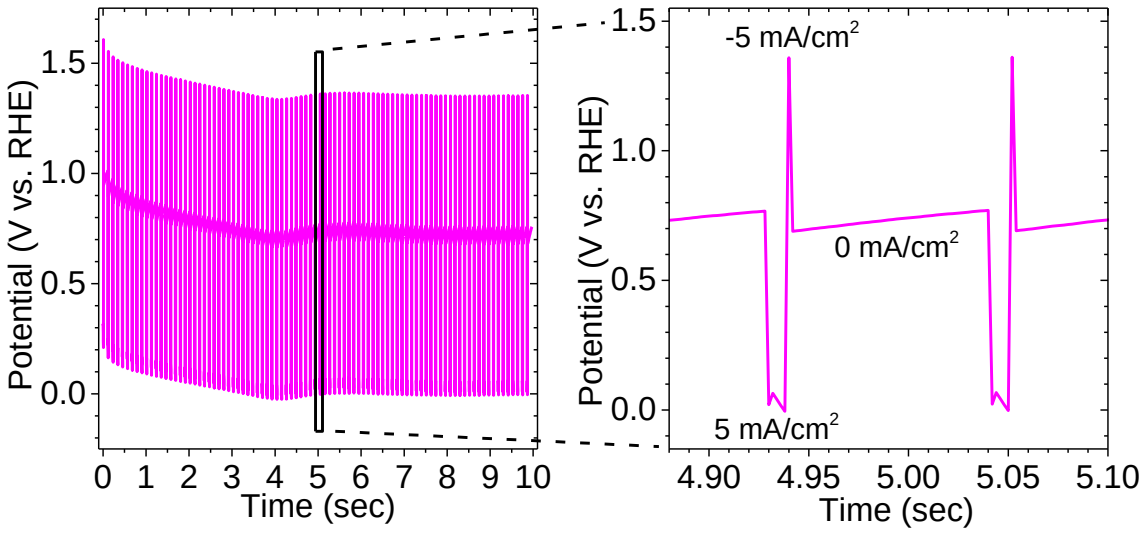


Figure D.1. Example of current controlled pulsed deposition sequence used to deposit Pt nanoparticles onto a p-Si/$W_2C$ photocathode in a solution of 1g/L $H_2PtCl_6 \cdot 6H_2O$ under illumination. The pulse sequence was 5 mA/cm$^2$ cathodic current for 10 ms followed by 5 mA/cm$^2$ anodic current for 2 ms followed by zero current for 100 ms. The sequence was repeated for a total deposition time of 10 sec.

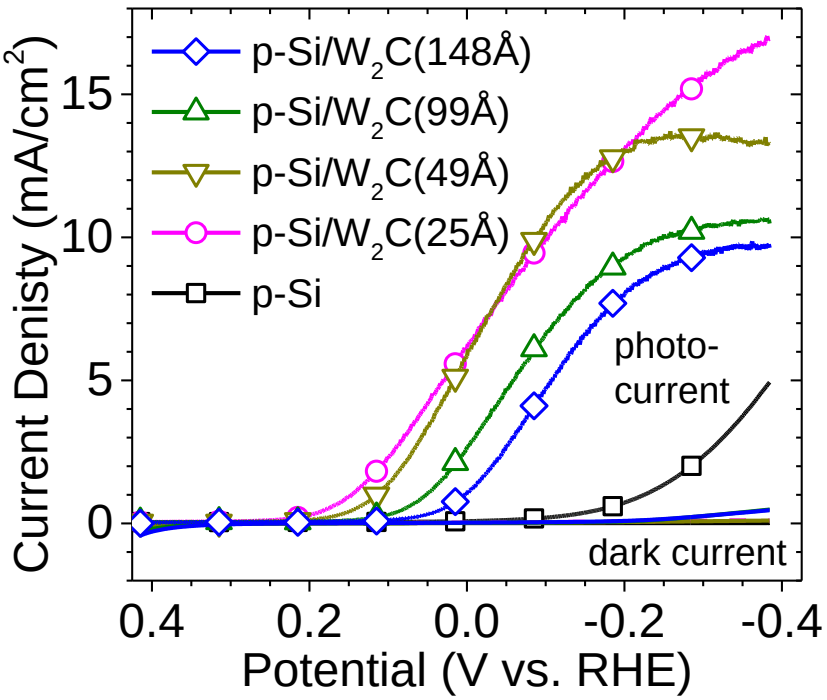


Figure D.2. LSV scans (dark and white light) for p-Si and p-Si/$W_2C$ photocathodes with $W_2C$ thicknesses of 25, 49, 99, and 148 Å as indicated in the figure legend. The photocathodes were not annealed. Measurements were conducted in $N_2$ purged 1 N $H_2SO_4$ using a scan rate of 25 mV/s and white light intensity of 100 mW/cm$^2$.

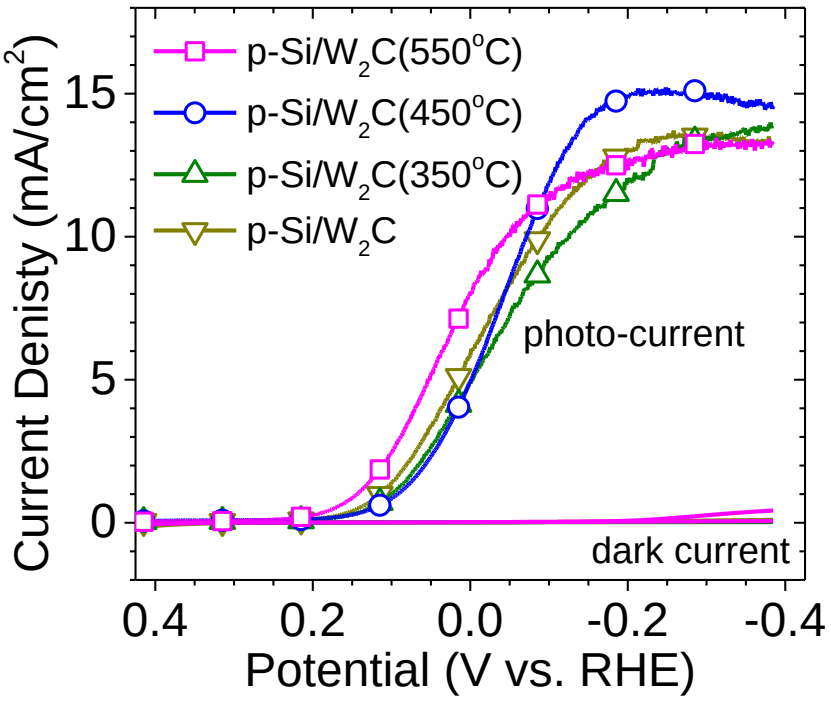


Figure D.3. LSV scans (dark and white light) for p-Si/$W_2C$ photocathodes as deposited and annealed under Ar flow at 350, 450, or 550 °C for 2 hrs as indicated by the figure legend. The photocathodes had a $W_2C$ thickness of 49 Å. Measurements were conducted in $N_2$ purged 1 N $H_2SO_4$ using a scan rate of 25 mV/s and white light intensity of 100 mW/cm$^2$.

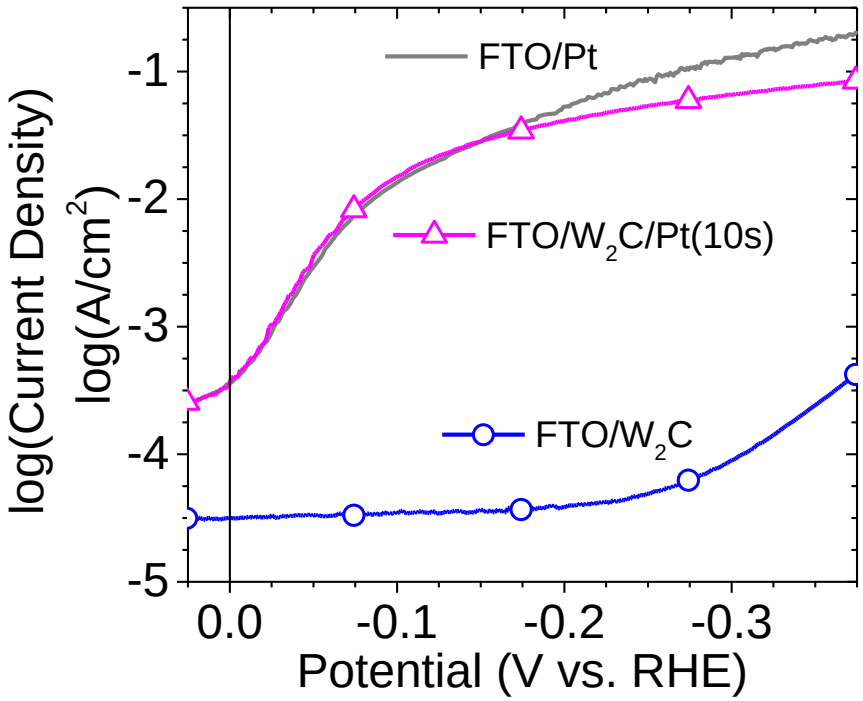


Figure D.4. Tafel plot for a FTO/Pt electrode and a FTO/$W_2C$ electrode with and without 10 sec of pulsed Pt deposition. Measurements were conducted in $N_2$ purged1 N $H_2SO_4$ using a scan rate of 1 mV/s with iR compensation.

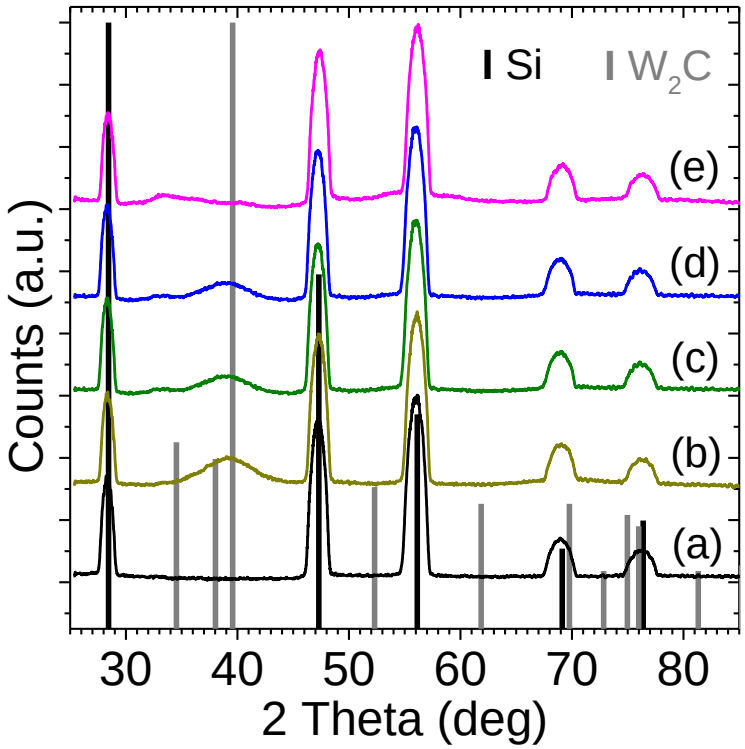


Figure D.5. XRD spectra for (a) p-Si, (b) p-Si/$W_2C$ as deposited, and p-Si/$W_2C$ after annealing at (c) 350 ºC, (d) 450 ºC, and (e) 550 ºC in Ar flow for 2 hrs. The $W_2C$ thickness was 148 Å thick. The black vertical lines are the reference pattern for Si (PDF#00-027-1402) and the grey vertical lines are the reference pattern for $W_2C$ (PDF#00-035-0776).

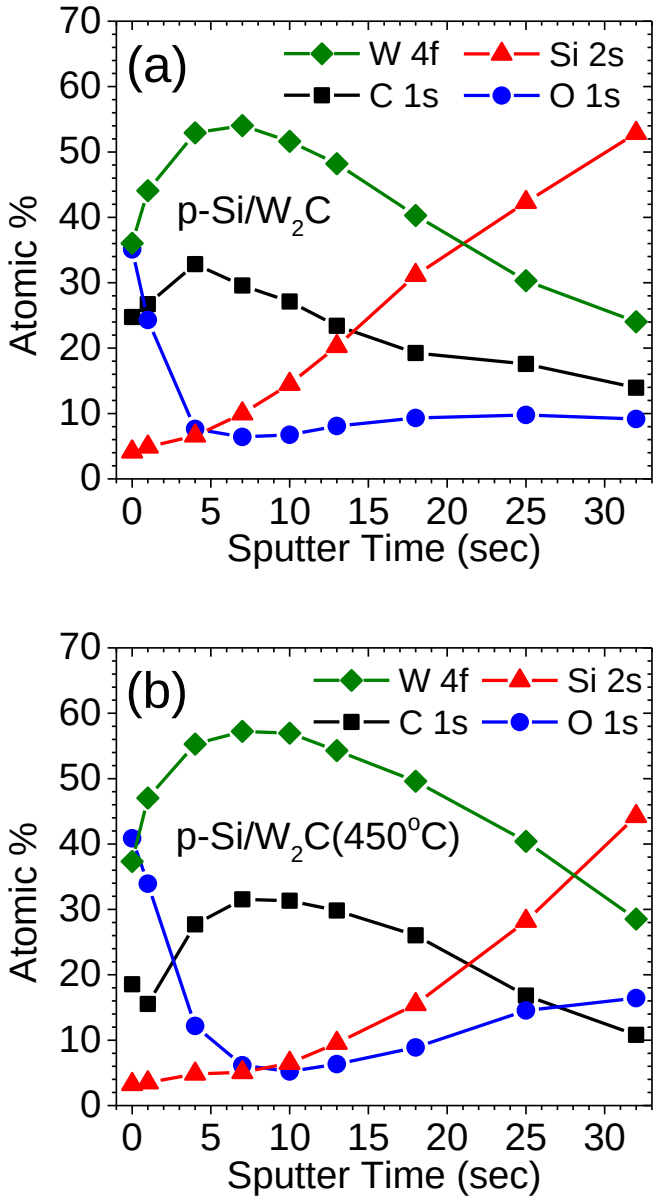


Figure D.6. Atomic concentration depth profiles obtained from XPS measurements for a p-Si/$W_2C$ photocathode (a) as deposited and (b) after annealing in Ar at 450 $^{o}$C for 2 hrs. The photocathodes had a $W_2C$ thickness of 49 Å. They were exposed to atmosphere before loading into the XPS chamber. Adventitious carbon (C 1s peak binding energy of 284 - 285 eV) was excluded from the atomic concentration calculations.

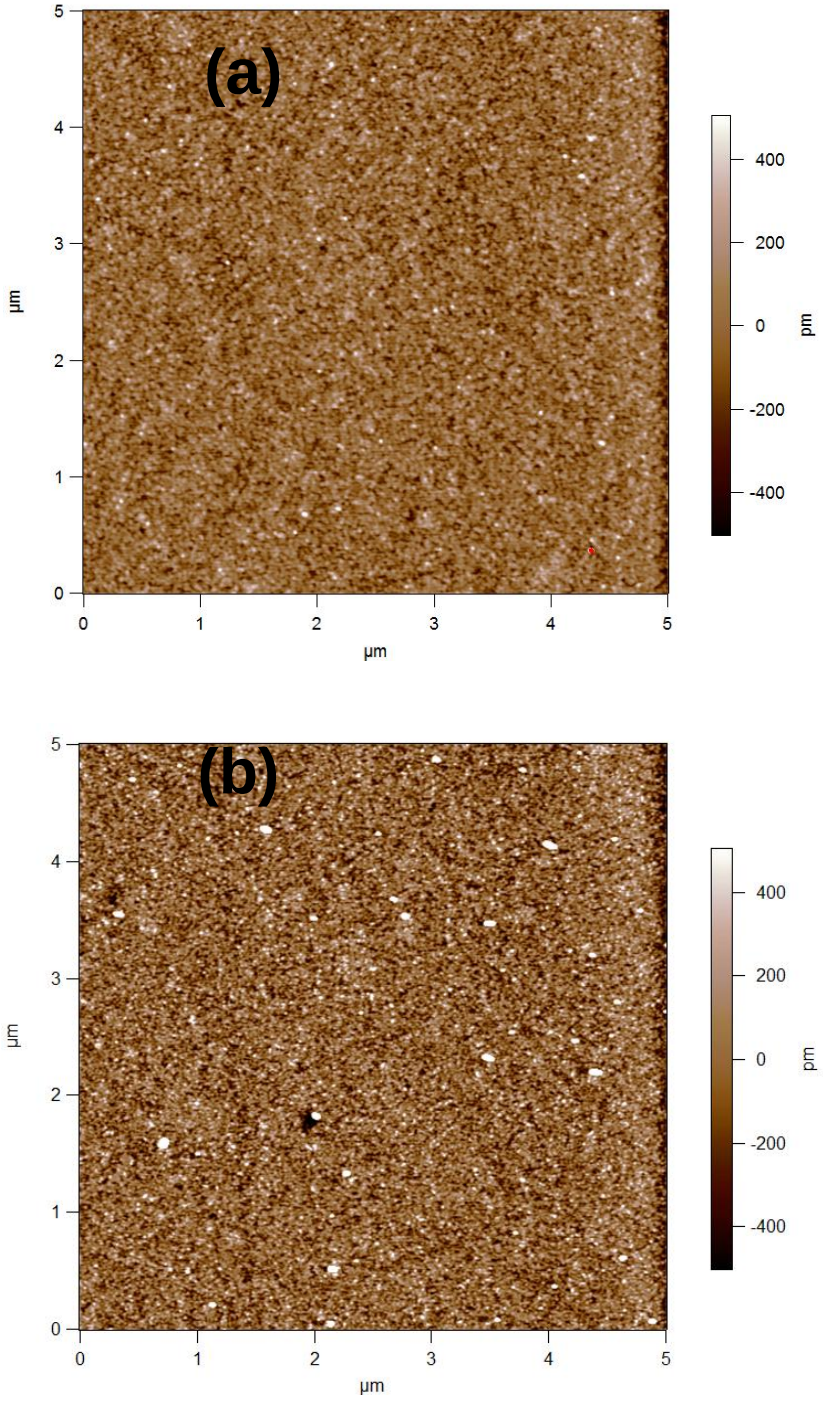


Figure D.7. Atomic force microscopy (AFM) results for p-Si/$W_2C$ (a) as deposited and (b) after annealing at (d) 450 $^oC$ in Ar flow for 2 hrs. The standard deviations were 1.2 Å and 3.1 Å for (a) and (b), respectively.

**Silicon Wafer Sputtering Rate in SIMS Dynamic Mode with $Bi_1^+$**

The sputtering rate of silicon in SIMS dynamic mode was calculated by AFM topographic measurement of a 50 µm x 50 µm area comprising a 20 µm x 20 µm area which was previously raster-scanned in 128 x 128 pixels by the $Bi_1$+ primary ion beam (~3 pA measured sample current) for 3000 seconds (Figure D.8). The 3D and 2D topography of the raster-scanned area are shown in Figures S8a and S8b, respectively. Sections of the AFM topographic map along the two major axis of the raster-scanned area are shown in Figure D.8c. The average depth of the sputtered crater was measured at about 12.5 nm resulting in a sputtering rate of about 0.042 Å/s.

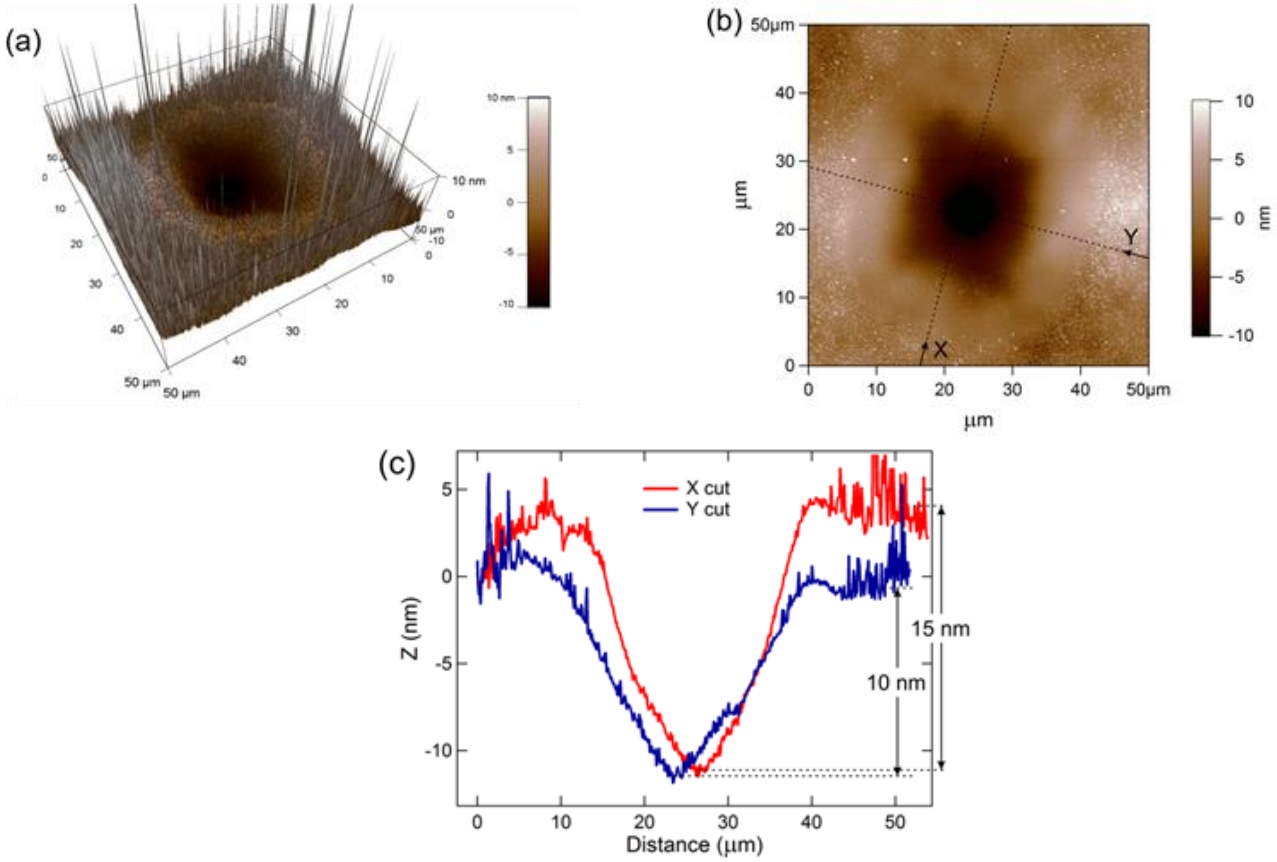


Figure D.8. AFM topography of the 20 µm x 20 µm sputtered area in (a) 3D and (b) 2D. (c) Topographic sections along the directions indicated in (b).

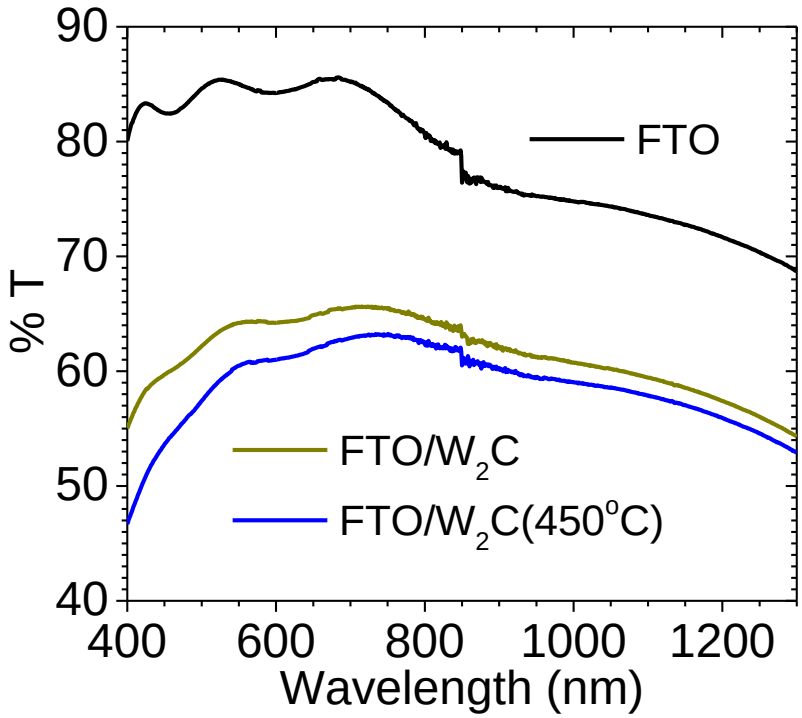


Figure D.9. UV-Vis transmission spectra for bare FTO and FTO/$W_2C$ electrodes. The $W_2C$ thickness was 49 Å. One of the FTO/$W_2C$ electrodes was not annealed and the other was annealed in Ar flow at 450°C for 2 hrs as indicated by the figure legend.

# Appendix E: Supplemental Information for Investigation of 35 Elements as Single Metal Oxides, Mixed Metal Oxides, or Dopants for Titanium Dioxide for Dye-Sensitized Solar Cells

## CHEMICALS

The following metal salts and chlorides were used to make arrays and films:

$NaNO_3$ (Alfa Aesar, 99.999%)
$KNO_3$ (Alfa Aesar, 99.997%)
$RbNO_3$ (Alfa Aesar, 99.975%)
$CsNO_3$ (Alfa Aesar, 99.999%)
$Mg(NO_3)_2 \cdot xH_2O$ (Alfa Aesar, 99.999%)
$Ca(NO_3)_2 \cdot 4H_2O$ (Fisher, Certified ACS)
$N_2O_6Sr$ (Alfa Aesar, 99.999%)
$BaN_2O_6$ (Alfa Aesar, 99.999%)
$Sc(NO_3)_3 \cdot xH_2O$ (Alfa Aesar 99.99%)
$Y(NO_3)_3 \cdot xH_2O$ (Alfa Aesar, 99.99%)
$La(NO_3)_3 \cdot 6H_2O$ (Alfa Aesar, 99.999%)
$Ce(NO_3)_3 \cdot 6H_2O$ (Alfa Aesar, 99.5%)
$TiCl_4$ (Alfa Aesar, 99.99%)
$ZrCl_4$ (Alfa Aesar, 99.5+%)
$VCl_3$ (Sigma Aldrich, 97%)
$NbCl_5$ (Sigma-Aldrich, 99.995%)
$TaCl_5$ (Alfa Aesar 99.99%)
$Cr(NO_3)_3 \cdot xH_2O$ (Alfa Aesar, 99.999%)
$(NH_4)_6Mo_7O_{24} \cdot 4H_2O$ (Sigma-Aldrich, 99.98%)
$(NH_4)_{10}W_{12}O_{41} \cdot 5H_2O$ (Sigma-Aldrich, 99.99%)
$Mn(NO_3)_2 \cdot xH_2O$ (Alfa Aesar, 99.999%)
$Fe(NO_3)_3 \cdot 9H_2O$ (Sigma Aldrich, 99.999%)
$Co(NO_3)_2 \cdot 6H_2O$ (Alfa Aesar, 99.999%)
$N_2NiO_6 \cdot 6H_2O$ (Alfa Aesar, 99.9985%)
$Cu(NO_3)_2 \cdot xH_2O$ (Alfa Aesar, 99.999%)
$AgNO_3$ (ACROS, p.a.)
$Zn(NO_3)_2 \cdot xH_2O$ (Sigma-Aldrich, 99.999%)
$Cd(NO_3)_2 \cdot 4H_2O$ (Alfa Aesar, 99.999%)
$Al(NO_3)_3 \cdot xH_2O$ (Alfa Aesar, 99.999%)
$Ga(NO_3)_3 \cdot xH_2O$ (Alfa Aesar, 99.999%)
$In(NO_3)_3 \cdot xH_2O$ (Alfa Aesar, 99.999%)
$GeCl_4$ (Gelest, 99.9+%)
$SnCl_4 \cdot xH_2O$ (Alfa Aesar, 98%)
$Pb(NO_3)_2$ (Fisher, Certified ACS)
$SbCl_3$ (AROS, 99.5%)
$Bi(NO_3)_3 \cdot xH_2O$ (Alfa Aesar, 99.999%)

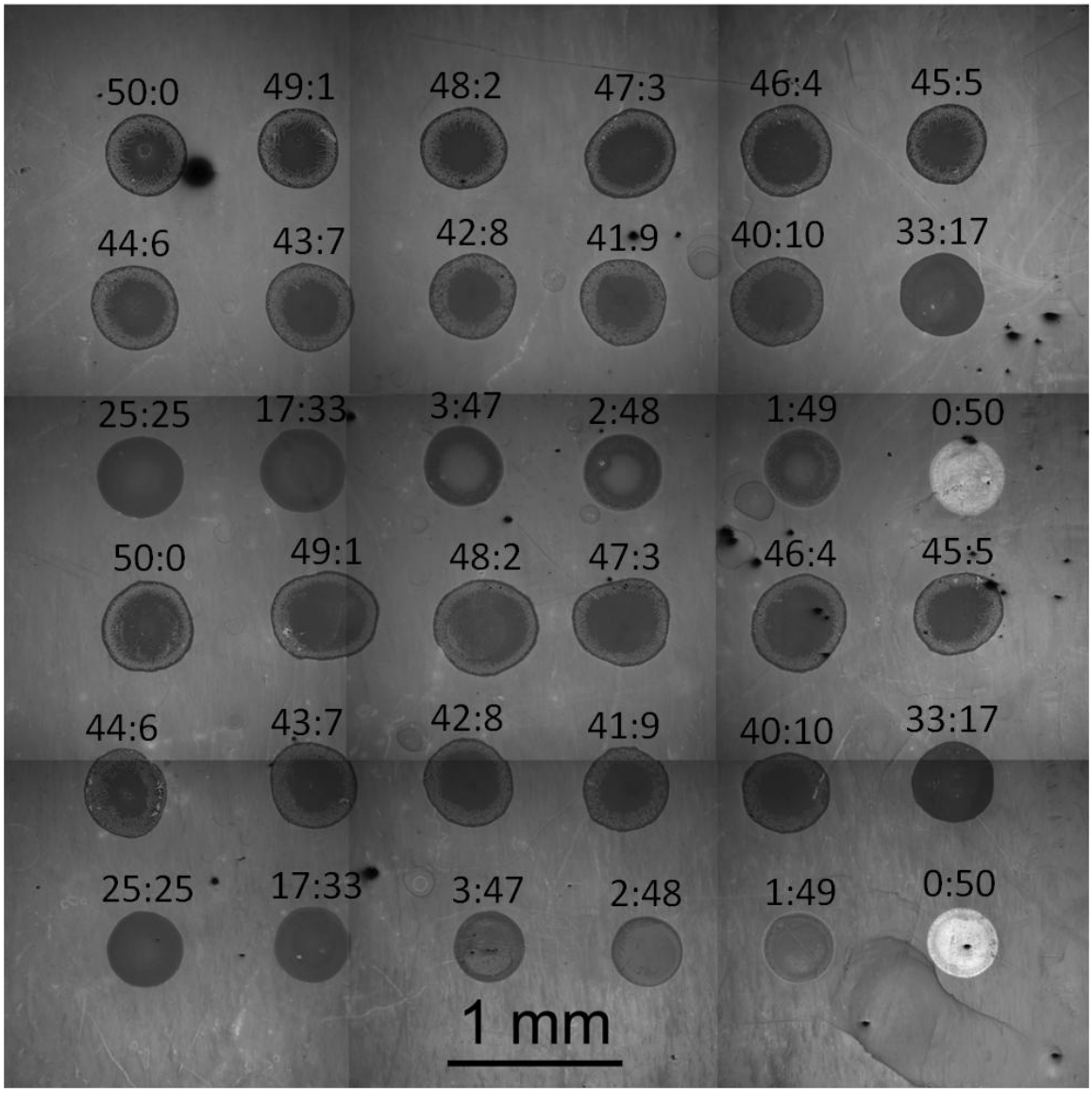


Figure E.1. Mosaic SEM image of the Ti-Sb array obtained using a Zeiss Supra 40 VP with ATLAS software. Each spot is labeled with the Ti:Sb atomic ratio. The image was flipped horizontally to match the array scan results for illumination through the backside of the FTO substrate.

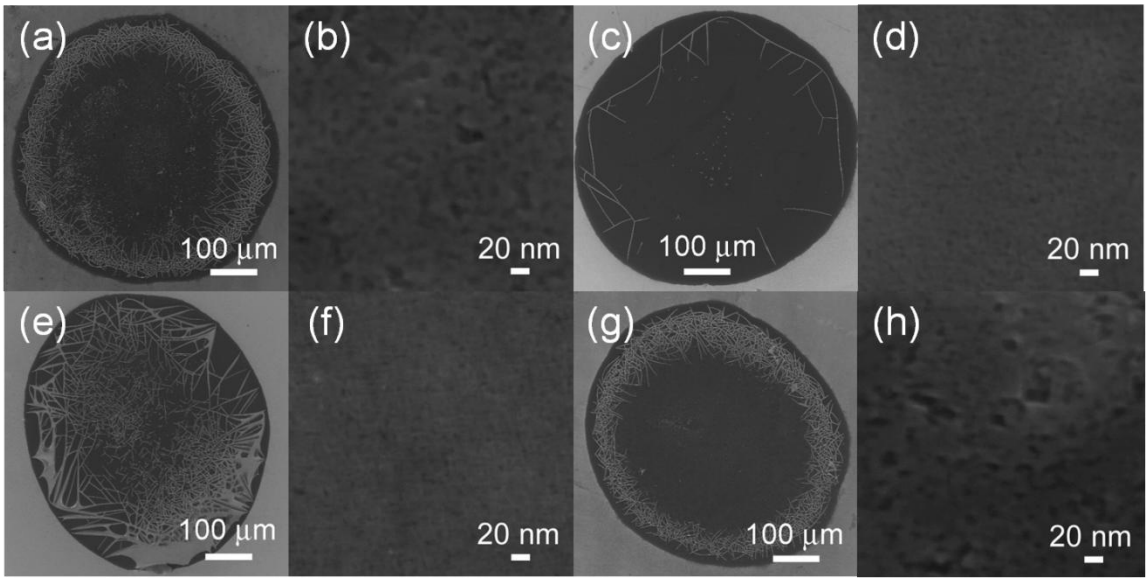


Figure E.2. Low magnification SEM images of (a) Ti oxide, (c) Ti:In=47:3 (6% In), (e) Ti:Sn=47:3 (6% Sn), and (g) Ti:Sb=47:3 (6% Sb) showing the entire array spots and high magnification SEM images of (b) Ti oxide, (d) Ti:In=47:3 (6% In), (f) Ti:Sn=47:3 (6% Sn), and (h) Ti:Sb=47:3 (6% Sb) from the center of the array spots.

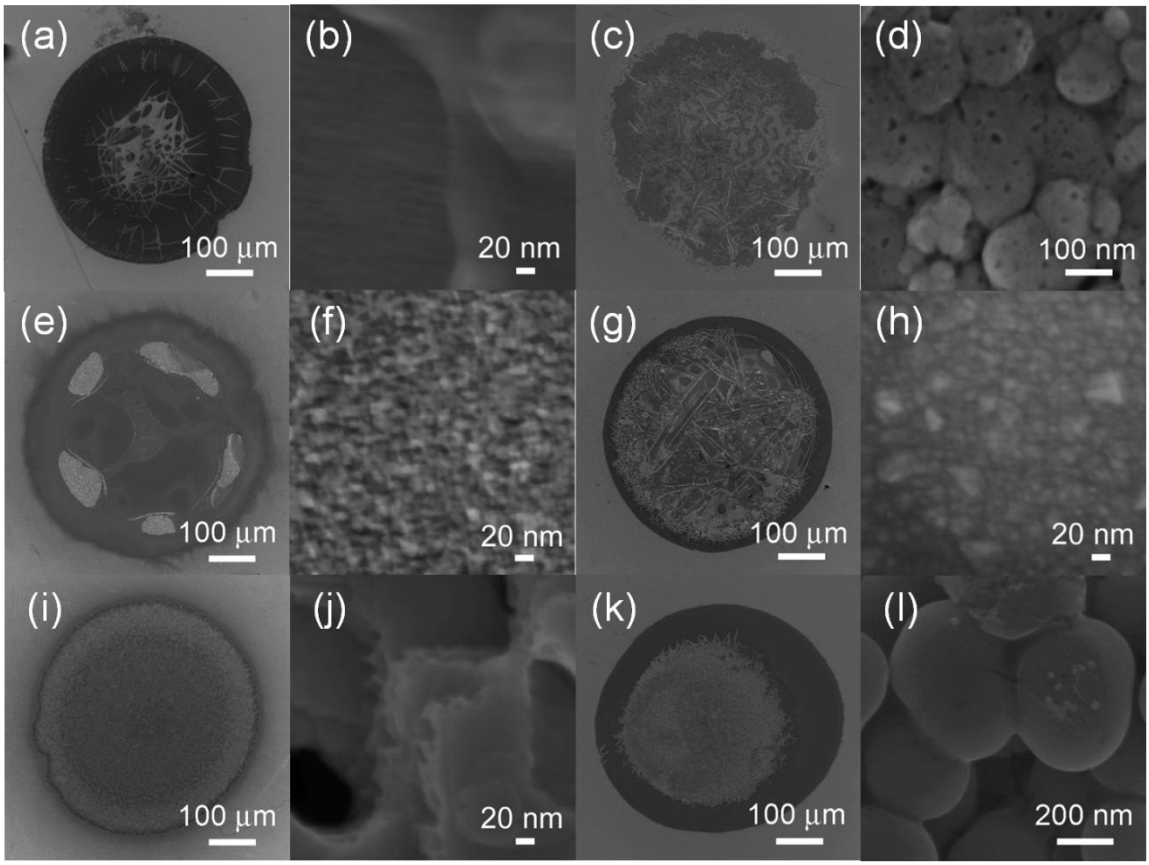


Figure E.3. Low magnification SEM images of (a) Fe oxide, (c) Zn oxide, (e) In oxide, (g) Sn oxide, (i) Bi oxide, and (k) Ti:W=33:17 oxide showing the entire array spots and high magnification SEM images of (b) Fe oxide, (d) Zn oxide, (f) In oxide, (h) Sn oxide, (j) Bi oxide, and (l) Ti:W=33:17 oxide from the center of the array spots.

| Film | Surface Composition from XPS Atomic % (metals basis) | Bulk Composition from EDS Atomic % (metals basis) |
|---|---|---|
| 6% In $TiO_2$ | 9.26% In | 5.85% In |
| 6% Sn $TiO_2$ | 9.61% Sn | 70.48% Sn* |
| 6% Sb $TiO_2$ | 7.56% Sb | 4.48% Sb |
| 2% Cr $TiO_2$ | 6.21% Cr | 5.28% Cr |
| 2% Cr, 6% Sb $TiO_2$ | 6.28% Cr, 5.72% Sb | 3.98% Cr, 9.35% Sb |

Table E.1. Surface and bulk compositions determined from XPS and EDS measurements for films synthesized by drop-casting. The integrated area of the XPS spectra were corrected using relative sensitivity factors (RSF) for the Kratos Axis Ultra along with a Shirley background.1 The EDS spectra were corrected using a Bremsstrahlung background. *For Sn, the bulk composition from EDS was high due to signal from the fluorine-doped tin oxide (FTO) substrate that the film was synthesized on.

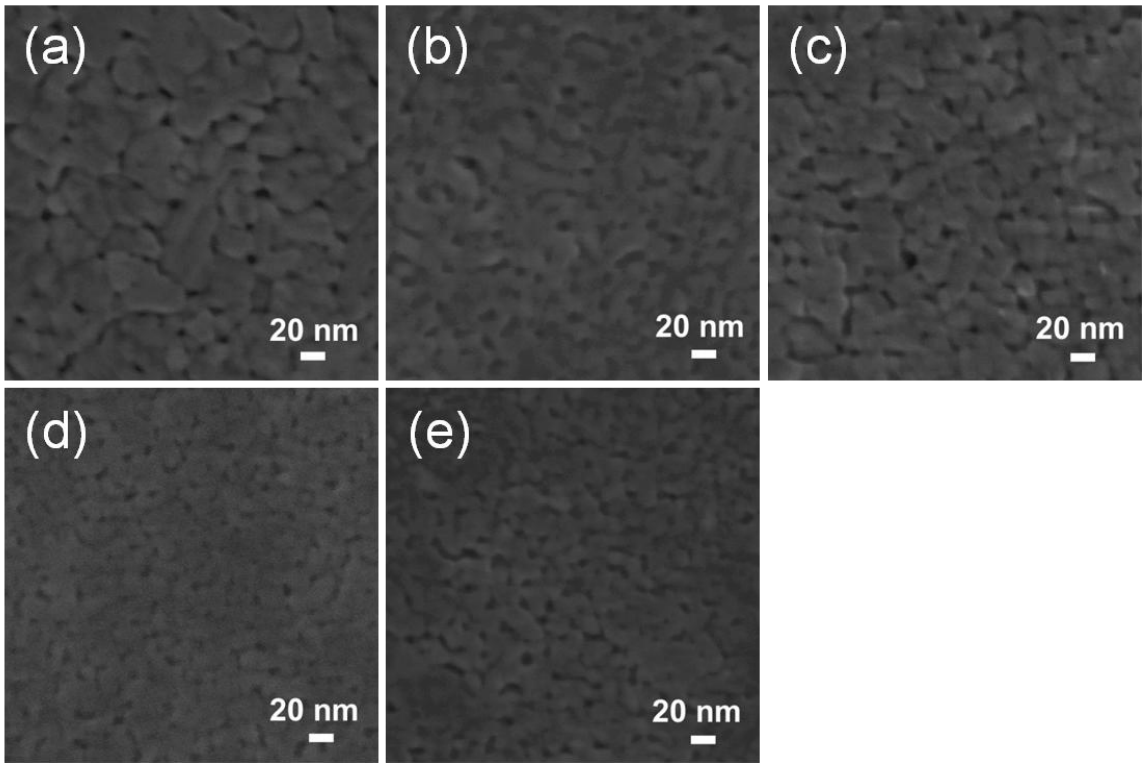


Figure E.4. SEM images of films synthesized by drop-casting composed of (a) $TiO_2$, (b) 6% In $TiO_2$ (c) 6% Sn $TiO_2$, (d) 6% Sb $TiO_2$, and (e) 2% Cr, 6% Sb $TiO_2$.

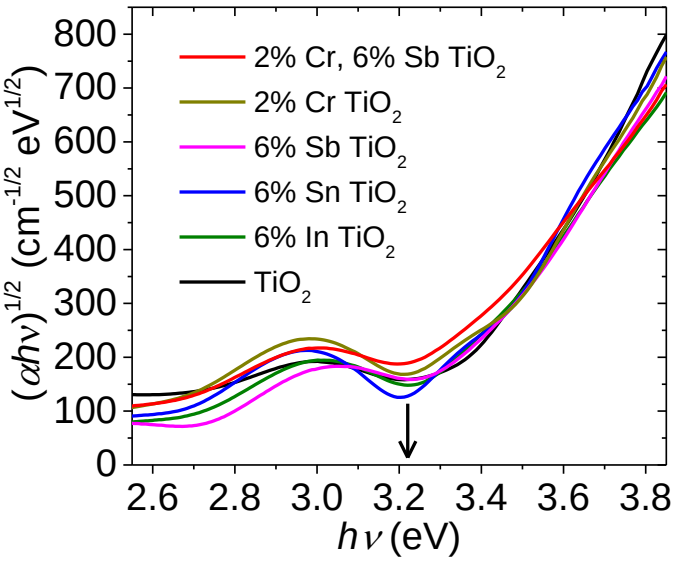


Figure E.5. Tauc plot for films synthesized by drop-casting with various compositions.

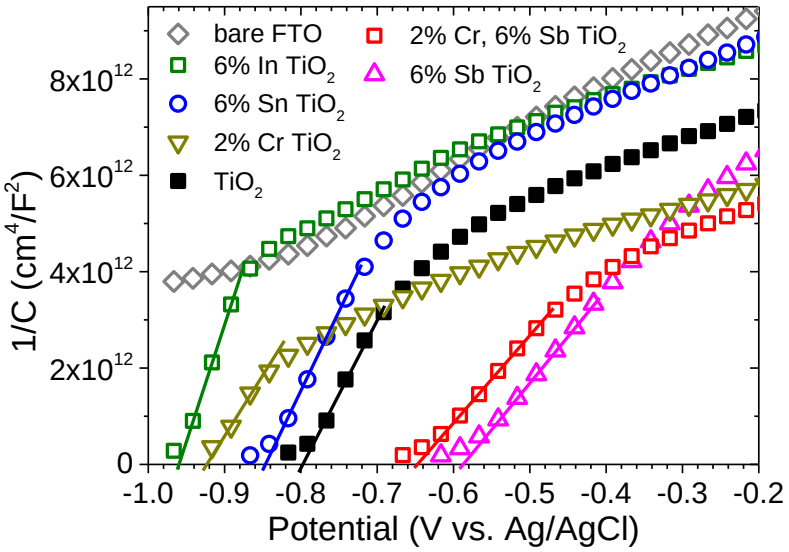


Figure E.6. Mott-Schottky plots for films synthesized by drop-casting with various compositions that had been used in typical DSC devices. $E_{FB}$ values were estimated as the Potential axis intercept values. Measurements were conducted in a 3-electrode cell containing 0.1 M NaOH aqueous electrolyte using voltage amplitude of 5 mV and frequency of 10 kHz

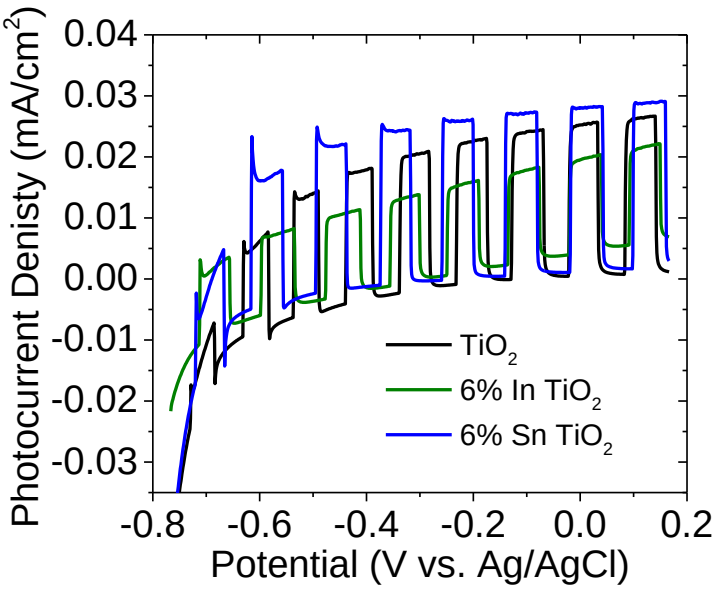


Figure E.7. Chopped (light/dark) J-V curves for films synthesized by drop-casting with compositions of $TiO_2$, 6% In $TiO_2$, 6% Sn $TiO_2$, and 6% Sb $TiO_2$ that had been used in typical DSC devices. Measurements were conducted in a 3-electrode cell containing 0.1 M NaOH aqueous electrolyte. The scan rate was 0.025 V/s. Backside illumination was used with a lamp power of 100 mW/cm$^2$.

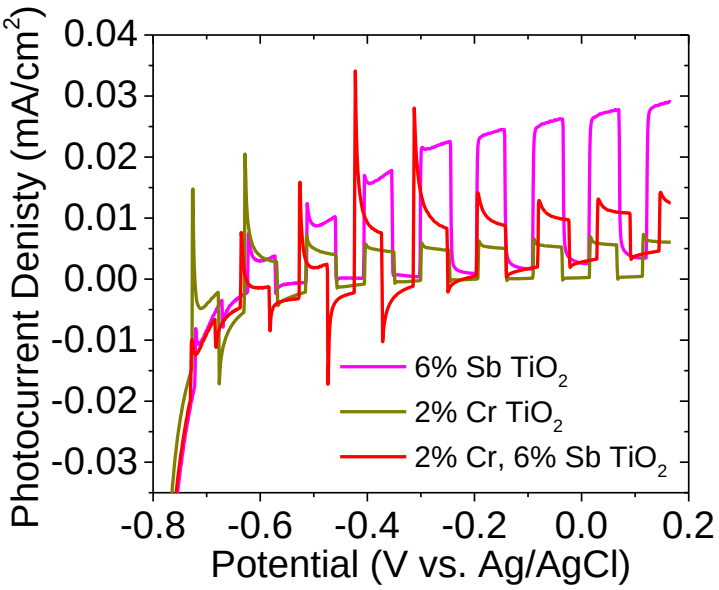


Figure E.8. Chopped (light/dark) J-V curves for films synthesized by drop-casting with compositions 6% Sb $TiO_2$, 2% Cr $TiO_2$, and 2% Cr, 6% Sb $TiO_2$ that had been used in typical DSC devices. Measurements were conducted in a 3-electrode cell containing 0.1 M NaOH aqueous electrolyte. The scan rate was 0.025 V/s. Backside illumination was used with a lamp power of 100 $mW/cm^2$.

## REFERENCES

Shirley, D. A. *Physical Review B* **1972**, *5*, 4709.

# Bibliography


Abdi, F. F.; Firet, N.; van de Krol, R. Chemcatchem 2013, 5, 490-496.

Abdi, F. F.; Savenije, T. J.; May, M. M.; Dam, B.; van de Krol, R. The Journal of Physical Chemistry Letters 2013, 4, 2752-2757.

Abelmann, L.; Lodder, C. Thin Solid Films 1997, 305, 1-21.

Adachi, M.; Sakamoto, M.; Jiu, J.; Ogata, Y.; Isoda, S. The Journal of Physical Chemistry B 2006, 110, 13872-13880.

Aharon-Shalom, E.; Heller, A. Journal of The Electrochemical Society 1982, 129, 2865-2866.

Anderman, M.; Kennedy, J. H. Journal of The Electrochemical Society 1984, 131, 21-26.

Annual Energy Outlook 2013, 2013.

Arai, T.; Konishi, Y.; Iwasaki, Y.; Sugihara, H.; Sayama, K. Journal of Combinatorial Chemistry 2007, 9, 574-581.

Ardo, S.; Meyer, G. J. Chemical Society Reviews 2009, 38, 115-164.

Armstrong, R. D.; Bell, M. F. Electrochimica Acta 1978, 23, 1111-1115.

Asahi, R.; Morikawa, T.; Ohwaki, T.; Aoki, K.; Taga, Y. Science 2001, 293, 269-271.

Aykan, K.; Halvorson, D.; Sleight, A. W.; Rogers, D. B. Journal of Catalysis 1974, 35, 401-406.

Bak, T.; Nowotny, J.; Rekas, M.; Sorrell, C. C. International Journal of Hydrogen Energy 2002, 27, 991-1022.

Bard, A. J.; Faulkner, L. R. Electrochemical Methods: Fundamentals and Applications; Second ed.; John Wiley & Sons, Inc.: New Jersey, 2001.

Bard, A. J.; Fox, M. A. Accounts of Chemical Research 1995, 28, 141-145.

Barrie, A.; Christensen, N. E. Physical Review B 1976, 14, 2442-2447.

Beer Annalen der Physik 1852, 162, 78-88.

Benson, J. E.; Kohn, H. W.; Boudart, M. Journal of Catalysis 1966, 5, 307-313.

Benziger, J. B.; Ko, E. I.; Madix, R. J. Journal of Catalysis 1978, 54, 414-425.

Berglund, S. P.; Flaherty, D. W.; Hahn, N. T.; Bard, A. J.; Mullins, C. B. The Journal of Physical Chemistry C 2011, 115, 3794-3802.

Berglund, S. P.; Lee, H. C.; Nunez, P. D.; Bard, A. J.; Mullins, C. B. Physical Chemistry Chemical Physics 2013, 15, 4554-4565.

Berglund, S. P.; Rettie, A. J. E.; Hoang, S.; Mullins, C. B. Physical Chemistry Chemical Physics 2012, 14, 7065-7075.

Bisquert, J.; Garcia-Belmonte, G.; Fabregat-Santiago, F.; Ferriols, N. S.; Bogdanoff, P.; Pereira, E. C. The Journal of Physical Chemistry B 2000, 104, 2287-2298.

Bluhm, H. Journal of Electron Spectroscopy and Related Phenomena 2010, 177, 71-84.

Bolton, J. R.; Strickler, S. J.; Connolly, J. S. Nature 1985, 316, 495-500.

BP Statistical Review of World Energy June 2013, 2013.

Briceño, G.; Chang, H.; Sun, X.; Schultz, P. G.; Xiang, X. D. Science 1995, 270, 273-275.

Brown, D. E.; Mahmood, M. N.; Man, M. C. M.; Turner, A. K. Electrochimica Acta 1984, 29, 1551-1556.

Brunschwig, B. S.; Chou, M. H.; Creutz, C.; Ghosh, P.; Sutin, N. Journal of the American Chemical Society 1983, 105, 4832.

Butler, M. A.; Ginley, D. S. Journal of the Electrochemical Society 1978, 125, 228-232.

Castillo, N. C.; Heel, A.; Graule, T.; Pulgarin, C. Applied Catalysis B: Environmental 2010, 95, 335.

Cesar, I.; Sivula, K.; Kay, A.; Zboril, R.; Grätzel, M. The Journal of Physical Chemistry C 2008, 113, 772-782.

Chandra, S. Photoelectrochemical Solar Cells; Gordon and Breach Science Publishers: New York, 1985.

Chatchai, P.; Murakami, Y.; Kishioka, S.-y.; Nosaka, A. Y.; Nosaka, Y. Electrochemical and Solid-State Letters 2008, 11, H160-H163.

Chatchai, P.; Murakami, Y.; Kishioka, S.-y.; Nosaka, A. Y.; Nosaka, Y. Electrochimica Acta 2009, 54, 1147-1152.

Chaudhary, Y. S.; Agrawal, A.; Shrivastav, R.; Satsangi, V. R.; Dass, S. International Journal of Hydrogen Energy 2004, 29, 131-134.

Chauhan, D.; Satsangi, V. R.; Dass, S.; Shrivastav, R. Bulletin of Materials Science 2006, 29, 709-716.

Chen, J. G. Chemical Reviews 1996, 96, 1477-1498.

Chen, W.-F.; Muckerman, J. T.; Fujita, E. Chemical Communications 2013, 49, 8896-8909.

Chen, X.; Shen, S.; Guo, L.; Mao, S. S. Chemical Reviews 2010, 110, 6503-6570.

Chen, Z. B.; Jaramillo, T. F.; Deutsch, T. G.; Kleiman-Shwarsctein, A.; Forman, A. J.; Gaillard, N.; Garland, R.; Takanabe, K.; Heske, C.; Sunkara, M.; McFarland, E. W.; Domen, K.; Miller, E. L.; Turner, J. A.; Dinh, H. N. Journal of Materials Research 2010, 25, 3-16.

Choi, W.; Termin, A.; Hoffmann, M. R. The Journal of Physical Chemistry 1994, 98, 13669-13679.

Dai, Q. X.; Xiao, H. Y.; Li, W. S.; Na, Y. Q.; Zhou, X. P. Applied Catalysis A: General 2005, 290, 25-35.

Dall'Antonia, L. H.; de Tacconi, N. R.; Chanmanee, W.; Timmaji, H.; Myung, N.; Rajeshwar, K. Electrochemical and Solid-State Letters 2010, 13, D29.

Danielson, E.; Golden, J. H.; McFarland, E. W.; Reaves, C. M.; Weinberg, W. H.; Wu, X. D. Nature 1997, 389, 944-948.

Dohnálek, Z.; Kimmel, G. A.; McCready, D. E.; Young, J. S.; Dohnálková, A.; Smith, R. S.; Kay, B. D. The Journal of Physical Chemistry B 2002, 106, 3526-3529.

Dominey, R. N.; Lewis, N. S.; Bruce, J. A.; Bookbinder, D. C.; Wrighton, M. S. Journal of the American Chemical Society 1982, 104, 467-482.

Dunkle, S. S.; Helmich, R. J.; Suslick, K. S. The Journal of Physical Chemistry C 2009, 113, 11980.

Esposito, D. V.; Hunt, S. T.; Kimmel, Y. C.; Chen, J. G. Journal of the American Chemical Society 2012, 134, 3025-3033.

Esposito, D. V.; Levin, I.; Moffat, T. P.; Talin, A. A. Nature Materials 2013, 12, 562-568.

Fabregat-Santiago, F.; Garcia-Belmonte, G.; Bisquert, J.; Bogdanoff, P.; Zaban, A. Journal of The Electrochemical Society 2003, 150, E293-E298.

Fabregat-Santiago, F.; Garcia-Belmonte, G.; Bisquert, J.; Zaban, A.; Salvador, P. The Journal of Physical Chemistry B 2001, 106, 334-339.

Fabregat-Santiago, F.; Garcia-Belmonte, G.; Mora-Sero, I.; Bisquert, J. Physical Chemistry Chemical Physics 2011, 13, 9083-9118.

Fabregat-Santiago, F.; García-Cañadas, J.; Palomares, E.; Clifford, J. N.; Haque, S. A.; Durrant, J. R.; Garcia-Belmonte, G.; Bisquert, J. Journal of Applied Physics 2004, 96, 6903-6907.

Fan, C. L.; Piron, D. L.; Sleb, A.; Paradis, P. Journal of The Electrochemical Society 1994, 141, 382-387.

Fan, C.; Piron, D. L.; Paradis, P. Electrochimica Acta 1994, 39, 2715-2722.

Feng, X.; Shankar, K.; Paulose, M.; Grimes, C. A. Angewandte Chemie International Edition 2009, 48, 8095-8098.

Flaherty, D. W.; Dohnálek, Z.; Dohnálková, A.; Arey, B. W.; McCready, D. E.; Ponnusamy, N.; Mullins, C. B.; Kay, B. D. The Journal of Physical Chemistry C 2007, 111, 4765-4773.

Flaherty, D. W.; Hahn, N. T.; Ferrer, D.; Engstrom, T. R.; Tanaka, P. L.; Mullins, C. B. The Journal of Physical Chemistry C 2009, 113, 12742-12752.

Flaherty, D. W.; Hahn, N. T.; May, R. A.; Berglund, S. P.; Lin, Y.-M.; Stevenson, K. J.; Dohnalek, Z.; Kay, B. D.; Mullins, C. B. Accounts of Chemical Research 2012, 45, 434-443.

Flaherty, D. W.; May, R. A.; Berglund, S. P.; Stevenson, K. J.; Mullins, C. B. Chemistry of Materials 2009, 22, 319-329.

Fosdick, S. E.; Berglund, S. P.; Mullins, C. B.; Crooks, R. M. Analytical Chemistry 2013, 85, 2493-2499.

Frank, A. J.; Kopidakis, N.; Lagemaat, J. v. d. Coordination Chemistry Reviews 2004, 248, 1165-1179.

Fujishima, A.; Honda, K. Nature 1972, 238, 37.

Galembeck, A.; Alves, O. L. Thin Solid Films 2000, 365, 90.

Gallop, M. A.; Barrett, R. W.; Dower, W. J.; Fodor, S. P. A.; Gordon, E. M. Journal of Medicinal Chemistry 1994, 37, 1233-1251.

Garcia-Esparza, A. T.; Cha, D.; Ou, Y.; Kubota, J.; Domen, K.; Takanabe, K. ChemSusChem 2013, 6, 168-181.

Gerischer, H. Journal of Electroanalytical Chemistry and Interfacial Electrochemistry 1977, 82, 133-143.

Ghijsen, J.; Tjeng, L. H.; van Elp, J.; Eskes, H.; Westerink, J.; Sawatzky, G. A.; Czyzyk, M. T. Physical Review B 1988, 38, 11322-11330.

Global Energy Perspectives, 2011.

Goldsmith, J. I.; Hudson, W. R.; Lowry, M. S.; Anderson, T. H.; Bernhard, S. Journal of the American Chemical Society 2005, 127, 7502-7510.

Gotic, M.; Music, S.; Ivanda, M.; Soufek, M.; Popovic, S. Journal of Molecular Structure 2005, 744-747, 535.

Grätzel, M. Journal of Photochemistry and Photobiology C: Photochemistry Reviews 2003, 4, 145-153.

Greeley, J.; Jaramillo, T. F.; Bonde, J.; Chorkendorff, I.; Norskov, J. K. Nat Mater 2006, 5, 909-913.

H. C. Casey, Jr.; Miller, B. I.; Pinkas, E. Journal of Applied Physics 1973, 44, 1281-1287.

Hafez, H.; Saif, M.; Abdel-Mottaleb, M. S. A. Journal of Power Sources 2011, 196, 5792-5796.

Hagfeldt, A.; Boschloo, G.; Sun, L.; Kloo, L.; Pettersson, H. Chemical Reviews 2010, 110, 6595-6663.

Hahn, N. T.; Holmberg, V. C.; Korgel, B. A.; Mullins, C. B. The Journal of Physical Chemistry C 2012, 116, 6459-6466.

Hahn, N. T.; Mullins, C. B. Chemistry of Materials 2010, 22, 6474-6482.

Hahn, N. T.; Ye, H.; Flaherty, D. W.; Bard, A. J.; Mullins, C. B. ACS Nano 2010, 4, 1977-1986.

Ham, D. J.; Ganesan, R.; Lee, J. S. International Journal of Hydrogen Energy 2008, 33, 6865-6872.

Han, L.; Koide, N.; Chiba, Y.; Mitate, T. Applied Physics Letters 2004, 84, 2433-2435.

Hardee, K. L.; Bard, A. J. Journal of The Electrochemical Society 1977, 124, 215-224.

Harnisch, F.; Sievers, G.; Schröder, U. Applied Catalysis B: Environmental 2009, 89, 455-458.

Hawkeye, M. M.; Brett, M. J. Journal of Vacuum Science & Technology A 2007, 25, 1317-1335.

He, H.; Xiao, P.; Zhou, M.; Zhang, Y.; Jia, Y.; Yu, S. Catalysis Communications 2011, 16, 140-143.

Heller, A.; Aspnes, D. E.; Porter, J. D.; Sheng, T. T.; Vadimsky, R. G. The Journal of Physical Chemistry 1985, 89, 4444-4452.

Herrmann, J.-M.; Disdier, J.; Pichat, P. Chemical Physics Letters 1984, 108, 618-622.

Higo, M.; Fujita, K.; Tanaka, Y.; Mitsushio, M.; Yoshidome, T. Applied Surface Science 2006, 252, 5083.

Hoang, S.; Berglund, S. P.; Hahn, N. T.; Bard, A. J.; Mullins, C. B. Journal of the American Chemical Society 2012, 134, 3659-3662.

Hoang, S.; Ngo, T. Q.; Berglund, S. P.; Fullon, R. R.; Ekerdt, J. G.; Mullins, C. B. ChemPhysChem 2013, 14, 2270-2276.

Hoffart, L.; Heider, U.; Jörissen, L.; Huggins, R. A.; Witschel, W. Solid State Ionics 1994, 72, Part 2, 195-198.

Hofmann, S. Thin Solid Films 2001, 398â€“399, 336-342.

Hoshikawa, T.; Yamada, M.; Kikuchi, R.; Eguchi, K. Journal of the Electrochemical Society 2005, 152, E68-E73.

Hwu, H. H.; Chen, J. G. Chemical Reviews 2004, 105, 185-212.

Irie, H.; Watanabe, Y.; Hashimoto, K. Chemistry Letters 2003, 32, 772-773.

Iwamoto, S.; Sazanami, Y.; Inoue, M.; Inoue, T.; Hoshi, T.; Shigaki, K.; Kaneko, M.; Maenosono, A. ChemSusChem 2008, 1, 401-403.

Iwanski, P.; Curran, J. S.; Gissler, W.; Memming, R. Journal of The Electrochemical Society 1981, 128, 2128-2133.

Jakšic, J. M.; Vojnovic, M. V.; Krstajic, N. V. Electrochimica Acta 2000, 45, 4151-4158.

Jandeleit, B.; Schaefer, D. J.; Powers, T. S.; Turner, H. W.; Weinberg, W. H. Angewandte Chemie International Edition 1999, 38, 2494-2532.

Jang, J. S.; Ham, D. J.; Lakshminarasimhan, N.; Choi, W. y.; Lee, J. S. Applied Catalysis A: General 2008, 346, 149-154.

Jang, J. S.; Lee, J.; Ye, H.; Fan, F.-R. F.; Bard, A. J. The Journal of Physical Chemistry C 2009, 113, 6719-6724.

Jang, J. S.; Yoon, K. Y.; Xiao, X.; Fan, F.-R. F.; Bard, A. J. Chemistry of Materials 2009, 21, 4803-4810.

Jaramillo, T. F.; Baeck, S.-H.; Kleiman-Shwarsctein, A.; Choi, K.-S.; Stucky, G. D.; McFarland, E. W. Journal of Combinatorial Chemistry 2004, 7, 264-271.

Jaramillo, T. F.; Baeck, S.-H.; Kleiman-Shwarsctein, A.; McFarland, E. W. Macromolecular Rapid Communications 2004, 25, 297-301.

Jiang, H.-q.; Endo, H.; Natori, H.; Nagai, M.; Kobayashi, K. Journal of the European Ceramic Society 2008, 28, 2955.

Jorand Sartoretti, C.; Alexander, B. D.; Solarska, R.; Rutkowska, I. A.; Augustynski, J.; Cerny, R. The Journal of Physical Chemistry B 2005, 109, 13685-13692.

Jose, R.; Thavasi, V.; Ramakrishna, S. Journal of the American Ceramic Society 2009, 92, 289-301.

Kanan, M. W.; Nocera, D. G. Science 2008, 321, 1072.

Kato, H.; Kudo, A. The Journal of Physical Chemistry B 2002, 106, 5029-5034.

Katz, J. E.; Gingrich, T. R.; Santori, E. A.; Lewis, N. S. Energy & Environmental Science 2009, 2, 103-112.

Kay, A.; Cesar, I.; Grätzel, M. Journal of the American Chemical Society 2006, 128, 15714-15721.

Ke, D.; Peng, T.; Ma, L.; Cai, P.; Jiang, P. Applied Catalysis A: General 2008, 350, 111.

Khaselev, O.; Turner, J. A. Science 1998, 280, 425-427.

Kim, C.; Kim, K.-S.; Kim, H. Y.; Han, Y. S. Journal of Materials Chemistry 2008, 18, 5809-5814.

Ko, K. H.; Lee, Y. C.; Jung, Y. J. Journal of Colloid and Interface Science 2005, 283, 482-487.

Koffyberg, F. P.; Benko, F. A. Journal of Applied Physics 1982, 53, 1173-1177.

Kohtani, S.; Yoshida, K.; Maekawa, T.; Iwase, A.; Kudo, A.; Miyabe, H.; Nakagaki, R. Physical Chemistry Chemical Physics 2008, 10, 2986.

Koops, S. E.; O'Regan, B. C.; Barnes, P. R. F.; Durrant, J. R. Journal of the American Chemical Society 2009, 131, 4808-4818.

Kudo, A.; Miseki, Y. Chemical Society Reviews 2009, 38, 253-278.

Kudo, A.; Omori, K.; Kato, H. Journal of the American Chemical Society 1999, 121, 11459-11467.

Kudo, A.; Ueda, K.; Kato, H.; Mikami, I. Catalysis Letters 1998, 53, 229.

Lazarov, V. K.; Plass, R.; Poon, H. C.; Saldin, D. K.; Weinert, M.; Chambers, S. A.; Gajdardziska-Josifovska, M. Physical Review B 2005, 71, 115434.

Lee, J.; Ye, H.; Pan, S.; Bard, A. J. Analytical Chemistry 2008, 80, 7445-7450.

Leonid, C.; Andrei, O.; Henryk, T.; Yang, J. W.; Chen, Q.; Khan, M. A. APPLIED PHYSICS LETTERS 1996, 69, 2531-2533.

Lettmann, C.; Hinrichs, H.; Maier, W. F. Angewandte Chemie International Edition 2001, 40, 3160-3164.

Levy, R. B.; Boudart, M. Science 1973, 181, 547-549.

Li, G.; Zhang, D.; Yu, J. C. Chemistry of Materials 2008, 20, 3983.

Li, M.; Zhao, L.; Guo, L. International Journal of Hydrogen Energy 2010, 35, 7127.

Liang, Y.; Tsubota, T.; Mooij, L. P. A.; van de Krol, R. The Journal of Physical Chemistry C 2011, 115, 17594-17598.

Lin, Y.; Battaglia, C.; Boccard, M.; Hettick, M.; Yu, Z.; Ballif, C.; Ager, J. W.; Javey, A. Nano Letters 2013.

Lin, Y.; Zhou, S.; Sheehan, S. W.; Wang, D. Journal of the American Chemical Society 2011, 133, 2398-2401.

Liu, H.; Nakamura, R.; Nakato, Y. ChemPhysChem 2005, 6, 2499-2502.

Liu, H.; Nakamura, R.; Nakato, Y. Electrochemical and Solid-State Letters 2006, 9, G187-G190.

Liu, H.; Nakamura, R.; Nakato, Y. Journal of The Electrochemical Society 2005, 152, G856-G861.

Liu, J.; Wang, H.; Wang, S.; Yan, H. Materials Science and Engineering B 2003, 104, 36.

Long, M.; Cai, W.; Cai, J.; Zhou, B.; Chai, X.; Wu, Y. The Journal of Physical Chemistry B 2006, 110, 20211-20216.

Long, M.; Cai, W.; Kisch, H. The Journal of Physical Chemistry C 2007, 112, 548.

Lü, X.; Mou, X.; Wu, J.; Zhang, D.; Zhang, L.; Huang, F.; Xu, F.; Huang, S. Advanced Functional Materials 2010, 20, 509-515.

Ma, C. a.; Liu, T.; Chen, L. Applied Surface Science 2010, 256, 7400-7405.

Ma, C.; Sheng, J.; Brandon, N.; Zhang, C.; Li, G. International Journal of Hydrogen Energy 2007, 32, 2824-2829.

Macagno, V. A.; Giordano, M. C.; Arvía, A. J. Electrochimica Acta 1969, 14, 335-357.

Maeda, K.; Domen, K. The Journal of Physical Chemistry C 2007, 111, 7851-7861.

Maier, W. F.; Stöwe, K.; Sieg, S. Angewandte Chemie International Edition 2007, 46, 6016-6067.

Marsen, B.; Cole, B.; Miller, E. L. Solar Energy Materials and Solar Cells 2008, 92, 1054-1058.

Maruska, H. P.; Ghosh, A. K. Solar Energy 1978, 20, 443-458.

May, R. A.; Flaherty, D. W.; Mullins, C. B.; Stevenson, K. J. The Journal of Physical Chemistry Letters, 2010, 1, 1264.

McKone, J. R.; Warren, E. L.; Bierman, M. J.; Boettcher, S. W.; Brunschwig, B. S.; Lewis, N. S.; Gray, H. B. Energy & Environmental Science 2011, 4, 3573-3583.

Meredith, J. C.; Smith, A. P.; Karim, A.; Amis, E. J. Macromolecules 2000, 33, 9747-9756.

Merrifield, R. B. Science 1965, 150, 178-185.

Mor, G. K.; Varghese, O. K.; Wilke, R. H. T.; Sharma, S.; Shankar, K.; Latempa, T. J.; Choi, K.-S.; Grimes, C. A. Nano Letters 2008, 8, 1906-1911.

Movchan, B. A.; Demchish, A. V. Physics of Metals and Metallography-USSR 1969, 28, 83.

Murakami, Y.; Ikarashi, M.; Hashizume, M.; Nosaka, A. Y.; Nosaka, Y. Electrochemical and Solid-State Letters 2008, 11, H42.

Nakaoka, K.; Ueyama, J.; Ogura, K. Journal of The Electrochemical Society 2004, 151, C661-C665.

Nakato, Y.; Tonomura, S.; Tsubomura, H. Berichte der Bunsengesellschaft für physikalische Chemie 1976, 80, 1289-1293.

Nakato, Y.; Yano, H.; Nishiura, S.; Ueda, T.; Tsubomura, H. Journal of Electroanalytical Chemistry and Interfacial Electrochemistry 1987, 228, 97-108.

Nakayama, A.; Suzuki, E.; Ohmori, T. Applied Surface Science 2002, 189, 260-264.

Navas, J.; Fernández-Lorenzo, C.; Aguilar, T.; Alcántara, R.; Martín-Calleja, J. physica status solidi (a) 2011, 209, 378-385.

Nayak, A. P.; Dolocan, A.; Lee, J.; Chang, H.-Y.; Pandhi, T.; Tao, L. I.; Holt, M.; Akinwande, D. Nano 2013, 0, 1450002.

Neves, M. C.; Trindade, T. Thin Solid Films 2002, 406, 93.

Ng, Y. H.; Iwase, A.; Kudo, A.; Amal, R. The Journal of Physical Chemistry Letters 2010, 1, 2607-2612.

Nikolov, I.; Petrov, K.; Vitanov, T.; Guschev, A. International Journal of Hydrogen Energy 1983, 8, 437-440.

Nozik, A. J.; Memming, R. d. The Journal of Physical Chemistry 1996, 100, 13061-13078.

Oh, J.; Deutsch, T. G.; Yuan, H.-C.; Branz, H. M. Energy & Environmental Science 2011, 4, 1690-1694.

O'Regan, B.; Grätzel, M. Nature 1991, 353, 737-740.

Oshikiri, M.; Boero, M.; Ye, J. H.; Zou, Z. G.; Kido, G. Journal of Chemical Physics 2002, 117, 7313.

Osterloh, F. E. Chemical Society Reviews 2013, 42, 2294-2320.

Osterloh, F. E. Chemistry of Materials 2007, 20, 35-54.

Palomares, E.; Clifford, J. N.; Haque, S. A.; Lutz, T.; Durrant, J. R. Chemical Communications 2002, 1464-1465.

Paracchino, A.; Laporte, V.; Sivula, K.; Grätzel, M.; Thimsen, E. Nat Mater 2011, 10, 456-461.

Park, H. S.; Kweon, K. E.; Ye, H.; Paek, E.; Hwang, G. S.; Bard, A. J. The Journal of Physical Chemistry C 2011, 115, 17870-17879.

Patt, J.; Moon, D.; Phillips, C.; Thompson, L. Catalysis Letters 2000, 65, 193-195.

Peter, L. M. Philosophical Transactions of the Royal Society a-Mathematical Physical and Engineering Sciences 2012, 369, 1840-1856.

Pilli, S. K.; Furtak, T. E.; Brown, L. D.; Deutsch, T. G.; Turner, J. A.; Herring, A. M. Energy & Environmental Science 2011, 4, 5028-5034.

Prins, R. Chemical Reviews 2012, 112, 2714-2738.

Raj, I. A. Journal of Materials Science 1993, 28, 4375-4382.

Rettie, A. J. E.; Lee, H. C.; Marshall, L. G.; Lin, J.-F.; Capan, C.; Lindemuth, J.; McCloy, J. S.; Zhou, J.; Bard, A. J.; Mullins, C. B. Journal of the American Chemical Society 2013, 135, 11389-11396.

Rivers, S. B.; Bernhardt, G.; Wright, M. W.; Frankel, D. J.; Steeves, M. M.; Lad, R. J. Thin Solid Films 2007, 515, 8684-8688.

Robbie, K.; Sit, J. C.; Brett, M. J. Advanced techniques for glancing angle deposition; AVS, 1998; Vol. 16.

Rullens, F. o.; Laschewsky, A.; Devillers, M. Chemistry of Materials 2006, 18, 771.

Saadi, S.; Bouguelia, A.; Trari, M. Renewable Energy 2006, 31, 2245-2256.

Santato, C.; Ulmann, M.; Augustynski, J. The Journal of Physical Chemistry B 2001, 105, 936-940.

Santos, J. B. O.; Valença, G. P.; Rodrigues, J. A. J. Journal of Catalysis 2002, 210, 1-6.

Sayama, K.; Nomura, A.; Arai, T.; Sugita, T.; Abe, R.; Yanagida, M.; Oi, T.; Iwasaki, Y.; Abe, Y.; Sugihara, H. The Journal of Physical Chemistry B 2006, 110, 11352-11360.

Sayama, K.; Nomura, A.; Zou, Z.; Abe, R.; Abe, Y.; Arakawa, H. Chemical Communications 2003, 2908-2909.

Sayama, K.; Sugihara, H.; Arakawa, H. Chemistry of Materials 1998, 10, 3825-3832.

Scaife, D. E. Solar Energy 1980, 25, 41-54.

Seabold, J. A.; Choi, K.-S. Journal of the American Chemical Society 2012, 134, 2186-2192.

Senkan, S. M. Nature 1998, 394, 350-353.

Serpone, N.; Lawless, D.; Disdier, J.; Herrmann, J.-M. Langmuir 1994, 10, 643-652.

Seyler, M.; Stoewe, K.; Maier, W. F. Applied Catalysis B: Environmental 2007, 76, 146-157.

Shannon, R. D. Acta Crystallographica Section A 1976, 32, 751-767.

Shirley, D. A. Physical Review B 1972, 5, 4709.

Sleight, A. W.; Aykan, K.; Rogers, D. B. Journal of Solid State Chemistry 1975, 13, 231-236.

Smith, D. R.; Fickett, F. R. Journal of Research of the National Institute of Standards and Technology 1995, 100, 119-171.

Smith, J. F. Journal of Alloy Phase Diagrams 1990, 6, 19.

Sokolsky, D. V.; Palanker, V. S.; Baybatyrov, E. N. Electrochimica Acta 1975, 20, 71-77.

Stefik, M.; Cornuz, M.; Mathews, N.; Hisatomi, T.; Mhaisalkar, S.; Grätzel, M. Nano Letters 2012, 12, 5431-5435.

Strobel, R.; Metz, H. J.; Pratsinis, S. E. Chemistry of Materials 2008, 20, 6346.

Su, J.; Guo, L.; Yoriya, S.; Grimes, C. A. Crystal Growth & Design 2009, 10, 856.

Svegl, F.; Orel, B.; Grabec-Svegl, I.; Kaucic, V. Electrochimica Acta 2000, 45, 4359.

Tachibana, Y.; Moser, J. E.; Grätzel, M.; Klug, D. R.; Durrant, J. R. The Journal of Physical Chemistry 1996, 100, 20056-20062.

Tang, H.; Prasad, K.; Sanjines, R.; Schmid, P. E.; Levy, F. Journal of Applied Physics 1994, 75, 2042-2047.

Terrier, C.; Chatelon, J. P.; Berjoan, R.; Roger, J. A. Thin Solid Films 1995, 263, 37-41.

Tilley, S. D.; Cornuz, M.; Sivula, K.; Grätzel, M. Angewandte Chemie International Edition 2010, 49, 6405-6408.

Tokunaga, S.; Kato, H.; Kudo, A. Chemistry of Materials 2001, 13, 4624-4628.

Trari, M.; Bouguelia, A.; Bessekhouad, Y. Solar Energy Materials and Solar Cells 2006, 90, 190-202.

Tsai, M. Y.; d'Heurle, F. M.; Johnson, R. W. Journal of Applied Physics 1981, 52, 5350-5355.

Tseung, A. C. C.; Chen, K. Y. Catalysis Today 1997, 38, 439-443.

Tsvetkov, N.; Larina, L.; Shevaleevskiy, O.; Ahn, B. T. Energy & Environmental Science 2010, 4, 1480-1486.

Tsvetkov, N.; Larina, L.; Shevaleevskiy, O.; Ahn, B. T. Journal of the Electrochemical Society 2011, 158, B1281-B1285.

Ueda, K.; Nakato, Y.; Sakai, Y.; Matsumura, M.; Tsubomura, H. Journal of Applied Physics 1988, 64, 1513-1518.

Umebayashi, T.; Yamaki, T.; Itoh, H.; Asai, K. APPLIED PHYSICS LETTERS 2002, 81, 454-456.

Valentin, C. D.; Pacchioni, G.; Onishi, H.; Kudo, A. Chemical Physics Letters 2009, 469, 166-171.

van de Krol, R.; Grätzel, M. Photoelectrochemical Hydrogen Production; Springer: New York Dordrecht Heidelberg London, 2012.

Vasic, D. D.; Pašti, I. A.; Mentus, S. V. International Journal of Hydrogen Energy 2013, 38, 5009-5018.

Wagner, C. D.; Naumkin, A. V.; Kraut-Vass, A.; Allison, J. W.; Powell, C. J.; John R. Rumble, J.; August 15, 2007 ed.; National Institute of Standards and Technology, Gaithersburg.

Wagner, R. S.; Ellis, W. C. Applied Physics Letters 1964, 4, 89.

Walsh, A.; Yan, Y.; Huda, M. N.; Al-Jassim, M. M.; Wei, S.-H. Chemistry of Materials 2009, 21, 547-551.

Walter, M. G.; Warren, E. L.; McKone, J. R.; Boettcher, S. W.; Mi, Q.; Santori, E. A.; Lewis, N. S. Chemical Reviews 2011, 111, 5815-5815.

Wang, D.; Li, R.; Zhu, J.; Shi, J.; Han, J.; Zong, X.; Li, C. The Journal of Physical Chemistry C 2012, 116, 5082-5089.

Wang, K.-P.; Teng, H. Physical Chemistry Chemical Physics 2009, 11, 9489-9496.

Wang, M.; Bai, S.; Chen, A.; Duan, Y.; Liu, Q.; Li, D.; Lin, Y. Electrochimica Acta 2012, 77, 54-59.

Weber, M. F.; Dignam, M. J. International Journal of Hydrogen Energy 1986, 11, 225-232.

Weidman, M. C.; Esposito, D. V.; Hsu, Y.-C.; Chen, J. G. Journal of Power Sources 2012, 202, 11-17.

Woodhouse, M.; Herman, G. S.; Parkinson, B. A. Chemistry of Materials 2005, 17, 4318-4324.

Woodhouse, M.; Parkinson, B. A. Chemistry of Materials 2008, 20, 2495-2502.

World Energy Outlook 2012, 2012.

Wu, M.; Shen, P. K.; Wei, Z.; Song, S.; Nie, M. Journal of Power Sources 2007, 166, 310-316.

Xi, G. C.; Ye, J. H. Chemical Communications 2010, 46, 1893.

Xu, Y.; Schoonen, M. A. A. American Mineralogist 2000, 85, 543-556.

Yamamoto, S.; Bluhm, H.; Andersson, K.; Ketteler, G.; Ogasawara, H.; Salmeron, M.; Nilsson, A. Journal of Physics-Condensed Matter 2008, 20, 14.

Yang, C.-J. Energy Policy 2009, 37, 1805-1808.

Yang, J. C.; Kim, Y. C.; Shul, Y. G.; Shin, C. H.; Lee, T. K. Applied Surface Science 1997, 121-122, 525-529.

Yao, W.; Iwai, H.; Ye, J. Dalton Transactions 2008, 1426-1430.

Yao, W.; Ye, J. The Journal of Physical Chemistry B 2006, 110, 11188-11195.

Ye, H.; Lee, J.; Jang, J. S.; Bard, A. J. The Journal of Physical Chemistry C 2010, 114, 13322-13328.

Ye, H.; Park, H. S.; Bard, A. J. The Journal of Physical Chemistry C 2011, 115, 12464-12470.

Yin, W.-J.; Tang, H.; Wei, S.-H.; Al-Jassim, M. M.; Turner, J.; Yan, Y. Physical Review B 2010, 82, 045106.

Yin, W.-J.; Wei, S.-H.; Al-Jassim, M. M.; Turner, J.; Yan, Y. Physical Review B 2011, 83, 155102.

Yokoyama, D.; Minegishi, T.; Maeda, K.; Katayama, M.; Kubota, J.; Yamada, A.; Konagai, M.; Domen, K. Electrochemistry Communications 2010, 12, 851-853.

Yu, J.; Kudo, A. Chemistry Letters 2005, 34, 850.

Yu, J.; Zhang, Y.; Kudo, A. Journal of Solid State Chemistry 2009, 182, 223.

Zaban, A.; Chen, S. G.; Chappel, S.; Gregg, B. A. Chemical Communications 2000, 2231-2232.

Zellner, M. B.; Chen, J. G. Catalysis Today 2005, 99, 299-307.

Zhang, H.; Liu, J.; Wang, H.; Zhang, W.; Yan, H. Journal of Nanoparticle Research 2008, 10, 767.

Zhang, L.; Chen, D.; Jiao, X. The Journal of Physical Chemistry B 2006, 110, 2668.

Zhang, X.; Liu, F.; Huang, Q.-L.; Zhou, G.; Wang, Z.-S. The Journal of Physical Chemistry C 2011, 115, 12665-12671.

Zhang, Y.; Wang, L.; Liu, B.; Zhai, J.; Fan, H.; Wang, D.; Lin, Y.; Xie, T. Electrochimica Acta 2011, 56, 6517-6523.

Zheng, Y.; Wu, J.; Duan, F.; Xie, Y. Chemistry Letters 2007, 36, 520.

Zhong, D. K.; Choi, S.; Gamelin, D. R. Journal of the American Chemical Society 2011, 133, 18370-18377.

Zhou, L.; Wang, W.; Liu, S.; Zhang, L.; Xu, H.; Zhu, W. Journal of Molecular Catalysis A: Chemical 2006, 252, 120.

Zhou, L.; Wang, W.; Zhang, L.; Xu, H.; Zhu, W. The Journal of Physical Chemistry C 2007, 111, 13659.

Zimmerman, J. D.; Lassiter, B. E.; Xiao, X.; Sun, K.; Dolocan, A.; Gearba, R.; Vanden Bout, D. A.; Stevenson, K. J.; Wickramasinghe, P.; Thompson, M. E.; Forrest, S. R. ACS Nano 2013, 7, 9268-9275.

Zou, Z.; Arakawa, H. Journal of Photochemistry and Photobiology A: Chemistry 2003, 158, 145-162.

Zou, Z.; Ye, J.; Sayama, K.; Arakawa, H. Nature 2001, 414, 625-627.

# Vita

Sean Patrick Berglund, the son of John and Judith Berglund, was born in Portland, Oregon. He had three siblings and grew up in the Portland metropolitan area. As an undergraduate student, Sean attended Oregon State University where he earned a B.S. degree in Chemical Engineering in 2003. He then worked as a process engineer at Intel Corporation in Hillsboro, Oregon for 4.5 years. In 2008 he decided to return to academia and enrolled in the chemical engineering Ph.D. program at the University of Texas at Austin. Shortly he began working in the research group of Prof. C. Buddie Mullins. In 2010 Sean received a National Science Foundation Graduate Research Fellowship.

Email Address: sean.berglund@gmail.com

This dissertation was typed by the author.